UNICAMP

ADRIANA BONILLA RIAÑO

FILM THICKNESS MEASUREMENT WITH HIGH SPATIAL AND TEMPORAL RESOLUTION PLANAR CAPACITIVE SENSING IN OIL-WATER PIPE FLOW

MEDIDA DA ESPESSURA DE FILME USANDO SENSOR CAPACITIVO DE ALTA RESOLUÇÃO ESPACIAL E TEMPORAL PARA ESCOAMENTOS ÓLEO–ÁGUA EM TUBOS

CAMPINAS
2015

UNIVERSIDADE ESTADUAL DE CAMPINAS
FACULDADE DE ENGENHARIA MECÂNICA
E INSTITUTO DE GEOCIÊNCIAS

ADRIANA BONILLA RIAÑO

FILM THICKNESS MEASUREMENT WITH HIGH SPATIAL AND TEMPORAL RESOLUTION PLANAR CAPACITIVE SENSING IN OIL-WATER PIPE FLOW

MEDIDA DA ESPESSURA DE FILME USANDO SENSOR CAPACITIVO DE ALTA RESOLUÇÃO ESPACIAL E TEMPORAL PARA ESCOAMENTOS ÓLEO – ÁGUA EM TUBOS

Thesis presented to the Mechanical Engineering Faculty and Geosciences Institute of the University of Campinas in partial fulfillment of the requirements for the degree of Doctor in Petroleum Sciences and Engineering in the area of Exploitation.

Tese apresentada à Faculdade de Engenharia Mecânica e Instituto de Geociências da Universidade Estadual de Campinas como parte dos requisitos exigidos para a obtenção do título de Doutora em Ciências e Engenharia de Petróleo na área de Explotação.

Orientador: Prof. Dr. Antonio Carlos Bannwart
Co-orientador: Prof. Dr. Oscar Mauricio Hernandez Rodriguez

Este exemplar corresponde à versão final da tese defendida pela aluna Adriana Bonilla Riaño, e orientada pelo Prof. Dr. Antonio Carlos Bannwart

CAMPINAS
2015

Ficha catalográfica
Universidade Estadual de Campinas
Biblioteca da Área de Engenharia e Arquitetura
Elizangela Aparecida dos Santos Souza - CRB 8/8098

Bonilla Riaño, Adriana, 1980-
B642f Film thickness measurement with high spatial and temporal resolution planar capacitive sensing in oil-water pipe flow / Adriana Bonilla Riaño. – Campinas, SP : [s.n.], 2015.

Orientador: Antonio Carlos Bannwart.
Coorientador: Oscar Mauricio Hernandez Rodriguez.
Tese (doutorado) – Universidade Estadual de Campinas, Faculdade de Engenharia Mecânica e Instituto de Geociências.

1. Sensor. 2. Medidas elétricas. 3. Escoamento multifásico. 4. Emulsão de óleo em água. 5. Método dos elementos finitos. I. Bannwart, Antonio Carlos,1955-. II. Hernandez Rodriguez, Oscar Mauricio. III. Universidade Estadual de Campinas. Faculdade de Engenharia Mecânica. IV. Título.

Informações para Biblioteca Digital

Título em outro idioma: Medida da espessura de filme usando sensor capacitivo de alta resolução espacial e temporal para escoamentos óleo-água em tubos
Palavras-chave em inglês:
Sensor
Electrical measurements
Multiphase flow
Emulsion of oil in water
Finite element method
Área de concentração: Explotação
Titulação: Doutora em Ciências e Engenharia de Petróleo
Banca examinadora:
Antonio Carlos Bannwart [Orientador]
Luiz Felipe Mendes de Moura
Niederauer Mastelari
Emerson dos Reis
Juliana Braga Rodrigues Loureiro
Data de defesa: 29-07-2015
Programa de Pós-Graduação: Ciências e Engenharia de Petróleo

UNIVERSIDADE ESTADUAL DE CAMPINAS

FACULDADE DE ENGENHARIA MECÂNICA

E INSTITUTO DE GEOCIÊNCIAS

TESE DE DOUTORADO

FILM THICKNESS MEASUREMENT WITH HIGH SPATIAL AND TEMPORAL RESOLUTION PLANAR CAPACITIVE SENSING IN OIL-WATER PIPE FLOW.

MEDIDA DA ESPESSURA DE FILME USANDO SENSOR CAPACITIVO DE ALTA RESOLUÇÃO ESPACIAL E TEMPORAL PARA ESCOAMENTOS ÓLEO–ÁGUA EM TUBOS

Autora: Adriana Bonilla Riaño

Orientador: Prof. Dr. Antonio Carlos Bannwart

Coorientador: Prof. Dr. Oscar Mauricio Hernandez Rodriguez

A banca examinadora composta pelos membros abaixo aprovou esta tese:

Prof. Dr. Antonio Carlos Bannwart, Presidente
DE/FEM/UNICAMP

Luiz Felipe Moura

Prof. Dr. Luiz Felipe Mendes de Moura
DE/FEM/UNICAMP

Niederauer Mastelari

Prof. Dr. Niederauer Mastelari
DSI/FEM/UNICAMP

Prof. Dr. Emerson dos Reis
IFSP/São João da Boa Vista

Juliana Loureiro.

Profa. Dra. Juliana Braga Rodrigues Loureiro
COPPE/UFRJ

Campinas, 29 de julho de 2015.

DEDICATION

In first place, I dedicate this work to God.

To my loving parents, Consuelo and Arquimedes, to my husband Hugo Fernando and to my little sisters, Angela and Paula.

ACKNOWLEDGEMENTS

This work would not have been carried out without the help and support of many people:

I would like to express my gratitude to my advisor and my co-advisor, Dr. Antonio Carlos Bannwart and Dr. Oscar Mauricio Hernandez Rodriguez, for their ideas, time and guidance.

I would like to thank to Professor H.-M. Prasser from ETH Zurich for his confidence and open his lab to me.

I would like to thank to me colleagues, Dr. Iara Hernandez and Dr. Hugo Velasco for sharing his knowledge and experience.

I would like to thank to the laboratory technicians in LETeF (Thermal-Fluids Engineering Laboratory), the Engineering School of São Carlos of the University of São Paulo, Jose Bogni, Roberto Prata and Jorge dos Santos for their help. Especially to Helio Trebi for sharing his expertise and for his excellent work.

I would also like to thank my friends in the LETeF, Marlon Hernandez, Márcia Osaki, Luis Vidal, Sávider Conti, and Marcelo de Castro.

I would also like to thank my family and friends in Colombia and Brazil for the support they provided me through my entire life. In particular, I must acknowledge my husband for his patience and love and my best friend, Daniel for helping me to improve my writing skills.

At last, I recognize that this research would not have been possible without the financial support of CAPES and Petrobras, and express my gratitude to those institutions.

"Learn from yesterday, live for today, hope for tomorrow. The important thing is not to stop questioning."

Albert Einstein

ABSTRACT

The development of a new technique for high spatial and temporal resolution film thickness measurement in oil-water flow is presented. A capacitance measurement system is proposed to measure thin water films near to the wall pipe. A planar sensor was chosen for sensing and some geometries were compared using finite elements method (FEM). The penetration depth, the sensitivity, the minimum spatial resolution (high spatial resolution) and the quasi-linear curve were the analyzed characteristics. Dispersed and unstable-annular oil-water flows patterns were studied in a 12-m long vertical glass pipe, with 50.8 mm of internal diameter, using mineral oil (828 kg/m3 of density and 220 mPa s of viscosity) and tap water. The experimental work was carried out in the multiphase-flow facilities of The Thermal-Fluids Engineering Laboratory (NETeF) of EESC-USP. Experiments with a high-speed video camera and the proposed capacitance system were performed to obtain images of the oil-water flow near the pipe wall. A pre-processing enhancement algorithm and a combined segmentation algorithm are proposed and allowed the measurement of characteristic space and time averaged water film thickness. Experimental results of the capacitive technique showed that the system could measure thickness between 400 μm and 2200 μm. It was possible to recognize and characterize typical behaviors of the two different flow patterns studied. Unstable-annular flow can be described by huge fluctuations on the flow direction and perimeter direction, and big interfacial structures (drops). On the other hand, dispersed flow has tiny fluctuations on the flow direction and perimeter direction, and smaller interfacial structures (droplets). A typical interfacial topology is observed near the pipe wall and it can be treated as an interface between wall and core regions. It is analyzed in time and frequency domains: amplitude, velocity and wavelength quantities can be related to the collected signal at each pair transmitter-receiver of the studied sensor. Correlations for the interfacial-structure velocity were found for dispersed oil-in-water flow and unstable-annular flow.

Key Word: Liquid-Liquid Flow, Film Thickness Measurement, Capacitive Sensor, Planar sensor, Oil-Water Flow.

RESUMO

Neste trabalho, é apresentado o desenvolvimento de uma nova técnica para a medição da espessura do filme de água com alta resolução espacial e temporal em escoamento óleo-água. É proposto o uso de um sistema de medição de capacitância elétrica para medir filmes finos de água na proximidade da parede do tubo. O sistema conta com um sensor planar e foi necessário determinar a melhor geometria via simulações baseadas no Método de Elementos Finitos (FEM) para o caso de escoamento óleo-água. As características comparadas foram a profundidade de penetração do campo elétrico no filme de água, a sensibilidade, a resolução espacial mínima e a resposta quase-linear. Padrões de escoamento óleo-água disperso e anular instável foram estudados numa tubulação vertical de 12 m de comprimento, feita de vidro, com 50,8 milímetros de diâmetro interno. Os fluidos usados foram óleo mineral (com densidade 828 kg/m3 e viscosidade 220 mPas) e água da torneira. O trabalho experimental foi realizado nas instalações de escoamento multifásico do Laboratório de Engenharia Térmica e Fluidos (NETeF) da EESC-USP. Foi medida a espessura média do filme de água usando o sistema capacitivo e uma câmera de vídeo de alta velocidade. Para obter a espessura do filme de água a partir das imagens, foi proposto um algoritmo de pré-processamento e um algoritmo de segmentação que combina vários métodos disponíveis na literatura. Os resultados experimentais do sensor capacitivo mostraram que o sistema pode medir espessuras entre 400 µm e 2200 µm. O escoamento anular instável é caracterizado por grandes flutuações na no sentido do escoamento e na direção do perímetro, e estruturas interfaciais grandes (gotas). Por sua vez, o escoamento disperso tem flutuações menores no sentido do escoamento e na direção do perímetro, e estruturas interfaciais menores (gotículas). Uma topologia interfacial típica é observada na região próxima à parede do tubo e pode ser tratada como uma interface entre a região próxima à parede do tubo e a região do núcleo. A análise da interface foi feita no domínio do tempo e da frequência: grandezas como amplitude, velocidade e comprimento da onda podem ser relacionadas ao sinal coletado em cada par transmissor-receptor do sensor. Foi possível estabelecer correlações para a velocidade das estruturas interfaciais em escoamento de óleo em água.

Palavras Chave: Escoamento Liquido-Liquido, Medição de Espessura de Filme, Sensor Capacitivo, Sensor Planar, Escoamento Óleo-Água.

TABLE OF CONTENTS

LIST OF FIGURES

LIST OF TABLES

LIST OF ACRONYMS

1D, 2D, 3D	One Dimensional, two dimensional, three dimensional
AC	Alternating Current
ADC	Analog-Digital Converter
ARE	Average Relative Error
BEM	Boundary Element Method
BD	Big Drops flow
BO	Oil Pump
BW	Water Pump
CAN	Controller Area Network
cdf	Cumulative Density Function
CFD	Computational Fluid Dynamics
CLAHE	Contrast Limited Adaptive Histogram Equalization
ConP	Conductance Probes
CP	Capacitance Probes
DPT	Differential Pressure Transducer
DRF	Drag Reduction Factor
D O/W	Disperser Oil-in-Water flow
DWT	Discrete Wavelet Transform
ECT	Electrical Capacitance Tomography
ERT	Electrical Resistance Tomography
ETH	Swiss Federal Institute of Technology
FCM	Fuzzy C-Means
FEM	Finite Element Method
FFT	Fast Fourier Transform
FND	False Negative Dice
FO	Oil Flow Meter
FPD	False Positive Dice
Fps	Frames Per Second

FPGA	Field Programmable Gate Array
Fr	Froude Number
FW	Water Flow Meter
HE	Histogram Equalization
HSC	High-Speed Camera
hom	Homogeneous model
I.D.	Inner Diameter
IDWT	Inverse Discrete Wavelet Transform
I-V	Current-Voltage
LED	Light-Emitting Diode
Log	Logarithmic
LeTeF	Thermal-Fluids Engineering Laboratory
LIFT	Laser-Induced Fluorescence Technique
LKE	Labor für Kernenergiesysteme
MAE	Mean Average Error
MD	Maximum Difference
MGL	Multiphase mixer
Np	Number of measurement points
MSE	Mean Squared Error
NI	National Instruments
NSD	Number of Sites of Disagreement
Op-Amp	Operational Amplifier
PC	Personal Computer
PCB	Printed Circuit Board
PCI	Peripheral Component Interconnect
pdf	Probability Density Function
PSF	Pixel Scale Factor
PSNR	Peak Signal to Noise Ratio
PXI	PCI eXtensions for Instrumentation
QCV	Quick Closing Valve
RO	Oil Tank

Re	Reynolds Number
RW	Water Tank
Rx	Receiver
SC	Structural Correlation
SLL	Coalescent-plates liquid-liquid separator
SX	Planar Sensor Spatial Resolution in x
SY	Planar Sensor Spatial Resolution in y
UA	Unstable Annular flow
VFP	Variable-frequency driver
Tx	Transmitter
VO	Visual Observation
Vol	Volume
WMS	Wire-Mesh Sensor
WMT	Wire-Mesh Tomography

LIST OF SYMBOLS

A	Cross-sectional area, amplitude
A_o	Area occupied by oil
A_w	Area occupied by water
a, b	Proportionality factors
B	Susceptance
C	Capacitance
c_o	Oil cut
c_w	Water cut
d	Drop diameter
dl	Dimensionless
D	Pipe diameter , Dice coefficient
$\vec{D}$	Electric displacement
$\vec{E}$	Electric field
F	Shear force
f	Friction factor, frequency, film
f_D	Dominant frequency
G	Conductance
g	Gravity coefficient
h	Phase volume fraction
$\tilde{h}$	Local phase fraction
I	Current
I_a	Manually segmented frame
I_m	Automatic segmented frame
i, j	Spatial indices
$\vec{J}$	Current density
J	Jaccard coefficient
j	Imaginary number

L	Inductance
m	Mixture, measured
min	Concerning the minimum value
max	Concerning the maximum value
N	Number of experiments
Ng	Number of pixels
Np_w	Number of white pixels in a column
o	Oil
P	Pressure
Q	Electric charge
q	Volumetric flow rate
r	Pipe radius
r_o	Oil radius
R	Resistance
S	Slip ratio
s	Wetted perimeter
sat	Saturation
t	Time
u	Uncertainty
U	Potential difference
V	Velocity [m/s]
$V_{w,f}$	Water-film velocity [m/s]
V_o	Oil in-situ velocity [m/s]
V_w	Water in-situ velocity [m/s]
$V_{frict,m}$	Mixture friction velocity [m/s]
V_{so}	Oil superficial velocity [m/s]
V_{sw}	Water superficial velocity [m/s]
w	Water
X	Reactance
Y	Admittance

Z	Impedance
Greek letters	
β	Pipe inclination
δ	Film thickness
$\delta_{sub,m}$	Thickness of the effective mixture laminar sublayer
$\overline{\delta}$	Average film thickness
ε	Permittivity
λ	Wavelength
μ	Viscosity
μ_o	Oil viscosity
μ_w	Water viscosity
ρ	Density
ρ_o	Oil density
ρ_w	Water density
ϕ	Electrical potential
σ	Conductivity
τ	Shear stress
τ_w	Shear stress at the wall
ω	Angular frequency

1 INTRODUCTION

The demand of energy has been rising steadily in the past few years. Fossil fuels are expected to continue supplying much of the energy used worldwide (Figure 1.1) (U.S. ENERGY INFORMATION ADMINISTRATION, 2013) and many of these resources are harder to produce at the present than in the past. The production difficulties are due in part to oil reservoirs localization, i.e. most of them are offshore, at great depths under the sea, and in some cases, to the high oil viscosity. Heavy oil represents a significant quantity of the total oil world reserves (SANTOS et al., 2014). Oil is classified as heavy oils when its viscosity is higher than 100 centipoise (cP). Some challenges in the heavy oil recovery from reservoirs are the high flow resistance, the pressure drop, the necessity of heating and dilution during transporting, and the inherent increased costs. This scenario has created an interest in researching new technologies, with the suitable characteristics, to improve the recovery factor of heavy oil fields (BANNWART, 2001).

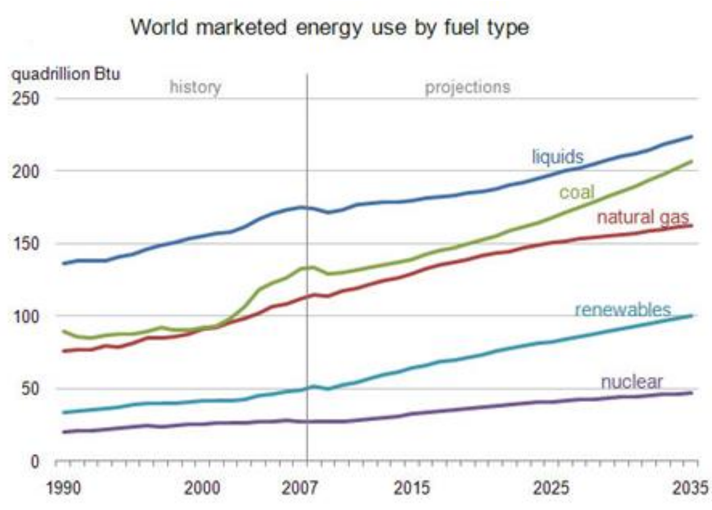

Figure 1.1 - World marketed energy use by fuel type (U.S. ENERGY INFORMATION ADMINISTRATION, 2013).

Particularly, there is a growing attention on methods or technologies to improve the heavy oil transportation process. The methods should be focus on decreasing flow resistance to enough low values that the pumping requirements and pipeline size will guarantee that the process will be economically viable (SANTOS et al., 2014). Lubricated transportation, using core-annular flow and reverse emulsion (oil-in-water emulsion), has been used to reduce the effects of frictional pressure loss caused by the viscous effects and the application in in heavy oil transportation is promising (BANNWART, 2001; BANNWART et al., 2011).

Given the relevance of lubricated transportation of heavy oil and the lack of understanding as far as the associated hydrodynamic phenomena are concerned, the goal of this research is to study a recently developed instrument and apply it for the first time in oil-water flow to study the flow near the pipe wall, where thin films are usually observed.

1.1 Core-Annular Flow

In core-annular flow, a water flow is injected in the pipe in a way that an annular flow pattern is generated, with water near the wall surrounding an oil core. The water flow avoids the oil from sticking to the pipe wall. Therefore, the wall shear stress is comparable to that observed in single-phase water flow, resulting in a significant decrease of the pressure drop due to friction. The more viscous the oil, the more intense the pressure-drop reduction. According to experimental studies, for the core–annular flow pattern to occur it is necessary that the core phase is much more viscous than the annular phase and that the volume fraction of the latter is lower than that of the former (BANNWART, 2001). In some works, geometrical and kinematic characteristics of the annular film have been studied, for example, Oliemans et al. (1987), Bannwart (1998) and Rodriguez & Bannwart (2006). However, works devoted to the study of detailed film topological properties and their relation with the hydrodynamic stability of the core-annular flow pattern have not been found in the literature.

1.2 Dispersed Oil-in-Water Flow (Reverse Emulsion)

Dispersed oil-in-water flow pattern, where oil is dispersed as droplets into the water-dominated flow, is common in crude oil transportation (MARTÍNEZ-PALOU et al., 2011). An interesting feature of this two-phase flow pattern is the drag reduction phenomenon, the pressure drop reaching values than can be even lower than those observed in single-phase water flow. The occurrence of drag reduction without the addition of any drag-reduction agent in dispersed flow has been reported in some works (PAL, 2007; OMER & PAL, 2010; ANGELI & HEWITT, 1998; LOVICK & ANGELI, 2004b; IOANNOU et al., 2005; RODRIGUEZ et al., 2012), but it has not been well understood yet. For instance, Rodriguez et al. (2012) observed a pressure-drop reduction of up to 25% in a viscous oil-water dispersed flow.

One can see in Figure 1.2 the Drag Reduction Factor, $(DRF = -(\partial p/\partial x)_{mixture}/-(\partial p/\partial x)_{water})$, as a function of the oil cut for a 26 mm I.D. acrylic pipe; drag reduction was observed for water superficial velocities higher than 2.0 m/s (RODRIGUEZ, 2014). A phenomenological model that assumes the existence of a thin water film adjacent to the pipe wall was proposed to explain the drag-reduction mechanism, but it lacks experimental confirmation. The model uses pressure-drop, holdup data and physical properties of the fluids to estimate the water film thickness, see Rodriguez et al. (2012).

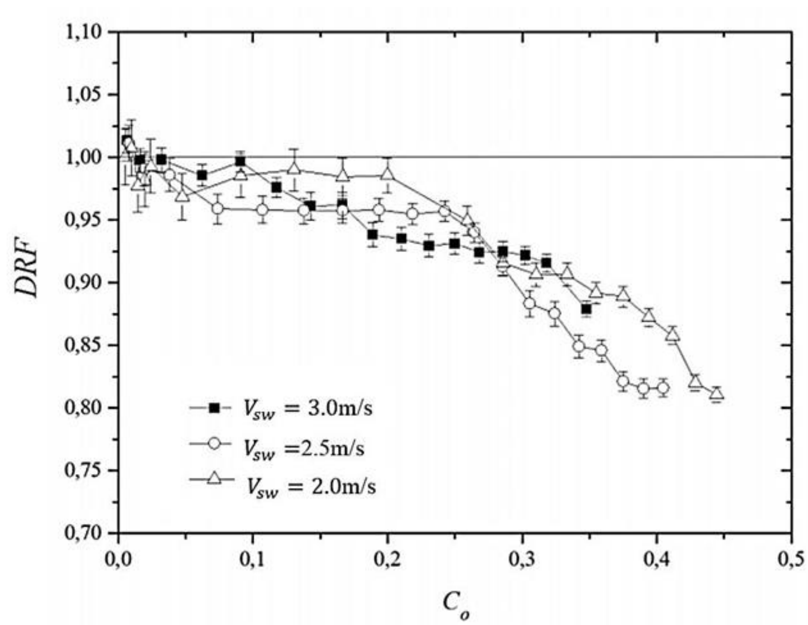

Figure 1.2 – Drag Reduction Factor (DRF) in acrylic pipe for high water superficial velocities (RODRIGUEZ, 2014).

The focus of this work is to verify experimentally the existence of the water film theorized by Rodriguez et al. (2012) in fully dispersed oil-in-water flow and quantify it. Notice that since the observed water-film region near the wall is not a region completely free from oil drops, an oil droplet may eventually be seen near the pipe wall. Nevertheless, according to Rodriguez et al. (2012), the oil droplets are always repelled towards the pipe core. The assumption that there is a stable water film near the wall in fully dispersed oil-in-water flow, with a characteristic space and time-averaged thickness, δ, is adopted in this work. In Figure 1.3 one can see an illustration of the dispersed oil-in-water flow; the blue line indicates the water film approximation that is considered by hypothesis in this work. The blue line represents the time and space-averaged water-film boundary that separates the water-film wall region (annulus) from the oil-in-water mixture (core). This pragmatic model is chosen since it allows the measurement of time and space-averaged water-film thickness with simplicity through both optical and electrical-impedance techniques. In addition, the water-film thickness is measured in core-annular flow as well.

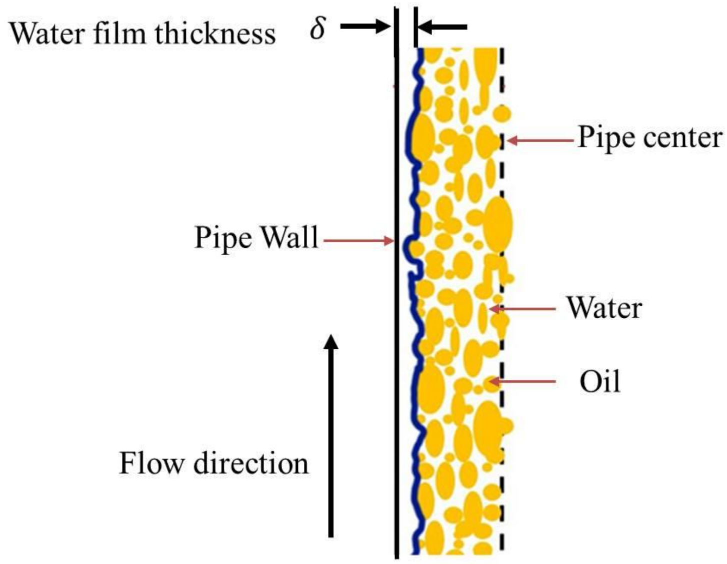

Figure 1.3 – Illustration of the water-film region near the pipe wall in dispersed oil-in-water flow.

It is relevant to point out that several measurement techniques have been developed for the investigation of multiphase flows. Moreover, the existing literature covers mainly applications in gas-liquid, and liquid-liquid flows using liquids with low viscosity (close to the water viscosity). These techniques are not always appropriate for viscous liquids.

1.3 Objectives

The main goal of this research project is to develop new experimental techniques to study water films in viscous-oil-water flow.

The following aims are proposed:

1) Literature review of dispersed and core-annular flow with special attention paid to liquid films and measurements.
2) Literature review of multiphase-flow instrumentation, especially impedance-based sensors, with special attention paid to applications in liquid-liquid flow.
3) Test and characterization of a new liquid-film-thickness measurement system with high temporal and high spatial resolution.
4) Application of the measurement system and development of an experimental methodology for the investigation of film characteristics, such as topology and velocity.
5) Acquisition of new oil-water flow data of turbulent fully dispersed oil-in-water flow.
6) Development of techniques for image and signal processing to visualize and analyze the data, respectively.

1.4 Overview of the Research

This thesis is divided into seven chapters, including this introduction. Chapter 2 presents a literature review on flow patterns in vertical oil-water flows, models and experimental studies on core-annular and dispersed flow, interfacial waves and multiphase-flow instrumentation. Chapter 3 provides details on the experimental set-up, facilities, equipment, instrumentation, test fluids and Finite Elements Method simulations setup. Chapter 4 presents the proposed measurement system and the experimental procedures. In Chapter 5, the development of a methodology for film-thickness measurements using high-speed camera images is presented. In Chapter 6, experimental results, including finite element method (FEM) simulation results and capacitance sensor results, the interfacial structure is studied using the proposed measurement-system data and the high-speed-camera image data. A summary of this research and recommendations for future work are given in Chapter 7.

2 LITERATURE REVIEW

In the next sections are reviewed the basic definitions of liquid-liquid flow and flow patterns, such as core-annular and dispersed flows. Moreover, a review of techniques for measurement of film thickness in oil-water pipe flow is presented.

2.1 Basic Definitions of Liquid-Liquid Flow

Considering oil and water flowing in a vertical pipe with cross-section area A. The input volumetric flow rates of oil and water are q_o and q_w, respectively (SHOHAM, 2006). The input volumetric oil and water fractions are given by:

$$c_o = \frac{q_o}{q_o + q_w} \qquad (2.1)$$

$$c_w = \frac{q_w}{q_o + q_w} \qquad (2.2)$$

where c_w refers usually also to water cut .

Superficial velocities of oil and water are based on the input flow rates and the cross sectional area of the pipe and are defined by:

$$V_{so} = \frac{q_o}{A} \qquad (2.3)$$

$$V_{sw} = \frac{q_w}{A} \qquad (2.4)$$

The in-situ velocity is different from the superficial velocity because the velocity is calculated from the volumetric flow rate passing a smaller area than the cross sectional area. If the cross section areas occupied by oil and water are respectively A_o and A_w, the in-situ velocities can be calculated as:

$$V_o = \frac{q_o}{A_o} \qquad (2.5)$$

$$V_w = \frac{q_w}{A_w} \qquad (2.6)$$

If one considers volume fraction as being area averaged quantity, then oil holdup and water holdup, $\tilde{h}_o$ and $\tilde{h}_w$ can be written as

$$\tilde{h}_o = \frac{A_o}{A}, \qquad (2.7)$$

$$\tilde{h}_w = \frac{A_w}{A}. \qquad (2.8)$$

However, holdup measurements are usually obtained via the collecting of volumes, rather than on cross-sections, then the volumetric holdups are defined as

$$h_o = \frac{Vol_o}{Vol_T} \qquad (2.9)$$

$$h_w = \frac{Vol_w}{Vol_T}, \qquad (2.10)$$

where Vol_o and Vol_w are the volumes of oil and water, respectively and Vol_T is a given total volume:

$$Vol_o + Vol_w = Vol_T. \qquad (2.11)$$

The mixture velocity is defined by dividing the total volumetric flow by the cross sectional area of the pipe:

$$V_m = \frac{q_o + q_w}{A}. \qquad (2.12)$$

Notice that the mixture velocity can also be given by:

$$V_m = V_{so} + V_{sw}. \qquad (2.13)$$

The slip ratio (S) is defined as a relation between the two phases' in-situ velocities and it is defined as (RODRIGUEZ et al., 2011):

$$S = \frac{V_o}{V_w} = \frac{A_w V_{so}}{A_o V_{sw}} \qquad (2.14)$$

If the slip ratio is greater than 1, it means that the oil flows faster than water; while if S is less than 1, it shows that the water is the faster phase. For same phases' velocities, $S = 1$.

Another parameter used in oil-water flow is the drag-reduction factor (DRF). DRF is the ratio between the measured two-phase flow pressure gradient and the equivalent single-phase water pressure gradient at same mixture flow rate.

$$DRF = \frac{-\left(\frac{\partial p}{\partial x}\right)_m}{-\left(\frac{\partial p}{\partial x}\right)_w} \qquad (2.15)$$

where$(\partial p/\partial x)_m$ is the pressure drop of the oil-water flow and $(\partial p/\partial x)_w$ is the pressure drop of single-phase water flow at same mixture flow rate of the oil-water flow. If the pressure gradient of oil-water flow is lower than that of single-phase water, the DRF is < 1, which indicates drag reduction (RODRIGUEZ et al., 2011).

2.2 Flow patterns in Oil-Water Vertical Flow

Many aspects influence the flow patterns, as fluid properties, flow rates, pipe geometry and orientation and operational conditions (e.g. temperature and flow direction). They influence quantities such as heat and momentum transfer capabilities, pressure gradient and mass transfer. Each flow pattern has its own hydrodynamic characteristics, therefore it is necessary to identify it *a priory* for better predicting oil-water flow behavior.

The oil-water flow patterns in an upward vertical pipe flow can be grouped into two categories: water-dominated flow (oil-in-water flow) and oil-dominated flow (water-in-oil flow) (FLORES et al., 1997). In Figure 2.1, it is presented the flow patterns classification proposed by Flores et al. (1997).

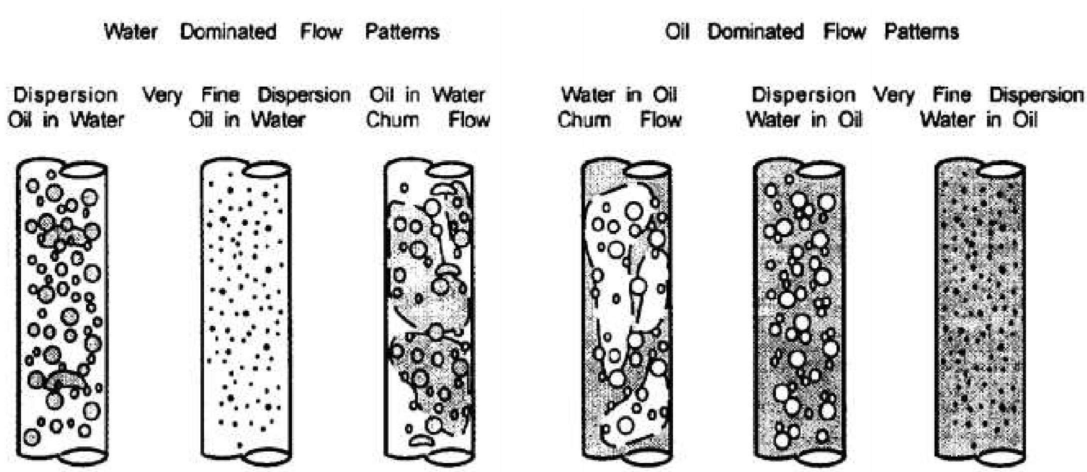

Figure 2.1 - Flow patterns in upward vertical oil-water flow with oil viscosity of 20 cP. (FLORES et al., 1997)

Bannwart et al. (2004) identified four basic flow patterns: bubbles, dispersed bubbles, intermittent and annular, in heavy oil-water flow (oil 500 times more viscous than water), Figure 2.2.

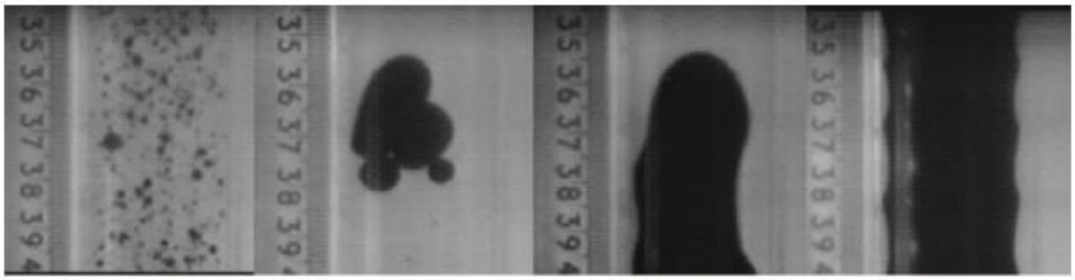

Figure 2.2 - Flow patterns in oil-water upward vertical flow with oil viscosity of 488 cP. (BANNWART et al., 2004)

Govier et al. (1961) identified four basic flow patterns, i.e., drops of oil-in-water, oil slugs, froth and drops of water in oil. In Figure 2.3 the flow-pattern classification proposed by Govier et al. (1961) is presented (the oil viscosity was 20.1 cP).

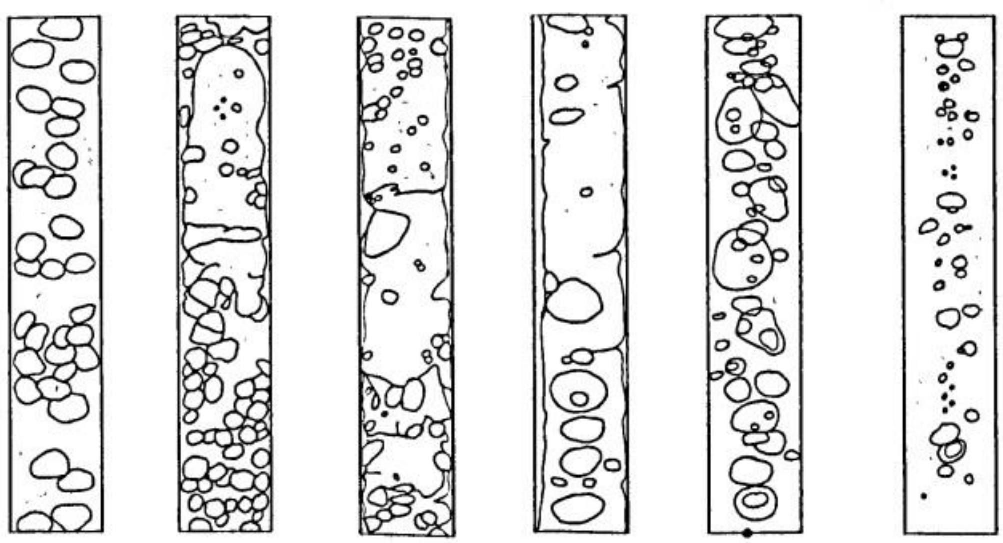

Figure 2.3 – Flow patterns in oil-water upward vertical flow with oil viscosity of 20.1 cP. (GOVIER et al., 1961)

In Table 2.1, some experimental studies about oil-water flow patterns in vertical pipes are listed. In most of the reported studies, the identification of flow pattern has been based on visual observations, high speed photographic and impedance probes. The classifications of flow pattern are subjective and often different from one another. It is important to note that a classification that covers the entire range of possible oil viscosities has not yet been reached.

Table 2.1 - Experimental studies about oil-water flow patterns in vertical pipes

Reference	Diameter (mm)	Oil viscosity (mPa.s)	Defined patterns	Pattern recognition technique
Govier et al. (1961)	26.36	20.1, 150 and 936	Drops of oil-in-water. Slug of oil-in-water. Froth of water in oil. Drops of water in oil.	Visual observation
Flores et al. (1997)	50.8	20	Dispersion of oil-in-water. Very fine dispersion of oil-in-water. Oil-in-water churn flow. Dispersion of water in oil. Very fine dispersion of water in oil.	Conductance probe
Dong et al. (2001)	125	Not reported	Bubble flow. Slug flow.	Electrical resistivity tomography
Bannwart et al. (2004)	28.4	488	Bubbles. Dispersed bubbles. Intermittent. Annular.	Visual observation
Du et al. (2012)	20	12	Very fine dispersed oil-in-water flow. Dispersed oil-in-water flow. Oil-in-water slug flow. Water-in-oil. Transition flow.	Mini-conductance probes
Mydlarz-Gabryk et al. (2014)	30	29.20	Drops of water in oil. Transitory area. Drops and plugs of oil-in-water. Drops of oil-in-water.	Visual observation
Kee et al. (2014)	102	2	Dispersed globules flow. Dispersed droplets.	Visual observation

2.3 Annular Flow

The liquid-liquid annular pipe flow (or core-annular flow) of two immiscible liquids with very different viscosities has been studied as an efficient and low cost method for producing heavy oils in vertical wells using water as a lubricant (BANNWART et al., 2004; BANNWART, 2001; BANNWART et al., 2011). Water is injected in the pipe so that it flows as an annular film adjacent to the pipe wall, whereas oil flows in the core region, Figure 2.4. Water keeps the oil from sticking to the pipe wall; therefore the wall shear is comparable to that of single phase water flow. This reduces the required pumping power and the operational costs (GHOSH et al., 2009).

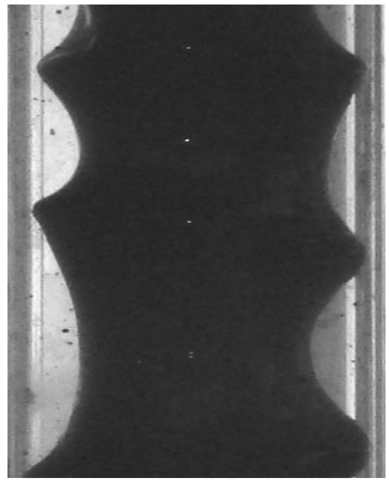

Figure 2.4 - Core-annular flow pattern.

The physical model of a two-phase flow is formed by a system of mathematical equations dependent on the flow conditions. In addition, constitutive relations are necessary to describe the mass exchange, momentum and energy transfer between the phases and the contours (walls). The constitutive relations also are dependent on the flow conditions. State equations, initial and boundary conditions are also required.

One can see in Table 2.2 a summary of studies on annular flow in pipes; most of them are experimental works in horizontal pipes. There are few works focused on the measurement of water film thickness.

Oliemans et al. (1987) performed experiments and proposed models for holdup and pressure drop prediction. They proposed a modified lubrication film model by incorporating the effect of turbulence in the water annulus. The authors presented empirical correlations to predict holdup and wavelength of the oil-water interface.

Bai et al. (1992) performed core-annular flow experiments. The most important result was the characterization of the bamboo waves in upflow and corkscrew waves in downflow. It was observed a pressure reduction of 200 times using core flow in comparison with single-phase oil flow. The experimental results were compared with predictions of the linear theory of stability and perfect core-annular flow theory.

Table 2.2 - Summary of Experimental Studies on oil-water annular flow in pipes.

Reference	Vso (m/s) and Vsw (m/s)	Oil viscosity (cP)	Orientation and diameter (mm)	Measurements	Meters
Oliemans et al. (1987)	0.5 – 1 and 0.03 – 0.25	3000	Horizontal and 50	Wave length Shape and amplitude; Pressure gradient	HSC
Bai et al. (1992)	0.003 – 0.79 and 0.003 – 3	600	Vertical and 9.5	Pressure gradient; Flow patterns	DPT VO
Arney et al. (1993)	0.20-1.16 and 0.061-0.65	390	Horizontal and 15.9	Pressure drop Holdup	Manometer Ball valves
Bannwart (1998)	0.25 - 0.62 and 0.03 – 0.28	2700	Horizontal and Vertical 22.5	Wave speed	HSC
Bai & Joseph (2000)	0.045 – 0.13 and 0.02	600	Vertical and 22.5	Wave speeds; Wave shapes	HSC
Rodriguez & Bannwart (2006)	0.007 - 2.5 and 0.04 - 0.5	500	Vertical and 28.4	Wave speed; Wave length; Amplitude and Wave profile Holdup	HSC
Grassi et al. (2008)	0.02- 0.7 and 0.02 – 2.5	800	Horizontal (Angles -15 to +15) and 21	Flow patterns; Frictional pressure differential	VO DPT
Sotgia et al. (2008)	0.19 – 0.97 and 0.01– 2.5	919	Horizontal and 21 to 41	Pressure drop; Flow pattern	DPT VO
Rodriguez et al. (2009)	0.88 - 1.82 and 0.14 - 0.50	500	Horizontal and vertical 28.4	Pressure gradient	DPT
	0.8, 1.0 and 1.1 0.24	36950	Vertical and 77		
Balakhrisna et al. (2010)	0.1 – 1 and 0.1 – 1	200 and 1.2	Horizontal and 12 – 25.4	Pressure drop; Flow patterns	DPT VO
Strazza, Grassi, et al. (2011)	0.05 – 0.7 and 0.2 – 1.5	900	Horizontal (Angles -10 to +15) and 22	Flow patterns; Pressure drop and Holdup	VO DPT CP
Strazza, Demori, et al. (2011)	0.19 – 0.67 and 0.45 – 2.04	900	Horizontal and 21	Holdup	CP QCV
Strazza & Poesio (2012)	0.71 and 0.32 - 1.69	900	Horizontal and 22	Pressure drop	DPT

HSC: High-speed camera, DPT: Differential Pressure Transducer, VO: Visual Observation, QCV: Quick Closing Valves, CP: Capacitance Probes

An experimental work with heavy oil is presented by Arney et al. (1993). The main contribution of the work is a correlation to estimate the holdup. Pressure drop and holdup values are also presented. An important finding is than when the oil sticks to the pipe wall the pressure drop increases, producing a corresponding rise in the friction factor.

In Bannwart (1998), it is presented a study of the speed of interfacial waves observed in core-annular flow of viscous oil and water. The horizontal and vertical experiments are compared with the kinematic wave theory. The theory provides information on the wave speed, the slip ratio and volumetric fraction of the core. The theory results have very good agreement with experimental data. It was developed a general correlation for the volumetric fraction of the core in core-annular flow at low viscosity ratio. The proposed correlation includes the effect of fluid properties and can be applied to upward, downward and horizontal flows.

Bai & Joseph (2000) presented a perturbation theory for flow and interface shapes of a highly viscous dispersed phase in core-annular flow. The theoretical results were compared with the experimental results. The theory was able to give a good description of the bamboo waves under certain conditions.

Rodriguez & Bannwart (2006) proposed a correlation for oil holdup estimation in fully developed core-annular flow, which considers the presence of interfacial waves and turbulent water flow. Furthermore, an experimental study on interfacial waves observed in core flow was made. The measured parameters were wave speed, wave length, amplitude and wave profile of interfacial waves, oil holdup and holdup ratio. The holdup was measured indirectly by measuring the speed of interfacial waves. This method presented good agreement with a direct optical measurement method. An important conclusion is that the oil core always flows faster than the water annulus in upward vertical flow.

Grassi et al. (2008) made an experimental work with the objective of validate theoretical models for core-annular and oil-in-water dispersion. The chosen models were the two-fluid model for core-annular flow and homogenous model for oil-in-water dispersion. Both models were found effective to predict the pressure gradients with an accuracy of 20%.

Sotgia et al. (2008) studied oil-water flow in seven different pipes with diameters between 21 to 40 mm. The results obtained were compared to empirical laws, theoretical findings and experimental results by different authors of the literature. The studied parameters were pressure drop, flow patterns and transitions and pressure reduction in core-annular flow. The authors concluded that the peak of pressure reduction is near to the transition between the annular and stratified flow regimes. An empirical law for the location of the annular/stratified transition was proposed.

Pressure drop in core-annular flow was studied in two different experimental setups by Rodriguez et al. (2009). The authors proposed a model for pressure-loss prediction in core-annular flow. The model was compared with other models and data in the literature and full-scale experimental data. It was reported an important decrease in pressure drop in the full-scale experiments.

The behavior of oil–water flow going through sudden contraction or expansion is studied in Balakhrisna et al. (2010). Flow patterns are observed for high viscous and low viscous oils. Three flow patterns were identified: core-annular flow, oil dispersed flow and plug flow. It was shown that the pressure profiles depend on the change of area and fluid viscosities. The pressure drop is less intense for core-annular flow than for other flow patterns.

In Strazza, Grassi, et al. (2011) it is presented an experimental study on oil–water core-annular flow in horizontal and inclined systems, particularly are shown flow maps, pressure drop and holdup data. Some theoretical models to predict core-annular flow existence limits and pressure drops are compared to the experimental results. The pressure gradient reduction for heavy oils transportation is remarkable.

Strazza, Demori, et al. (2011) developed a capacitance probe for holdup measurements in core-annular flow. The results were compared with quick closing valves and a capacitance model of the fluids with good agreement. In Strazza & Poesio (2012) it is presented a study of the start-up of core-annular flow from a stratified arrangement, focusing on the pressure drop and using water to clean the pipe up. It is measured the maximum pressure drop that occurs during start-up and the time required to remove the thin layer of oil stuck to the pipe wall. A comparison between the experimental data and a model available in literature was made.

2.3.1 Holdup Prediction for Annular Flow

Some empirical relations for holdup determination are presented in Table 2.3.

Table 2.3 – Empirical relations for holdup in oil-water annular flow

Reference	Holdup Correlation
Oliemans et al. (1987)	$h_w = c_w\left[1+0.2\left(1-c_w\right)^5\right]$
Arney et al. (1993)	$h_w = c_w\left[1+0.35\left(1-c_w\right)\right]$
Bai et al. (1992)	$\frac{h_w}{L} = \frac{1}{\left(1+0.72\frac{V_{so}}{V_{sw}}\right)}$ For Vertical Upflow
Bannwart (1998)	$V_{so}\left(1-h_o\right)-s_o V_{sw} h_o = 0$ Horizontal system $V_{so}(1-h_o)-s_o V_{sw} h_o - V_{ref} F(h_o) = 0,$ Vertical system where $s_o = 2$ and $V_{ref} = \frac{\left(\rho_o-\rho_w\right) g D^2}{16\mu_o}$ $F(h_o) = -h_o^2\left[2\left(1-h_o\right)+\left(1+h_o\right)\ln h_o\right].$
Rodriguez & Bannwart (2006)	The drift-flow relation can be written as: $V_{so}(1-h_o)-s_0 V_{sw} h_o - cV_{ref} h_o{}^q (1-h_o)^m = 0$ where V_{so} is the oil superficial velocity, V_{sw} is the water superficial velocity and V_{ref} is: $V_{ref} = a_i^{\frac{1}{n_i-2}}\sqrt{gD}\left(\frac{\rho_2-\rho_1}{\rho_2}\right)^{\frac{1}{2-n_i}}\left(\frac{\rho_2\sqrt{gD}D}{\mu_2}\right)^{\frac{n_i}{2-n_i}}$ $q = \frac{7-3n_i}{4-2n_i}.$ where, $c = 0.0122$, $m = 0$, g is the gravitational constant, D is the pipe diameter, ρ is the density, μ is the viscosity, and subscripts 1 and 2 stand for oil and water, respectively. The constants a_i and n_i are 0.079 and 0.25, respectively, for transitional/turbulent annulus flow or $a_i = 16$ and $n_i = 1$ for laminar annulus flow.
Rodriguez et al. (2009)	The holdup can obtained from the solution of the equation: $V_{so}(1-h_o)-1.17V_{sw}h_o - 0.02h_o^{1.79} = 0.$

2.4 Dispersed Oil-in-Water Flow

The oil-in-water dispersed flow pattern, where the oil is dispersed as droplets into the water (Figure 2.5), occurs in liquid-liquid pipe flow at high velocities. This pattern is common in crude oil production and offshore pipelines; however, it has not been studied as intensively as separated or intermittent flows. The dispersed oil-in-water flow pattern can be stable or unstable, which refers to the capability of the dispersed phase to coalesce.

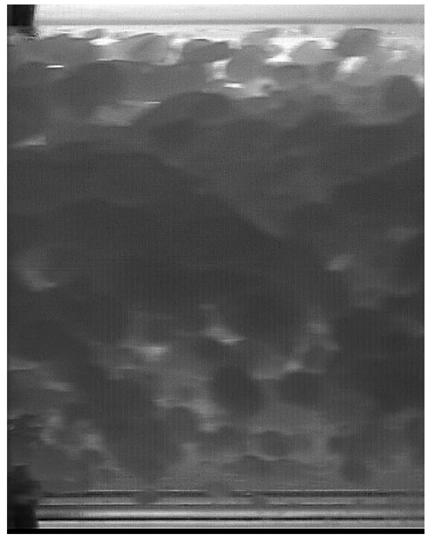

Figure 2.5 – Oil-in-water dispersed flow pattern.

Oil-in-water dispersed flow can flow under laminar or turbulent regimes. Turbulent dispersed oil-water flow has an interesting feature: the drag reduction phenomenon (DRP). The drag reduction phenomenon can be defined as a reduction in two-phase pressure gradient when compared to that of an equivalent single-phase flow, see section 2.1.

An experimental work on laminar and turbulent flow behaviors of oil-in-water emulsions was presented by Cengel et al. (1962). The comparison parameter was the viscosity. The authors concluded that the apparent viscosity does not depend on the Reynolds number and pipe diameter for laminar flow with low oil holdup. The apparent viscosity decreases when the Reynolds number increases, for oil fractions between 20% and 50%. Additionally, the apparent viscosity depends on the pipe inclination for oil fractions larger than 50%. The emulsions showed a drag reduction behavior in the turbulent region and this behavior was increased with the increase of the oil fraction.

Angeli & Hewitt (1998) carried out pressure-gradient measurements in horizontal oil-water flow in two different pipes (steel and acrylic). The pressure gradients measured in the acrylic tube were lower than those measured in the steel tube. The differences could be explained by the different wetting characteristics. The friction factors were lower than those expected for single-phase flow when oil was the continuous phase and about the same when water was the continuous phase. The authors mentioned that flow characteristics had not been understood completely and more studies would be needed. Under the same flow conditions, Angeli & Hewitt (2000a) presented an experimental study on drop size and the interfacial area. The measurements were made using an endoscope. The endoscope was able to reach other regions in the pipe than that near the pipe wall. Two tubes of different materials (steel and acrylic) were used and it was possible to conclude that the pipe material affect the drop size.

In Lovick & Angeli (2004a), drop size and distribution in horizontal dispersed flow were studied. Drop velocities and chord lengths were measured at different locations with a double sensor impedance probe. The experimental data were compared with existing models, and the agreement was poor. At similar experimental conditions, Lovick & Angeli (2004b) measured pressure gradient, holdup and phase distribution in dual continuous flow. For all the experiments, the two-phase pressure gradient was lower than the measured in single-phase oil flow at the same mixture velocity. At the lowest mixture velocity, there was little variation of the pressure gradient with volume fraction. At the other velocities, the addition of water in single-phase oil resulted initially in a decrease in pressure gradient, even reaching values lower than those obtained with single-phase water flow. Another important parameter was the velocity ratio (defined as the ratio of the in-situ oil to water velocity, V_o/V_w). The velocity ratio increased during dual continuous as the oil input fraction increased. At high input oil fractions, however, the velocity ratio decreased as the mixture velocity increased. The authors concluded that this behavior could be explained by the change of interface shape.

In Rodriguez & Oliemans (2006), experimental results of pressure gradient, flow patterns and holdup are presented. The studied flow patterns were stratified and dispersed. The measurements were compared to the two-fluid model for stratified flow and the homogeneous model for dispersed flow. For the stratified flow patterns, the two-fluid model had the best agreement for water holdup and pressure gradient predictions. Otherwise, the homogeneous model was better for dispersed flow patterns. This behavior was similar in horizontal and vertical flows.

Zhao et al. (2006) performed experiments to determinate the local interfacial-area concentration, the local oil-phase fraction, interfacial velocity and oil-drop Sauter mean diameter of an oil-water upward vertical pipe flow. The measurements were made using a double-sensor conductivity probe. They related water flow rates with the local oil phase fraction, oil-drop Sauter mean diameter and the interfacial velocity. The local oil phase fraction and oil-drop Sauter mean diameter decreased with increasing the water flow rate (at constant oil flow rate) and the interfacial velocity increased. An interesting finding was that the measurements do not depend on the sampling frequency of the double-sensor conductivity probe when the sampling frequency is higher than 40 kHz.

Pal (2007) proposed that drag reduction in dispersions is caused by a significant reduction in effective viscosity of the dispersion when the flow regime changes from laminar to turbulent. This reduction occurs due to extensive stretching of droplets in the direction of flow. The degree of reduction is higher when the oil is the continuous phase. However, his model was not able to fit the experimental data at several flow conditions.

A dual-plane electrical impedance tomographic technique was used to study oil-in-water vertical pipe flow (LI et al., 2008). The local volume fraction distributions and velocity profiles obtained via tomography was compared to that obtained by a local conductance probe. The electrical impedance tomography showed to be highly sensitive to the accuracy of the electrical measurements and the chosen image reconstruction algorithm. In general, there was a good agreement between electrical impedance tomography and conductance probe. The conductance probe offered a better description of the velocity profiles. It is necessary to improve the calibration and the reconstruction algorithm.

In Wang et al. (2011), it is presented an experimental study of pressure gradient and flow patterns in oil-water flow. It was observed that at low water fractions the flow was fully dispersed, while at intermediate ones water started to segregate as the mixture velocity increased. At high water fractions, water continuous layers formed and the pattern was either separated or annular with an oil continuous emulsion in the core. Pressure drop increased as the oil continuous emulsions occupied the whole pipe, but it decreased when water started to segregate and form a separated layer.

Picchi et al. (2015) investigated a dilute and highly viscous oil-in-water dispersion. They measured holdup data using the QCV technique and a capacitance probe. It was measured pressure gradient too. The results were compared with a two-fluid model and homogenous model. The experimental data had a good agreement with the homogeneous model predictions for low holdup values. The two-fluid model had a better agreement for entire range of oil holdup. An important conclusion of this work is that the slip ratio was greater than unity, thus the oil was flowing faster in the pipe.

A literature review on experimental studies in oil-in-water dispersed flow in pipes is summarized in Table 2.4. In the most of the works, low-viscosity oils were used. In this work, it is used a high-viscosity oil. Water-film studies were not found. The instrumentation is made of differential pressure transducers, quick closing valves and video cameras. In few cases, there were impedance sensors and gamma densitometers. Studies that relate the characteristics of the liquid film, as amplitude and frequency of interfacial waves, with the drag reduction phenomenon were not found.

Table 2.4 - Summary of Experimental Studies on oil-water dispersed flow in pipes

Reference	V_{so} (m/s) and V_{sw} (m/s)	Oil viscosity (cP)	Orientation and diameter (mm)	Measurements	Meters
Cengel et al. (1962)	-	0.976	Horizontal and vertical 22.2	Pressure gradient	DPT
Nadler & Mewes (1997)	0.1 to 1.6 and 0.1 to 1.6	22, 27 and 35	Horizontal and 59	Pressure gradient	DPT
Angeli & Hewitt (1998)	0.3 to 3.9 and 0.3 to 3.9	1.6	Horizontal and 24.3	Pressure gradient	DPT
Angeli & Hewitt, (2000b)	0.3 to 3.9 and 0.3 to 3.9	1.6	Horizontal and 24.3	Drop size	Video with endoscope
Lovick & Angeli (2004a)	0.3 to 2.0 and 0.3 to 2.0	6	Vertical and 38	Flow patterns Size and vertical distribution of drops	HSC Conductivity and impedance probe Dual sensor impedance probe
Lovick & Angeli (2004b)	0.08 to 2.7 and 0.08 to 2.7.	6	Vertical and 38	Pressure gradient Holdup Phase dsitribution	DPT QCV Impedance probe
Ioannou et al. (2005)	Large pipe 3.5 to 5 Small pipe 4 to 7	2.3	Horizontal and 60 and 32	Pressure gradient Flow patterns	DPT Impedance rings

HSC: High-speed camera, DPT: Differential Pressure Transducer, VO: Visual Observation, QCV: Quick Closing Valves, CP: Capacitance Probes, Wire-Mesh Sensor: WMS

Table 2.4 – (Continuation) Summary of Experimental Studies on oil-water dispersed flow in pipes

Reference	V_{so} (m/s) and V_{sw} (m/s)	Oil viscosity (cP)	Orientation and diameter (mm)	Measurements	Meters
Hussain et al. (2008)	0.72 to 1.7 and 0.72 to 1.7	1.6	Horizontal and 25.4	Holdup	Gamma densitometer
Li et al. (2008)	0.027 to 0.124 and 0.3 to 0.5	1.6	Vertical and 80	Holdup Velocity profiles	Dual-plane electrical impedance Tomography Conductance probe
Xu et al. (2010)	0 to 1.87 and 0 to 1.24	44	Vertical and 50	Pressure gradient Holdup Flow patterns	DPT QCV High-speed camera
Wang et al. (2011)	0.09 to 0.72 and 0.01 to 0.77	628.1	Horizontal and 25.4	Pressure gradient Flow patterns Holdup	DPT VO QCV
Rodriguez et al. (2011)	0.27 to 3.6.and 0.09 to 2.8	100	Horizontal and 26	Holdup Phase distribution Flow patterns	WMS QCV HSC
Rodriguez et al. (2012)	0.27 to 3.6.and 0.09 to 2.8	100	Horizontal and 26	Pressure gradient Holdup Phase distribution	DPT WMS QCV HSC
Picchi et al. (2015)	0.02 to 0.15 and 0.74 to 2.83	900	Horizontal and 22.8	Pressure gradient Holdup	DPT QCV CP

HSC: High-speed camera, DPT: Differential Pressure Transducer, VO: Visual Observation, QCV: Quick Closing Valves, CP: Capacitance Probes, Wire-Mesh Sensor: WMS

2.4.1 Dispersed Oil-in-Water Models

The prediction of pressure gradient in dispersed oil-water flow is usually made by using the homogeneous model. When there is doubt about preponderant topology of the flow pattern, as in stratified flow with mixture at the interface or dual continuous flow, the two-fluid model can also be applied.

The homogeneous model assumes that: (1) the two phases can be treated as a pseudo single-phase fluid with suitable average properties that obeys the equations of single-phase flow; and (2) the slip ratio is 1. The pressure gradient is often given as:

$$\left(\frac{\partial p}{\partial x}\right)_m = -\frac{f_{m,\mathrm{hom}}\rho_{m,\mathrm{hom}}V_m^2}{2D} - \rho_{m,\mathrm{hom}} g \sin\theta. \qquad (2.16)$$

Here $f_{m,hmo}$ is the mixture friction factor, $\rho_{m,hom}$ is the mixture density, V_m is the mixture velocity and D the pipe's internal diameter.

$$V_m = V_{sw} + V_{so} \qquad (2.17)$$

$$\rho_{m,\mathrm{hom}} = \rho_w h_{w,\mathrm{hom}} + (1 - h_{w,\mathrm{hom}})\rho_o, \qquad (2.18)$$

where the water and oil holdups are, respectively:

$$h_{w,\mathrm{hom}} = \frac{V_{sw}}{V_{sw} + V_{so}}. \qquad (2.19)$$

$$h_{\mathrm{o,hom}} = 1 - h_{w,\mathrm{hom}} \qquad (2.20)$$

And the friction coefficient can be determined by inserting the mixture Reynolds number into, for instance, the Blasius equation:

$$f_{m,\mathrm{hom}} = 0.312\,\mathrm{Re}_m^{-0.25} \qquad (2.21)$$

$$\mathrm{Re}_{m,\mathrm{hom}} = \frac{\rho_m V_m D}{\mu_m}. \qquad (2.22)$$

Single-phase-flow friction factor correlations depend on an apparent or effective viscosity μ_m. There is not a general apparent viscosity correlation that allows the prediction of the apparent viscosity for different operational conditions and different liquid-liquid systems. Table 2.5 summarizes some correlations for oil-in-water dispersed flow found in the literature.

Table 2.5 - Summary of apparent viscosity correlations

Reference	Apparent viscosity
Einstein (1906)	$\mu_m = \mu_w(1+2.5h_o)$
Duckler et al. (1964)	$\mu_m = h_w\mu_w + h_o\mu_o$
Angeli & Hewitt (1998)	$\mu_m = \mu_w(1-h_o)^{-2.5}$
Pal (2001)	$\mu_m^{2/5}\left[\frac{2\mu_m+5K}{2+5K}\right] = (1-h_o)^{-1}$ $K = \frac{\mu_o}{\mu_w}$
Guet et al. (2006)	$\mu_m = \mu_w$
Toda & Furuse (2006)	$\mu_m = \frac{1-0.5h_o}{(1-h_o)^3}$ For concentrated dispersions $\mu_m = \frac{1+0.5kh_o-h_o}{(1-kh_o)^2(1-h_o)}$ For dispersions with large particles where $k = 1+0.5h_o$

2.5 Interfacial Waves

Interfacial waves have been widely studied in annular flow and stratified flow. Behavior of interfacial waves, including film thickness, wavelength, frequency and shape, affects many flow characteristics, as flow pattern stability, pressure drop and heat transfer. A proper understanding of the interfacial waves is necessary for the development of suitable mechanistic models.

Most of the studies on interfacial waves were devoted to gas-liquid flow. There are a few on liquid-liquid flow, but mostly with low viscosity fluids. Works on the interfacial wavy structure in viscous liquid-liquid flow are scanty and almost only on core-annular flow. Experimental studies on interfacial waves in gas-liquid and liquid-liquid flows are summarized in this section.

2.5.1 Interfacial Waves in Gas-Liquid Flow

Annular gas-liquid pipe flow is characterized by a gas core, a liquid film adjacent to the pipe wall and a wavy gas-liquid interface. However, a fraction of the liquid travels as droplets in the gas core due to a process known as liquid entrainment (GERACI et al., 2007). The interface between the liquid film and the gas core has a complex topology that is constantly changing in time and space. The interface can be characterized as having low-frequency disturbance waves, known as roll waves, along with high-frequency waves known as ripple waves. The latter are usually related to the liquid entrainment process. Figure 2.6 shows a diagram of an upward-vertical annular pipe flow where the two kinds of waves can be identified.

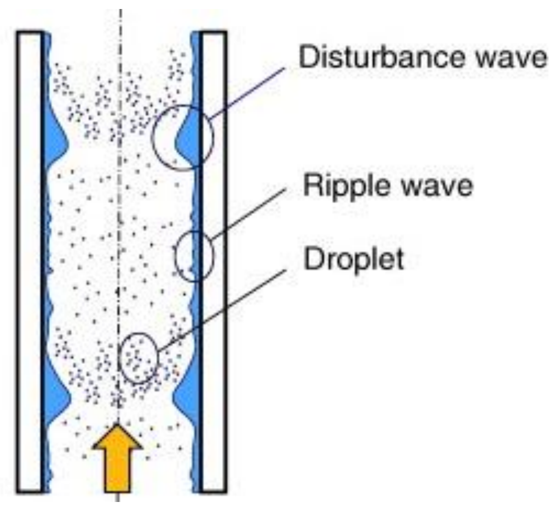

Figure 2.6 - Diagram of upward-vertical annular pipe flow. (ARAI et al., 2015)

Ripple waves or ephemeral waves have small amplitudes, compared with the liquid film thickness, short life times, high frequency and usually do not occupy the whole tube circumference. Ripple waves dominate the interface when the liquid flow rate is low, such that the interface appears smooth. These waves exist for liquid-film Reynolds numbers below a critical value between 200 and 330. In addition, the gas velocity must be above a critical velocity. For air-water flow, the gas superficial velocity must be greater than 20 m/s. (LEVY, 1999; RODRIGUEZ, 2011).

Disturbance waves, sometimes called “roll waves”, have a longer life time and amplitudes usually several times the liquid film thickness (BELT et al., 2010). Several investigations on the disturbance-wave configuration have been performed (SEKOGUCHI & TAKEISHI, 1989; ASALI & HANRATTY, 1993; SCHUBRING & SHEDD, 2008).

Disturbance waves appear when the liquid flow rate is above a critical value and they have an important influence on the flow pattern due to their large size and dynamic properties. Table 2.6 presents some studies on interfacial waves. Disturbance waves have been characterized by measuring film thickness and interfacial velocity. Few authors have given a quantitative description of the interfacial structures (ALEKSEENKO et al., 2009; BELT et al., 2010; SCHUBRING & SHEDD, 2008).

Waves play crucial roles in transport processes in annular flow such as mass transfer, momentum transfer and heat transfer between the phases. Furthermore, there is a relation between the disturbance waves and droplet entrainment (JACOWITZ & BRODKEY, 1964; HAN & GABRIEL, 2007). However, the exact mechanism of droplet detachment is still a topic of discussion (ALEKSEENKO et al., 2009; ALEKSEENKO et al., 2010).

Some authors believe that ripple waves should be disregarded because disturbance waves govern the interface shape. For example, Sekoguichi et al. (1978) found that ripple waves are generated and absorbed by the roll waves. In Figure 2.7, one can see wavy interface in upward-vertical annular flow. The two types of waves, ripple and disturbance, can be seen. One can see ripple waves among disturbance waves, but due to poor space sensitivity it was not possible to study the details of the dynamics of the ripple waves. On the other hand, Alekseenko et al. (2014) and Cherdantsev et al. (2014) have shown that the mechanism of droplet formation and detachment may have to do with the interaction between ripple and roll waves.

Table 2.6 - Summary of experimental studies on interfacial waves in gas-liquid flow in pipes

Reference	Studied waves	Fluids – Diameter (mm)	Measurement technique
Nedderman & Shearer (1963)	Disturbance Waves (velocities, frequencies, wave number)	Air-water 31.75	HSC
Taylor et al. (1963)	Disturbance Waves (velocities, and frequencies)	Air-water 31.75	HSC ConP
Miya et al. (1970)	Disturbance Waves (Wave ampitudes)	Air-water Rectangular channel 304.8 mm x 25.4 mm	Resistive sensor
Bruno & Mccready (1988)	Disturbance Waves (Wave amplitudes and velocities)	Air-water Rectangular channel 304.8 mm x 25.4 mm	ConP
Wolf et al. (1996)	Disturbance Waves (Wave amplitudes)	Air-water 31.8	HSC
Azzopardi (1997)	Disturbance Waves (Frequencies and velocities)	Air-water 10 , 32, 58 e 125	HSC

HSC: High-speed camera, CP: Capacitance Probes, ConP: Conductance Probes, Laser-Induced Fluorescence Technique: LIFT

Table 2.6 – (Continuation) Summary of experimental studies on interfacial waves in gas-liquid flow in pipes

Reference	Studied waves	Fluids – Diameter (mm)	Measurement technique
Wang et al. (2005)	Disturbance waves (Wave shapes, amplitudes and velocities)	Air-water 9.53	HSC
Han et al. (2006)	Disturbance waves (Wave amplitudes and velocities, wavelength)	Air-water 9.525	ConP
Hazuku et al. (2008)	Disturbance Waves (Wave amplitudes and frequencies)	Air-water 11	Laser focus displacement mete
Sawant et al. (2008)	Disturbance Waves (Wave amplitudes and velocities, frquencies and wavelenght)	Air-water 9.4	ConP
Damsohn & Prasser (2009)	Disturbance Waves (Wave amplitudes and velocities, frequencies and wavelength)	Air-water Rectangular channel 50mm x 50mm	ConP
Johnson et al. (2009)	Disturbance Waves (Wave amplitudes and velocities, frequencies and wavelength)	Sulfur Hexafluoride – water 100	ConP
Alekseenko et al. (2009)	Disturbance Waves and ripple waves (Wave amplitudes)	Air-water 15	LIFT
Schubring et al. (2010)	Disturbance Waves (Wave amplitudes and velocities, and wavelength)	Air-water 23.7	HSC
Belt et al. (2010)	Disturbance Waves (Wave amplitudes and velocities, and frequencies)	Air-water 50	ConP
Zhao et al. (2013)	Disturbance Waves (Wave amplitudes and frequencies)	Air -water with added potassium nitrate salt 34.5	ConP
Gawas et al. (2014)	Disturbance Waves (Wave celerity, amplitude and frequency)	Air -water 152.4	CP
Alekseenko et al. (2014)	Disturbance waves and ripple waves (Wave amplitudes and velocities)	Air - Water and two water-glycerol solutions 15	LIFT
Cherdantsev et al. (2014)	Disturbance and ripple waves (Wave amplitudes, velocities and shapes)	Air - Water Rectangular cannel 161.4 mm x 25 mm	LIFT

HSC: High-speed camera, CP: Capacitance Probes, ConP: Conductance Probes, Laser-Induced Fluorescence Technique: LIFT

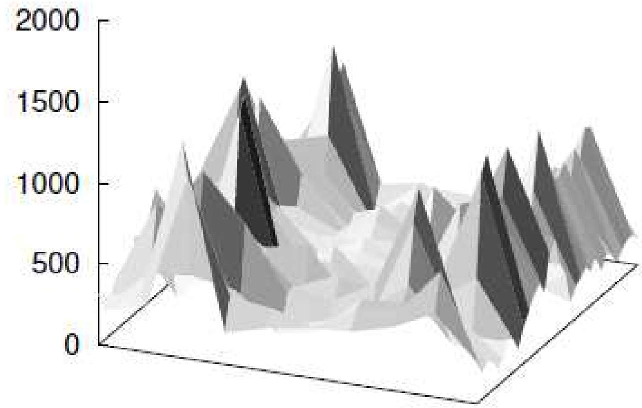

Figure 2.7 - Liquid film thickness (in μm) for gas-liquid annular flow at $V_{SL} = 0.08\ m/s$ and $V_{SG} = 42\ m/s$. Taken from Belt et al. (2009)

2.5.2 Interfacial Waves in Liquid-Liquid Flow

There are relatively few studies about interfacial waves in liquid-liquid flow; some of them are summarized in Table 2.7. They are focused on stratified and core-annular flow. Most of these studies present visual observations using high-speed video cameras. It is clear that it is important to develop new methodologies for interfacial-wave measurements, particularly using instruments that would provide more information than that offered by video recording.

Oliemans et al. (1987) developed a study on interfacial waves in core-annular flow. Wavelengths were found to vary from 6 mm to 60 mm, while wave amplitudes were of the order of 1-2 mm. It was presented a correlation for wavelength depending on pipe radius, input water fraction and oil superficial velocity.

A kinematic wave theory to describe interfacial waves in on core-annular flow was presented by Bannwart (1998). The theory offers information about the slip ratio and volumetric fraction of the core, but kinematic-wave information should be available *a priori* for the model to be applied. It was proposed a correlation between the wave speed and oil holdup. The theoretical holdup predictions were compared with horizontal and vertical experimental data. The theory showed good agreement with the experimental data.

In Rodriguez & Bannwart (2006) experiments to measure wavelength, wave amplitude, wave profile, wave speed and holdup using a high speed video camera were carried out. It was proposed a method for indirect determination of holdup based on the kinematic wave theory and it was compared with the experimental data.

In Al-Wahaibi & Angeli (2011) and Al-Wahaibi & Angeli (2007) the interfacial wave characteristics were studied. The distribution of wave amplitudes and wavelengths were obtained at different oil and water velocities. The waves were recorded at two locations to study the development of the waves along the pipe. The authors remarked the dependence of the wave characteristics on the phase velocities, for instance the wave amplitudes increased as the superficial velocities increased. Another important conclusion was that the wave amplitudes, closer to the point of injection of fluids, were smaller than those farthest, while the wavelengths were relatively longer. Furthermore, it was established a relation between the wave characteristics and drop formation.

Wave amplitudes, wavelengths and wave speed were studied experimentally in stratified oil–water flow (CASTRO, PEREIRA, SANTOS, & RODRIGUEZ, 2012). The wave characteristics were found to be dependent on holdup, inclination of the pipe and phases velocities. In addition, a methodology for the determination of the average interfacial wave shape was presented and a two-phase Froude number was proposed to correlate the data.

Interfacial waves in stratified oil–water flows was studied with high speed imaging by Barral et al. (2015) . The waves appeared when the flow rates were different. The wave frequencies were found between 11–20 Hz. The wave amplitude decreased while wavelength and wave velocity increased as waves move downstream.

Castro & Rodriguez (2015) developed a study about interfacial waves in stratified oil–water flow. Wave amplitude, wavelength and wave speed were measured using high-speed imaging. Correlations for wave aspect ratio, wave shape and wave speed were proposed. The proposed correlations showed good agreement with the experimental data. The correlation for wave shape was based on a second order Fourier equation.

Table 2.7 - Summary of experimental studies on interfacial waves in liquid-liquid flow in pipes

Reference	Studied features	Oil viscosity (cP) – Pipe diameter (mm) – Orientation – Flow pattern	Measurement technique
Oliemans et al. (1987)	Wave amplitudes Wavelength Wave profile	3000 - 50 Horizontal pipe Core-annular flow	HSC
Bannwart (1998)	Wave speed	2700 - 22.5 Horizontal and vertical pipes Core-annular flow	HSC
Rodriguez & Bannwart (2006)	Wave speed Wavelength Wave amplitudes Wave profile	500 - 28.4 Vertical pipe Core-annular flow	HSC
Al-Wahaibi & Angeli (2011)	Wave amplitudes Wavelength	5.5 - 38 Horizontal pipe Stratified flow and transition to dual continuous flow	HSC Parallel wires conductivity probe
Castro et al. (2012)	Wave amplitudes Wavelength Wave speed	300 - 26 -20°, -10°, 0°, 10°, 20° Stratified flow	HSC
Barral et al. (2015)	Wave velocity Wave amplitude and frequency Wavelength	5.5 - 38 Horizontal pipe Stratified flow	HSC
Castro & Rodriguez (2015)	Wave amplitude Wavelength Wave speed	300 - 26 Horizontal pipe Stratified flow	HSC

HSC: High-speed camera

2.6 Measurements in Multiphase Flows

Several measurement techniques have been developed for the investigation of multiphase flows. Moreover, the existing literature covers mainly the application of these techniques in gas-liquid flows. Specifically, some measurement techniques used for liquid-liquid flows are: conductive/capacitive probes, Electrical Capacitance/Resistance Tomography (ECT/ERT), conductive/capacitive Wire-Mesh Tomography (WMT), and single or multi-beam x/gamma-ray densitometry.

Conductive/capacitive probe emits a two-state signal indicating which phase surrounds the sensing part of the electrode, based on the detection of differences between the electrical properties of the two phases. From the fraction of the time that the probe resides in a given phase, the local volume fraction of that phase can be determined. In Zhao & Lucas (2011) it was used an impedance probe and a conductive probe to obtain the phase distribution of oil and water over the pipe´s cross-section in bubbly oil-in-water pipe flows, Figure 2.8. Even though images of oil-fraction distribution were generated, they only show time-averaged data.

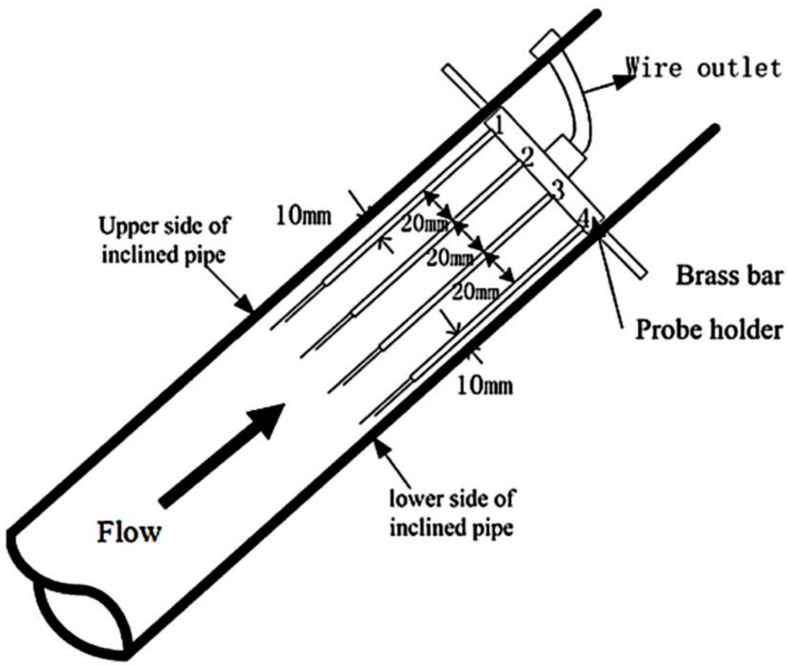

Figure 2.8 - Schematic diagram of the conductive probe used in Zhao & Lucas (2011).

With ECT it is possible to determine the dielectric permittivity distribution in the interior of an object through external capacitance measurements. The ECT sensor consists of a total of M electrodes that are symmetrically mounted outside of a cylindrical container. During each scanning frame, an excitation signal in the form of an alternating voltage is applied to one of the M electrodes and the remaining electrodes are kept at the ground potential, acting as detector electrodes. The measured capacitances can then be represented in a matrix and used to reconstruct the tomographic image of the object. One disadvantage of ECT is that it produces low spatial resolution images. Zhao & Lucas (2011) have used ERT to measure oil fraction distributions and Hasan & Azzopardi (2007) have employed ECT to investigate stratifying kerosene-water flow, Figure 2.9.

The wire-mesh sensor is an intrusive imaging device that provides flow images at high spatial and temporal resolutions. The sensor is made of two sets of stainless steel wires stretched over the cross-section of a vessel or pipe with a small axial separation between them. Each plane of parallel wires is positioned perpendicular to each other, thus forming a grid of electrodes

(Figure 2.10). The associated electronics measure the local conductivity or permittivity (capacitance) in the gaps of all crossing points at a high repetition rate. The spatial resolution of the images generated by the sensor corresponds to the wire separation within a single plane. It measures the local permittivity or conductivity in the gaps of all crossing points by successively applying an excitation voltage to each one of the sender electrodes at one wire plane, while measuring in parallel the current flowing toward the receiver electrodes at the other wire plane. In Rodriguez et al. (2012), a wire-mesh based in capacitance measurements is applied to investigate dispersed flow of oil and water in a horizontal glass pipe.

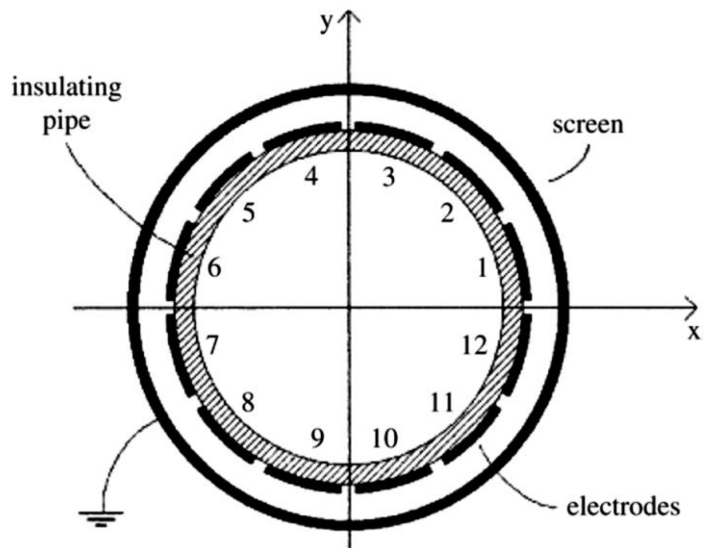

Figure 2.9 - Schematic diagram of the ECT sensor used in Hasan & Azzopardi (2007).

Single or multi-beam gamma-ray densitometry is a non-intrusive method that has also been applied for measuring local phase fractions in oil-water flow systems showing good spatial resolution, but relatively bad temporal resolution. Basically the gamma-ray attenuation technique makes use of the observation that a stationary homogeneous material will absorb a monochromatic beam of constant intensity and short wavelength radiation. The absorption occurs exponentially with increasing absorption length at constant linear absorption coefficient. In Kumara et al. (2010), a single gamma-ray densitometer was used to measure the cross-sectional distributions of oil and water phases in horizontal and slightly inclined oil–water flow.

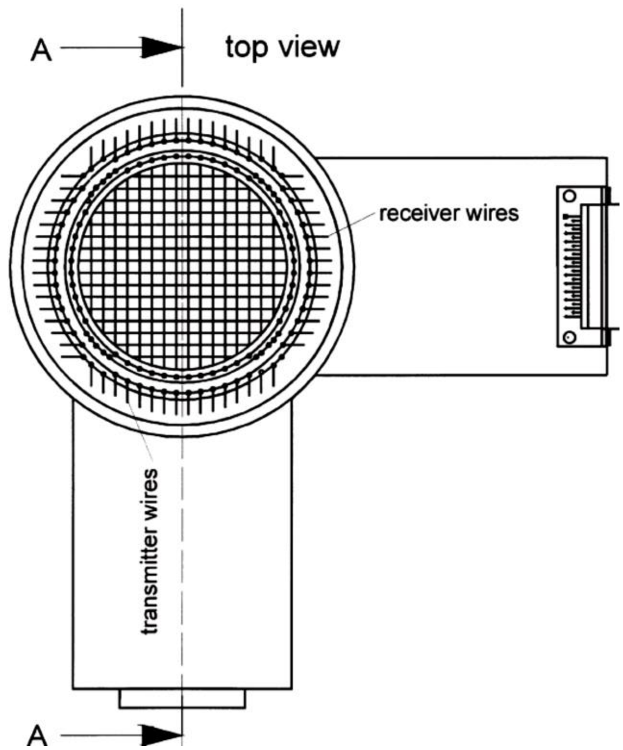

Figure 2.10 -Schematic diagram of the a WMS from Prasser (1998).

2.6.1 Film Thickness Measurements in Gas-Liquid flows

In Clark (2002), twenty film thickness measurement techniques for gas-liquid flows are mentioned, divided into four groups. Film-average methods are for obtaining an average film thickness value measured over a considerable length of film. However, the application of these methods is possible only through the assumption that all the present liquid is in the form of a uniform symmetrical film. There has been little study using film average methods due predominantly to their inability to provide information on local interface phenomena, i.e., waves. Some methods in this group are the holdup measurement (BURNS, 2003) and the conductance method (KANG & KIM, 1992). Localized methods include techniques that give local film thickness measurements (a few millimeters to a few centimeters averaged over a given area), but it is not possible to obtain from it an instantaneous point value. Two methods of this group are the capacitance probe (DEMORI et al., 2010) and ultrasonic pulse-echo methods (WADA et al., 2006). Point methods include all methods in which continuous or statistical information is obtained at a point in a liquid film where film thickness can be measured over small areas. These methods have not been as extensively used as localized methods because, generally, they are harder to implement and the results more difficult to analyze. Some examples are the needle contact probe (TAKESHIMA et al., 2002), the hot-wire method (FRANCO, 2007) and the fiber-optic techniques (ADDLESEE & CORNWELL, 1997). Spatial Methods involve the performance of point or localized measurements simultaneously in different areas of the film in order to build up a global picture of the film thickness structure for the area under study. These techniques offer information of the three-dimensional wave structures. These methods include light absorption (MOUZA et al., 2000), multiple electrodes probes (BELT et al., 2010; DAMSOHN & PRASSER, 2009A, 2009B; JIN, WANG, & XU, 2003; KANG & KIM, 1992), pigment luminance method (SCHAGEN et al., 2006), fluorescent imaging (ALEKSEENKO et al., 2010; SCHUBRING et al., 2010) and ultrasonic transmission (KAMEI & SERIZAWA, 1998). Some methods were chosen as representatives and are presented next.

The first are optical techniques, such as photography, absorption, fluorescence and diffraction. These techniques require a transparent tube or windows, in some cases fluorescent elements applied to the liquid and preferably transparent phases. But these conditions are not always possible, especially in oil-water flow. (ALEKSEENKO et al., 2010; ALEKSEENKO et al., 2008; ALEKSEENKO et al., 2004; FARIAS et al., 2010; HAZUKU, TAKAMASA, & MATSUMOTO, 2008; OLIVEIRA, YANAGIHARA, & PACÍFICO, 2006; SAWANT et al., 2008; SCHAGEN et al., 2006; SCHUBRING et al., 2010; SCHUBRING, SHEDD, & HURLBURT, 2010; SCHUBRING & SHEDD, 2008)

Alekseenko et al. (2008) studied spatial-temporal evolution of disturbance waves and ripple waves in annular gas-liquid flow using high-speed modification of laser-induced fluorescence. Experiments were performed in a vertical Plexiglas cylindrical channel with an inner diameter of 15 mm and a length of 1 m. Continuous green laser with wavelength 532 nm and power 50 mW was used as the light source. Rhodamin-6G was used as fluorescent matter. All experiments were conducted in a measurement area with a length of 20 cm with a spatial resolution 0.1 mm. The exposure time was 150 μs and the registration frame rate of 2000 fps. Registered image brightness was converted into local film thickness using a calibration curve obtained in a set of in situ calibration tests.

Schubring et al. (2010) used planar laser-induced fluorescence to provide direct visualization of the liquid film in an upward vertical air-water annular flow. A small concentration of a fluorescent dye was introduced into the water, causing the liquid film to appear as bright regions on the images once exposed to laser light. Images were processed to locate the edge of the bright region, asserted to be the gas-liquid interface. For the experiments, a polypropylene tube was placed inside a black-walled box, with only two windows, one for the laser and one for the camera. Four hundred pictures were recorded in each experiment and thickness values were between 60 μm and 300 μm.

Multi-conductance sensors (ALEKSEENKO ET AL., 2009; BELT ET AL., 2010; DAMSOHN & PRASSER, 2009a, 2009b; SAWANT et al., 2008) have been widely applied for many years in the study of air-water annular pipe flows. The main disadvantage of conductance sensor is that it cannot measure the film thickness of a non-conductive phase, as it is the case in oil-water dispersed flow. Damsohn & Prasser (2009) built two conductance sensors with different properties, each consisting of an array of 64 × 16 points of measurement and a time resolution of 10000 fps. The first sensor can measure up to 800 μm films. The electrodes are spaced 1560μm, which leads to a spatial resolution of 3120 μm. The second sensor can measure films between 100 μm and 700 μm with spatial resolution of 2 × 2 mm^2. They were made with a standard printed-circuit board (PCB). The geometry of the sensor was optimized in terms of the sensor characteristic by potential-field simulations. The first sensor measures thin films, like disturbance waves with films less than 100 μm and the second resolves smaller structures, but has low sensitivity for thin films. The authors suggest the combination of the two sensors to take advantage of each one and to build the sensor on a flexible PCB in order to be adapted into a cylindrical tube (experiments were done in cubic structures).

The wire-mesh sensor combines intrusive local measurement of phase fraction and tomographic cross-sectional imaging. The wire-mesh sensor based on measurements of electrical permittivity (capacitance) allows studying flows involving non-conducting fluids, such as oil-air flow. The advantages of this technique are: low cost, simplicity when compared with other tomography systems, and high spatial and temporal resolution. In Lopez et al. (2012), a wire-mesh based on capacitance measurements to investigate falling liquid film in gas-liquid flows was presented. In that work, the local gas void fraction distribution was assumed to have a linear relationship with the measured permittivity and, by using a geometrical ratio the liquid film thickness was found. In addition, the liquid film velocity, the liquid entrainment fraction and image of the section were obtained. The most important disadvantage of this method is the intrusiveness.

2.6.2 Film Thickness Measurements in Liquid-Liquid Flow

Only a few measurement techniques for liquid-liquid flows have been proposed. Table 2.8 has a comparison between those methods. Depending on the specific application is appropriate to use one or the other. For example, a high temporal resolution is desirable in the case of oil-in-water dispersed flow where the water velocity is high (greater than 5000 fps) and a high spatial resolution (the highest possible) is necessary for detecting small waves (ripple waves) in annular flow.

In Oliemans et al. (1987), a photographic method was used to study water film thickness in core-annular flows. Wavelengths were seen to vary from 6 to 60 mm, while wave amplitudes were of the order of 1 to 2 mm. Authors mentioned the problem of optical distortion due to diffraction. A disadvantage of this method is that the measurements are only taken in a given area, i.e. in front of the camera (top and bottom for horizontal pipe, right and left for vertical pipe).

Conductance/Capacitive sensors have been widely applied for many years in the area of flows in pipes. Normally, they are simpler, have fast response, are non-intrusive and non-invasive, and have flexibility in electrode design. If the electrodes are flush to the wall, these methods are non-intrusive, but limited to low viscosity fluids. Conductance/Capacitive planar sensors have been used to investigate film thickness of conductive or nonconductive liquids, respectively. They make use of the relationship between electrical capacity and film thickness. Only a few flow applications of planar sensors on multiphase measurements have been reported in the past (BONILLA et al., 2014; THIELE et al., 2009). During the development of this work, a conductance planar sensor with 64 x 16 measuring points was used for water film thickness measurements in oil-water flows (BONILLA et al., 2014). The measured water film thickness had between 100 µm and 700 µm. The sensor could not measure the water film when oil had touched the surface of the sensor before the measurements, because oil stuck to the sensor produced an isolation effect. To avoid this limitation, it was proposed to use capacitive measurements instead of conductive. Thiele et al. (2009), presented a capacitive planar sensor to visualize flows of multiphase mixtures along the surface of objects. The sensor comprises a matrix of 1024 interdigital sensing structures which are individually interrogated based on capacitance wire-mesh sensor electronics (SILVA, SCHLEICHER, & HAMPEL, 2007). The maximal liquid thickness, which influences the measurements at a sensor, is 750 µm. No application of this method in pipelines was found.

In summary, there are a few film thickness measuring techniques for oil-water flow in the literature. These techniques have been used in studies of annular flow (gas-liquid and liquid-liquid flows). No applications in dispersed flows were encountered.

Table 2.8 - Comparison of Liquid-Liquid Measurement Techniques

Technique	Spatial resolution (mm)	Temporal resolution (frames/s)	Min - Max film thickness (µm)	Application
Photographic (OLIEMANS et al., 1987)	-	2000 - 10000	1000-2000	Core-Annular flow
Capacitive Planar Sensor (THIELE et al., 2009)	2x1	15000	Up to 750	Isopropyl alcohol -benzene mixture
Conductive Planar Sensor (BONILLA et al., 2014)	2x2	10000	100-700	Oil-water mixture
Capacitive Planar Sensor (In this work)	4x4	5000	400-2200	Oil-water flow

2.7 Planar Sensor

A planar sensor is a sensor where the electrodes are placed in a co-planar plane. Two important advantages of these kinds of sensors are: only a single-side access to the test material is required and the strength of the output signal can be controlled by changing the area of the sensor, the number of electrodes or the spacing between them. There are several applications of the planar sensor in proximity/displacement measurement (CHEN & LUO, 1998), nondestructive testing (SHARMA, 2011), material characterization (MAMISHEV et al., 2004), humidity measurement (STEELE et al., 2008), flow studies (BELT et al., 2010) and health monitoring (NASSR & EL-DAKHAKHNI, 2011).

The operating principle of planar sensors is based on the interaction between a test substance or material and the interrogating electric field. The disturbance in the electric field can be detected by a receiver and is related to the properties of the conductive or dielectric material or substance near the sensor (HU & YANG, 2010).

A planar sensor is normally an array of electrode pairs, named transmitter and receiver, flush mounted on an insulating surface. An electrical stimulus is applied to a transmitter electrode while a measurement is taken from a receiver electrode. According to the frequency of the electrical stimulus, the measurements can be related with the permittivity or/and the conductivity of the test material. Figure 2.11 shows a planar sensor and the electric field lines between the electrodes (in green).

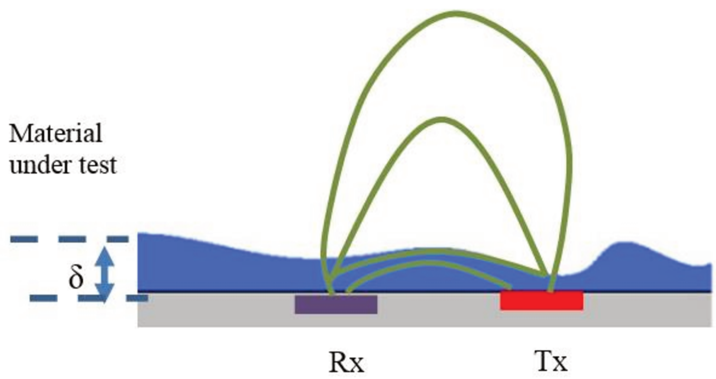

Figure 2.11 - The electric field lines between the electrodes in a planar sensor.

The interaction between the test material and electric field ($\vec{E}$) can be described by (SILVA, 2008)

$$\vec{J} = \sigma\vec{E} + j\omega\vec{D} \quad (2.23)$$

where $\vec{J}$ is the current density, σ is the conductivity, $\omega = 2\pi f$ (f is the frequency), $j = \sqrt{-1}$ and $\vec{D}$ is the electric displacement. This equation is valid assuming that there is not externally generated current density and the magnetic field effects are negligible. The relation between the electric displacement and the electric field is expressed as

$$\vec{D} = \varepsilon_0\varepsilon_r\vec{E}, \qquad (2.24)$$

where $\varepsilon_0 = 8.8541 \times 10^{-12}\mathrm{F/m}$ is the vacuum permittivity, permittivity of free space or electric constant and ε_r is the relative permittivity.

The electric field, $\vec{\mathrm{E}}$, is related to the electric potential, ϕ, by (SERWAY & JEWTT, 2014)

$$\vec{E} = -\nabla\phi, \qquad (2.25)$$

and the continuity equation is

$$\nabla \cdot \vec{J} = \frac{\partial\rho}{\partial t} \qquad (2.26)$$

where ρ is the electric charge density.

Combining eq. (2.23) to (2.26) and assuming free charge density, one can obtain

$$\nabla \cdot \left[-\left(\sigma + j\omega\varepsilon_0\varepsilon_r\right)\nabla\phi\right] = 0. \qquad (2.27)$$

For electrostatic approximation and assuming no free charge in the sensing space, the eq. can be written as

$$\nabla(\varepsilon_0 \varepsilon_r \nabla \phi) = 0. \qquad (2.28)$$

The capacitance C in Farads of a capacitor is the ratio of the magnitude of the charge Q on one of the plates to the potential difference between them (U).

$$C = \frac{Q}{U} \qquad (2.29)$$

By Gauss's law, the electric net flux through any closed surface is

$$\oint \vec{E} \cdot d\vec{A} = \frac{Q}{\varepsilon_0} \qquad (2.30)$$

For a capacitor filled by a dielectric with relative permittivity ε_r, the capacitance C is

$$C = \frac{\varepsilon_r \varepsilon_0 \oint \vec{E} \cdot d\vec{A}}{\int \vec{E} \cdot d\vec{l}} \qquad (2.31)$$

The analytic solution of eq. (2.27) is only possible for some simple cases and limited cases, then it is necessary an approach method. There are many options to obtain an approximate response, for example, finite elements method (FEM), finite difference method, boundary element method (BEM), etc. A solution of this equation produced the three-dimensional field line plot. A sketch of the field lines, in a plane, can be seen in Figure 2.11.

2.7.1 Circuits

The permittivity and the conductivity of a sample cannot be measured directly. But, its impedance is measurable and the conductivity and the relative permittivity can be determined from this.

Impedance (Z) is generally defined as the total opposition a device or circuit offers to the flow of an alternating current (AC), and is represented as a complex quantity,

$$Z = R + jX \qquad (2.32)$$

where there is a real part (resistance, R) and an imaginary part (reactance, X) (AGILENT, 2003).

Sometimes it is more convenient to use the inverse of Z, the admittance

$$Y = \frac{1}{Z} = G + jB \qquad (2.33)$$

where G is the conductance and B is the susceptance.

For a simple geometry, as parallel plate capacitor, the capacitance and conductance can be defined as

$$C = k_g \varepsilon_0 \varepsilon_r$$
$$G = k_g \sigma \qquad (2.34)$$

where k_g is a constant related to the geometry, ε_r is the relative static permittivity (sometimes called the dielectric constant) of the test material, ε_0 is the electric constant ($\varepsilon_0 \approx 8.854 \times 10^{-12}$ F m^{-1}) and σ is the conductivity.

There are several impedance measurement methods. Traditional methods include: bridge, resonant, Current-Voltage (I-V), network analysis and auto-balancing bridge (AGILENT, 2003). The measurements using wire-mesh sensors are made with auto-balancing bridges. This circuit allows remaining all receiver electrodes very close to ground potential. This is an important feature to suppress cross-talk to far located receiver electrodes, as discussed in Prasser et al. (1998).

Figure 2.12 presents a basic schematic circuit of the auto-balancing bridge, where U_{in} is the excitation voltage, Z_x represents the unknown impedance and Z_f the feedback network. Assuming that the op-amp is ideal the output voltage U_{out} is determined by

$$U_{out} = -\frac{Z_f}{Z_x} U_{in} \qquad (2.35)$$

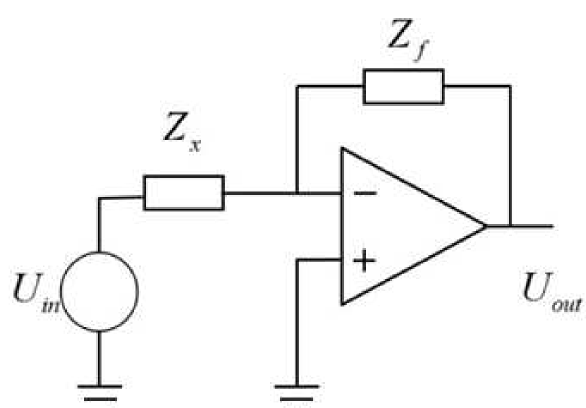

Figure 2.12 - Basic circuit configuration of the auto-balancing bridge impedance measuring method.

The proper dimensioning of the C_f and G_f is important for the correct operation of the auto-balancing bridge. Additionally, the operation frequency and the characteristics of the op-amp used must be taken into account. According to the frequency, the circuit may then be dimensioned as capacitance or resistance dominant (SILVA, 2008). As a result, C_x and G_x from a material under test can be measured.

Given that,

$$R_f = 1/G_f \qquad (2.36)$$

$$R_x = 1/G_x \qquad (2.37)$$

the gain of the circuit can be written as

$$\frac{U_{out}}{U_{in}} = -\frac{G_x + j2\pi f C_x}{G_f + j2\pi f C_f} \quad (2.38)$$

And the magnitude of eq. (2.38) is

$$\left|\frac{U_{out}}{U_{in}}\right| = \frac{\sqrt{G_x^2 + (2\pi f)^2 C_x^2}}{\sqrt{G_f^2 + (2\pi f)^2 C_f^2}} \qquad (2.39)$$

The frequency response of a practical auto-balancing bridge has two frequency bands with a constant gain, with values of G_x/G_f and C_x/C_f, correspondingly, see Figure 2.13 . An auto-balancing bridge was used to measure conductance using a resistance in the feedback network in Damsohn & Prasser (2009) and capacitance using a pair resistance-capacitor in the feedback network in Thiele et al. (2009).

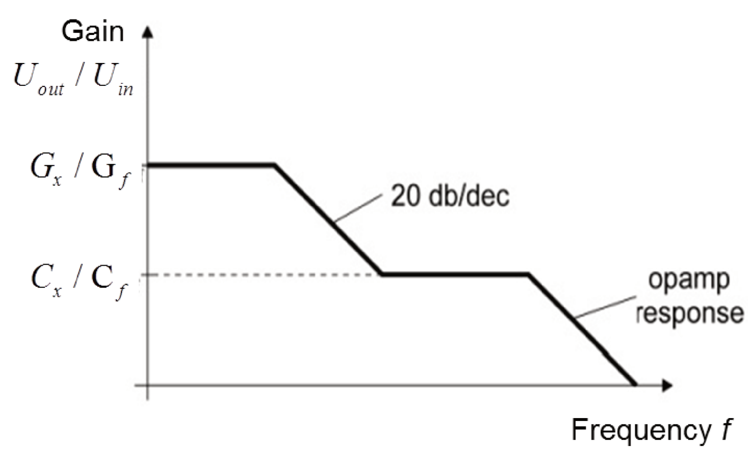

Figure 2.13 - Frequency response of a practical auto-balancing bridge (SILVA, 2008).

2.7.2 Conductance System

The conductance sensor system, designed in Swiss Federal Institute of Technology Zurich (ETHZ) (DAMSOHN & PRASSER, 2009), has 64 x 16 measuring points and measuring area of 128 mm x 32 mm and a time resolution of 10000 fps. The system can measure films between 100 μm and 700 μm with spatial resolution of 2 mm × 2 mm. Figure 2.14 shows the conductance system. In the planar sensor, the transmitting electrodes are connected in one direction (transmitter lines), while the receiver electrodes are coupled perpendicular to this direction (receiver lines).

A voltage pulse is supplied to the first electrode of each pair and current flows to the second electrode, which is put to zero potential. The current depends on the thickness of the electrically conducting liquid film covering both electrodes. Through a process of switching, each transmitter electrode is activated sequentially, i.e., it sends an electrical signal to the fluid. Then, the receiver electrode gets a signal that contains the information that identifies the type of fluid at each active area. When the sequence of switching for the entire set of transmitters is complete, one frame with the information of the fluid or phase over the sensor surface is available, within a time interval (PRASSER et al. 1998).

The circuit in Figure 2.14 uses a low impedance transmitter driver for each transmitter and a transimpedance amplifier for each receiver. The crossing points of the active transmitter and the transimpedance amplifiers constitute several auto-balancing bridges. The transmitter driver and the transimpedance amplifier guarantee that the potential at all non-activated transmitter electrodes and all receiver electrodes remains very close to ground potential, which prevents crosstalk between transmitters located far away (not actives) and the receiver electrodes. Therefore, parasitic currents traveling from not activated transmitters to receivers as well as from a receiver electrode to a neighboring one are not induced and their effect are minimized.

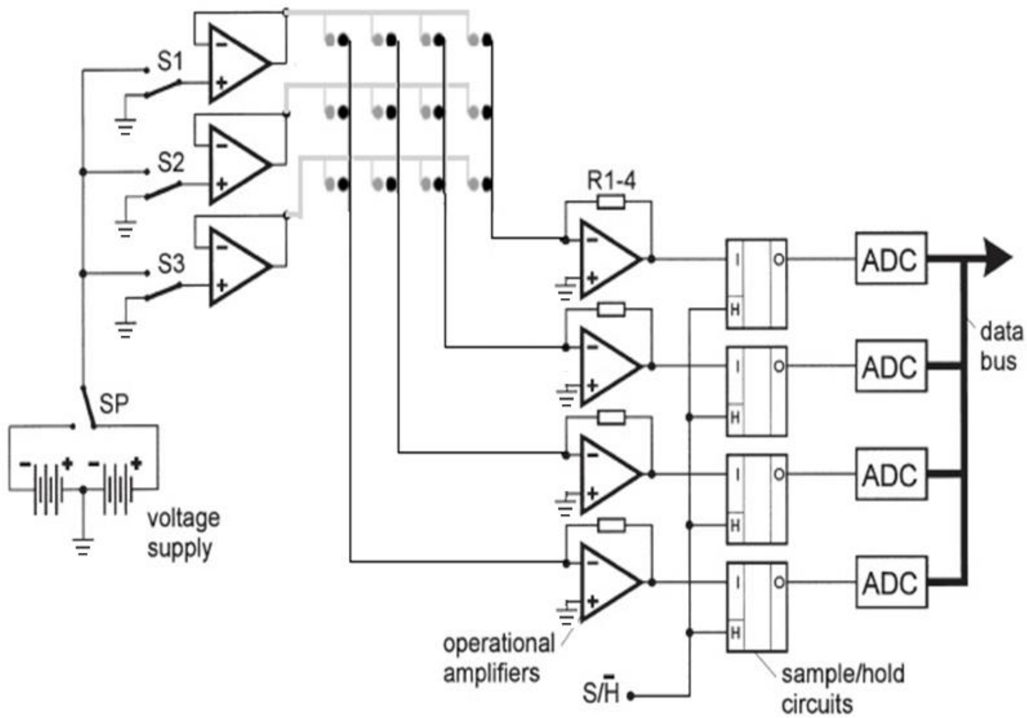

Figure 2.14 – Circuit of the conductance system, adapted from Prasser et al. (1998) and Damsohn & Prasser (2009).

2.7.2.1 Calibration and Compensation

Since the relationship between measured current and film thickness is non-linear because the potential field has a higher concentration in the region near to the wall and decreases with the distance, a calibration procedure is necessary. Also, the calibration is able to counteract variances in the measured values of a transmitter-receptor pair due to differences in the electrical characteristics of the individual components, for instance resistor tolerances, op-amp gains, among others.

Damsohn (2011) proposed a procedure where the sensor is immersed into water with an inclined angle and various cylinders made of nonconductive material with a known gap (they have gaps between 0 μm and 1000 μm) are rolled over the sensor. The calibration value is taken from the minimum measured value, when the cylinder is passing over the measuring point. The calibration values for each measurement point are fitted with a fourth order rational polynomial.

Finally, eq. (2.40) is used to relate the conductance with the film thickness δ in each measurement point,

$$\delta = a_1 G_m^4 + a_2 G_m^3 + a_3 G_m^2 + a_4 G_m + a_5, \quad (2.40)$$

where a_1 to a_5 are the polynomial coefficients determined by the calibration curve fitting.

In Damsohn (2011) was proposed a simple and robust solution for temperature compensation where the sensor is replaced with known reference resistors. The resistors are arranged such that each receiver line is connected to three resistors of different resistances. The voltage in the reference resistors is measured in two moments: (1) immediately after the calibration process, $U_{ref,cal}$, and (2) after each experiment in the pipeline, $U_{ref,meas}$. Then, the ratio φ between those values is the compensation factor, eq (2.41).

$$\varphi = \frac{U_{ref,cal}}{U_{ref,meas}} \quad (2.41)$$

The measure value of G_m with the conductance circuit and using the compensation of Damsohn (2011) can be calculated as

$$G_m = \frac{U_m}{U_{sat}} \varphi, \quad (2.42)$$

where U_{m} is the measured value and U_{sat} is the saturation value corresponding to the value obtained when the measuring point is not covered with the cylinder, but only by water.

2.7.3 Capacitance System

In Silva (2008), the sensor system has 32 × 32 measuring points, a measuring area of 620 mm x 500 mm, and a time resolution of 2500 fps. The sensor can measure films up to 690 µm with spatial resolution of 7.8 mm × 6.6 mm. This sensor is arranged in a matrix, with transmitters connected in one direction and receptors connected perpendicularly to the transmitters.

The transmitter electrodes are successively excited by an AC signal, while all the other transmitter electrodes are connected to ground potential, Figure 2.16. The electrical currents flowing from the activated electrode to the receptor electrode is converted to voltage by an auto-balancing bridge, Figure 2.15. This routine is repeated for all transmitter electrodes being activated.

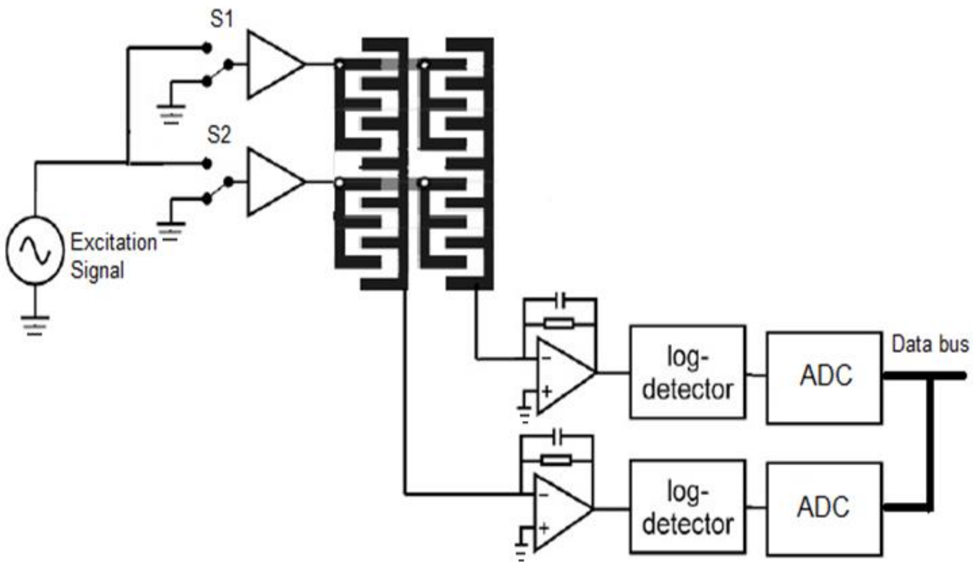

Figure 2.15 – Circuit of the capacitance system, adapted from Thiele et al. (2009).

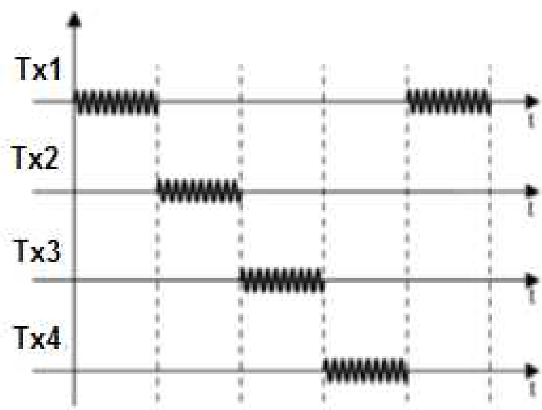

Figure 2.16 - Excitation scheme of the comb sensor, adapted from Silva et al. (2007).

Thiele et al. (2009) presented the process to calculate the fluids permittivity using the circuit in Figure 2.15. The procedure starts by covering the entire sensor with a low permittivity substance, ε_L, oil for example, $\varepsilon_L = 3.5$, and measuring. The procedure is repeated with another substance with high permittivity, ε_H, for example water ($\varepsilon_H = 80$). Then, two factors (a and b) are calculated for each measuring area as follow,

$$a(i,j) = \frac{U_H(i,j) - U_L(i,j)}{\ln(\varepsilon_H) - \ln(\varepsilon_L)}$$
$$b(i,j) = \frac{U_L(i,j)\ln(\varepsilon_H) - U_H(i,j)\ln(\varepsilon_L)}{\ln(\varepsilon_H) - \ln(\varepsilon_L)} \tag{2.43}$$

U_L and U_H are the measured voltages with the low permittivity substance and the high permittivity, respectively, and the indices i and j represent the position in the sensor matrix, i.e. the index of the pair transmitter-receiver. The measured permittivity, ε_m, is calculated as

$$\varepsilon_m(\mathrm{i},\mathrm{j}) = exp\left(\frac{U_m(\mathrm{i},\mathrm{j}) - b(\mathrm{i},\mathrm{j})}{a(\mathrm{i},\mathrm{j})}\right) \tag{2.44}$$

These works showed the permittivity distribution for a two-fluids mixture, where each fluid had a different permittivity.

Thiele et al. (2009) proposed a calibration procedure using a polyvinyl chloride (PVC) plate. The plate was placed covering the entire sensor. One of its endpoints was raised by a thin plastic spacer of 1.5 mm thickness, while the other one was in direct contact with the sensor, creating an inclined plane. This assembly was immersed in ethyl alcohol, which resulted in a liquid film of continuously increasing thickness over the sensor surface.

2.7.4 Geometries

Different geometries of planar sensors have been proposed in the literature, depending mainly on the application and test characteristics. They are not suitable geometries for all the cases. It is necessary to do a particular study for each case, taking into account the required characteristics and purpose, before to select the best geometry for a specific application. Figure 2.17 presents some photos and diagrams of planar sensors used to measure two phase mixtures. In the figure R refers to receptor electrode, T to transmitter electrode and G to ground electrode. The features of these sensors are summarized in Table 2.9.

Table 2.9 – Planar sensor features.

Reference	Spatial resolution (mm) and number of measurement points	Temporal resolution (frames/s)	Min - Max film thickness (μm)	Application
Damsohn & Prasser (2009)	3.2×3.2 and 1024 points	10000	100-600	Air-water annular flow
Thiele et al. (2009)	2×1 and 1024 points	15000	0-750	Isopropyl alcohol -benzene mixture
Belt et al. (2010)	4.9×19.5 and 320 points	5000	0-3000	Air-water annular flow

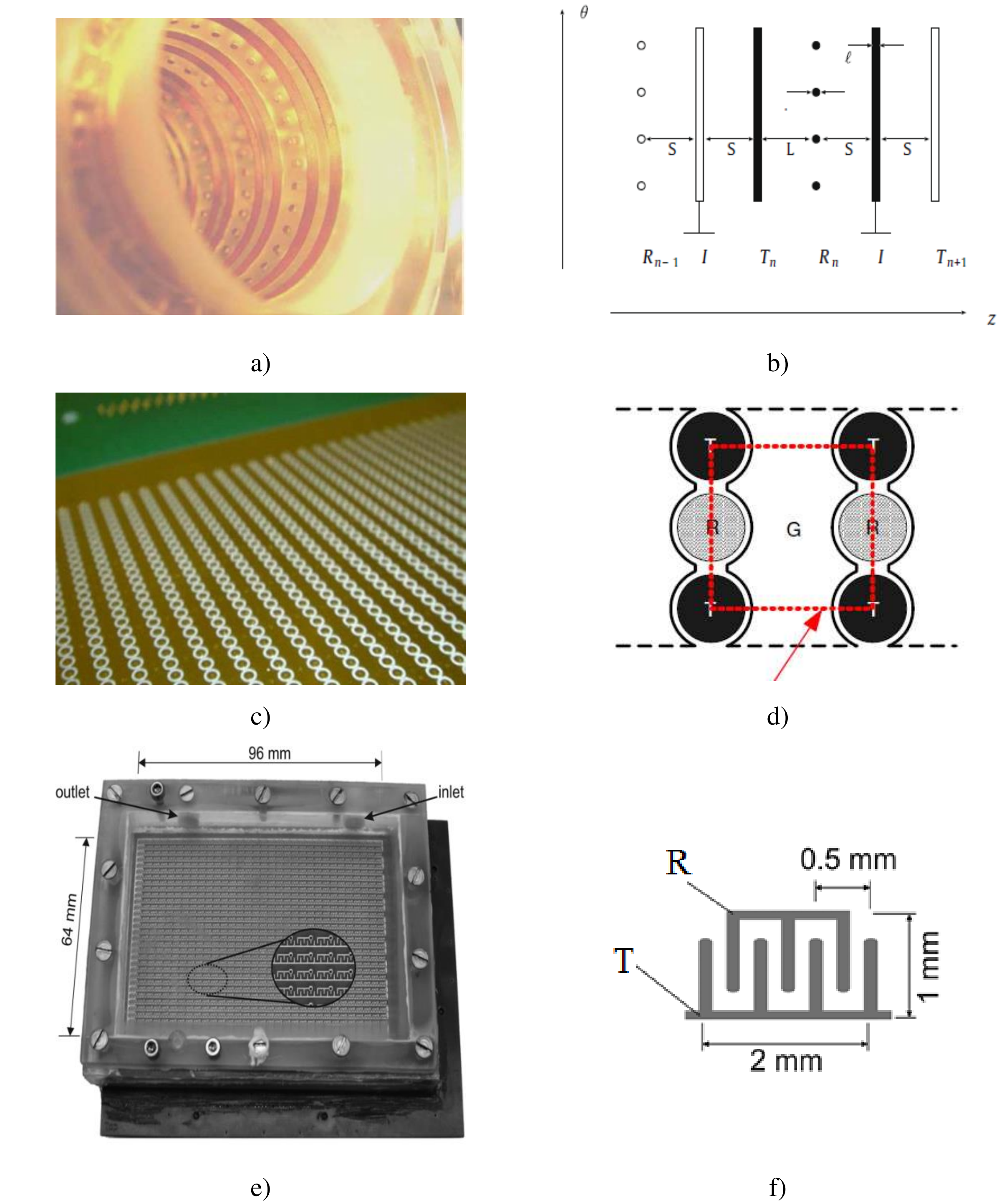

Figure 2.17 – Examples of planar sensor geometries. a) Photo and b) schematic of the geometry proposed by Belt et al. (2010); c) photo and d) schematic of the geometry proposed by Damsohn & Prasser (2009); e) photo and f) schematic of the geometry proposed by Thiele et al. (2009).

3 MATERIALS AND METHODS

The experimental work was performed at the Multiphase-Flow-Loop Test Facility of LETeF (Thermal-Fluids Engineering Laboratory), the Engineering School of São Carlos of the University of São Paulo, where simultaneous flow of oil, water and gas can be generated with any combination of the phases. A schematic view of the facilities is shown in Figure 3.1 and Table 3.1 lists the main instruments and equipment.

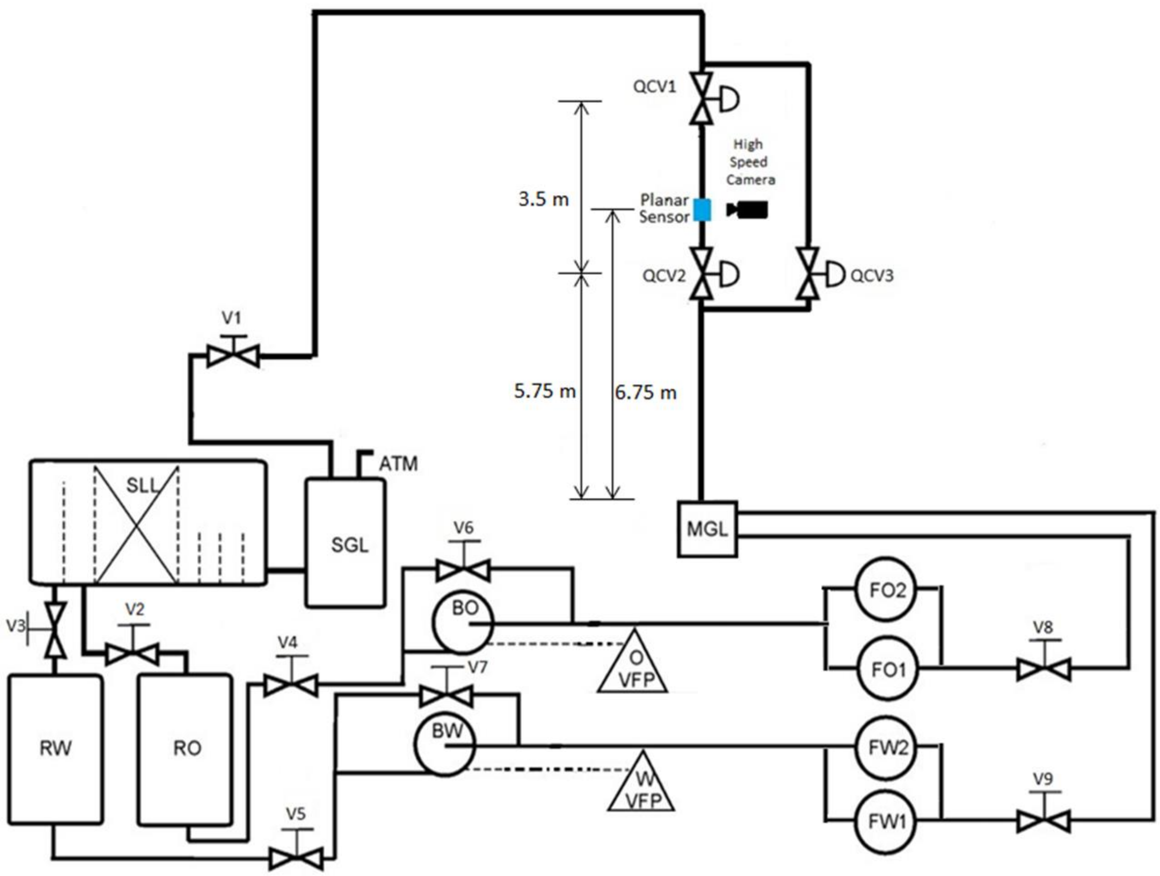

Figure 3.1 - Schematic of the experimental multiphase flow facility at LETeF.

The test pipe consists of a 12-meters-height glass section of 50.8 mm i.d. Water and oil are used as test fluids. Both water and oil are kept in polyethylene reservoirs tanks, (RW) and (RO), respectively. Each phase is pumped, from its respective storage tank, to the test section, by positive displacement pumps (BW and BO, respectively), both remotely controlled by variable-frequency drivers. Oil and water are mixed at the beginning of the glass pipe via a Y-junction (MGL) as shown in Figure 3.1.

Positive displacement and vortex flow meters are used to measure high and low oil flow rates (FO1 and FO2, respectively) and high and low water flow rates (FW1 and FW2, respectively), see Table 3.2. After the test line, the mixture goes to a coalescent-plate separator tank (SLL). The phases, once separated, are returned to their respective storage tanks by gravity (RW and RO). A computer and LabVIEW™ is used to conduct the tests and collect the data.

Table 3.1 - Main Instruments and Equipment of the Facility.

Symbol	Description	Symbol	Description
	W VFP – Water Variable-frequency driver O VFP – Oil Variable-frequency driver		FO1, FO2– Oil Flow Meters FW1, FW2 – Water Flow Meters
	QCV1, QCV2, QCV3 - Quick Closing Valve		Control Valve
	Differential Pressure Transducer		BW – Water Pump BO – Oil Pump
SLL	Coalescent-plates liquid-liquid separator	RW	Water Tank
MGL	Multiphase mixer	SGL	Gas-liquid separator Tank
RO	Oil Tank		

In-situ phase volume fractions (holdup) are measured using the quick-closing-valves technique (QCVs). Solenoid valves V1 and V2 are normally open. The open-close time is of 0.11 s. In steady-state flow regime, the solenoid valves number V1 and V2 are open, allowing the fluid to pass through the test line. During the tests, by energizing V1, V2 and the valves in the test section, the mixture is trapped in the test line and the two-phase flow deviated to the by-pass line. After the drainage of the test line, it is possible to measure the value of the volumetric fraction of each phase. The flow patterns can be identified via visualization technique.

A high-speed video camera (Olympus i-Speed 3) records a projected lateral view of the flow at up to 40.000 fps.

3.1 Flow-loop Facilities

3.1.1 Water and Oil Pumps (BW and BO)

Two 10-hp positive displacement pumps, Weatherford model 2WHT 53/F, are used in the flow loop to pump oil and water. Each pump is controlled by a variable-frequency drive of 12 KW (W VFP and O VFP).

3.1.2 Air Compressor

A 30-hp screw compressor Schulz SRP 3030 is responsible for the air supply to the flow loop. It has an effective flow rate of 3511 L/min and outlet working pressure of 7.5 bar. The compressed air coming out of compressor is cooled by a heat exchanger, followed by a three-way branch containing pneumatic control valves in each one.

3.1.3 Flow Meters

Table 3.2 shows some specification of the available flow meters.

Table 3.2 - Characteristics of the flow meters in the flow loop.

Meter	Fluid	Flow	Uncertainty (% of measured value)	Superficial velocity 2” pipe (m/s)
OGT Oval (FW1)	Water	1.0 – 35 L/min	±0.75	0.00848 – 0.297
EX-DELTA VXW1050 Oval (FW2)	Water	33.33-1300 L/min	±1.0	0.28 – 11.03
LSF45 Oval M-III (FO1)	Oil	0.05-8.0 L/min	±1.0	0.000424 – 0.0679
FLOWPET-EG LS5376 Oval (FO2)	Oil	2.5 – 106. 7 L/min	±1.0	0.0212 – 0.905

3.1.4 Oil-Water Separator

A coalescing-plate separator (SLL) with a capacity of 220 L is used for the separation process of the mixture of oil and water that comes from the test section. Both tap water and oil are kept in the same large coalescent-plate separator. Because of the difference in density, oil lies in the upper part of the separator, while water remains in the lower part. Once separated, oil and water are driven by gravity to their own tanks. Each phase is separately pumped through its own series of pipes and flow and temperature meters from the respective tanks to the mixing section. After the outlet of the test section, pipes carry the mixture to a gas separator tank. The mixture reaches the top of the separator tank and escapes through a chimney, while the liquids get back to the coalescing-plate separator.

3.1.5 Other Meters

There were thermocouples in the oil line (type k) to measure temperature. It was considered that the water would have similar temperature than the oil. There is a pressure gauge, in the oil line, for pressure control and safety reasons, to prevent accidents.

3.1.6 Quick-Closing-Valves

Three ball solenoid valves let the flow goes through the pipeline or the bypass. The flow in the principal pipeline is controlled by two normally open valves and a normally closed valve is used to control entry of the fluids into the bypass line. Each valve is activated by its own pneumatic actuator. The supply pressure is 4 bar and the torque is 6 N·m. The open/close time is 0.11 s.

3.2 Data Acquisition System

A computer with a data acquisition card NI PCI-6224 and LabVIEW controls the system. This system receives and sends signals to different gauges and equipment, both for operating and analysis purposes. The NI PCI-6224 had an ADC with 16 bits of resolution, 48 digital channels and 32 analog channels.

The digital channels were used for the activation of the quick-closing valves and analog inputs were used to connect all the meters. The actuators that control water, air and oil flows were triggered via low frequency CAN system.

3.3 Fluids and Test Matrix

The fluids used in the experiments consisted of a refined mineral oil and tap water. Oil and water physical properties are listed in Table 3.3. The electrical characteristics of the fluids were measured with an impedance analyzer Solartron 1260 at frequency of 5 MHz with an accuracy of 0.1%. Oil-water Interfacial tension was of 0.033 N/m.

Table 3.3 - Characteristics of the fluids.

Fluid	Viscosity (cP at 25°)	Density (kg/m^3)	Relative Permittivity (-)	Conductivity (S/m)
Water	1	988	79	4.12×10^{-3}
Oil	220	860	3.5	0.04×10^{-15}

Due to facility limitations, the experimental regions were restricted to the areas plotted in red on the flow pattern map of Bannwart et al. (2011), Figure 3.2. As mentioned before, the interest of this work is to study dispersed oil-in-water and annular flows. The water superficial velocity was changed between 0.1 m/s and 0.3 m/s for annular flow and between 0.7 m/s and 1.96 m/s for dispersed oil-in-water flow. The oil superficial velocity was varied between 0.3 m/s and 0.8 m/s for both cases. The experimental points were chosen such that the water film thickness could be measured with the capacitive system, i.e. when the film thickness was lower than 2200 µm. In preliminary experiments, the water film thickness for the stable annular flow (0.05 m/s < V_{so} < 0.3 m/s) was observed higher than 3000 µm and higher than 2500 µm for dispersed oil-in-water flow when the oil superficial velocity is lower than 0.06 m/s.

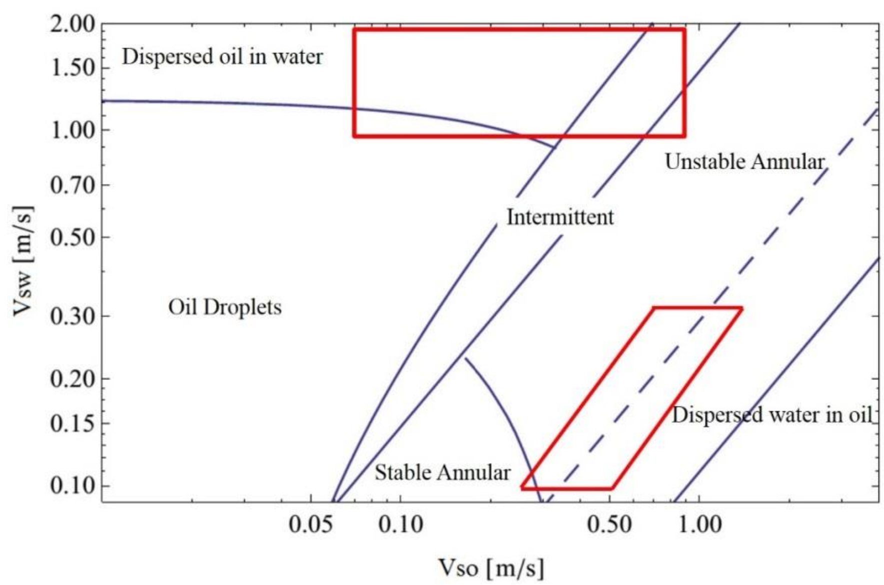

Figure 3.2 – Flow map of superficial velocities, upward-vertical oil-water flow for 50.8 mm pipes.

3.4 Finite Element Simulations

As mentioned in section 2.7, the sensor behavior, with a liquid film over it, can be studied by solving the three-dimensional electric potential equation using a FEM software, equations (2.27) and (2.28). In this research Comsol Multiphysics and Matlab were used to simulate.

Electrostatic simulations were carried out to compare sensor geometries found in the capacitive sensing literature and determine the best geometry for measuring water film thickness in oil-water flows. The best geometry was simulated in frequency conditions (at 5 MHZ) using electric current simulations.

The geometry in both simulations was similar. Each simulated sensor had two transmitter electrodes, two receptors and ground electrodes around them. The boundary of the simulation space is set to be a square infinite element (dimensions 13 mm ×13 mm × 13 mm). The structure was composed by the sensor, aluminum (to simulate the section where the sensor was placed), water, and oil, represented for rectangular shapes, Figure 3.3.

The sensor had two parts: the electrodes and the insulating surface (PCB). The structure of the sensors was on the order of microns. The electrodes height was 50 μm, and PBC size was 8 mm ×8 mm × 0.45 mm.

The width of water, oil and air changed in each simulation. The width of the water layer over the sensor is the studied film thickness. The characteristics of the used material are in Table 3.4.

Table 3.4 - Characteristics of the materials.

Material	Domains	Relative Permittivity (-)	Conductivity (S/m)
Air	Arround the structure	1	0
Cooper	Electrodes	1	5.998×10^{7}
Polyimide	PCB	3.3	7×10^{-16}
Aluminum	Under PCB	1.8	35×10^{6}
Water	Over the electrodes and PCB	79	4.12×10^{-3}
Oil	Over the water	3.5	0.04×10^{-15}

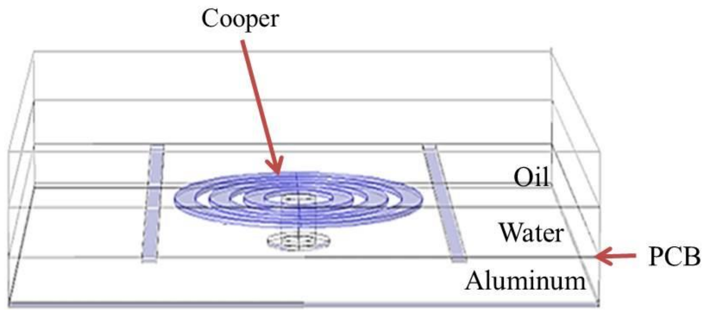

Figure 3.3 – Example of structure geometry.

The conditions used for the simulation were: one transmitter electrode was set to 1 Volt and the other transmitter and the receivers were set to 0 Volt. One can see in Figure 3.4 the electric field lines when a transmitter is active.

3.4.1 Geometries Testing

The procedure consisted on implementing the geometries with the minimum values (for the PCB parameters) and changing the spacing between the electrodes, trying to keep the spatial resolution in the minimum possible. The geometries were simulated for various water films. The capacitance was found for those film thicknesses.

In that study, the technological limits of the PCB-production were considered as boundary conditions. Those boundary parameters were: the trace width, the annular ring, the via size and the minimum spacing. Also, they were designed to avoid having right or acute angles, ≤ 90°, (GUTIERREZ & COATES, 2010).

3.4.2 Selected Geometry

The selected geometry was simulated taking into account the electric currents and the electrostatic field. It was used a frequency of 5 MHz, that it is the operation frequency of the capacitance measurement system. In this case, the water height was varied between 100 µm and 3500 µm in steps of 100 µm.

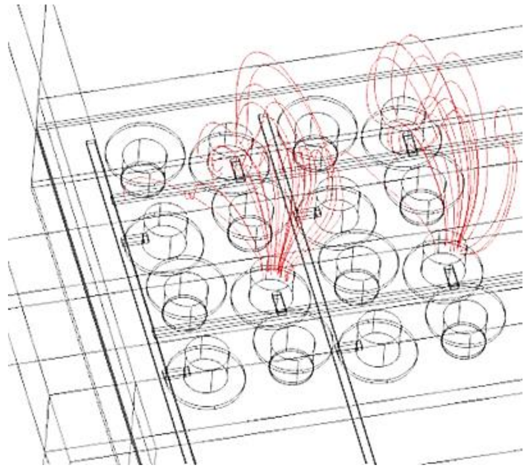

Figure 3.4 – Example of streamlines in a simulation

4 CAPACITANCE LIQUID-FILM THICKNESS MEASUREMENT SYSTEM

The proposed liquid-film thickness measurement system is presented in Figure 4.1 and Figure 4.2. The system consists of eight parts. The waveform generator, the analog-digital converter (ADC) and the FPGA (1, 5 and 6 in the Figure 4.1 and Figure 4.2) are integrated through a National Instrument PXI-1072 equipment. The transmitter and reception circuits were built during this work (2 and 4 in the figures), they are based on the circuits used in the capacitance Wire-Mesh sensor (SILVA, 2008). The planar sensor was provided by Professor Horst-Michael Prasser from ETH Zurich. The circuits and FPGA programs were made with the help of Dr. Hugo Fernando Velasco.

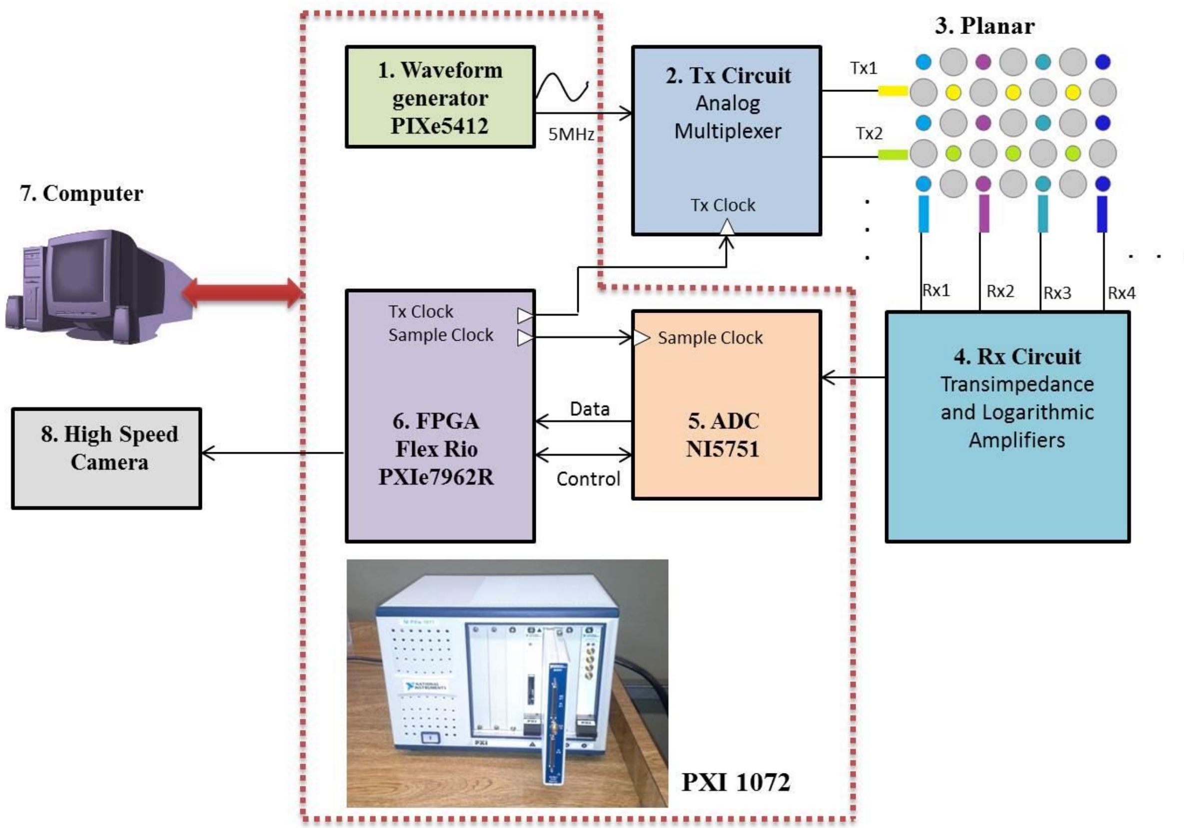

Figure 4.1 - Schematic arquitecture of the proposed liquid-film thickness measurement system.

Figure 4.2 presents the information flow in the system. The FPGA controls the system by producing signals to activate each transmitter and the high speed camera, synchronously. The analog multiplexer leads the signal to the transmitter electrodes (Tx) in the planar sensor. The amplifiers give a signal proportional to the capacitance of the fluids over each pair transmitter-receiver (Tx-Rx). The ADCs convert the measured signal in a digital signal and the signals are storage in the computer.

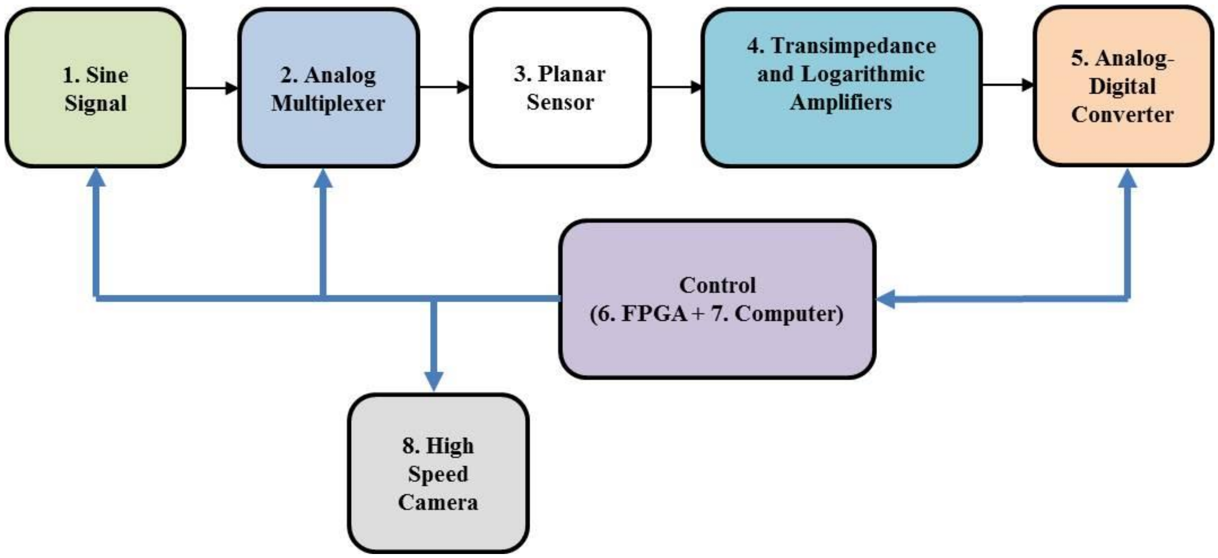

Figure 4.2 – Schematic diagram of the information flow for the proposed liquid-film thickness measurement system.

The main characteristics of the system are listed in Table 4.1. The system can be characterized by: (i) the spatial resolution of 4×4 mm^2 (one pixel in the resulting frame represents a square area with that size), (ii) the depth resolution of 6.2 µm calculated by measuring the maximum and minimum voltages and taking in account the ADC resolution, see calculation in APPENDIX B (it is possible to differentiate changes in the film height of 6.2 µm) and (iii) the temporal resolution of 200 µs (one frame time) which depends on the time to reach a steady state at the signal in a transmitter, see calculation in APPENDIX B. Consequently, the waves or structures near to the pipe wall could have a maximum velocity of $V_{max} = 3$ m/s to allow detection of their variations. The measurement range of the sensor is from 400 µm to 2200 µm from the pipe wall.

A schematic view of the circuit used in the system is showed in Figure 4.3. The measurement system is supplied by a sinusoidal signal. The system has 208 measuring points, each row is activated (each Tx) sequentially by the analog multiplexer. There are 16 transimpedance amplifiers and 16 logarithmic amplifiers. The used ADC has 16 simultaneous channels. In the figure, the Tx2 is active; the dashed line over the sensor represents the sensing area of the pair Tx2-Rx2. The spatial resolution is the region of measuring of a pair Tx-Rx (the blue region in the Figure 4.3), which corresponds to the spatial separation between electrodes. The electrodes are the only conductive portion of the sensor in contact with the fluids.

Table 4.1 - Characteristics of the measurement system.

System Characteristic	Value
Spatial resolution	4 × 4 mm2
Depth resolution	6.2 µm
Temporal resolution	5000 frames/s
Work frequency	5 MHz (ajustable)
Measurement range	400 µm to 2200 µm
Measuring points	208 (13 Tx and 16 Rx)
Measuring area	52 mm × 64 mm

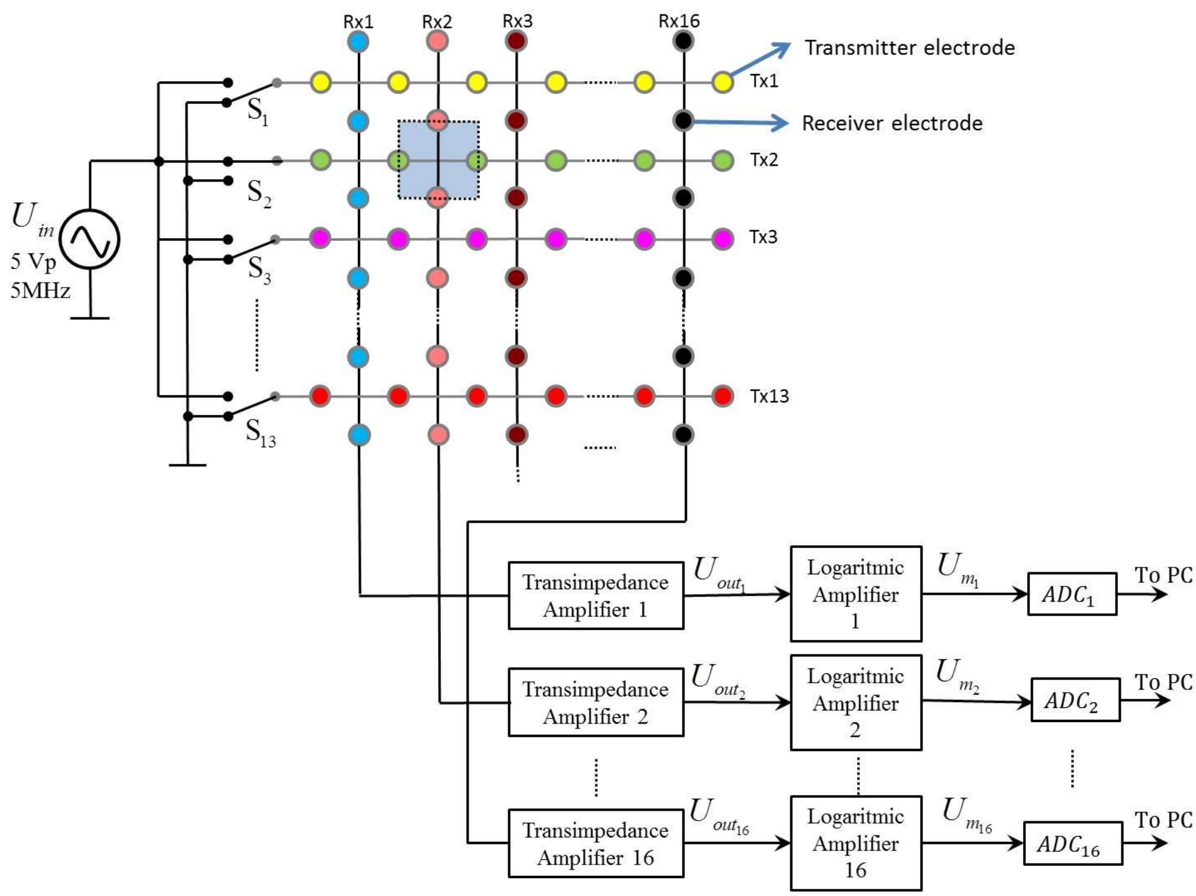

Figure 4.3 – Schematic view of the circuit used in the proposed liquid-film thickness system.

4.1 Waveform Generator

The first part is the signal generator, which is responsible for generating a sinusoidal signal; this was made using the 100 MS/s sampling rate, 14-bit resolution arbitrary waveform generator, NI PXI-5412.The generator is able to produce sinusoidal signals up to 20 MHz and 12 Volts peak. A computer, using software developed in LabVIEW™, programs the frequency, amplitude and waveform. In this work, the sinusoidal signal had 5V peak and frequency of 5 MHz. At this frequency, the gain of the auto-balancing bridges only depends on the feedback capacitor and the fluids capacitance (SILVA, 2008); refer to Figure 2.13 for the fluids used in this work.

4.2 Transmission Circuit

The generated signal is applied to the transmitters (in the sensor) through an analog multiplexer (ISL84051IBZ). In order to guarantee that the signals have low impedance, buffers (LMH6559MA) are used at the output of the multiplexer. When a transmitter is active, the others are grounded; this scheme was explained in section 2.7. Figure 4.4 shows the homemade transmission-circuit board built in this work.

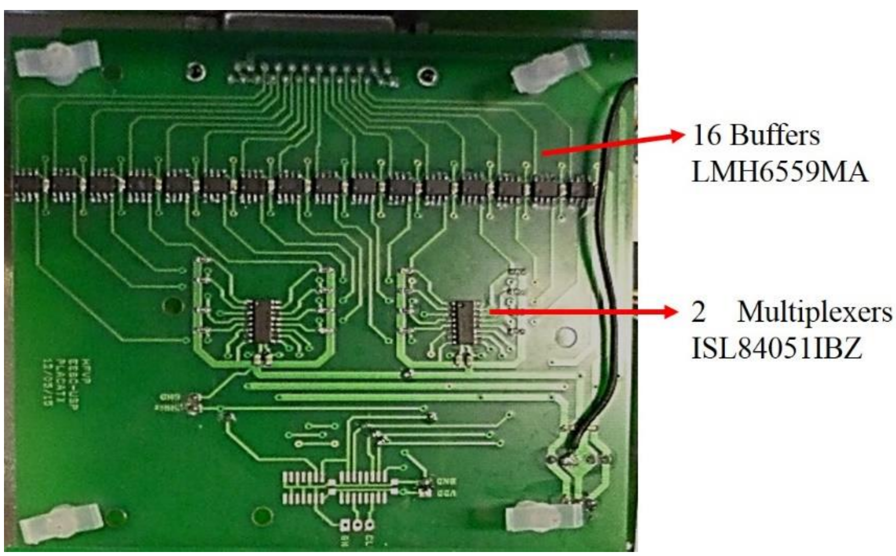

Figure 4.4 – Homemade transmission circuit board.

4.3 Planar Sensor

The heart of the system is the planar sensor (Figure 4.5 and Figure 4.6). The sensor has three types of electrodes: transmitters, receivers and ground. The sensor is arranged in a two-dimensional array, where the transmitters are connected in one direction (transmitter lines), while the receivers are placed perpendicular to this direction (receiver lines). It was manufactured using multilayer PCB fabrication technology and flexible material; some of the sensor characteristics are summarized in Table 4.2.

Table 4.2 - Characteristics of the planar sensor.

Feature	Value
PCB material	Polyimide
Conductive material	Cooper
Coating material	Gold (to prevent corrosion)
Coating layer size	5 μm
Number of layers	9
Laser-drilled holes diameter	0.25 mm
Path sizes	0.1 mm
Space between insulating and electrodes	20 μm
Mean sensing area thickness	0.40 mm

The sensor used in this investigation was developed in LKE Lab in ETH Zurich. It was lent to the USP via an inter-institutional cooperation. The sensor has a sensing area of length of 192 mm and width of 52 mm. It consists of 5221 big electrodes (diameter 0.9 mm) and 5220 small electrodes (diameter 0.5 mm). In total there are 48 transmitter lines and 176 receiver lines. The sensor is detailed in Tiwari et al. (2014). Three different combinations of receiver and transmitter electrodes are nested into one another. The different arrangements possible of sensors in the planar sensor (matrix) are summarized in Table 4.3. Each matrix corresponds to a set of pair Tx-Rx with the same spatial resolution.

Table 4.3 - Characteristics of each matrix of the planar sensor.

Matrix	Number of Tx	Number of Rx	Spatial Resolution	Measurement range
Near field	26	96	2×2 mm^2	100 μm to 700 μm*
Middle field	13	48	4×4 mm^2	400 μm to 2200 μm*
Far field	9	32	12×12 mm^2	1000 μm to 3500 μm

* Measured values using the proposed capacitance system.

The matrix with spatial resolution of 4×4 mm^2 (middle field, in Table 4.3) was selected according to the expected film-thickness in this work and preliminary experiments using high-speed camera.

The middle field matrix has 48 receivers, but just 16 receivers were actually used as the analog-digital converter stage had 16 analog inputs only. In Figure 4.6, it is detailed the effective sensing area used in this work.

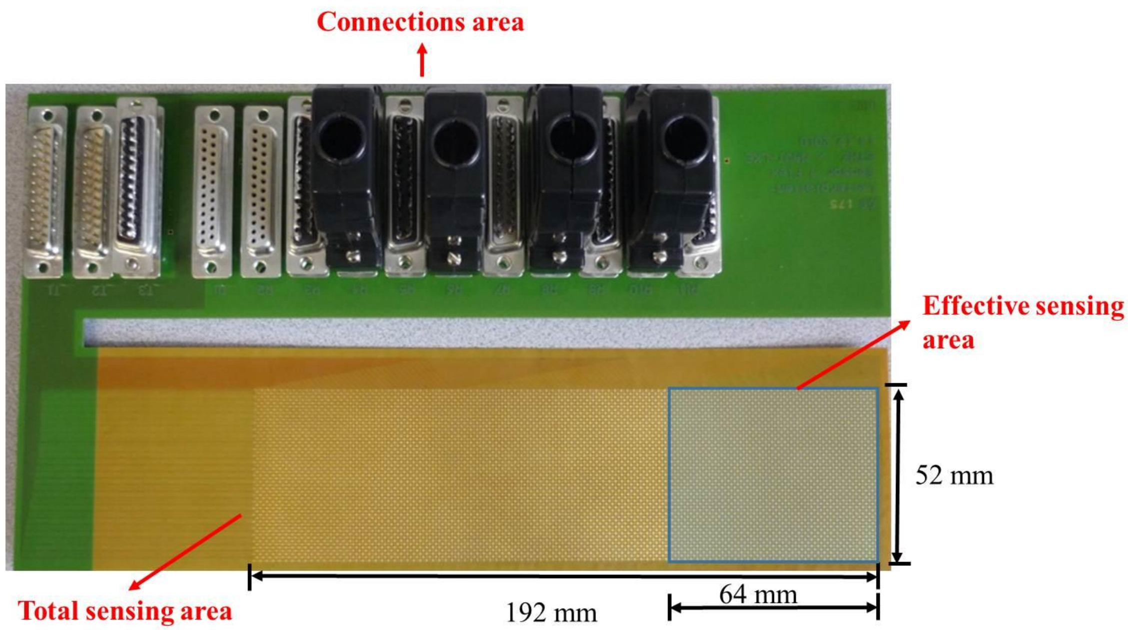

Figure 4.5 - General view of the planar sensor used in this work.

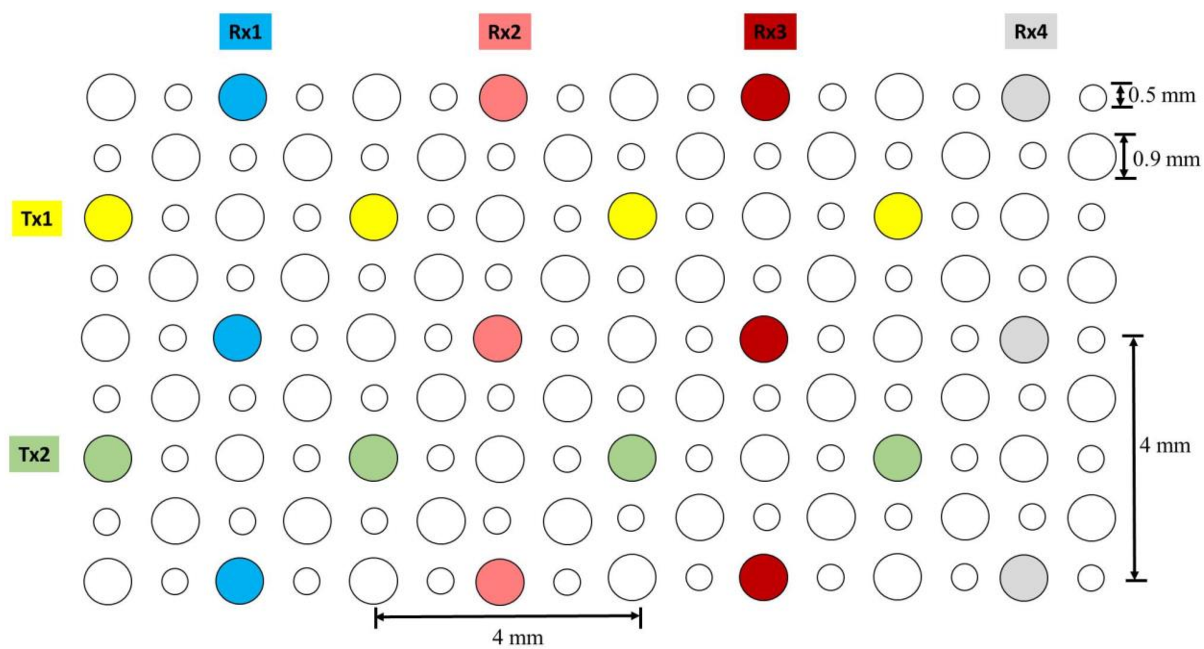

Figure 4.6 - Detailed view of the planar sensor used in this work. Transmiters and receivers of the middle field matrix are colored and ground electrodes are in white.

4.4 Reception Circuit

The receivers are connected to auto-balancing bridges (Figure 4.7) where the fluids over the electrodes have an impedance represented by C_x and G_x, as described in section 2.7.1. The operational amplifiers used (OP-AMPS) are OPA656 with 500 MHz unity gain bandwidth and feedback components of C_f=10 pF and G_f=1/200 kΩ. Afterwards, logarithmic amplifiers (AD8307ARZ) are used to increase the signal difference between the measurements when they are small. At last, there are other operational amplifiers, OPA656, to prepare adequately the analog signals prior to submitting these to the ADC for digitization. One can see in Figure 4.8 the transmission circuit board built in this work.

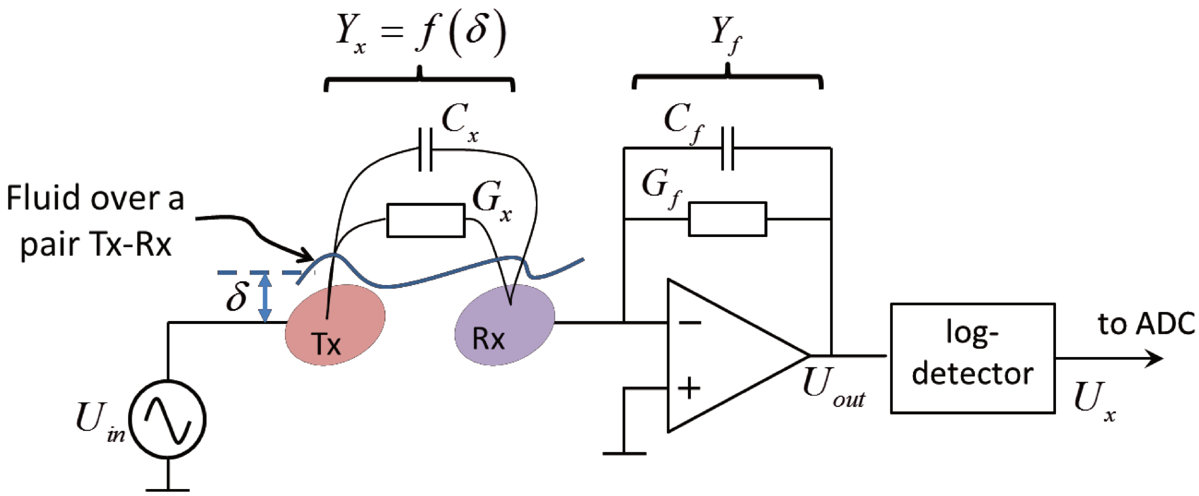

Figure 4.7 – Reception circuit schematic.

At low frequencies (f<100´s MHz), the admittance of a fluid can be modeled as a conductance (G_x) in parallel with a capacitance (C_x) (SIHVOLA, 1999). The conductance is $G_x=k_g\sigma_x$ and the capacitance is $C_x=k_g\varepsilon_0\varepsilon_x$, where k_g is a variable associated to the electrodes shape and the film thickness, σ_x is the equivalent conductivity, ε_0 is the vacuum permittivity (8.85 pF/m) and ε_x is equivalent relative permittivity. Assuming that the equivalent conductivity and permittivity are dominated by the water values (σ_w= 0.00412 S/m and ε_w=80), the gain of the auto-balancing bridge will be

$$\frac{U_{out}}{U_{in}} = -\frac{k_g(\sigma_w + j2\pi f\varepsilon_0\varepsilon_w)}{G_f + j2\pi fC_f}. \quad (4.1)$$

At the work frequency, 5 MHz, eq. (4.1) denominator is approximately equal to $j2\pi fC_f$ and the numerator is $k_g(0.00412 + j0.0222)$ S/m. Thus, the capacitive part contribution is 84.4%. Therefore, the circuit is dominated by the capacitive component. This approach is rough, but it is enough for practical analysis.

The output of the circuit is proportional to the fluids capacitance over the pair Tx-Rx,

$$U_x = A\ln(U_{out}) + B \qquad (4.2)$$

where

$$U_{out} = -\frac{C_x}{C_f}U_{in} \qquad (4.3)$$

and A and B depend on the geometric parameters and circuit parameters. Given that the geometric parameters change during the measurements, A and B cannot be estimated for all the cases. Instead, to solve Eq. (4.2), an empirical approximation is used to correlate the film thickness (δ) with U_x. The empirical relation is established by a calibration process proposed by Damsohn (2011), section 2.7.2.1. Known water-film thickness is produced over the sensor and the output voltage is recorded, for each thickness. At last, it is possible to obtain an equation relating the water-film thickness and the output voltage.

In order to minimize the variation in the circuit parameters and the possible deposition of oil on the sensor surface, a measurement of voltage with the system saturated (U_{sat}, i.e. the sensor covered with water with a bigger thickness than the thickness of saturation) is made during the process of calibration and before and after each experimental run in the pipeline. Thus, the dimensionless voltage (U_{dl}) is defined as

$$U_{dl} = \text{Dimensionless Voltage} = \frac{U_x}{U_{sat}} \qquad (4.4)$$

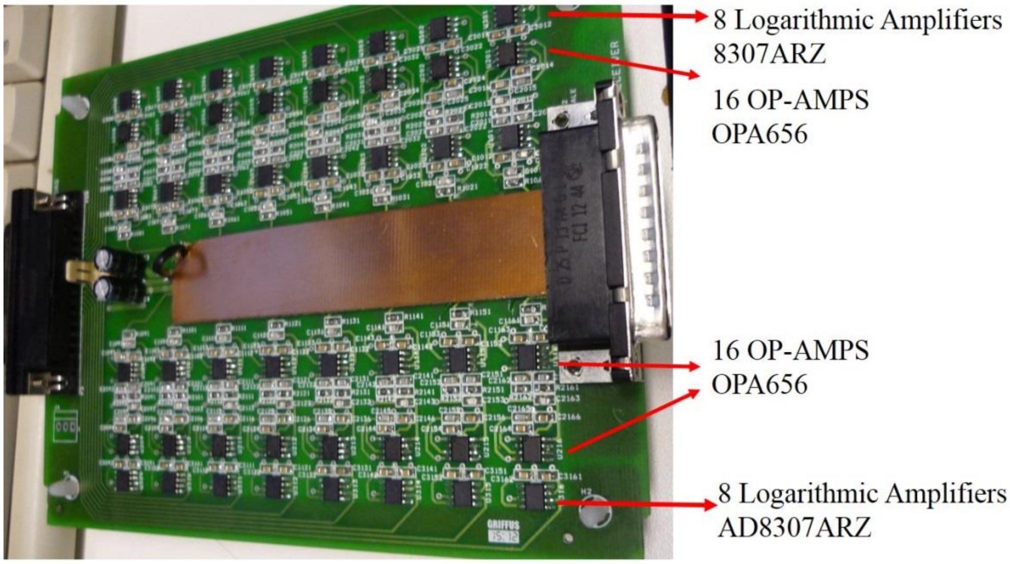

Figure 4.8 – Homemade reception circuit board.

4.5 Analog-Digital Converter

The output-voltage signals (after the logarithmic amplifiers) are converted to digital signals by a digitizer NI 5751**.** This is an analog-digital converter with 16 simultaneously sampled 50 MS/s channels, DC coupling, input impedance of 50Ω and 14-bit resolution. This converter admits a maximum input voltage of 1V peak. For this constraint, the output voltage must be adapted, making necessary to use a special circuit to couple (to 50 Ω impedance) and to limit.

4.6 FPGA

A FPGA Flex Rio PXIe7962R is used to control the measurement system. The FPGA features are listed in Table 4.4.

Table 4.4 - PXIe7962R features.

FPGA	FPGA Slices	FPGA DSP Slices	Block RAM	Onboard Memory (DRAM)
Virtex-5 SX50T	8,160	288	4,752 kbit	512 MB

The FPGA has two state machines. The machines control the synchronization between the transmitter circuit board (Figure 4.4), the digitizer (NI 5751) and the computer. Figure 4.9 shows the Acquisition State Machine and Figure 4.10 shows the Control State Machine. Both machines run at 50 MHz.

A new whole acquisition begin when the variable ‘Reset_WMS’ is activated. When this command is received, the first task is to reset the Acquisition State Machine, Figure 4.9. Later, the Control State Machine creates a set of signals to synchronize the transmitter (Tx) lines and the sampling instant. Also, creates the signal to synchronize the high-speed camera. A counter ‘Ctr_Fr’ compares the number of frames acquired with the number of desired frames ‘Frames’, when the counter reaches the desired number, the generation of synchronization signals stops. Finally, the machine returns to the initial state, ready to start a new whole acquisition.

The signals generated during the state ‘Acq_WMS’ are shown in Figure 4.11. The first step is to reset the Acquisition State Machine. After, trough the signal ‘Tx_Clk’, a pulse changes the actual Tx, activating the Tx0. The signal to trigger the acquisition process is delayed to allow the propagation and stabilization of the signal. Each time that the Tx0 is active, i.e. begins a new frame, a pulse is generated in Fr_Clk. It is used to synchronize the high-speed camera.

The Acquisition State Machine, Figure 4.9, receives the trigger signal ‘DI0’ generated by the Control State Machine. When the trigger is received, DI0=’1’, one sample of each receiver (Rx) line is taken and it is sent to the computer. It is possible take several samples, ‘Sp/C’, each time that one Tx is activated. In this work, just one sample is taken when a Tx is active. A counter Ctr_Sp/C stores the number of samples taken by each Tx. When the number of samples is reached the machine returns to the initial state.

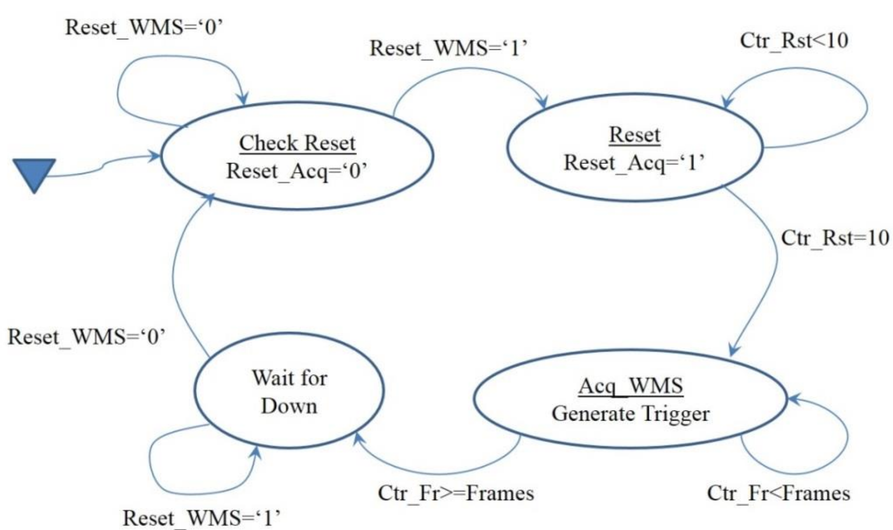

Figure 4.9 – Control State Machine

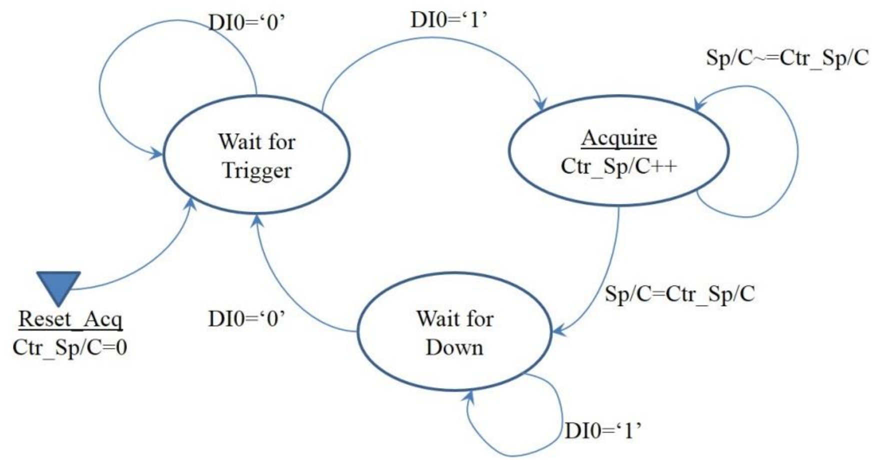

Figure 4.10 – Acquisition State Machine.

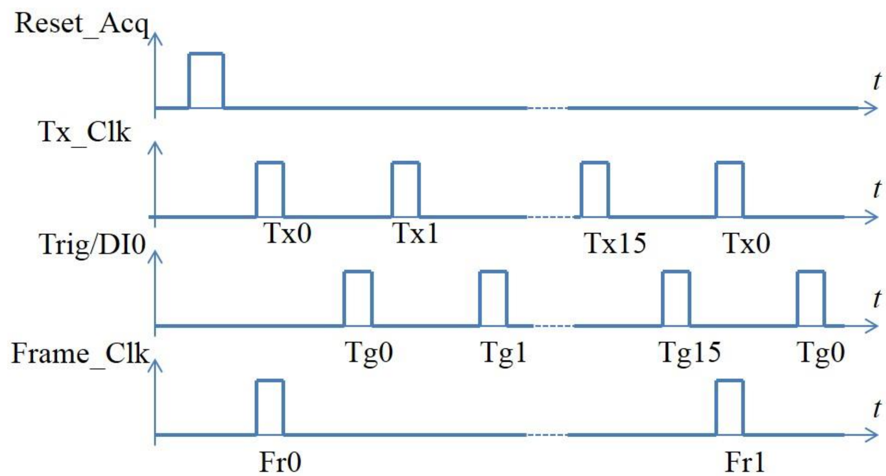

Figure 4.11 – Signals of control.

4.7 Computer

The digitalized signals are sent and processed in a computer. This computer has special characteristics to have high transference and storage speed of data, Table 4.5.

The data are processed with a program created in Matlab. Figure 4.12 is presented the flow diagram of data processing.

Table 4.5 – Computer configuration.

Characteristic	Value
Processor	Intel i7 4900MQ
RAM	64 GB
Platform Controller Hub	Intel X79
Solid state hard drive	200 GB
Hard drive	2 TB
Control of PXI Express	PXIe-PCIe-8381

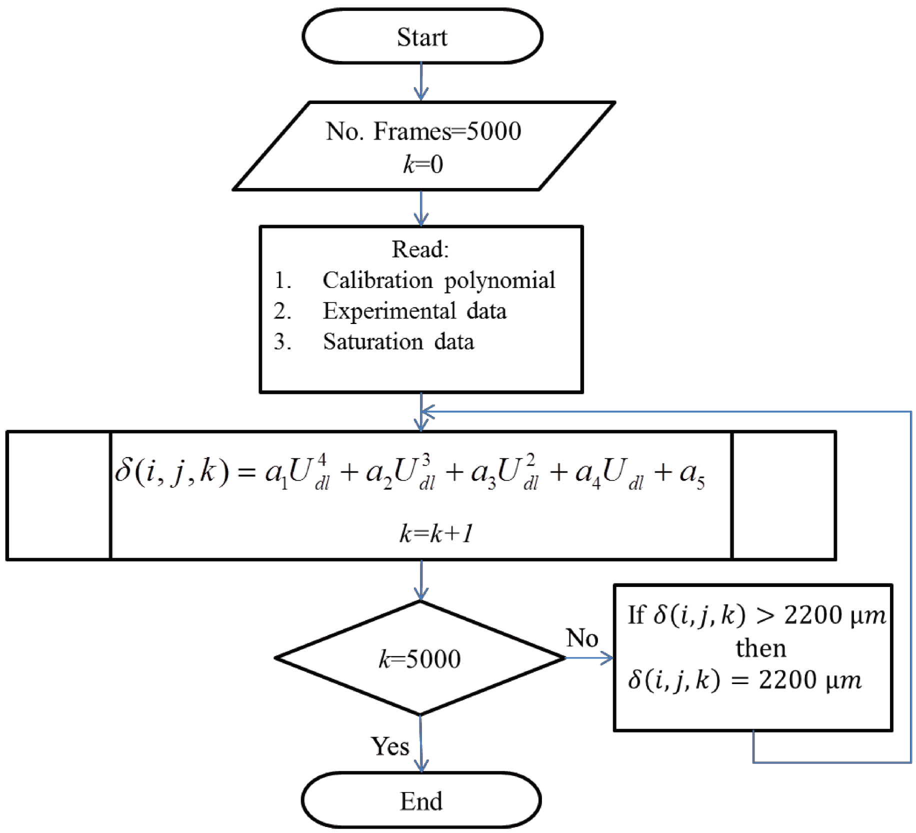

Figure 4.12 – Film-thickness data processing.

4.8 High Speed Camera

Flow images were recorded with a high-speed video camera Olympus i-speed3. The high-speed camera was synchronized with the measuring system. The synchronization was possible through two digital signals. These signals came from the PXI; the first one is an enable signal which makes the camera ready to record, and the second one was generated at the same time with the Tx0 activation signal, i.e one camera frame is recorded when a new capacitance-system frame begin. The configuration used in the experiments can be seen in Table 4.6. This configuration was used in all the experiments (Chapter 5 and Chapter 6).

Table 4.6 – Camera configuration.

Feature	Value
Resolution	804 × 600 pixels
Frames per second	5000
Shutter	190 µs
Trigger mode	ROC (Record on Command)
Trigger event	Falling
Lens	AF-S Micro Nikkor 60 mm f/2.8D

4.8.1 Camera Setup

The first challenge was to correct the optical distortions (parallax and lens effects) due to the pipe wall. There are several methods for correcting, minimizing or preventing optical distortion caused by pipe curvature (WITT et al., 2008; LOWE & KUTT, 1992; NARROW et al., 2000; BUDWIG, 1994). Some tests were carried out using a transparent box filled with fluids with different refractive indexes, but close to that of the pipe material. Another attempt was made by using a solid acrylic box designed and constructed as an independent piece and then installed in the horizontal pipeline (Figure 4.13b). The latter showed the best results.

The next stage was to select a pattern length to insert into the visualization section for image calibration. A 0.2 mm × 0.2 mm square pattern length was chosen after preliminary tests (Figure 4.13c). The square pattern was attached to a piece of acrylic and placed within the acrylic box in the center of the tube and perpendicular to the camera view (Figure 2b). Another acrylic box constructed with the same dimensions of the previous one was used for the flow visualization (Figure 4.14). It is important to note that the flow is recorded upstream of the pattern, as shown in Figure 4.14, with the mixture flowing from bottom to top. This configuration ensures that the pattern does not disturb the flow.

For the lighting system, two LED lamps of 30W and 2300 lumen were used. Preliminary lighting tests were also made in order to find the best configuration/position of the lamps to obtain sharper images and a good contrast between the phases, oil and water. The lighting arrangement that presented best results was the one with the lamps positioned at the back and the bottom of the section. In addition, a halogen lamp was located above the visualization section during the tests.

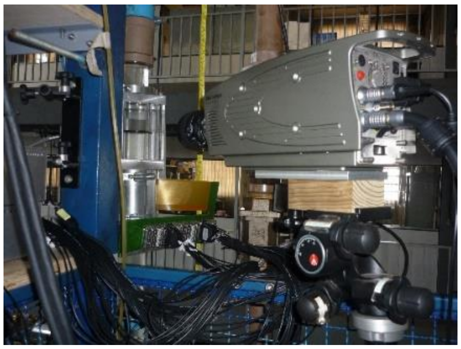

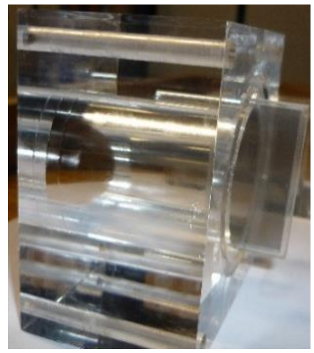

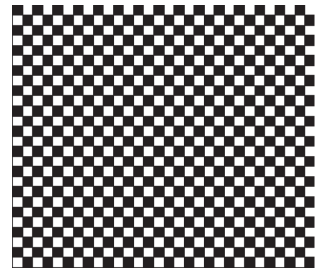

a) b) c)

Figure 4.13 - (a) Camera setup; (b) Side view of the acrylic box with the square pattern attached; (c) Square pattern used for image calibration (0.2mm×0.2mm).

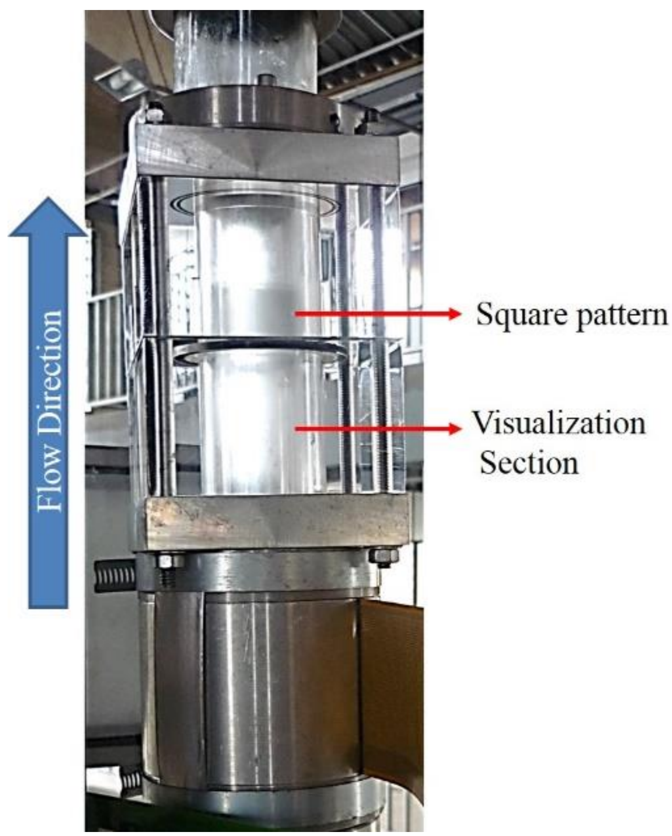

Figure 4.14 - Detail of visualization section

4.9 Setup Preparation

As mentioned before, the planar sensor was made of a flexible material, which allowed it to be taped to the internal wall of the tube. An especial union was designed and manufactured to insert the sensor between two sections of the tube, including a visualization system.

Special flanges made of 4 parts of aluminum were used. Two of them give support to the sensor, emulating the internal walls of the tube. The first piece was designed to let the internal face of the sensor fit with the internal face of the tube; i.e. to guarantee the same radius. The sensor was glued on that support, Figure 4.15. The second piece completes the sensor wall, Figure 4.16. Two circular flanges were used as guide system for the support pieces, letting a perfect match, Figure 4.17. A plate of aluminum gives support to the connectors of the sensor. This part was isolated from the sensor to avoid short-circuit. The pieces were made by the technician Hélio Trebi.

The planar sensor was located just upstream the visualization section, which consisted of two transparent acrylic pieces, which allowed the direct visualization of the flow pattern inside the tube. In addition, the visualization section permits the mounting of a traditional WMS between the acrylic pieces for cross-sectional tomography. The second piece contains the image calibration pattern, as will be presented in the next section. Figure 4.18 shows an exploded-view drawing and a photograph of the entire system placed in the pipeline. The installation was possible with the help of the technicians Hélio Trebi and Jose Bogni. Every day the entire system had to be disassembled and cleaned up to avoid damaging the sensor. The possible damages include oxidation, accumulation of oil on the surface, growing of humidity inside the sensor, among others.

Figure 4.15 – Flexible planar sensor mounted on its support piece.

Figure 4.16 – Flexible planar sensor installed between the two pieces. It is possible to see the sensor is over a half wall of the pipe.

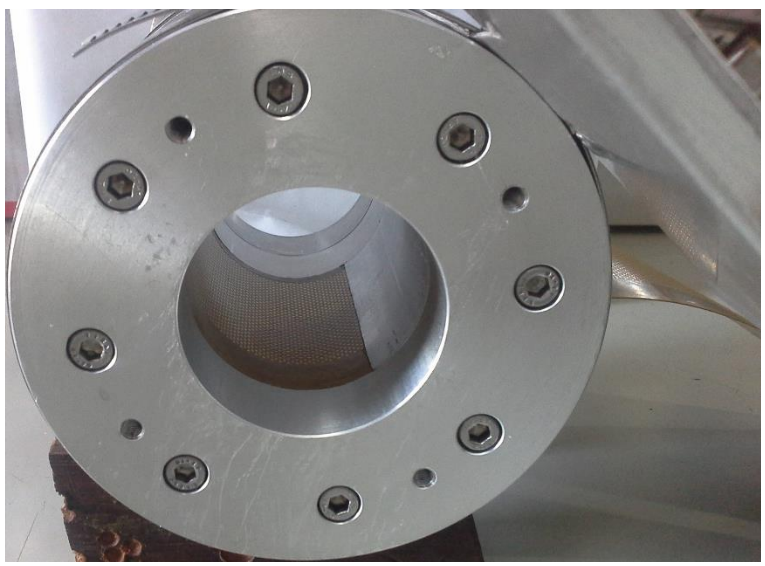

Figure 4.17 – Flexible planar sensor and support pieces with the flange.

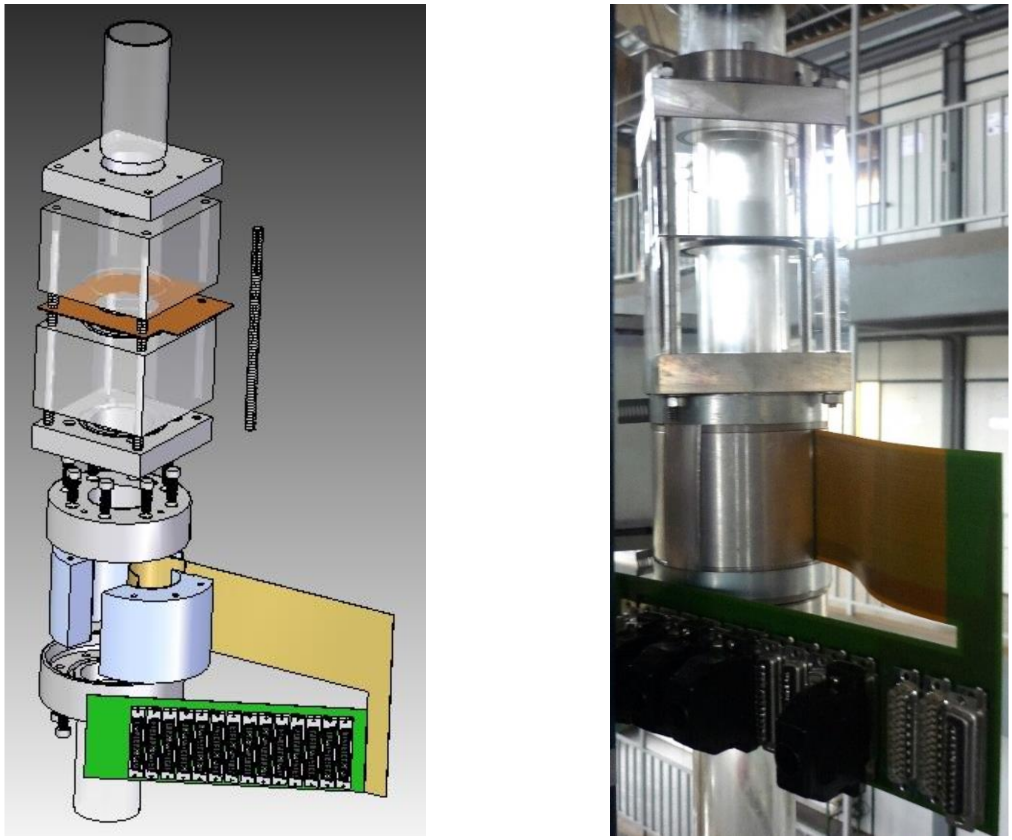

a) b)

Figure 4.18 – a) Exploded-view drawing showing the planar sensor and visualization section. b) Photo of the entire system placed in the pipeline.

4.10 Experimental Procedure

The experimental procedure had the following steps:

1) The pipe was first filled with water, the measurement system saturation data and an image of the square pattern were recorded (Figure 4.19).
2) Experiments begin with single-phase water flow. After some time, oil is gradually added. Once the flow pattern is steady, i.e. when the oil and water superficial velocities do not vary, the acquisition systems are activated. As a result, the capacitance system starts the measurements and high-speed camera begins to record the flow. The duration of each measurement was of 1 second with 5000 frames collected. Figure 4.20 shows snapshots of flows of mixtures with different oil and water superficial velocities, V_{so} and V_{sw}, respectively. It is possible to observe strips

near the pipe wall free of oil droplets, at the left and right side of the image, which is the object of this investigation. In red are marked the regions of interest for film thickness measurements (Figure 4.20).

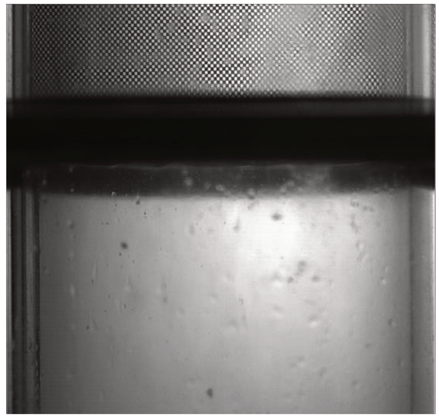

Figure 4.19 - Square pattern and visualization section with the pipe filled with water.

3) The holdup is then measured. For this purpose, two quick-closing valves are closed to trap the mixture in a 3.5-meter-length section, while another valve is simultaneously opened to allow the flow through the bypass. It was necessary to wait for a half an hour to allow the oil-water separation for annular flow experiments and for an hour for dispersed oil-in-water flow experiments. Afterwards, the oil-water interface is located and the oil holdup is calculated as follows:

$$h_o = \frac{\text{oil-water-interface length m}}{3.5\text{ m}} \qquad (4.5)$$

4) The pipe was cleaned with water and new measurement system saturation data were recorded.
5) The last step consists in data treatment and processing of the images for quantification of water-film thickness.

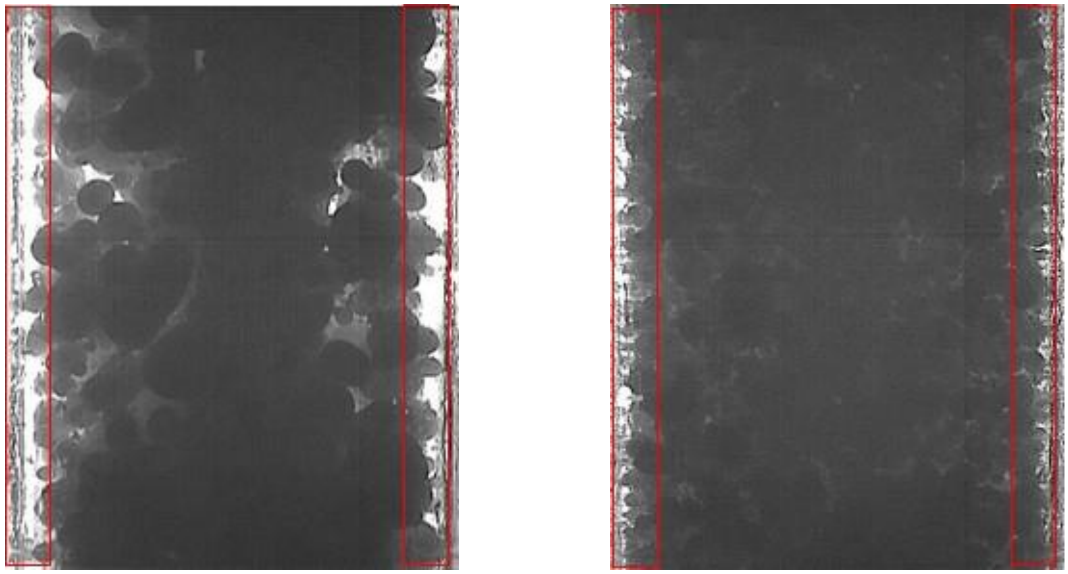

a) b)

Figure 4.20 - Images of the oil-water flow. (a) Unstable annular flow V_{sw} =0.56 m/s, V_{so} =0.5 m/s; (b) dispersed oil-in-water flow V_{sw} =1.12 m/s, V_{so} =0.4 m/s. In red are marked the regions of interest for the measurements of water-film thickness.

5 FILM THICKNESS MEASUREMENT IN OIL-WATER PIPE FLOW USING IMAGE PROCESSING TECHNIQUE

High-speed-camera images of the flow were processed to obtain data of average water-film thickness which could be used to validate the capacitive measurement system. An automatic processing algorithm was proposed. The proposed algorithm has the following stages: (i) pre-processing, (ii) segmentation and (iii) film thickness estimation. The first task was to improve the images, because the dispersed oil-in-water flow images had noise and low contrast, which makes the image processing difficult. Afterwards, image segmentation was applied to separate oil regions and water regions. Hence, it was possible to estimate the water film thickness from the segmented images. The methods used at each stage were selected through qualitative and quantitative comparisons.

The experimental setup and methods are shown. Thereafter, the image processing algorithm used to measure the film thickness is described. Results are presented and compared against predictions of a model available in the literature.

5.1 Experimental Setup

The images were recorded with a high-speed video camera (Olympus ispeed3, at 5000 fps) in the Multiphase-Flow-Loop Test Facility of LETeF (Thermal-Fluids Engineering Laboratory), Engineering School of São Carlos of the University of São Paulo. The camera was installed at 10.3 m from the tube entrance of a horizontal transparent acrylic pipeline of 26 mm-I.D. and 12 m length, Figure 5.1 (a). Tap water and oil ($828\ \mathrm{kg/m^3}$ of density and 220 cP at 25° C) were used as test fluids. The experiments were made possible with the help of Dr. Iara Hernandez.

The experimental procedure started with single-phase water flow. After some time, oil was gradually added. After reaching steady state, the high-speed camera was activated. Figure 5.1 (b and c) shows frames for two experiments with different oil and water superficial velocities (V_{so}, V_{sw}). It is possible to observe small regions clearly dominated by water at the top and bottom of the pipe, near to the wall.

In this study measurements were made for mixture superficial velocities varying from 3.1 to 4.2 m/s and input oil fractions from 0.14 to 0.43, in total 12 experimental points. The acquisition rate was 5000 frames/second and were acquired two seconds by experiment.

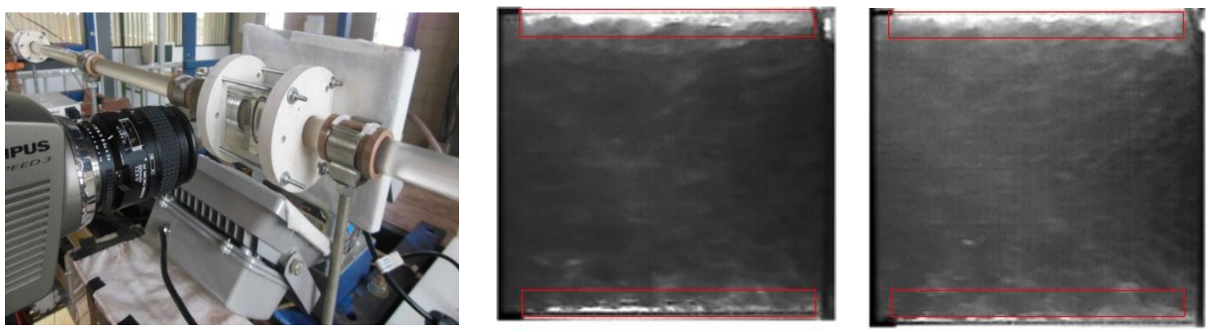

a) b) c)

Figure 5.1 - a) Camera experiments setup. Images dispersed oil-in-water flow pattern; b: (a) $V_{sw} = 2.5\ m/s, V_{so} = 1.2\ m/s$; (b) $V_{sw} = 2.5\ m/s, V_{so} = 1.5\ m/s$. In red are marked the regions of interest used to film thickness measurements.

5.2 Image Processing

An automatic image-processing algorithm is proposed in Figure 5.2. The algorithm includes pre-processing, segmentation and film thickness estimation. The pre-processing includes cutting, improving and calibrating the image. In the segmentation stage it is important to select a suitable method to manipulate such images, for instance in Bonilla Riaño, Bannwart, & Rodriguez, (2013) two segmentation methods were tested for oil-water core-annular flow image analysis. Finally, the average water film thickness is calculated in the film thickness estimation stage.

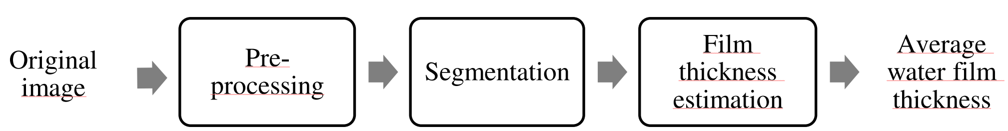

Figure 5.2 - Proposed algorithm for the film thickness calculation.

5.2.1 Pre-Processing

The images of dispersed oil-in-water flow present noise and low contrast, which makes the processing image difficult. The purpose of image enhancement is to improve the interpretability of information contained in the image for providing a “better” input for other automated image processing systems (KAUR et al., 2011). The image enhancement algorithm receives an original image, applies a set of intermediate steps on that image, and finally outputs the enhanced image. There are many techniques for improving image quality. Some popular techniques are contrast improvement, edge enhancement (e.g. deblurring), spatial (e.g. averaging, median, Wiener, frost filters) and frequency filtering (Fourier and Wavelet domain)(GONZALES & WOODS, 2002).

5.2.1.1 Contrast improvement

The images of the dispersed oil-water flow present non-uniform illumination and low contrast. Contrast enhancement techniques expand the range of brightness values in an image, thus the effect is to increase the visual contrast between two areas of different uniform densities. A histogram based contrast improvement was selected for that purpose.

Given a gray scale image with L levels of gray, the gray intensity histogram is the number of pixels in the image N_g that have intensity equal to g.

$$h(g) = N_g \qquad (5.1)$$

Histograms are frequently normalized by the total number of pixels of the image. Assuming an M × N image, a normalized histogram is:

$$p(g) = \frac{N_g}{MN} \qquad (5.2)$$

where $p(g)$ is the probability of occurrence of g in the image. The sum of all components of a normalized histogram is equal to 1.

The histogram of a low contrast image is usually skewed either to the left (mostly dark), or to the right (mostly light). In our case, the values are in the left side, Figure 5.3.

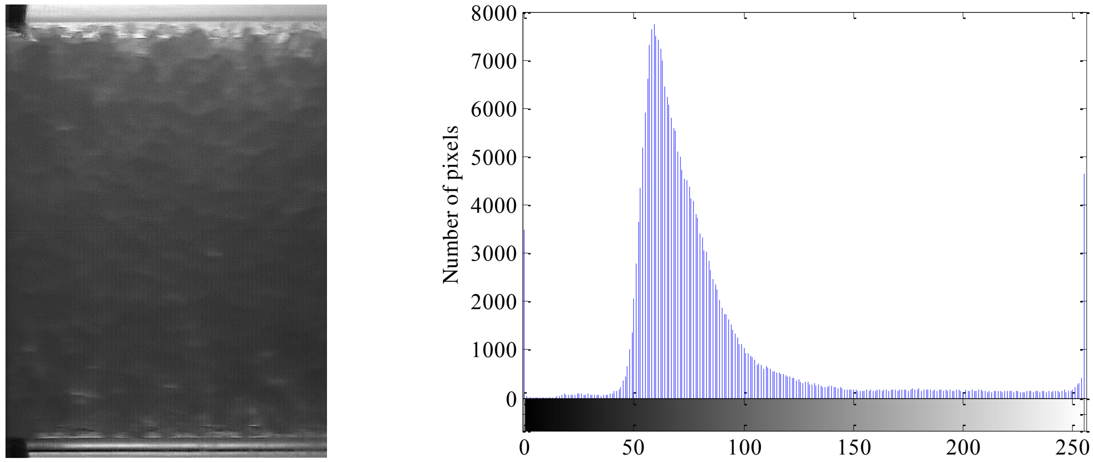

(a) (b)

Figure 5.3 - (a) Instantaneous image; (b) histogram. Flow conditions: Vsw =2.5 m/s and Vso =1.2 m/s.

Contrast stretching is a point image enhancement method that attempts to improve an image by stretching the range of gray values, i.e., to use all the possible values. A disadvantage of the method of histogram stretching is that they require user input. This method was not used in this case because it is non-practical to study each histogram to estimate the lower and upper gray levels (we have 120000 images).

In Histogram Equalization (HE), the gray pixel value of enhanced image depends on the global value of the respective pixel of the original image. It is the probability density function (pdf) that will be transformed, i.e., it changes the pdf of a given image into one of a uniform pdf that spreads out from the lowest pixel value to the highest pixel value $(L-1)$. In a digital image, the pdf is a discrete function that can be approximated by using the probability based on the histogram$p(g)$, as follows:

$$pdf\left(x\right)=p\left(g\right)=\frac{N_g}{MN}. \qquad (5.3)$$

From this pdf, we can then obtain the cumulative density function (cdf) as follows:

$$cdf\left(x\right)=\sum_{g=0}^{L-1}pdf\left(x\right). \qquad (5.4)$$

The transformed pixel can be obtained by:

$$tt=floor\left(cfd\left(x\right)\left(L\text{-}1\right)\right) \qquad (5.5)$$

where floor rounds to the nearest integer (BAGADE & SHANDILYA, 2011).

HE can be a good approach when automatic enhancement is required, even though there are cases where it may not be the best approach, causing results extremes (SINGH et al., 2011).

The method Contrast Limited Adaptive Histogram Equalization (CLAHE) computes several histograms, each corresponding to a distinct region of the image, and applies the histogram equalization to each one with a defined distribution. The objective of the process is to improve the local contrast of an image.

The method uses a limit parameter value of the histogram in order to obtain adequate brightness and contrast on the enhanced image. The contrast limit is controlled on the histogram equalization process. A criterion for the desired histogram distribution is defined based on the contrast range of the original image. The criterion for histogram distribution is either uniform, exponential, or Rayleigh. Therefore, the natural properties of the original image can be maintained since the distribution form is not significantly changed after enhancement process (JULIASTUTI & EPSILAWATI, 2012).

5.2.1.2 Denoising

Noise is any degradation in the image signal, caused by any external disturbance. Digital images may be contaminated by a variety of types of noise. Noise is the result of errors in the image acquisition process that result in pixel values that do not reflect the true values of the real scene. Generally, noisy pixels appear as dots with different gray levels with respect to its neighborhood. These points appear random or distributed systematically. Image noise can be classified as impulse noise, Gaussian noise, Poisson noise, quantization noise, film grain, non-isotropic noise, multiplicative noise and periodic noise (VERMA & ALI, 2013). Following are described some noises that can contaminate dispersed oil-in-water flow images.

In impulse noise or salt-and-pepper noise, the noise arises in the image because of sharp and sudden changes of image signal. In this type of noise only two values are possible, a and b, and the probability of obtaining each of them is less than 0.1. For instance in an 8 bits image, the typical value for pepper noise is close to 0 and for salt is close to 255.

Gaussian or amplifier noise is caused by random fluctuations in the signal. Some sources of Gaussian noise are: different gains in the sensor, electrical noise in the digitizers, poor illumination and high temperature, between others. The Gaussian noise has a normal probability distribution function, i.e., the values that the noise can take on are Gaussian-distributed.

Poisson or shot photon noise arises when the number of photons sensed by the sensor is not sufficient to provide detectable statistical information. This noise has root mean square value proportional to square root intensity of the image.

Noise reduction (denoising) in digital images has been studied for many years. Image denoising methods can be categorized as either spatial domain methods or transform domain methods. Spatial domain methods suppress noise directly in the spatial domain (e.g., spatial filtering). Transform domain methods first transform an image from the spatial domain into a different domain (e.g., frequency domain, wavelet domain) and suppress noise in the transform domain (GONZALES & WOODS, 2002). According to noise nature and its characteristics, a given denoising method can be more effective than another. Some of these methods are presented below.

Spatial filtering techniques are transformations pixel by pixel, depending not only on the gray level of the pixel, but also on the value of the gray levels of neighboring pixels. The filtering process is performed using masks, which are applied on the image. Applying the mask centered at the pixel $P(i,j)$, where i is the row number and j the column number in the image, means to replace the pixel value at position (i,j) for a new value, where the value depends on the values of neighboring pixels and weights on the mask. Examples of such filters are averaging filters, median filters and adaptive filters.

Averaging filters replace each pixel value in an image with the average value of its neighbors, including itself. This has the effect of eliminating pixel values which are unrepresentative of their surroundings. The result will depend on the window size, i.e., the number of pixels averaged. Its implementation can be generalized as the sum of the pixel values in the region multiplied by a set of mask weights ($W_{x,y}$), Eq. (5.6). This process results in an image with reduced "sharp" transitions in gray levels and less noise because random noise typically consists of sharp transitions in gray levels. Nevertheless, edges (which almost always are desirable features of an image) also are characterized by sharp transitions in gray levels, so averaging filters have the undesirable side effect that they blur edges.

$$P(i,j) = \sum_{x,y=-m}^{m} W_{x,y} P_{x+i,y+j} \qquad (5.6)$$

where m represents the size of the mask, P is the pixel value.

In median filters, the gray level of each pixel is replaced by the median of the gray levels in the neighborhood. For example, in a neighborhood of 3×3 pixels, the median is the fifth largest value; in a neighborhood of 5×5 pixels is the thirteenth largest value, and so on. Median filter is good for salt and pepper noise. The median filter can eliminate the effect of input noise values with extremely large magnitudes. These filters are widely used as smoothers in image processing (GONZALES & WOODS, 2002).

An adaptive filter changes its behavior on the basis of statistical characteristics of the image region, encompassed by the filter region. This approach produces good results preserving edges and other high frequency parts of an image. In this work a Wiener filter (JIN et al., 2003) and a frost filter (YU & ACTON, 2002) were used.

Another important method of noise reduction is the technique known as "wavelet shrinkage". This method was originally proposed by Donoho & Johnstone (1994) and applied by many authors to reduce noise in signals and images (LUISIER et al., 2007; ERGEN, 2012).

The wavelet transform is basically a convolution operation, which is equivalent to passing an image through low-pass and high-pass filters. The low frequency image or low frequency sub-band still contains spatial correlation and by filtering recursively the low frequency image a multi-resolution image representation can be obtained. Thus, the image is decomposed into a set of sub-images with different resolutions for different frequency bands. Most of the wavelet detail coefficients are equal or close to zero in the regions of smooth image intensity variation.

Wavelet denoising consists of three main stages:

- Perform a discrete wavelet transform (DWT) to the noisy image.
- Application of threshold, in order to suppress coefficients due to noise.
- Reconstruct the denoised image by applying the inverse discrete wavelet transform (IDWT) on the processed highpass wavelet subimages to obtain an estimate of the noise-free image.

There are some variables of the wavelet denoising method of images to be studied: the wavelet function and the level N of wavelet decomposition, the wavelet thresholding function and the threshold itself.

5.2.1.3 Deblurring

Denoising reduces the noise level but the resultant image could be blurred or over smoothed due to losses like edges or lines. Unsharp filter was selected to deblurring the images after the denoising step. The Unsharp filter enhances edges (and other high frequency components in an image) via a procedure which subtracts an unsharp or smoothed version of an image from the original image (GONZALES & WOODS, 2002).

5.2.2 Segmentation

Segmentation is the separation of digital images in multiple regions that are homogeneous with respect to one or more attributes (GONZALES & WOODS, 2002). For the pre-processed dispersed oil-water flow images, it is assumed that there are two different classes: oil and water.

5.2.2.1 Segmentation by Thresholding

Thresholding is the most basic pixel-based segmentation. The application of this method results in a binary image with different objects. Depending on the application, objects are represented by a gray level 0 (white) and the background is represented as 1 (black) or vice versa.

One way to remove objects to the background is to choose a threshold T. Thus, any point (x, y) for which $f(x, y) > T$ is called object, in the opposite case the point is called background (GONZALEZ & PEREZ, 1987).

There are many algorithms to calculate the threshold. The first one used in this work was Otsu´s algorithm, which is one of the classical methods. The pixels of the image are divided into two classes, C_1 with gray levels $[0\ to\ T]$ and C_2 with gray levels $[T + 1\ to\ L - 1]$. The gray level probability distributions (w_1, w_2) for the two classes are:

$$w_1 = \Pr(C_1) = \sum_{i=0}^{T} p(g), \qquad (5.7)$$

$$w_2 = \Pr(C_2) = \sum_{i=T+1}^{L-1} p(g). \qquad (5.8)$$

The means of the classes (μ_1, μ_2) are

$$\mu_1 = \sum_{g=0}^{T} gp(g) / w_1, \qquad (5.9)$$

$$\mu_2 = \sum_{g=T+1}^{L-1} gp(g) / w_2. \tag{5.10}$$

The class variances (σ_1^2, σ_2^2) are given by

$$\sigma_1^2 = \sum_{g=0}^{T} (g-\mu_1)^2 p(g) / \Pr(C_1), \tag{5.11}$$

$$\sigma_2^2 = \sum_{g=T+1}^{L-1} (g-\mu_2)^2 p(g) / \Pr(C_2). \tag{5.12}$$

The intra-class variance (σ_w^2) is

$$\sigma_w^2 = w_1\sigma_1^2 + w_2\sigma_2^2. \tag{5.13}$$

The Otsu method chooses the optimal threshold T by minimizing the intra-class variance (OTSU, 1979; BINDU, 2009).

The second one is the ISODATA algorithm, which is an iterative algorithm. In general, it assigns an arbitrary initial value of threshold. The second step classifies each pixel to the closest class. In the third step, the mean values (μ_1 and μ_2) of each class are estimated using Gaussian distribution. In the next step it is calculated a new threshold as $\mu_1 + \mu_2/2$. The second and third steps are repeated until the change between the iteration is small enough (DIAS, 1980; EL-ZAART, 2010).

The last one is fuzzy partition and Tsallis entropy based thresholding (SARKAR & DAS, 2013). In this case, the image is divided into different classes by selecting multiple threshold points by performing fuzzy partition on a 2D histogram based on fuzzy relation and maximum fuzzy entropy principle. The entire distribution is divided into n classes, and the Tsallis entropy for each distribution is determined as

$$H_n^\alpha = \frac{1}{\alpha-1}\left[1 - \sum_{g=0}^{L-1}\left(\frac{p(g)M_n}{w_n}\right)^\alpha\right], \tag{5.14}$$

where α is a real positive parameter not equal to one and M_n is the fuzzy membership function.

The optimum value of parameters can be obtained by maximizing the total entropy

$$\varphi = Arg\max\left(\left[H_1^\alpha + H_2^\alpha + \ldots + H_n^\alpha + (1-\alpha)H_1^\alpha H_2^\alpha \ldots H_n^\alpha\right]\right). \tag{5.15}$$

5.2.2.2 Mathematical Morphology

Mathematical morphology is a non-linear image processing technique. Morphology operates on image regions that can be reshaped under the control of a structuring element. It is composed of two basic operators: erosion and dilatation. Other operators can be defined based in these two basic operations, for example opening and closing (HARALICK et al., 1987).

The proposed algorithm for segmentation using mathematical morphology may be split up into the following steps: converting the grayscale image to a binary image, selecting the structuring element for the image, applying dilation operator until most of the holes are filled (typically two times), which was necessary because the non-uniform illumination produced holes on the oil region, applying erosion operator, applying open operator and classifying (black area will be denoted as the homogeneous mixture of oil and water and white area as the water phase).

5.2.2.3 Wavelet Transform

The main feature of the wavelet transform for segmentation is that it is capable of representing a signal in the spectral and temporal domain simultaneously (KURNAZ et al., 2003). The pixels features are extracted after the Wavelet transform, i.e. forming for each original pixel a feature vector. This feature vector is composed by the original gray value and five intensities from sub-images approximation coefficients at the same coordinate.

For classification, self-organizing neural networks were used in Kurnaz et al. (2003), but k-means or any other unsupervised learning algorithm could be used. In our work, fuzzy c-means and k-means algorithms were used.

K-means

It is a cluster analysis technique that classifies N elements into K groups or clusters. Based on a data matrix X, the function minimized in the classification process is the sum of squared errors.

In practice, the technique is based on the following iterative algorithm, given an initial partition in K clusters:

1. Calculation of positions of the centroids $x(k)$ of the K clusters.
2. For each item, calculate its distance from the K centroids.

3. Reallocation of each object to the cluster whose centroid is closest (KANUNGO et al., 2002).

Fuzzy c-means

Classification by fuzzy C-means (FCM) is a technique that has been applied successfully in image segmentation. Since an image can be defined by its characteristics, the FCM algorithm performs the classification of the image by grouping pixels with similar characteristics. This group is improved iteratively minimizing the cost function depending on the distance of pixels to the cluster centers in the characteristic domain.

The FCM algorithm generates a partition of the data set using a membership function. To do this, we minimize iteratively the objective function J defined as:

$$J = \sum_{j=1}^{N} \sum_{i=1}^{c} u_{ij}^{m} \left\| x_j - v_i \right\|^2 , \qquad (5.16)$$

where u_{ij} is the degree of membership of pixel x_i in the i-th cluster, v_i is the centroid of the i-th cluster and m is the weight parameter that determines the degree to which members of a group affect the classification outcome.

The cost of the objective function is minimized when pixels near the centroid of their group are given a high degree of membership. The membership function represents the probability that the pixel belongs to a particular group, this probability depends only on the distance between the pixel and the centroid of each group in the characteristic domain. The membership function and centroid are defined as follows, respectively:

$$u_{ij} = \frac{1}{\sum_{k=1}^{c} \left(\frac{\left\| x_j - v_i \right\|}{\left\| x_j - v_k \right\|} \right)^{2/(m-1)}} , \qquad (5.17)$$

$$v_i = \frac{\sum_{j=1}^{N} u_{ij}^{m} x_j}{\sum_{j=1}^{N} u_{ij}^{m}} . \qquad (5.18)$$

The algorithm starts with default values for the centroid groups; FCM converges to a solution for v_i representing the local minimum of the objective function. Convergence is detected by comparing changes in the membership function through changes in the centroids values in consecutive iterations.

5.2.3 Film Thickness Estimation

The segmented images are calibrated to establish the relationship between pixel and length magnitudes, i.e., to determine what a pixel represents in terms of size or distance. The calibration was made using as square pattern with squares of 0.2 mm × 0.2 mm. The pixel scale factor (PSF) obtained was 0.06 mm/pixel near to the pipe wall and 0.05 mm/pixel near to the pipe center.

Figure 5.16f shows an example of a segmented image where black represents oil and white represents water. Considering the flow lateral projection, the rows are in the horizontal direction (each row has its own pixel scale factor - PSF) and the columns are in the vertical direction. The water film thickness is estimated from a segmented image multiplying each white pixel ($pixel_n$) by the corresponding PSF (PSF_n) and adding the results by columns.

$$\delta = \sum_{n=1}^{Np_w} pixel_n \times PSF_n, \qquad (5.19)$$

where Np_w is the number of white pixels in a column.

Figure 5.4 is the magnification of a small portion of the image. The value in millimeters of the pixel of each row is showed at the right side and the sum result for each column is showed at the bottom. For instance, there are two pixels segmented as water in Column 2. The value in mm of the pixels is 0.06 mm, for both rows (Row 1 and Row 2). Thus, the sum for that column, i.e., the local water film thickness is equal to 0.12 mm.

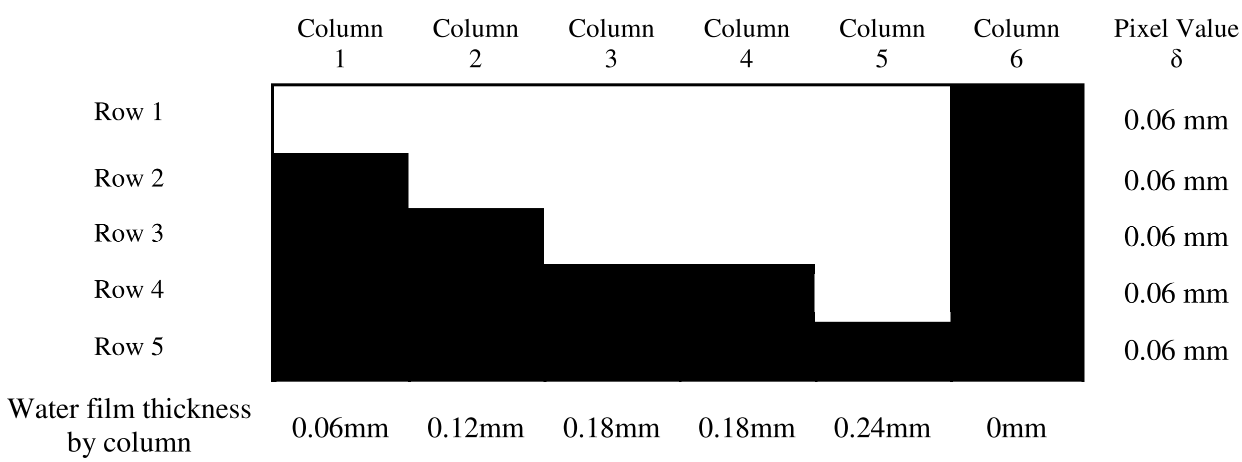

Figure 5.4 - Illustration of estimation of water film thickness.

The averaged water-film thickness ($\overline{\delta}$) is determined as:

$$\overline{\delta} = \frac{1}{N_{frames}} \sum_{frame=1}^{N_{frames}} \left(\frac{1}{N_{columns}} \sum_{Column=1}^{N_{columns}} F_{Column} \right)_{frame}, \tag{5.20}$$

where N_{frames} is the total number of frames collected for each experiment (10000 frames, in this case), $N_{colunms}$ is the number the columns in one frame, and $F_{colunms}$ is the water film thickness measured in each column of the image.

5.3 Results of the Image Processing Algorithms

5.3.1 Image Pre-Processing

In the pre-processing step, each image corresponding to each experimental point was improved using the proposed algorithm. A total of 120,000 images were processed. First, each method presented in the section 5.2.1 was applied to the images to compare their results and select the best technique.

The performance of image enhancement methods can be evaluated using quality metrics. Given an original image $\mathrm{x_o}$ with N columns and M rows, after an enhancement process is obtained an improved image $\mathrm{x_e}$ with the same size. The quality parameters used in this paper are in Table 5.1 (PAVITHRA et al., 2010).

5.3.1.1 Contrast Enhancement Results

Histogram equalization and contrast limited adaptive histogram equalization were tested. The results of image enhancement of the same image with several methods and also plot of histogram distribution are showed on Figure 5.5 and Figure 5.6.

According to the quality metrics the best method for contrast improvement for the tested images was CLAHE with Rayleigh distribution. CLAHE with Rayleigh have better values in MSE, MAE, MD and PSNR, following by CLAHE with exponential distribution, Figure 5.7.

Table 5.1 - Quality metrics used to compare the enhancement methods.

Metric	Definition	Equation	Better quality if
Mean Squared Error (MSE)	Global difference between an enhanced image and an original image.	$MSE = \frac{1}{NM}\sum_{0}^{N-1}\sum_{0}^{M-1}(x_o(n,m) - x_e(n,m))^2$	Low value
Mean Average Error (MAE)	Average magnitude of the errors.	$MAE = \frac{1}{NM}\sum_{0}^{N-1}\sum_{0}^{M-1}\lvert x_o(n,m) - x_e(n,m)\rvert$	Low value
Peak Signal to Noise Ratio (PSNR)	Comparison between noise and signal peak. The unit of PSNR is dB (decibel).	$PSNR = 20\log_{10}\left(\frac{255}{MSE}\right)$	High value
Structural Correlation (SC)	Similarity of the structure of two images.	$SC = \frac{\sum_0^{N-1}\sum_0^{M-1}(x_o(n,m))^2}{\sum_0^{N-1}\sum_0^{M-1}(x_e(n,m))^2}$	Low value
Maximum Difference (MD)	Maximum of the difference between original and enhanced image.	$MD = \max(\lvert x_o(n,m) - x_e(n,m)\rvert)$	Low value
Contrast	Comparison between original and enhanced image contrast.	$Contrast = \frac{\frac{1}{NM}\sqrt{\sum_0^{N-1}\sum_0^{M-1}\lvert x_e(n,m) - Mean_e\rvert}}{\frac{1}{NM}\sqrt{\sum_0^{N-1}\sum_0^{M-1}\lvert x_o(n,m) - Mean_o\rvert}}$ where Mean is the global mean.	High value

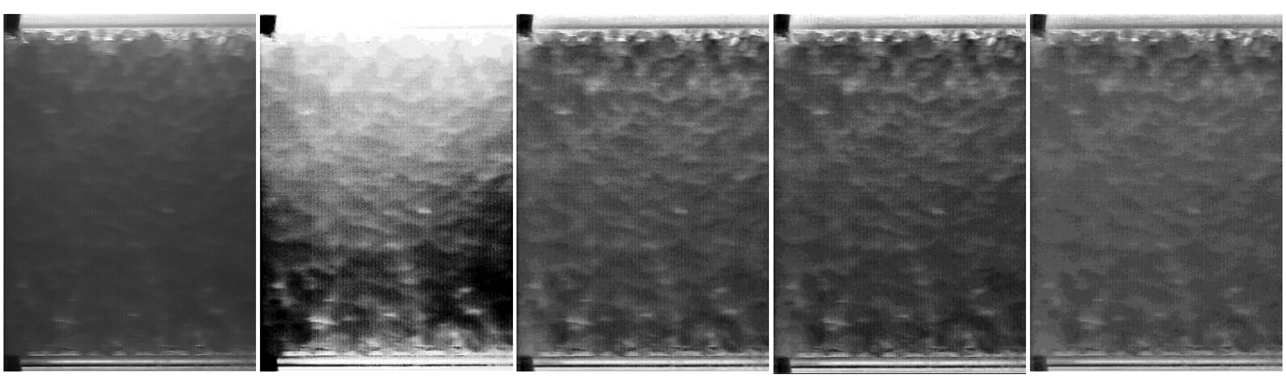

a) b) c) d) e)

Figure 5.5 - Original image V_{sw}=2.5 m/s, V_{so}=1.2 m/s; b) Image after HE; Image after CLAHE with: c) Uniform distribution; d) Exponential distribution; e) Rayleigh distribution.

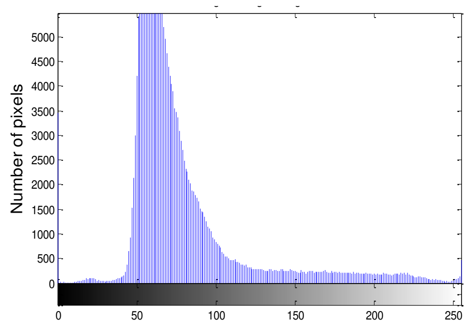

a)

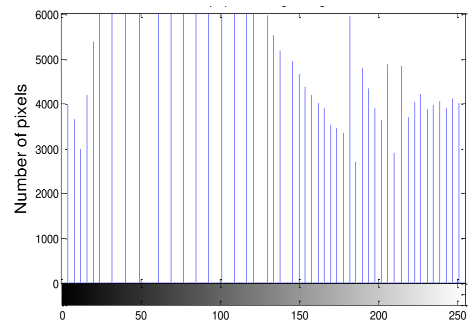

b)

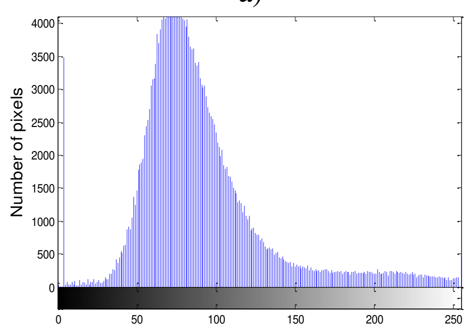

c)

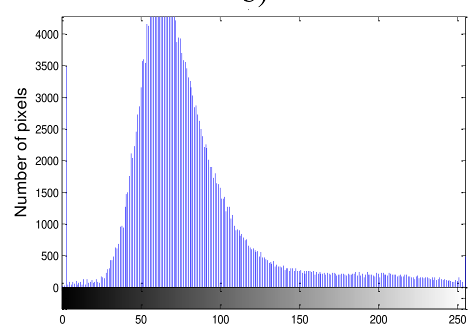

d)

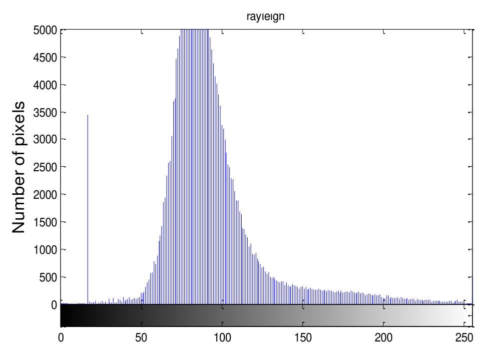

e)

Figure 5.6 - Histogram of image V_{sw} =2.5 m/s, V_{so} =1.2 m/s; b) Histogram after HE; Histogram after CLAHE with: c) Uniform distribution; d) Exponential distribution; e) Rayleigh distribution.

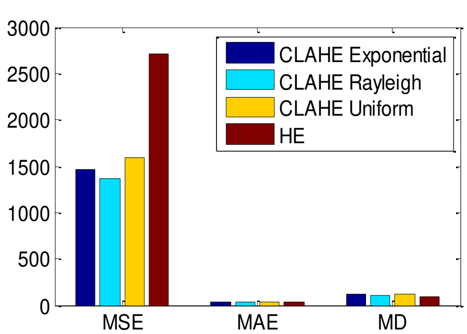

a)

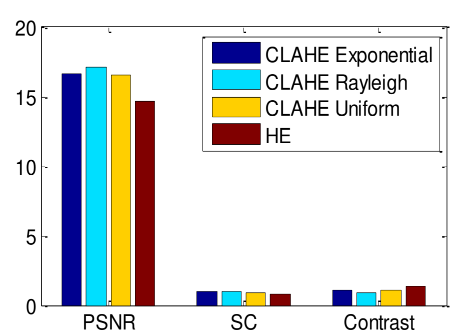

b)

Figure 5.7 - Mean of image quality metrics for different methods of contrast improvement; a) MSE, MAE and MD; b) PSNR, SC and Contrast.

5.3.1.2 Noise reduction results

The results of applying filters to one image are shown in Figure 5.8. The filters were implemented with masks of 3 × 3 and 5 × 5 pixels.

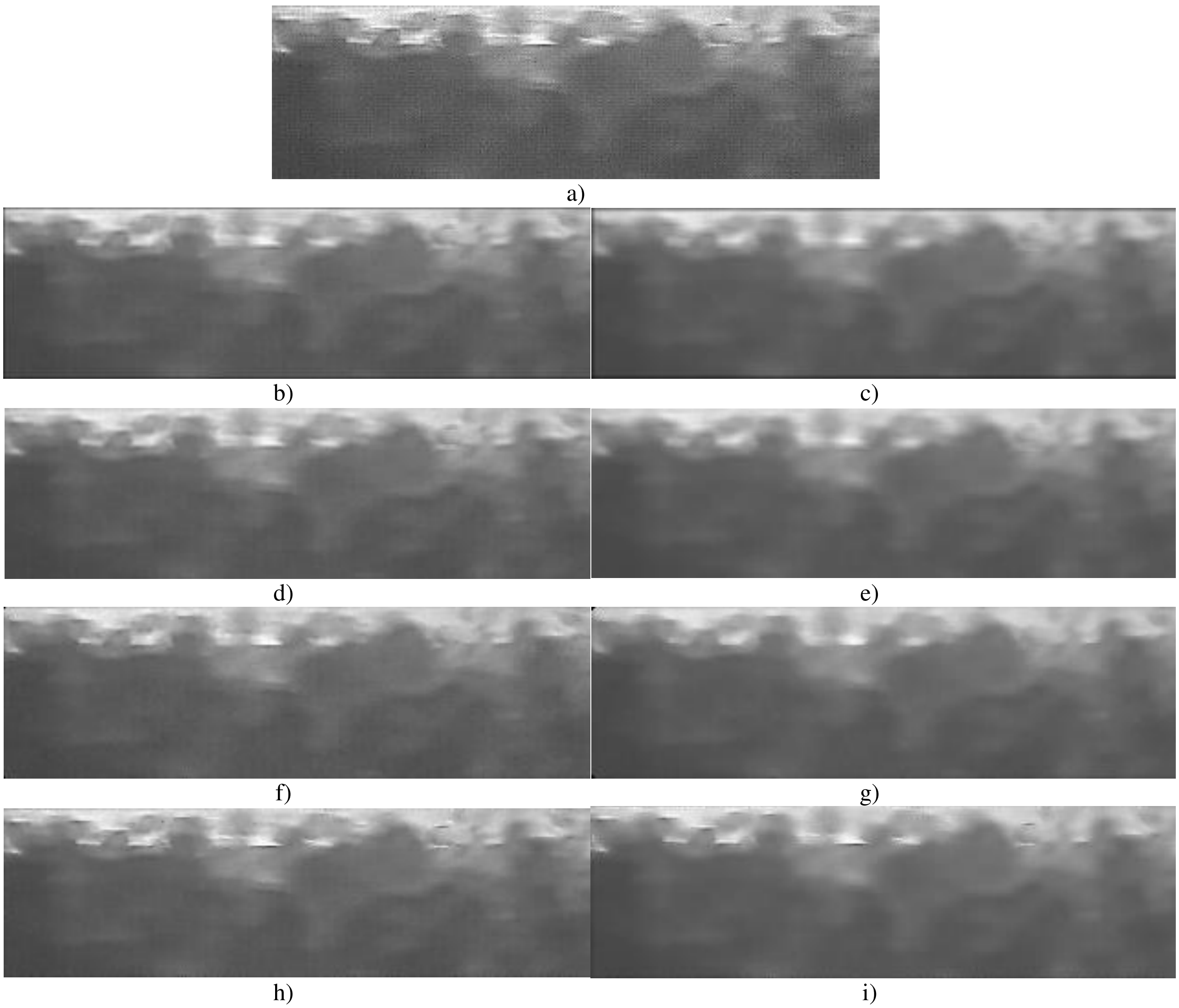

Figure 5.8 - Visual enhancement results of different algorithms for one image V_{sw} =2.5 m/s, V_{so} =1.2 m/s; a) Original image; b) Averaging filter 3×3; c) Averaging filter 5×5; d) Frost filter 3×3; e) Frost filter 5×5; f) Median filter 3×3; g) Median filter 5×5; h) Wiener filter 3×3; i) Wiener filter 5×5.

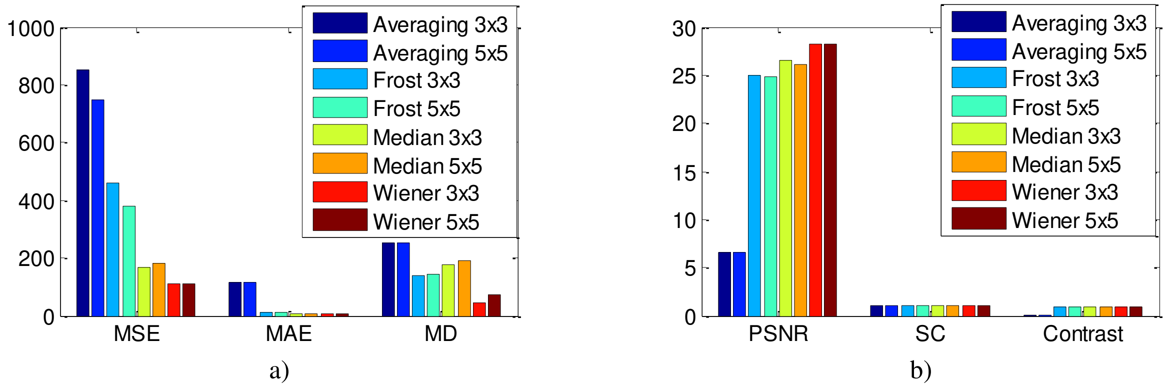

Figure 5.9 - Mean of image quality metrics for different filters; a) MSE, MAE and MD; b) PSNR, SC and Contrast.

Due to spatial filters employ a low pass filtering on groups of pixels, with the assumption that the noise occupies the higher region of frequency spectrum, not only smooth away noise but also blur edges in the images (Figure 5.8). This blur increases with the mask size. It can be seen that correlation between image characteristic related with performance of image enhancement method is close (Figure 5.8 and Figure 5.9). In this case, the best tested filtering method was Wiener filter with mask of 3x3.

A series of steps were made to find the best combination of parameters for Wavelet noise reduction. First, different Wavelets functions were compared. Those Wavelet functions were: Haar, Daubechies (db) from 2 to 40, Symlets (sym) from 1 to 8, Coiflets (coif) from 1 to 5, biorthogonal (bior) from 1.1 to 6.8 and reverse biorthogonal (rbio) from 1.1 to 6.8. Noise reduction was performed with WDT with two-level decomposition and the soft Rigrsure threshold. In the second step were tested different levels of decomposition (1 to 40), using the best Wavelet function found in the previous step and at last were compared two classical thresholds (soft threshold and hard threshold). The main image quality metric was PSNR. Figure 5.10 shows Wavelet denoising results with different Wavelet functions, on the top are presented the best cases and immediately after the worst cases, chosen by their PSNR.

In accordance to the results of the image quality metrics MSE, MAE, PSNR, SC and MD (Figure 5.11 and Table 5.2), the best parameters for Wavelet denoising are: Wavelet function reverse biorthogonal 4.4 (rbio4.4), one decomposition level and threshold hard. In Figure 5.12 is presented a Wavelet denoising result to an image. It has been found that wavelet based denoising is effective in noise reduction with edge features without much damage.

Best cases

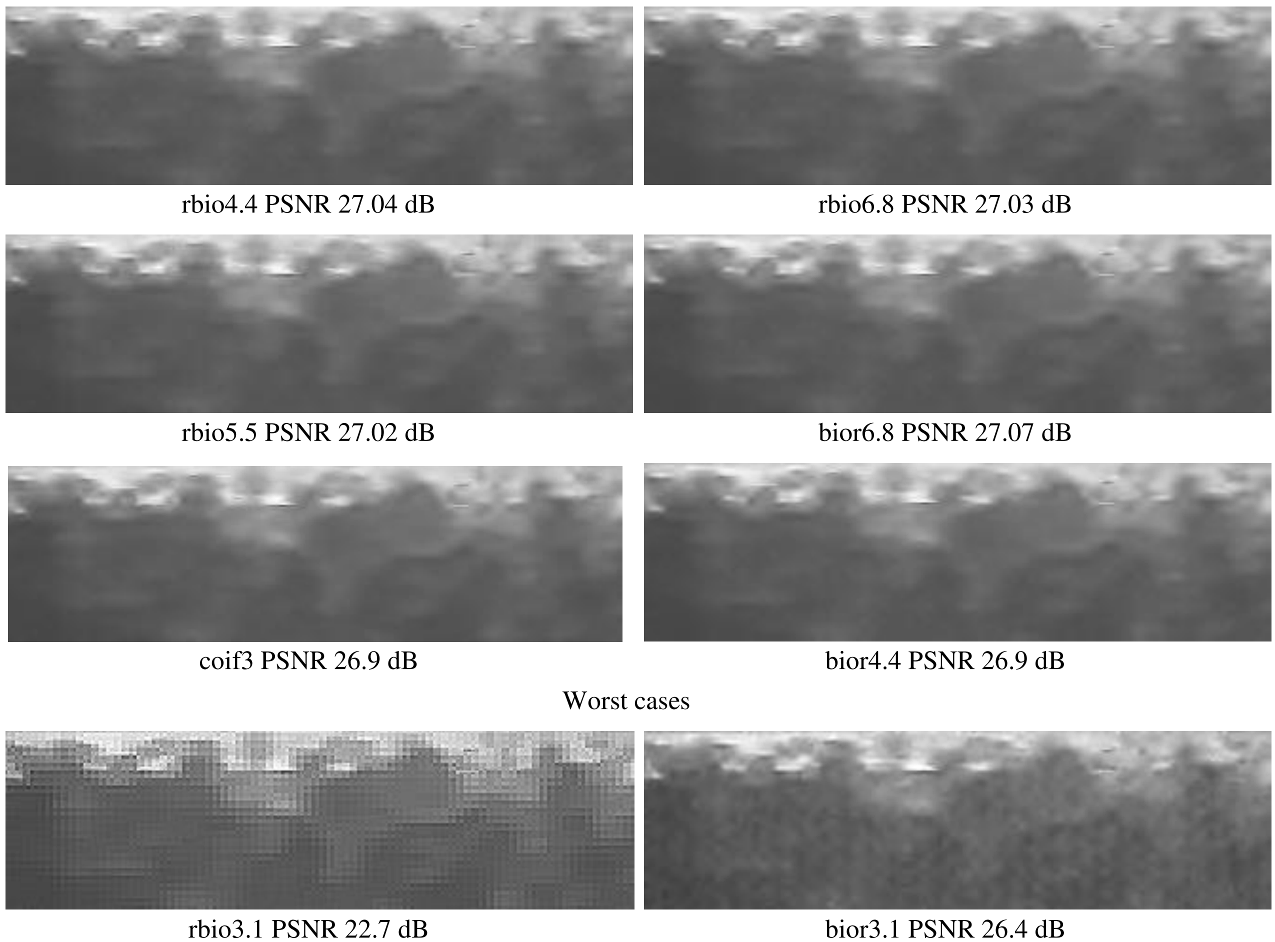

Figure 5.10 - Visual enhancement results of wavelet denoising using different Wavelet functions for one image V_{sw} =2.5 m/s, V_{so} =1.2 m/s.

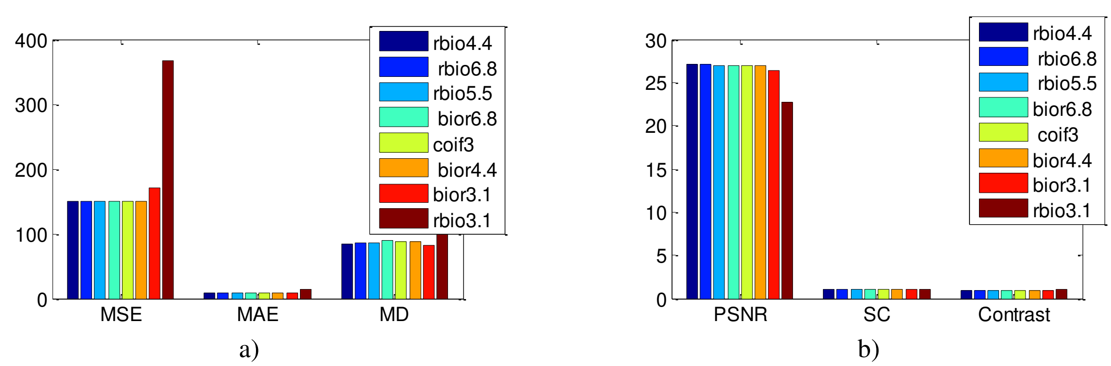

Figure 5.11 - Mean of image quality metrics for different Wavelet; a) MSE, MAE and MD; b) PSNR, SC and Contrast.

Table 5.2 - Mean of image quality metrics for different levels and thresholds.

		MSE	MAE	PSNR	SC	MD	Contrast
Levels	1	121.72	7.68	27.98	1.015	73.07	0.984
	2	149.13	8.32	27.03	1.019	83.55	0.981
	3	162.36	8.68	26.60	1.022	86.65	0.979
	4	170.99	8.98	26.35	1.026	88.02	0.976
	5	175.18	9.14	26.24	1.028	87.62	0.973
Threshold	Hard	111.72	7.42	28.40	1.013	55.75	0.985
	Soft	121.72	7.68	27.98	1.015	73.07	0.984

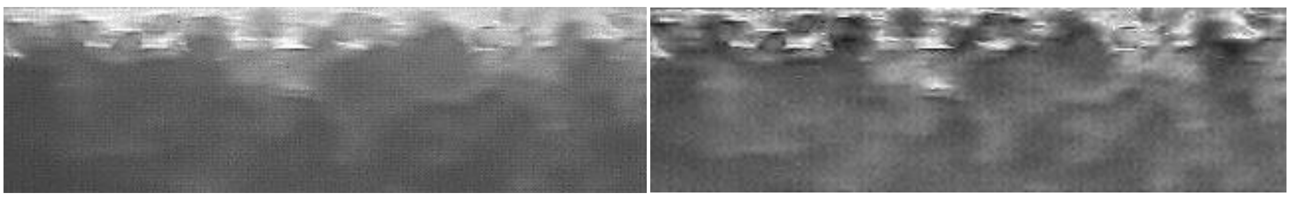

a) b)

Figure 5.12 - Visual enhancement results of Wavelet denoising for one image V_{sw} =2.5 m/s, V_{so} =1.2 m/s; a) original image; b) Denoised image.

5.3.1.3 Deblurring

An example of application of Unsharp filtering is presented in Figure 5.13.

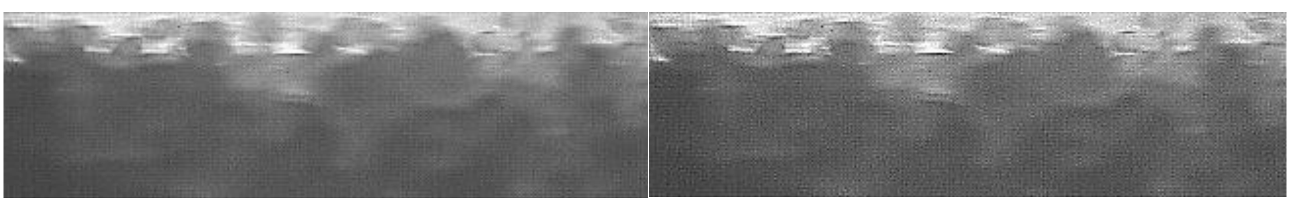

a) b)

Figure 5.13 - Visual enhancement results of unsharp filtering for one image V_{sw} =2.5 m/s, V_{so}=1.2 m/s; a) original image; b) enhancement image

5.3.1.4 Proposed Algorithm

Subsequent to have the outcome of every technique is necessary to determine how will be the sequence of the algorithm for improving dispersed oil-in-water flow images. The proposal is to use the best proven techniques combined. The possible combination were implemented and compared. The techniques combined were CLAHE with Rayleigh distribution (Contrast in Figure 5.14), Wavelet denoising with rbio4.4 Wavelet, one decomposition level and hard thresholding (Denoising in Figure 5.14) and unsharp filter (Unsharp in Figure 5.14). The most favorable option is appliying the techniques in the sequence Wavelet denoising, Unsharp filtering and CLAHE with Rayleigh distribution (orange in Figure 5.14). The proposed combination has the lowest values of MSE, MAE, MD; the highest PSNR and the visual result is better than using an single method, Figure 5.15.

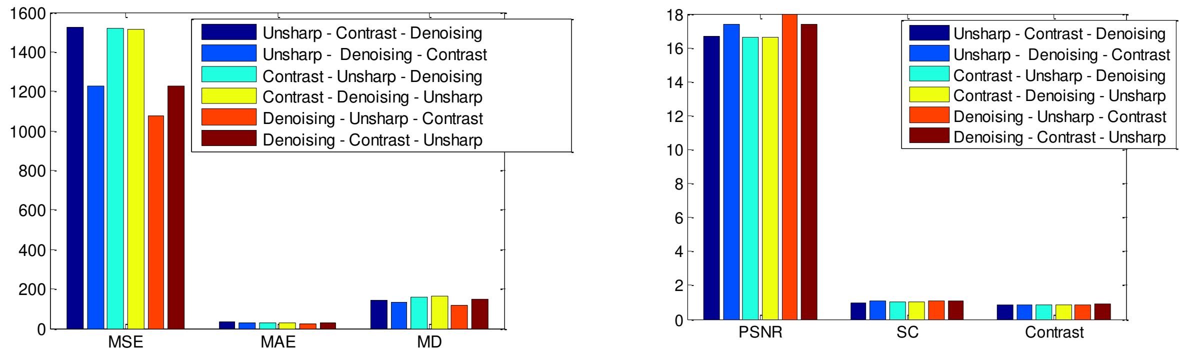

a) b)

Figure 5.14 - Mean of image quality metrics for different combinations; a) MSE, MAE and MD; b) PSNR, SC and Contrast.

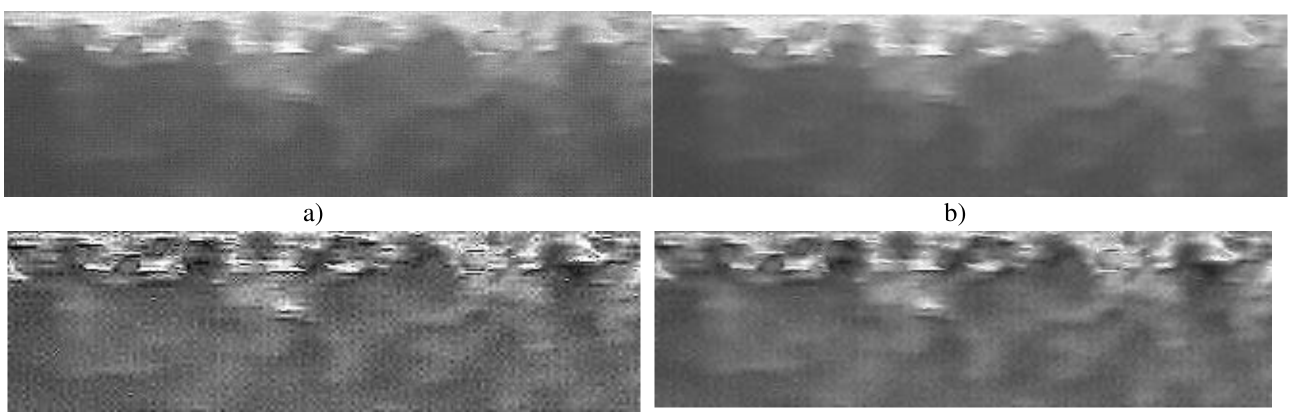

a) b) c) d)

Figure 5.15 - Visual enhancement results of different combinations for one image Vsw =2.5 m/s, Vso =1.2 m/s; a) Original image; b) after Wavelet denoising; c) Denoised image after unsharp filtering; d) Unsharped image after contrast improvement with CLAHE with Raylegh distribution.

5.3.2 Segmentation

Some frames were segmented manually and these images were compared with the automatic segmented images provided by different methods: morphology, thresholding (Otsu, ISODATA, Fuzzy), Wavelet (with K-Means and C-Means) and the proposed combined method.

Hence, a manually segmented frame (I_m) of each experiment is used as reference and compared with the image obtained from each automatic segmentation method (I_a). Both segmented images (manual and automatic) are binary, where oil is represented by value 0 and water by value 1. Table 5.3 presents the parameters used to compare the segmentation methods in this work (JACOB & WYAWAHARE, 2013). The results can be seen in Figure 5.17.

Table 5.3 - Selected parameters used to compare the segmentation methods.

Parameter	Definition	Equation	Image segmentation better if
Dice coefficient (Dice)	Measures the spatial overlap between two binary images. 0% (no overlap) and 100% (perfect agreement)	$D = \frac{2(I_a \cap I_m)}{I_a + I_m} \times 100\%$	High value
Jaccard coefficient (Jaccard)	Measures the spatial overlap between two binary images. 0% (no overlap) and 100% (perfect agreement)	$J = \frac{I_a \cap I_m}{I_a \cup I_m} \times 100\%$	High value
False Positive Dice (FPD)	Measures over-segmentation	$FDP = \frac{2(I_a \cap \overline{I}_m)}{I_a + I_m} \times 100\%$	Low value
False Negative Dice (FND)	Measures under-segmentation	$FND = \frac{2(\overline{I}_a \cap I_m)}{I_a + I_m} \times 100\%$	Low value
Number of Sites of Disagreement (NSD)	Percentage of different pixels within the manually segmented image and the automatic method.	$NSD = \frac{1}{NM}\left(\sum_{0}^{N-1}\sum_{0}^{M-1}\left\lvert I_a - I_m \right\rvert\right)*100\%$	Low value

5.3.2.1 Proposed Combined Method

A combined method for dispersed oil-water flow image segmentation is proposed in this work. The segmentation algorithm includes: wavelet decomposition, fuzzy partition and Tsallis entropy based thresholding with three thresholds (each pixel on the image is approximated to one of this thresholds), conversion to binary using the histogram and morphological opening (to fill small holes). The flowchart of the combined algorithm and the results for each step are shown in Figure 5.16. The processed images correspond to the top and bottom of the pipe (Figure 5.1), in

Figure 5.16 (b) is shown a snapshot of an image of the water film obtained in the upper part of the pipe.

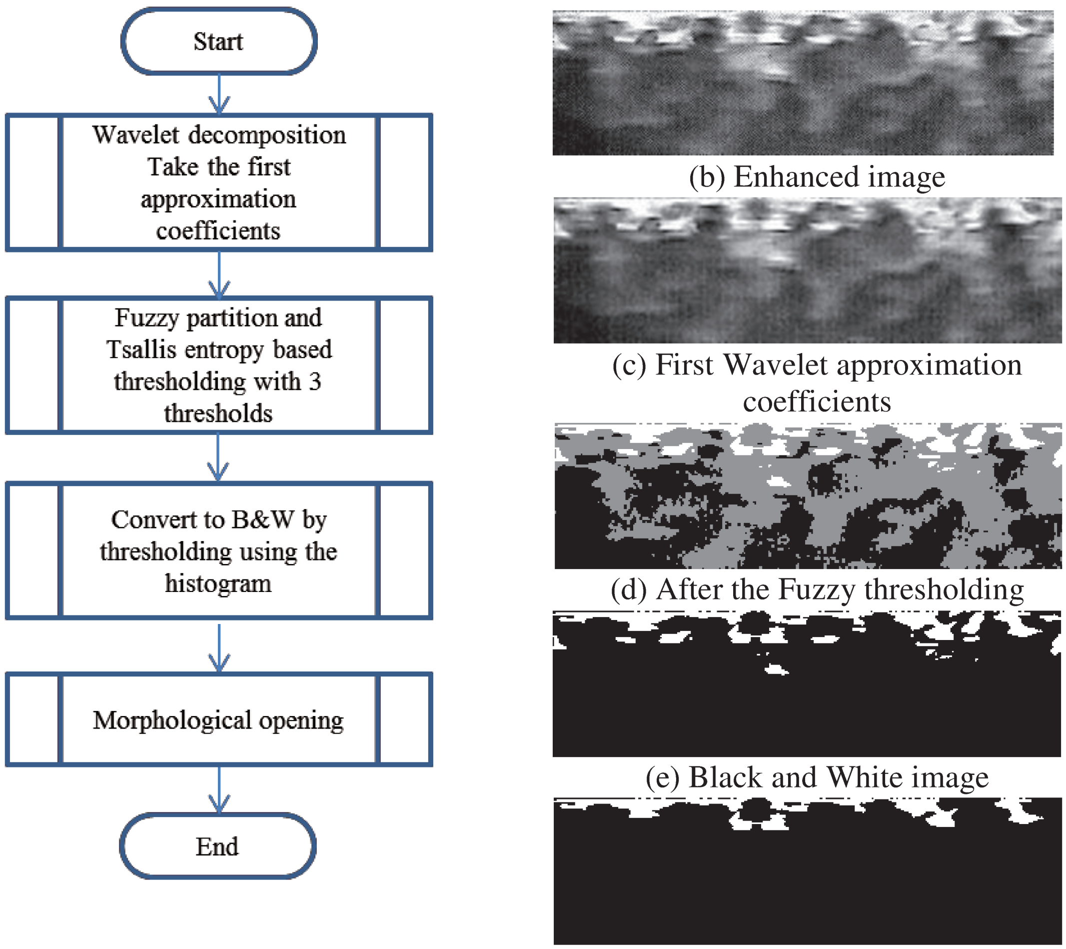

(b) Enhanced image

(c) First Wavelet approximation coefficients

(d) After the Fuzzy thresholding

(e) Black and White image

(f) After Open (Segmented image)

(a) Combined segmentation algorithm

Figure 5.16 - Segmentation using the proposed combined algorithm for an instantaneous image for the flow conditions: V_{sw}=3.0m/s and V_{so}=1.2m/s: (a) Flowchart of combined segmentation algorithm; (b) Enhanced image; (c) Image of first wavelet approximation coefficients; (d) Image after Fuzzy thresholding ; (e) Image in black and white; (f) Segmented image.

In accordance to the value of the parameters (quality metrics) and through visual inspection, it was possible to conclude that the proposed combined method presented the best results for the segmentation of the dispersed oil-water flow images (Figure 5.17)**.** Particularly, the Dice and Jaccard parameters are higher, and FDP and NDS present lower values, which indicates that the performance of the proposed segmentation algorithm is better in comparison to the other methods. One can see in Figure 5.18 the segmented images obtained by applying the different segmentation methods and the proposed combined method. Figure 5.18 corresponds to the flow condition $V_{sw} = 3.0\,m/s$ and $V_{so} = 1.2\,m/s$ and top side of the pipe. In general, the combined method was able to find the interface between water and oil. The other methods overestimate the water area.

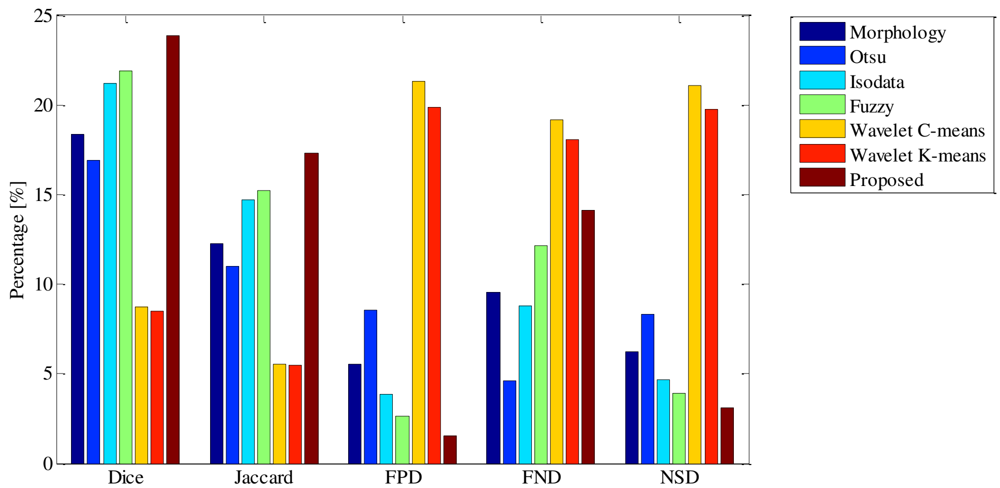

Figure 5.17 - Mean of parameters used to compare the segmentation algorithms.

5.3.3 Film Thickness Estimation and Comparison with a Model from the Literature

One can see in Table 5.4 the values of film thickness obtained by the combined segmentation method described in Section 3.3 for mixture velocities (V_m) varying from 3.1 to 4.2 m/s and input oil fractions (c_o) from 14% to 43%. For these flow conditions, it was observed a dispersed flow pattern which is characterized by oil droplets uniformly dispersed throughout the continuous water phase. However, a thin water film can be noticed near the pipe wall, i.e., near the top and bottom of the pipe.

The water film at the bottom of the pipe was in general thicker than that measured at the upper part of the tube, which is expected because of the density difference between the fluids (oil and water) and the effect of gravity. However, it is possible to observe in Figure 5.19 that with increasing the mixture velocity the film thickness decreases, especially at the bottom of the pipe. The thicknesses measured at the top and bottom of the pipe become closer, indicating a possible formation of a more axisymmetric flow. The bars, in Figure 5.19 and Figure 5.20, represent the uncertainty of the measurements corresponding to the half of the minimum scale of the square pattern used for calibration, i.e. 100 μm, see Figure 4.13.

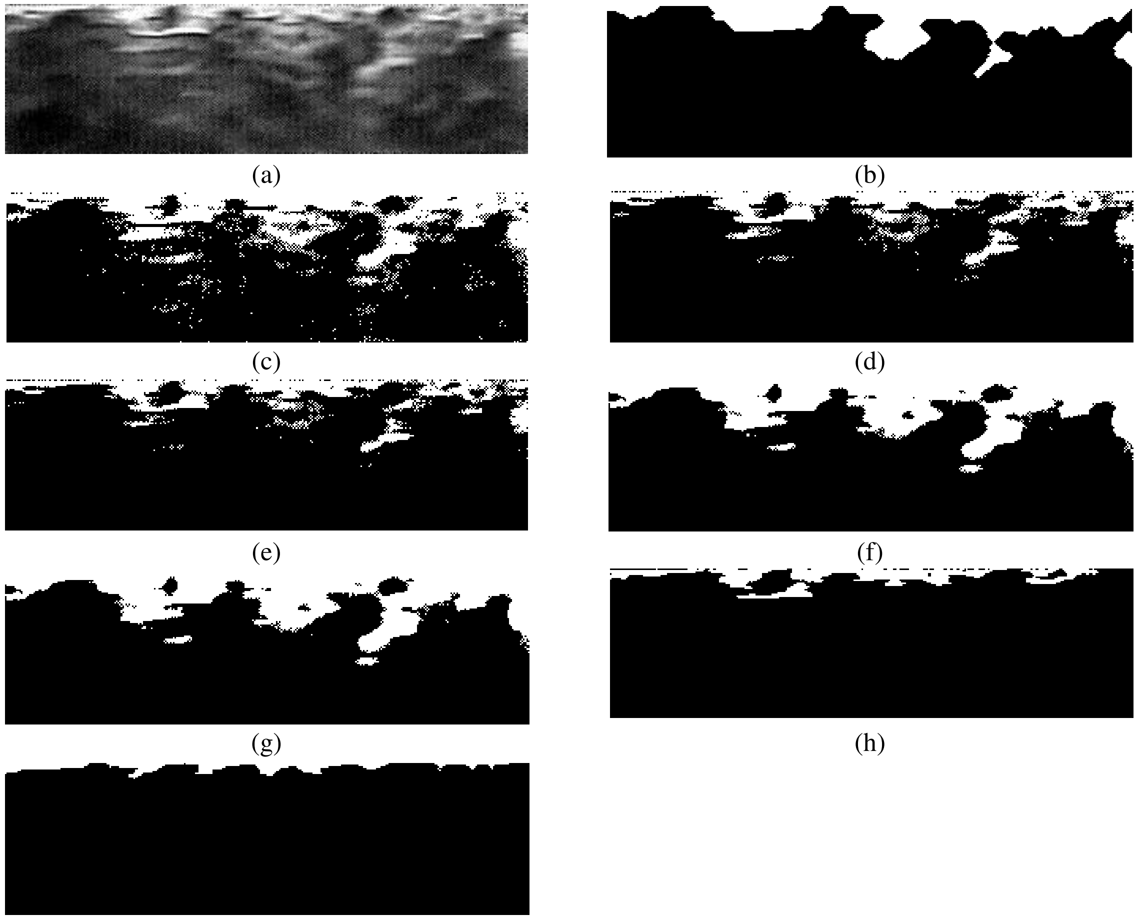

(a) (b) (c) (d) (e) (f) (g) (h) (i)

Figure 5.18 - Segmentation results obtained from different methods for a snapshot and flow condition V_{sw} =3.0 m/s and V_{so} = 1.2 m/s: (a) enhanced image; (b) segmented using morphology; (c) segmented by Otsu thresholding; (d) segmented by ISODATA thresholding; (e) segmented by fuzzy thresholding; (f) segmented using wavelet and K-Means; (g) segmented using wavelet and C-Means; (h) segmented using combined method; (i) manually segmented.

A phenomenological model has been developed by Rodriguez et al. (2012) and Rodriguez (2014) to predict the water film thickness in dispersed oil-in-water flow. The model is based on the assumption of existence of a thin laminar water film flowing adjacent to the pipe wall and surrounding a turbulent core of oil-water dispersion. It uses pressure-drop, holdup data and physical properties of the fluids to estimate the film thickness.

The following average relative error (*ARE*) is considered in this part of the work:

$$ARE = 100\frac{\sum_{1}^{N} abs\left(\frac{\delta_{model} - \delta_{top}}{\delta_{top}}\right)}{N}[\%], \qquad (5.21)$$

where δ_{model} and δ_{top} denote the film thickness predicted by the model and that estimated by image processing using the proposed algorithm, respectively. N is the number of experimental points.

One can see in Figure 5.20 a comparison between the film thickness estimated by the proposed visual technique (top side of the pipe) and the film thickness predicted by the model. The model underestimates the experimental data with an average relative error of 34%. Nevertheless, the model captures the trend, i.e., a reduction in the film thickness with increasing the mixture velocity. On the other hand, by inspection of Figure 5.18 one might infer that the proposed visual technique could be overestimating the water film thickness.

Table 5.4 - Film thickness estimated at the top and bottom of the pipe for different flow conditions.

Exp	$\boldsymbol{c_o}$ (-)	$\boldsymbol{V_m}$ (m/s)	$\boldsymbol{\delta_{top}}$ (mm)	$\boldsymbol{\delta_{bottom}}$(mm)
1	0.14	3.5	0.42	2.30
2	0.19	3.7	0.37	1.68
3	0.19	3.1	0.48	2.57
4	0.21	3.8	0.31	1.11
5	0.24	3.3	0.39	2.10
6	0.25	4.0	0.35	0.78
7	0.26	3.4	0.34	1.38
8	0.29	4.2	0.30	0.66
9	0.29	3.5	0.43	1.25
10	0.32	3.7	0.37	0.96
11	0.38	3.2	0.58	1.31
12	0.43	3.5	0.34	0.38

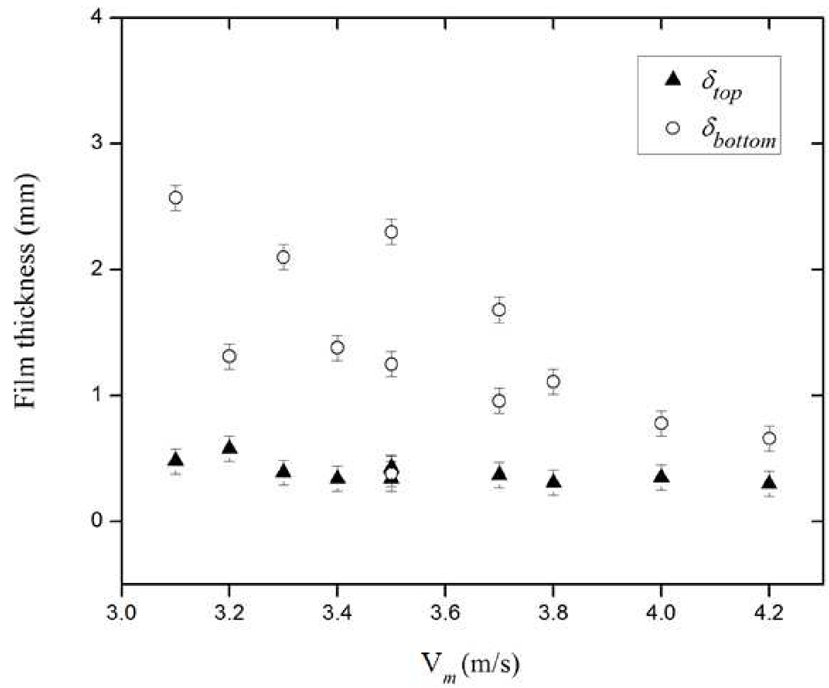

Figure 5.19 - Comparison between the film thicknesses measured at the top and bottom of the pipe using the proposed algorithm for each experiment.

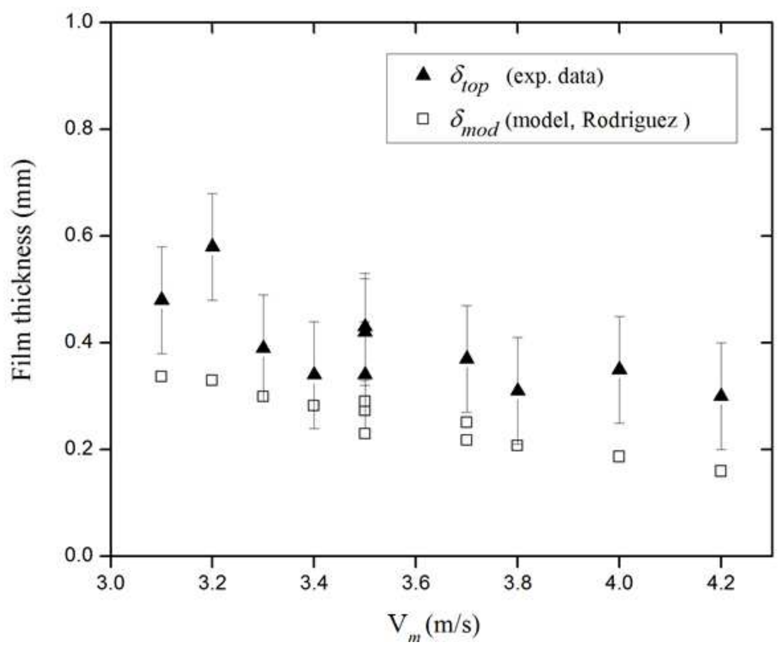

Figure 5.20 - Comparison between the film thickness predicted by Rodriguez et al. (2012) model and the one measured using the image processing technique.

6 RESULTS AND DISCUSSION

Different sensor geometries were numerically simulated to compare their characteristics and choose the best to measure water film thickness in oil-water flows through capacitance-based technique. The selected geometry was simulated at an operational frequency of 5 MHz, and its conductance and capacitance were estimated from the admittance values.

The water-film thickness data obtained by the two proposed techniques, visual and capacitive, in unstable annular and dispersed oil-water flow are compared. Finally, the water-film topology is studied.

6.1 Finite Elements Model Simulations

6.1.1 Selecting a Sensor Geometry

It is important to determine the best geometry for measuring water film thickness in oil-water flows. The reason for that is the fact that the sensor design determines the system capabilities from which the most important are spatial resolution and depth sensitivity. Five capacitive sensor geometries (Figure 6.1) were implemented and simulated in Comsol package and Matlab in order to compare their characteristics and choose the best one.

The geometries 1 and 3 were designed for an automatic car-wiper system, i.e. they were not used to measure water film thickness (LI & HE, 2011). The geometry 2 was proposed for nondestructive evaluation (NDE) of materials (CHEN, 2012). The geometry 4 (SILVA et al., 2007) and 5 (DAMSOHN & PRASSER, 2009) were designed and tested for water film thickness in gas-water flow and oil-water mixtures, respectively.

The sensors behaviors were studied by solving the three-dimensional potential equation within the liquid film on top of the sensor electrode system using finite elements method, refer to section 3.4.

The optimum size for the geometry 5 (Figure 6.1e) was determined in Tiwari et al. (2014). This geometry sensor had its shape and size of the transmitting, receiving and ground electrodes optimized with the purpose of having quasi linear characteristic for low film thicknesses, high measurement depth, minimization of cross-talk phenomenon and high spatial resolution.

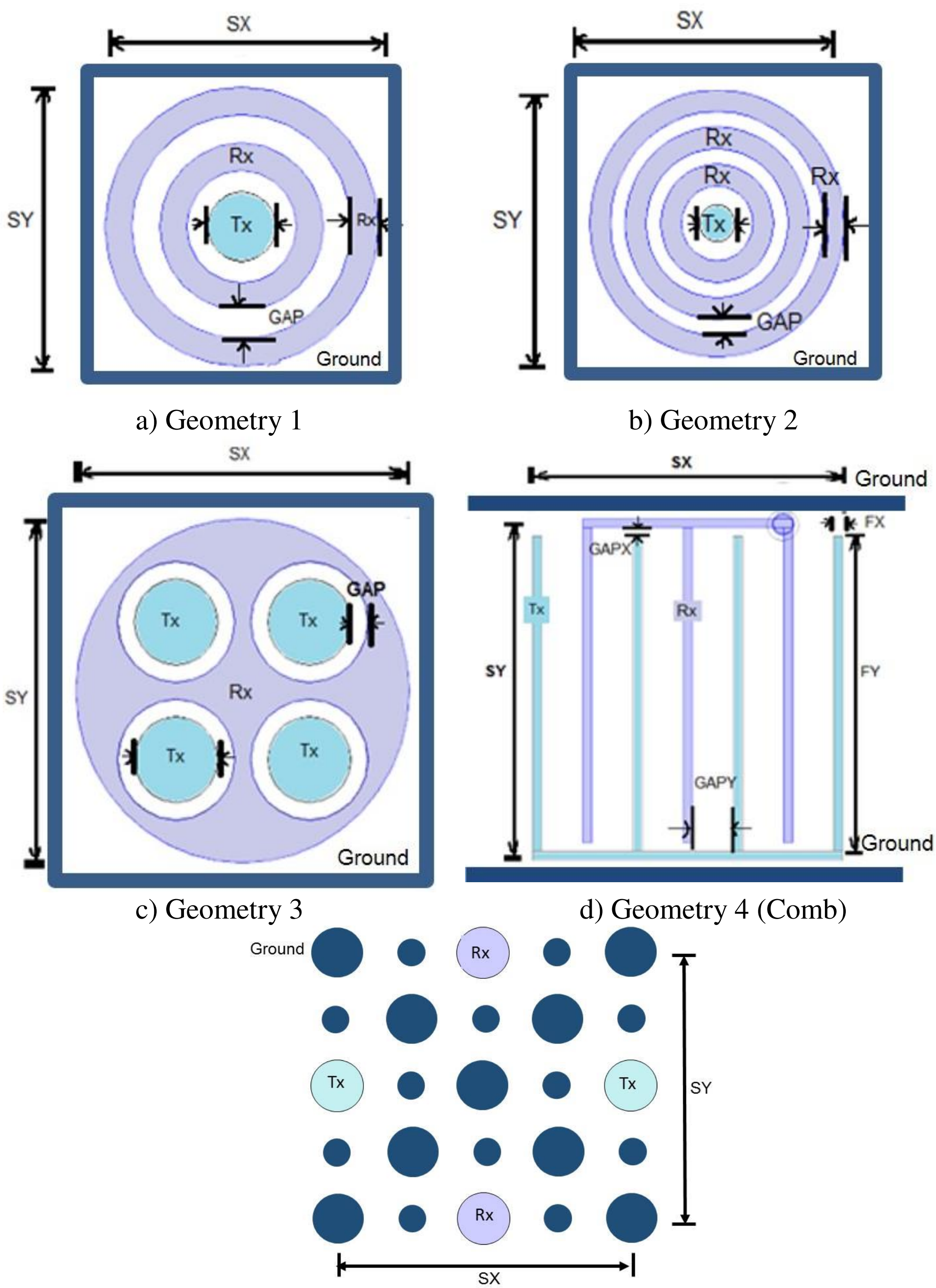

a) Geometry 1
b) Geometry 2
c) Geometry 3
d) Geometry 4 (Comb)
e) Geometry 5 (Points)

Figure 6.1 – Selected geometries of planar sensors.

The first tested geometry, Figure 6.1a, the pair Tx-Rx is composed by one transmitter electrode, one receiver electrode (as two concentric rings) and a ground electrode.

The second geometry, Figure 6.1b, is similar to the first one; the unique difference is that it has the receiver electrode with three concentric rings. Two results for the geometry 1 and the geometry 2 are in Figure 6.2. In this figure, one can see that the geometry 1 and 2 are able to measure film thickness below 600 μm. It is possible to increase the maximum depth reached, increasing the receiver area and/or the distance between the transmitter and the receiver. Table 6.1 presents sizes of the sensors with geometries 1, 2 and 5.

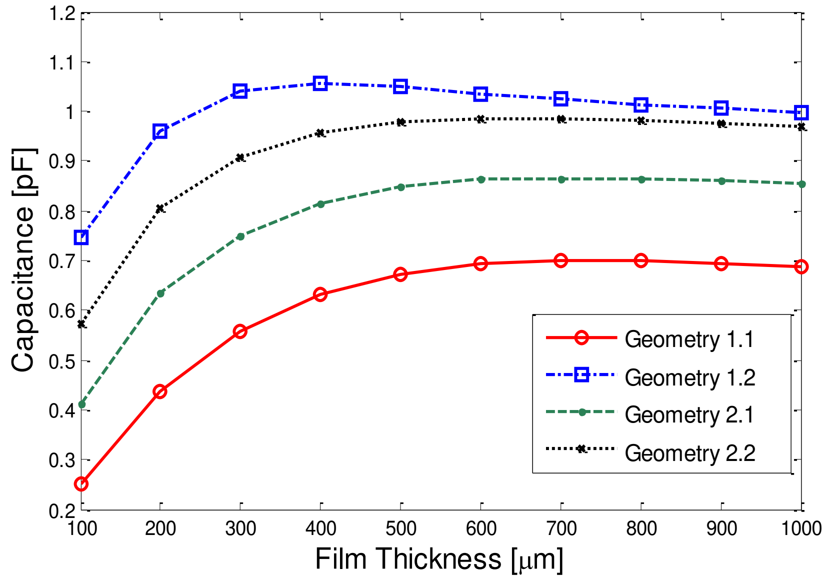

Figure 6.2 - Summary of simulation results for sensors with geometry 1 and 2.

Table 6.1 - Sizes of the sensors for geometries 1,2 ,3 and 5.

Geometry	Spatial resolution, SX×SY [mm]	Spacing between Tx and Rx, GAP [mm]	Annular ring width, Rx [mm]	Transmitter size Diameter, Tx [mm]
1.1	4 × 4	0.95	0.3	0.5
1.2	2 × 2	0.15	0.2	0.5
2.1	4 × 4	0.45	0.3	0.5
2.2	3.6 × 3.6	0.25	0.3	0.5
3.1	2.4 × 2.4	0.10	-	0.5
3.2	4 × 4	0.2	-	1.0
5	4 × 4	2.0	-	0.9

The third geometry, Figure 6.1c, has a transmitter made of four circular parts, surrounded by the receiver, which is circular. A summary of simulation results for the geometry 3 is presented in Figure 6.3, it is clear that the depth reached and the quasi linear characteristic are improved by increasing the receiver area.

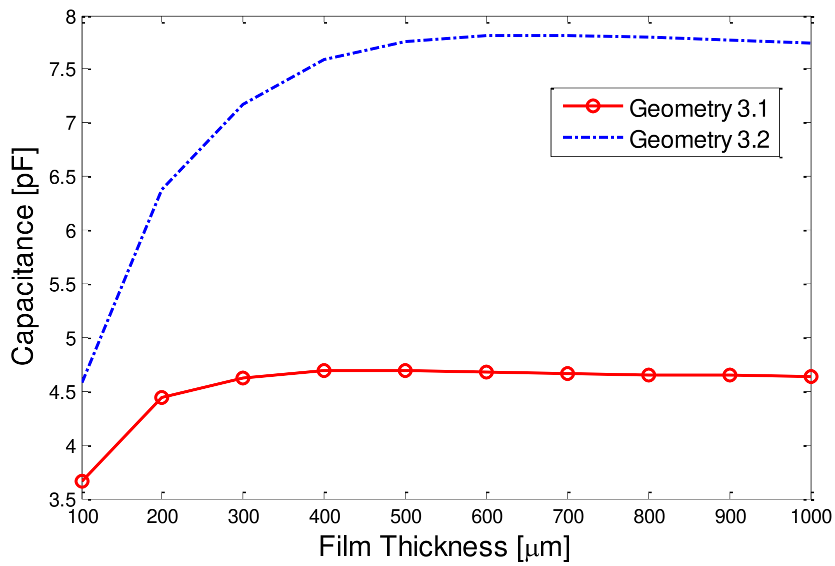

Figure 6.3 - Summary simulation results for sensors with geometry 3.

The fourth geometry has a comb shape as shown in Figure 6.1d, the transmitter has four fingers and the receiver has three fingers. Figure 6.4 presents a summary of simulation results for the geometry 4. Correspondingly, Table 6.1 presents the sizes of the sensors with geometries 1 to 3 and 5, and Table 6.2 presents the sizes of the sensors with geometries 4.

Similarly, the simulation results (geometry 4) for different finger length and spacing between a transmitter finger and receiver finger are presented in Figure 6.5 and Figure 6.6. In Figure 6.5, the finger size (FX×FY) is 0.170 x 6.12 mm^2 and spacing between a transmitter finger and receiver finger (GAPX) was changed, starting at 0.68 mm and finishing at 2.38 mm. In this case, by increasing the spacing, the film-thickness saturation grows and it decreases the capacitance value. In Figure 6.6, the spacing between a transmitter finger and receiver finger (GAPX) is 1.7 mm, finger size in x (FX) is 0.17 mm and finger size in y (FY) was changed, between 0.68 mm and 5.7 mm. By increasing the finger size, it increases the film thickness saturation and the capacitance value.

Figure 6.7 shows the simulation results of the fifth geometry (Figure 6.1e).

Table 6.2 - Size of the sensor for geometry 4.

Geometry	Spatial resolution SX×SY (mm)	Spacing between transmitter and receiver (mm)		Finger size, FX×FY(mm^2)
		GAPX	GAPY	
Geometry 4.1	5.78 × 6.63	0.86	0.17	0.17 × 6.12
Geometry 4.2	2.72 × 6.63	0.425	0.17	0.17 × 6.12
Geometry 4.3	5.78 × 6.63	0.86	0.17	0.17 × 0.68

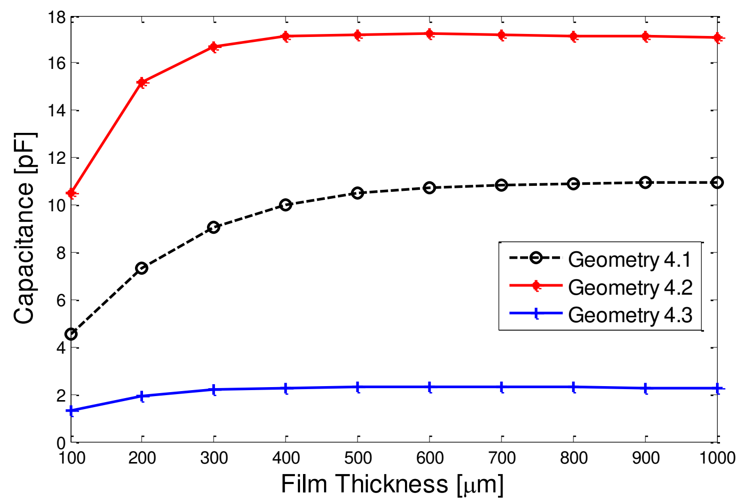

Figure 6.4 - Summary simulation results for sensors with geometry 4.

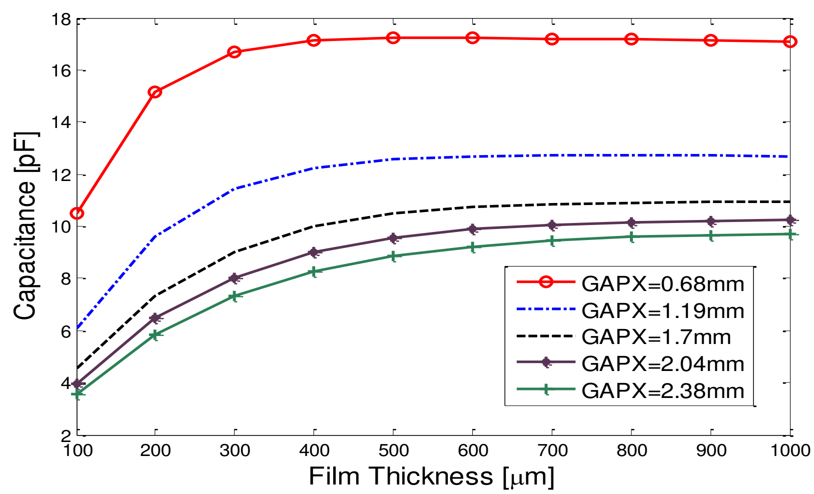

Figure 6.5 - Simulation results for sensors with geometry 4 where GAPX was increased.

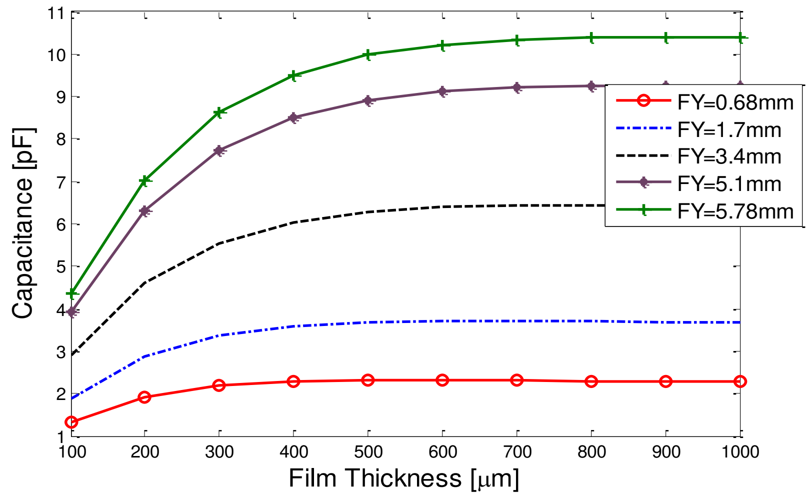

Figure 6.6 - Simulation results for sensors with geometry 4 where FY was increased.

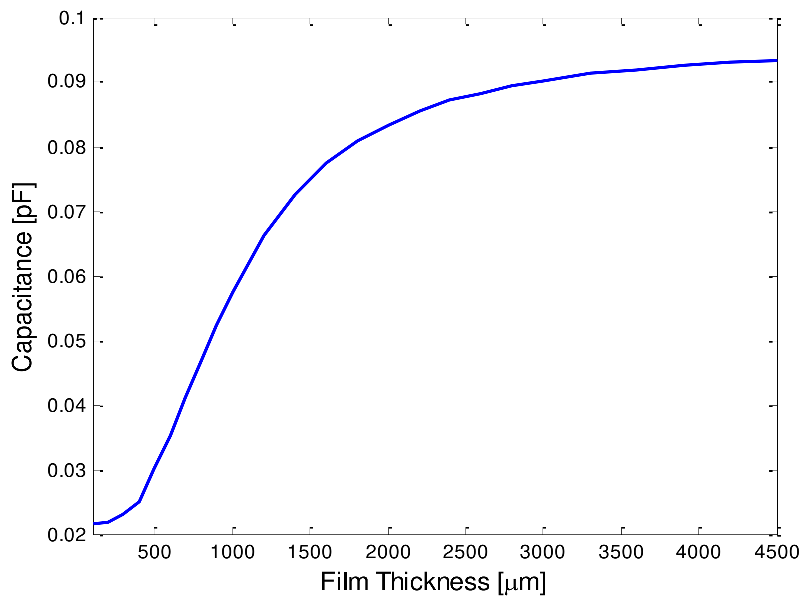

Figure 6.7 - Simulation results for sensor with geometry 5.

According to these results, it is possible to conclude that (1) the capacitance is very small (between 0.02 pF and 17 pF) and its value can be enhanced by either changing the distance between the transmitter and receiver electrodes or increasing the effective sensing area, regardless of the concerned geometry. (2) Increasing the distance between the electrodes, the saturation film thickness grows, which is evident in Figure 6.3 and Figure 6.5. (3) Increasing the electrode size improves the measurement sensitivity of the sensor, Figure 6.2,Figure 6.3 and Figure 6.6.

The best design geometry to achieve a balance between the penetration depth, the sensitivity, the minimum spatial resolution (4 × 4 mm^2) and the quasi-linear characteristic is the geometry 5, Figure 6.1e. The saturation thickness is higher than 2500 µm while for other geometries is maximum 700 µm.

6.1.2 Testing the Selected Sensor Geometry

In the section 6.1.1, the selected geometry was tested using an electrostatic FEM simulation in electrostatic conditions. Usually, the literature considers this approximation as valid for capacitive sensors (NASSR et al., 2008; MUKHOPADHYAY et al., 2005). But, this simulation does not consider the conductance and the frequency.

An electric current FEM simulation was carried out to study the selected sensor behavior in frequency domain. The simulation considers the electrostatic field, the electric currents and the frequency of operation. This simulation was made at frequency of 5 MHz, that it is the operation frequency of the capacitance measurement system. For this type of simulation, the solution is obtained by solving the following equations presented in section 2.7. The studied result was the admittance. The admittance for a measured pair Tx-Rx can be written as

$$Y_s = \sigma_s + j2\pi f C_s, \qquad (6.1)$$

where Y_s is the simulated admittance, σ_s is the simulated conductance, f is the simulated frequency (5 MHz) and C_s is the simulated capacitance.

For the purpose of comparison, the capacitance and conductance were dimensionless as:

$$\mathrm{C}_{dl} = \text{Dimensionless Capacitance} = \frac{C - C_{\min}}{C_{\max} - C_{\min}} \qquad (6.2)$$

where C is the capacitance value, C_{max} is the maximum capacitance value and C_{min} is the minimum capacitance values.

$$\mathrm{G}_{dl} = \text{Dimensionless Conductance} = \frac{G - G_{\min}}{G_{\max} - G_{\min}} \qquad (6.3)$$

where G is the conductance value, G_{max} is the maximum conductance value and G_{min} is the minimum conductance value.

The comparison between the dimensionless capacitance and conductance for the sensor is shown in the Figure 6.8. The response is pretty much the same in both cases, including the nonlinear behavior and the lower and upper limits. Thus, the measurement of film thickness by conductive or capacitive technique depends on the properties of the fluids and the conditions of the experiments. For example, the conductance can be used if the liquid film is conductive and the capacitance if the film liquid is non-conductive. The saturation thickness is near to 2200 µm.

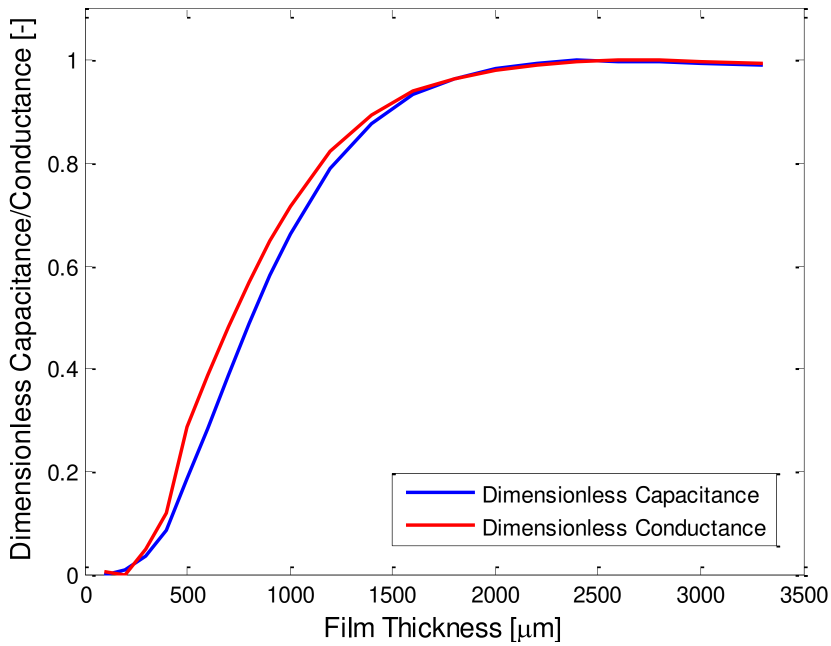

Figure 6.8 – Conductance and capacitance results using electric current simulations for resolution of 4×4 mm^2.

Figure 6.9 shows a comparison between the electrostatic and electric current simulations of the sensor. It is possible see that the dimensionless capacitance has a different behavior, for instance in the upper limit. For the electrostatic case the upper limit is 3000 µm, but it is only of 2200 µm for the electric current case. On the other hand, the lowers limits do not show a significant variation. The difference between the electrostatic and electric current simulations shows that it is important to consider the conductance and frequency to calculate the film thickness limits.

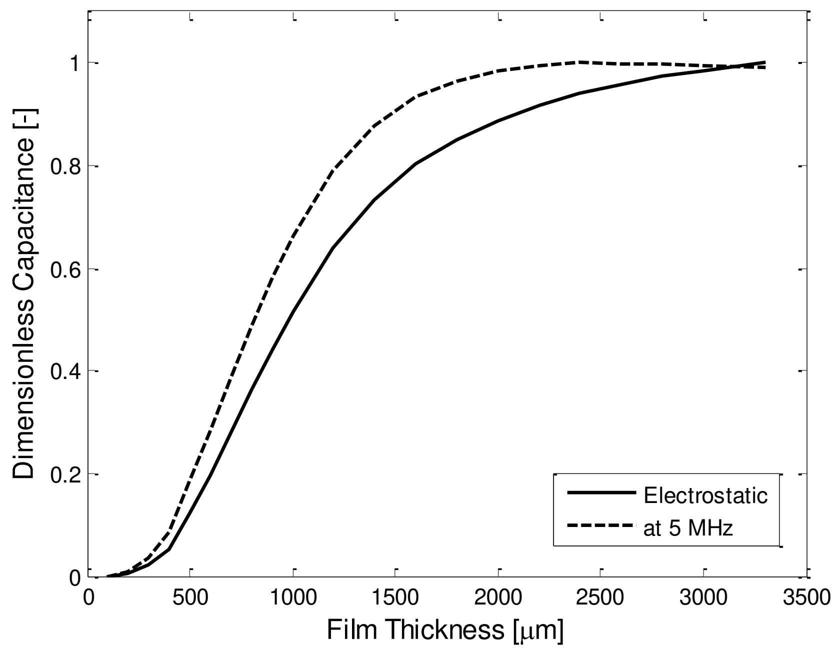

Figure 6.9 – Capacitance results using electrostatics and electric current simulations for resolution of 4×4 mm^2.

6.2 Experimental Results

After preliminary experiments using high-speed camera, it was established that the expected water film thickness would be between 400 μm and 2000 μm. The sensor with spatial resolution of 4 × 4 mm^2 would be suitable for the measurement of these thicknesses, see section 4.3. The effective measuring area for this sensor is of 64 mm by 52 mm. The temporal resolution in all the experiments was 5000 frames per second.

6.2.1 Calibration

In order to correlate the signal obtained from the receiver electrodes to film thickness, a calibration was necessary prior to the measurements. During the calibration experiments, the sensor is immersed into water with an inclined angle and various cylinders with a known gap are rolled over the sensor. The measured value is the minimum measured value, when the cylinder is passing over the measuring point (Figure 6.10). Figure 6.11 shows the calibration elements; one can see the calibration box, where the sensor was fixed and maintained straight, and some of the cylinders used in the tests.

The experiments were made using eighteen cylinders made of polyvinyl chloride, PVC, with a relative permittivity of three (the similar to oil). The cylinders have gaps (δ) between zero and 2400 μm, Figure 6.10. Each cylinder was rolled over the sensor ten times.

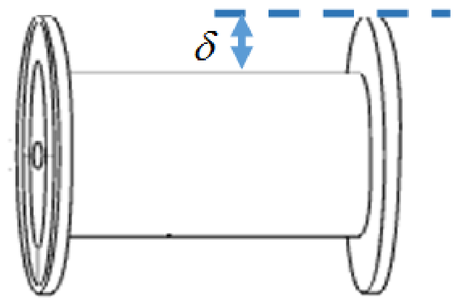

Figure 6.10 – Cylinder with a gap of δ micrometers.

The calibration value is taken from the minimum measured value, when the cylinder is passing over the measuring point. The calibration values for each measurement point are fitted with a fourth order rational polynomial.

The film thickness δ, in each measurement point, can be calculated as

$$\delta = a_1 U_{dl}^4 + a_2 U_{dl}^3 + a_3 U_{dl}^2 + a_4 U_{dl} + a_5 \quad (6.4)$$

where a_1 to a_5 are the polynomial coefficients determined by the calibration curve fitting and U_{dl} is calculated by eq. (4.4).

a) b)

Figure 6.11 – Calibration elements. a) Calibration box and b) Sample of cylinders.

Figure 6.12 presents the calibration results for each measurement point (each pair Tx-Rx). Experimental results show that the system can measure thickness between 400 μm and 2200 μm.

These results show that the simulations results represent correctly the practical behavior (refer to Figure 6.9). In the same way, they confirm that it is possible to measure the water film thickness with the capacitance system.

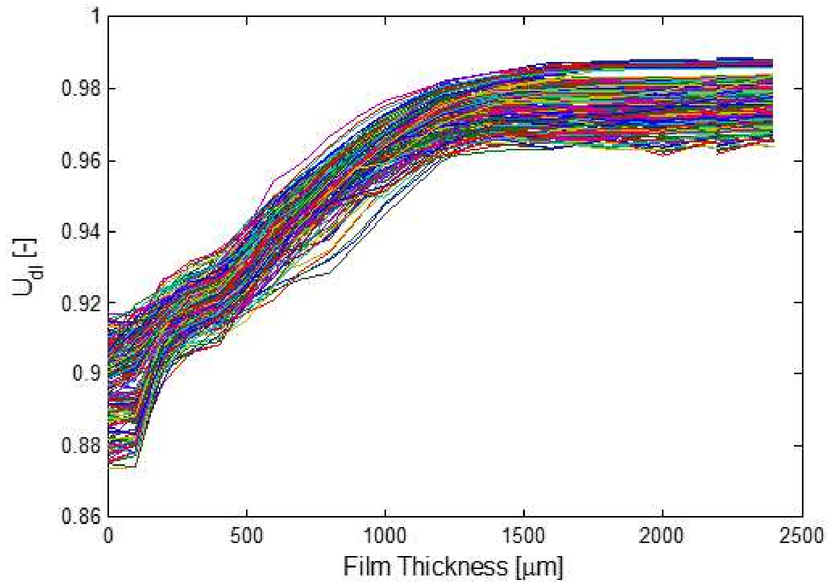

Figure 6.12 – Dimensionless voltage for each measurement point using the different cylinders.

6.2.2 Uncertainty Analysis

Three sources of errors were taken into account to determinate the uncertainty of the film thickness measurement system presented in this work. First, the measurement of the gap in the calibration cylinders (calibration error). Second, the deviation from the calibration curve. At last, the statistical variations of the measured values (data acquisition system error).

6.2.2.1 Calibration Error

As seen in the last section, the system calibration is made using a calibration cylinders. Each cylinder has a known gap and is passed over the sensor ten times. The voltage in every measuring point is recorded. The calibration values for each measurement point are fitted with a fourth order rational polynomial. There are two sources of error in this case, one due to the cylinder gap measurements and other due to the curve fitting.

To calculate the gap are measured the internal diameter of the cylinder (D_i) and the external diameter (of the rim), D_e.

$$Gap = \frac{D_e - D_i}{2} \quad (6.5)$$

A caliper, with an uncertainty of $u_{Caliper}$ =±0.01 mm, is used to measure these diameters. Several measurements of the diameters of each cylinder were made, with the caliper, to estimate the standard uncertainty of the internal diameter and the external diameter measurements. The standard uncertainty for the internal diameter was $u_{D_{is}}$=±0.025 mm and for the external diameter was $u_{D_{es}}$=±0.022 mm. Combining the uncertainty of the caliper and the standard uncertainty, u_{D_i}=0.026 mm and u_{D_e}=0.024 mm.

The uncertainty of the calibration cylinder gaps can be estimated as

$$u_{Gap}(\mathrm{D}_i, \mathrm{D}_e) = \sqrt{\left(\frac{\partial Gap}{\partial D_i}\right)^2 \mathrm{u}_{\mathrm{D}_i}^2 + \left(\frac{\partial Gap}{\partial D_\mathrm{e}}\right)^2 \mathrm{u}_{D_e}^2 + 2\left(\frac{\partial Gap}{\partial D_i}\right)\left(\frac{\partial Gap}{\partial D_\mathrm{e}}\right)\mathrm{u}_{D_i}\mathrm{u}_{D_e}\, r(D_i, D_e)}. \quad (6.6)$$

where $r(D_i, D_e)$ is the correlation coefficient and is -0.34. The uncertainty of the cylinder gap measurements is u_{Gap}=±0.020 mm.

On the other hand, the uncertainty due to the polynomial fitting process is the standard deviation of each coefficient in eq. (6.4). The standard deviation is given as an out parameter of the used Matlab function. An example of the uncertainty of the coefficients is (these are representative for the measurement system):

$$\begin{aligned} u_{a_1} &= 0.041 \text{ mm} \\ u_{a_2} &= 0.065 \text{ mm} \\ u_{a_3} &= 0.032 \text{ mm} \\ u_{a_4} &= 0.005 \text{ mm} \\ u_{a_5} &= 0.0002 \text{ mm} \end{aligned} \quad (6.7)$$

6.2.2.2 Data Acquisition System Error

It was used the deviation of the measured voltages U_x for a measuring pair (Tx5-Rx5) to estimate the uncertainty of the measurement system due to random error. The sensor was covered with water with a film thickness higher than the saturation one, and 5000 frames were recorded at 5000 fps. The sine excitation had 5 V peak and 5MHz of frequency. The uncertainty of the data acquisition system was taken as the maximum value of deviation in the voltage measurements, $u_{U_x} =$ 4.7 mV, Figure 6.13.

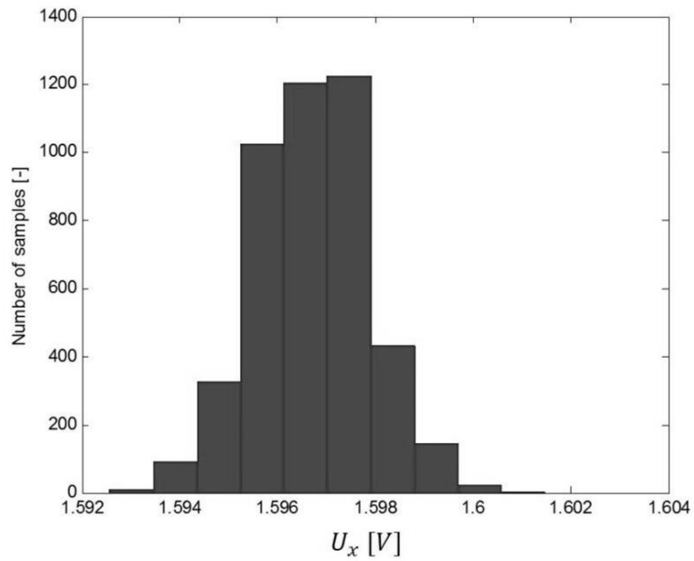

Figure 6.13 - Distribution of the voltage measurements for pair Tx5-Rx5 for 5000 frames with the sensor covered with water (on saturation condition).

6.2.2.3 Film Thickness Measurement Uncertainty

Remembering that the film thickness δ, in each measurement point, is calculated as

$$\delta = a_1 U_{dl}^4 + a_2 U_{dl}^3 + a_3 U_{dl}^2 + a_4 U_{dl} + a_5$$

where a_1 to a_5 are the polynomial coefficients determined by the calibration process and U_{dl} is

$$U_{dl} = \frac{U_x}{U_{sat}}$$

where U_x is the measured voltage and U_{sat} is the measured voltage when the sensor is covered by water with a thickness higher than 2200 μm.

The uncertainty for U_{dl} can be calculated as

$$u_{U_{dl}}(U_x, U_{sat}) = \sqrt{\left(\frac{\partial U_{dl}}{\partial U_x}\right)^2 u_{U_x}^2 + \left(\frac{\partial U_{dl}}{\partial U_{sat}}\right)^2 u_{U_{sat}}^2}$$

$$u_{U_{dl}}(U_x, U_{sat}) = \frac{0.0047\ \mathrm{V}}{U_{sat}^2} \sqrt{U_{sat}^2 + U_x^2}, \qquad (6.8)$$

where $u_{U_x} = u_{U_{sat}} = 4.7$ mV.

Moreover, the uncertainty for film thickness estimation, u_{δ}, can be obtained by combining the uncertainty of the coefficients (section 6.2.2.1) and the U_{dl} uncertainty:

$$u_{\delta}(a_1,a_2,a_3,a_4,a_5,\mathrm{U}_{dl}) = \sqrt{\left(\sum_{i=1}^{5}\left(\frac{\partial\delta}{\partial a_i}\right)^2 u_{a_i}^2\right)+\left(\frac{\partial\delta}{\partial U_{dl}}\right)^2 u_{U_{dl}}^2}, \tag{6.9}$$

$$u_{\delta} = \sqrt{U_{dl}^8 u_{a_1}^2 + U_{dl}^6 u_{a_2}^2 + U_{dl}^4 u_{a_3}^2 + U_{dl}^2 u_{a_4}^2 + u_{a_5}^2 + \left(4a_1U_{dl}^3 + 3a_2U_{dl}^2 + 2a_3U_{dl} + a_4\right)^2 u_{U_{dl}}^2}. \tag{6.10}$$

Combining the uncertainty of the calibration error and the film thickness estimation we have the uncertainty of the film thickness measurement system equal to

$$u_{system} = \sqrt{\left(u_{Gap}\right)^2 + \left(u_{\delta}\right)^2}. \tag{6.11}$$

Thus, the uncertainty of the film thickness measurement system for all the range in Figure 6.12, taking Tx5-Rx5 as reference, is

$$\pm 85\ \mu\text{m} < u_{system} < \pm 105\ \mu\text{m}. \tag{6.12}$$

The first bound is related to water film thickness of 100 µm and the second is related to the larger measured film thickness (2200 µm).

For the experiments, in section 6.2.3, the measured film thickness was between 1000 µm and 2100 µm . For those limits, the uncertainty is

$$\pm 101\ \mu\text{m} < u_{system} < \pm 105\ \mu\text{m}. \tag{6.13}$$

6.2.3 Pipe Flow Results

One of the main goals of this research is to assess the capability of a capacitive planar-sensor system for measuring a thin water film thickness in oil-water flow. For these purpose, experimental points were selected based on the water and oil superficial velocities for upward-vertical pipe flow with special attention paid to semi-annular and fully dispersed oil-in-water flow patterns. Annular flow is characterized by an oil core surrounded by a water film. It can be rather unstable and drops of several different sizes and shapes can be observed around the oil core. At fully dispersed oil-in-water flow a water film adjacent to the pipe wall has been identified recently. In total, 44 oil-water experiments (33 annular and 11 dispersed) were carried out in a glass pipe with 50.8 mm of I.D, refer to Table A.1. The film thickness was recorded at

5000 frames/second for one second by the capacitance measurement system and the high-speed camera.

6.2.3.1 Observed Flow Patterns

Water and oil flow rate ranges were 0.1 m/s to 2.0 m/s and 0.3 m/s to 0.8 m/s, respectively. It was possible to observe big drops, unstable or semi-annular flow and dispersed oil-in-water flow, Figure 6.14. In the next sections, big drops and unstable annular flow will be analyzed as a single pattern, because near to the pipe wall their behaviors are similar (oil drops and a water film). One can see in Figure 6.15 the observed flow patterns as function of oil superficial velocities and water superficial velocities. These experimental points were chosen such that the water film thickness could be measured with the capacitive system. The transition boundary between dispersed oil-in-water flow and unstable annular corresponds to the theoretical one (Figure 3.2).

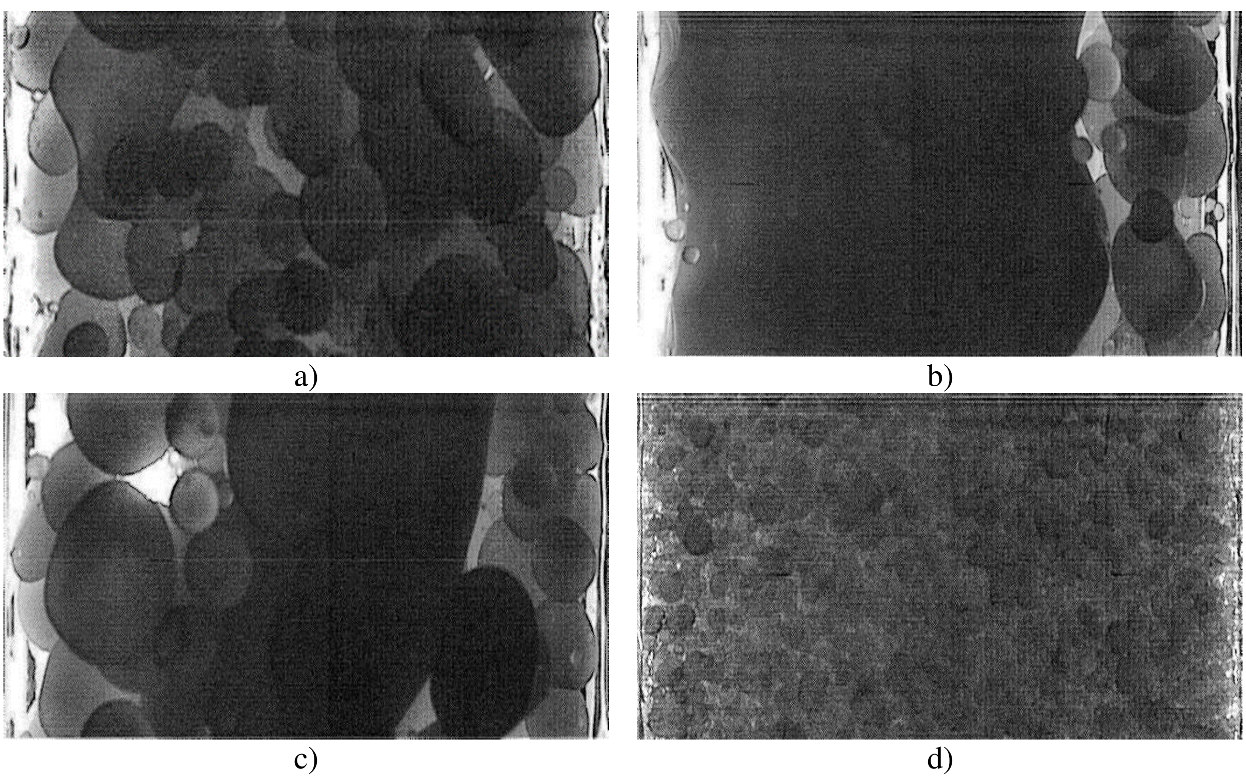

Figure 6.14 – Observed flow patterns. a) Big drops, V_{so} =0.4 m/s and V_{sw} =0.2. b) Unstable annular flow, V_{so} =0.3742 m/s and V_{sw} =0.15. c) Unstable annular flow, V_{so} =0.3 m/s and V_{sw} =0.1 m/s. d) Dispersed oil-in-water, V_{so} =0.5 m/s and V_{sw} =1.5 m/s.

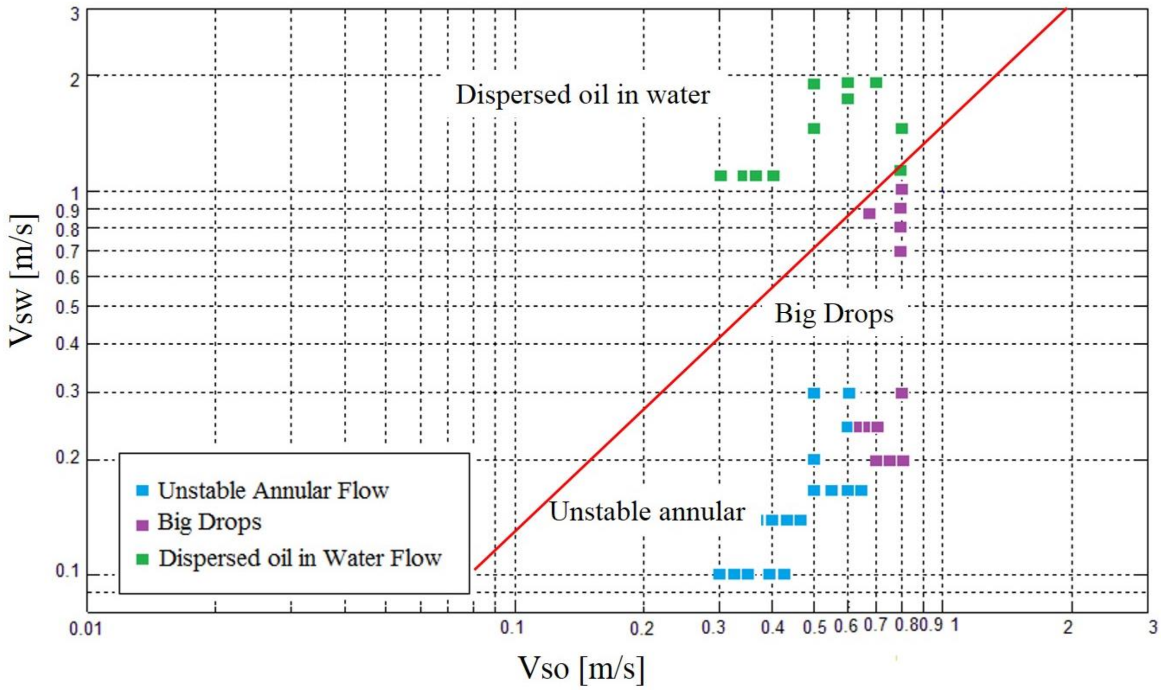

Figure 6.15 – Observed flow patterns as function of oil superficial velocities and water superficial velocities.

6.2.3.2 Water Film Thickness

The high-speed camera images were processed using the algorithms presented in Chapter 0. First of all, the images were pre-processed. After the pre-processing, the image size is 668 × 481 pixels. Next, the images were segmented using the proposed algorithm. One can see in Figure 6.16 an original snapshot, the resulting image after applying the pre-processing step and the result of the segmentation stage.

The mean film thickness was determined for each experiment by averaging 5000 frames of instantaneous film thickness measurements, in both high-speed-camera images and capacitive technique. The definitions of mean film thickness $\bar{\delta}$ for one frame is

$$\bar{\delta} = \frac{1}{Np}\sum_{i=1}^{Np}\delta_i \qquad (6.14)$$

where Np is the number of measurement points (13 × 16 points for the measurement system and 668 columns for the images) and each pixel has a film thickness δ_i, calculated using eq. (6.4) for the measurement system and eq. (5.19) for the images.

The mean film thickness for an experiment is calculated as

$$\overline{\delta}_{Exp} = \frac{1}{N_{frames}} \sum_{1}^{N_{frames}} \overline{\delta} \quad (6.15)$$

where N_{frames} is 5000 frames.

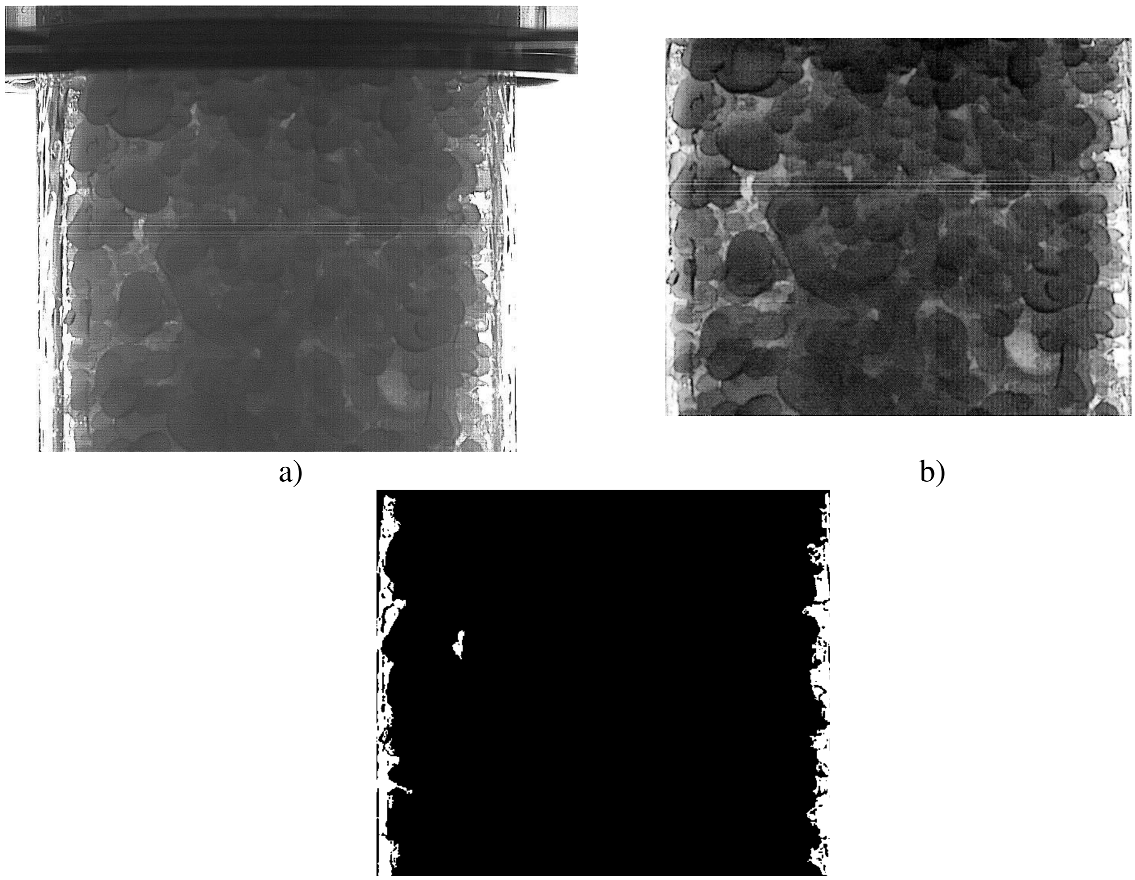

a) b) c)

Figure 6.16 – Image processing results. a) Original snapshot , Vso =0.8 m/s and Vsw =0.8 m/s experiment. b) Pre-processing result. c) Segmentation result.

The measured mean film thickness obtained by the capacitance system for each experiment was compared with the one obtained by the high-speed-camera image technique, Figure 6.18 and Figure 6.19. The flow patterns unstable annular and big drops were analyzed as a unique pattern called unstable annular flow, as mentioned in section 6.2.3.1. The average relative error (*ARE*) considered to compare the system and camera measurements is:

$$ARE = 100 \frac{\sum_{1}^{N} abs\left(\frac{\delta_{camera} - \delta_{system}}{\delta_{system}}\right)}{N} [\%], \quad (6.16)$$

where δ_{camera} and δ_{system} denote the film thickness predicted by the high-speed camera images and that estimated by the proposed system, respectively. N is the number of experimental points. The average relative error (ARE) is 21.8% and the deviation is -30% for unstable annular flow and 3.6% and -10% for dispersed flow. The black triangles are the results of the measurement system, the red squares are the results of the high-speed camera images and the blue line denotes a -30% deviation having as reference the film thickness estimated using the images. The uncertainty of the measurements using the images was of 100 μm, corresponding to the half of the minimum scale of the square pattern used for calibration, see Figure 4.13. As one can see in Figure 6.18 and Figure 6.19, the water film thickness ranged from 900 μm to 2100 μm for the unstable-annular flow pattern and from 1300 μm to 2200 μm for dispersed flow, respectively. The image technique always overestimated the capacitance-system data, the disagreement being more pronounced for the unstable-annular-flow case.

The capacitive measurement system is able to record the water film thickness in different directions. It allows having information about 3-D variations, so one should expect that the average film thickness would be overestimated in comparison with the image-analysis-based technique, which only records 2-D projection of the film. However, the opposite is observed. This is an indication that the proposed image-analysis-based technique may be overestimating the value of the water film thickness maybe due to segmentation errors, i.e. some oil-drop pixels, with gray values near to water, could have been segmented as water (refer also to Figure 5.20).

The lower computed error for dispersed flow could be because in this kind of flow the oil droplets are uniformly distributed in the perimetral and axial directions near the tube wall. This fact was confirmed by visual inspection (Figure 6.14d). Otherwise, for unstable-annular flow the difference between capacitive and image-based data is larger, between 20% and 35%. Oil drops are elongated in the axial direction and tend to coalesce, while in the perimetral direction larger distances between them were visually observed (Figure 6.17 and Figure 6.14a). Distortions related to problems about keeping the focus of the camera on the diametrical-vertical plane may have become more pronounced in this flow situation. Optical distortions are probably the reason behind the observed disagreement.

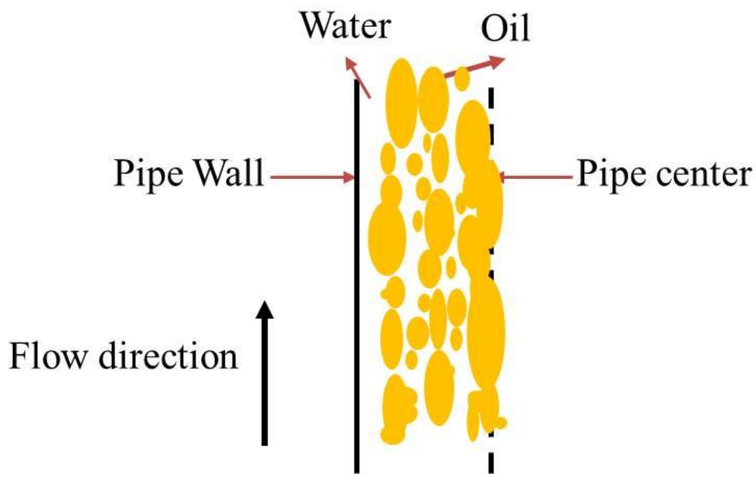

Figure 6.17 – Illustration of the unstable annular flow.

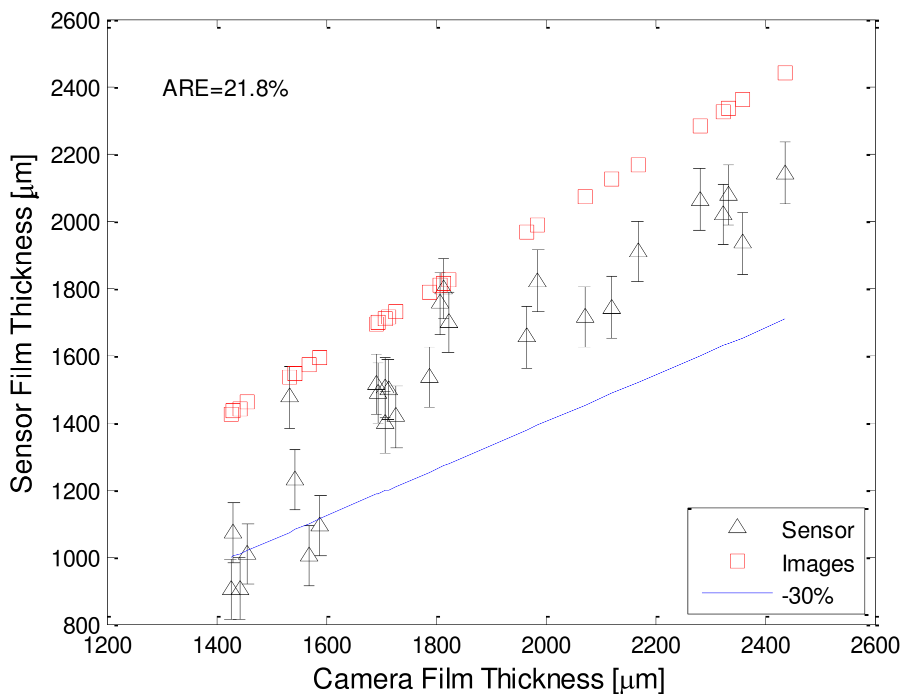

Figure 6.18 – Measured water film thickness using capacitance system versus measured by high-speed-camera image technique for unstable-annular flow.

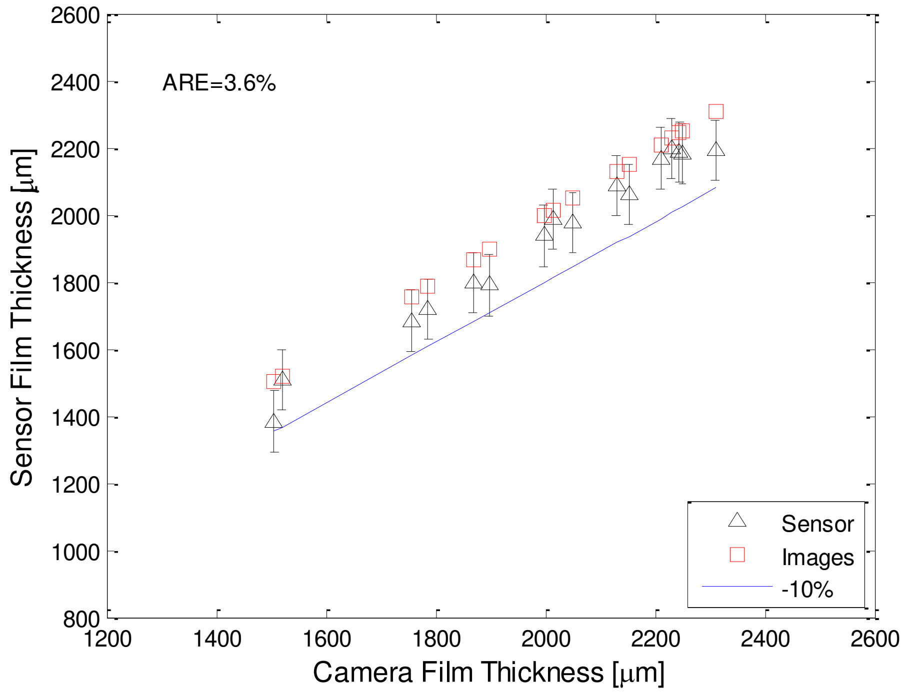

Figure 6.19 – Measured water film thickness using capacitance system versus measured by high-speed camera images for dispersed oil-in-water flow.

The liquid-film thickness is plotted against oil volume fraction for both flow patterns in Figure 6.20. The oil fractions below h_o=0.45 correspond to dispersed flow and above h_o=0.48 correspond to unstable annular flow. The general trend of the liquid film thickness is to decrease as the oil fraction increases, for all unstable annular flow. For dispersed flow, there is the same trend for oil fractions between 0.16 and 0.4. An explanation is that as the oil volumetric fraction increases, the oil tends to take over the entire cross-section.

The dimensionless water-film thickness is plotted against the water-film Reynolds number in Figure 6.21. Rodriguez et al. (2012) presented the dimensionless water-film thickness, Film Thickness $(\delta)/\delta_{sub,m}$, where the water-film thickness is normalized by the thickness of an effective viscous sublayer of a turbulent homogeneous mixture of oil in water. The latter is given by

$$\delta_{sub,\mathrm{m}} = \frac{5\left(\dfrac{\mu_w}{\rho_{m.\mathrm{hom}}}\right)}{V_{frict,m}}, \quad (6.17)$$

where $V_{frict,m}$ is the mixture friction velocity,

$$V_{frict,m} = \left(\frac{\tau_w}{\rho_{m.\text{hom}}} \right)^{1/2}, \quad (6.18)$$

where τ_w is the shear stress at the wall defined as

$$\tau_w = -\left(\frac{R}{2} \right) \left(\frac{\partial p}{\partial x} \right)_m . \quad (6.19)$$

The water-film Reynolds number is given by:

$$\text{Re}_f = \frac{\rho_w V_{w,f} (2\delta)}{\mu_w}, \quad (6.20)$$

and $V_{w,f} = V_o/2$ is the water-film velocity.

The explanation given in Rodriguez et al. (2012) for the drag reduction phenomenon was the existence of a thin laminar water film near the pipe wall. A linear relation between the dimensionless water-film thickness and water-film Reynolds number was found and transition from laminar to turbulent film flow was related to lower or even no drag reduction. One can see in Figure 6.21 that a linear fitting could approximate the relation obtained in this work for dispersed flow, but the film-Reynolds number is quite high, in between 2500 and 5750. According to that model, the water-film flow is likely to be in the turbulent regime. Perhaps it is interesting to inform that some preliminary pressure-drop tests were conducted during this work and no drag reduction was detected.

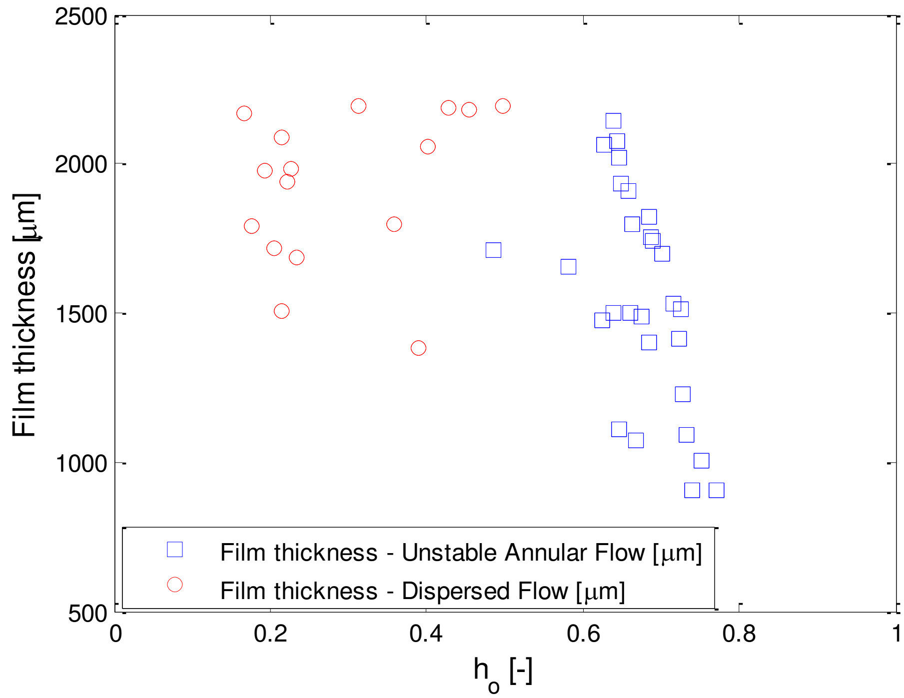

Figure 6.20 – Measured water film thickness using capacitance system against oil fraction.

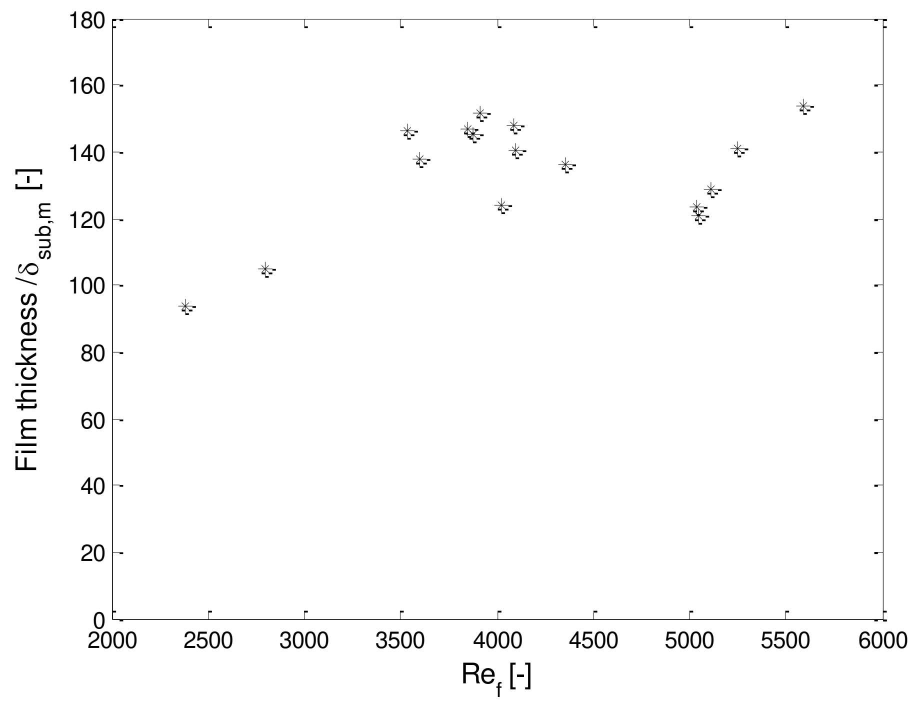

Figure 6.21 – Dimensionless water-film thickness against the water-film Reynolds number for dispersed oil-in-water flow.

6.2.3.3 Holdup

Figure 6.22 presents the comparison between the water holdup from the quick-closing valves (QCV), and the water holdup obtained by the homogeneous model, for the unstable annular and dispersed flow patterns. The water holdup predicted by the homogeneous model shows a deviation of about -30% compared to the QCV value, and the average relative error is 20.1%. The black line denotes the ideal agreement and the green one the deviation. The values predicted by the model are lower than the values obtained experimentally, which shows the presence of slip between the phases, with oil flowing faster than water. One can see that for dispersed flow the homogeneous model has a significantly lower error (5.1%) than for unstable annular flow, which is consistent as no-slip between phases is expected in fully dispersed flow.

The water-holdup data obtained by the quick close valves are compared with predictions of the correlation for core-annular flow of Rodriguez et al. (2009), which considers the presence of interfacial waves , turbulent water flow, the presence of dispersed oil droplets and slip between the phases. The predicted water holdup shows a deviation of about +20% compared to the QCV value and the average relative error is 10.1%, Figure 6.23. The agreement between holdup predictions and measurements is better for the entire experimental range in general. However, the correlation of Rodriguez et al. (2009) is valid for core-annular flow only and, in principle, should not be applied to dispersed flow. As expected, the agreement is worse for dispersed flow, in comparison with that observed in Figure 6.23. The higher the water holdup, the worse the disagreement.

In conclusion, as far as the typical oil-water flow studied in this work is concerned, the homogenous model should be used for predicting the water holdup in the dispersed oil-in-water flow (Figure 6.22) and the correlation of Rodriguez et al. (2009) should be used for prediction the water holdup in the unstable-annular flow (Figure 6.23).

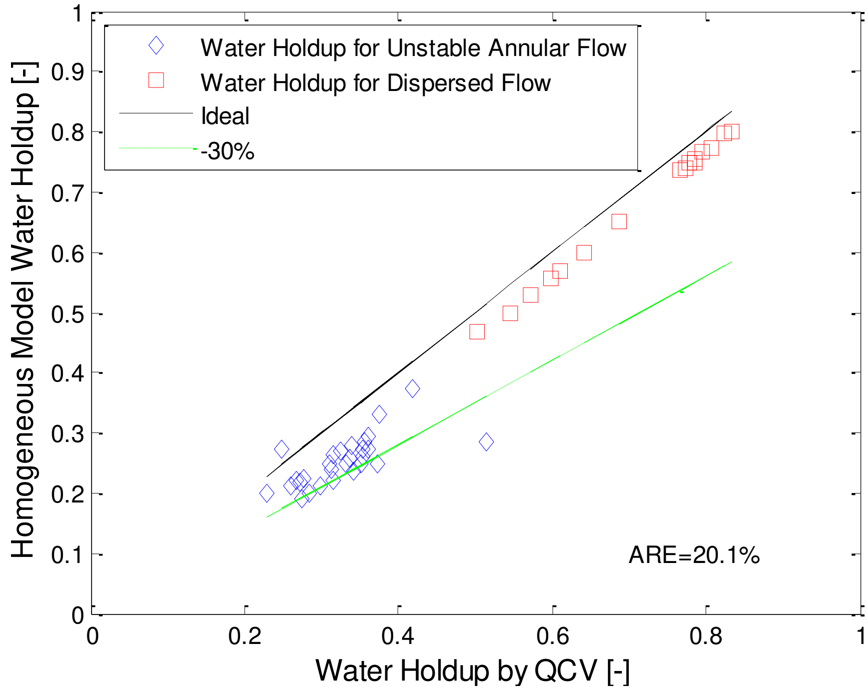

Figure 6.22 – Water holdup according to the Homogeneous Model against the water holdup obtained from QCV.

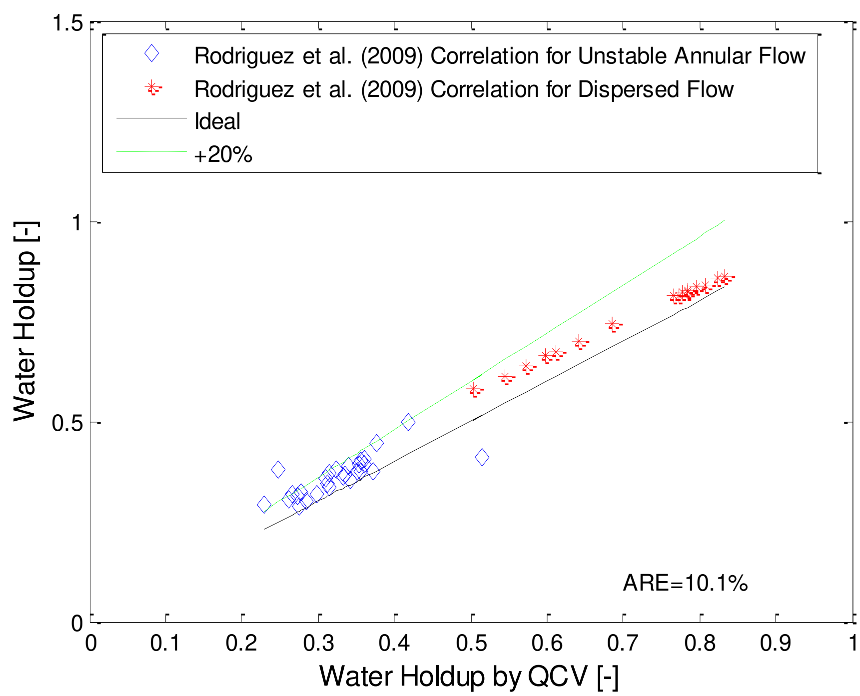

Figure 6.23 – Water holdup according to the correlation proposed by Rodriguez et al. (2009) against the water holdup obtained from QCV.

Comparision with capacitance system data

The data obtained with the capacitance system was used to estimate the oil holdup. It is assumed that the statistically axisymmetric oil core can be treated as a side view of a solid body of revolution and its volume is calculated using the disk method. Figure 6.24 presents a sketch of an ideal axisymmetric core-annular flow.

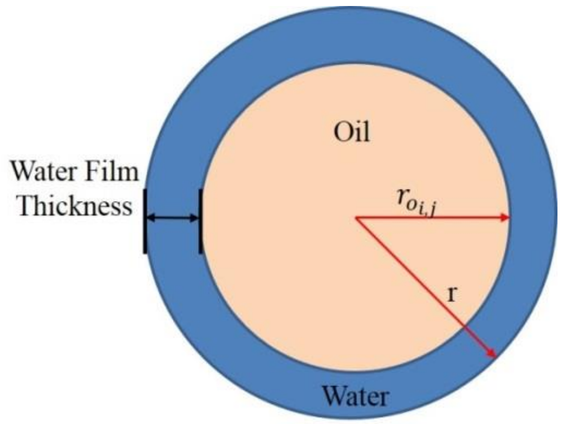

Figure 6.24 – Ideal core-annular flow sketch.

The capacitance system measures the water film thickness in each measurement point (pair Tx-Rx), Figure 6.25. The oil radius ($r_{o_{i,j}}$) in each measure point is estimated as

$$r_{o_{i,j}} = r - \delta_{i,j} \quad (6.21)$$

where *r* is the pipe diameter and $\delta_{i,j}$ is the measured water film thickness in a pair Tx-Rx*(i,j)*. The subscripts *i* and *j* indicate position in the axial direction (Txs direction) and in the perimetral position (Rxs direction).

A polynomial fitting is used to obtain $r_{o_j}(x)$ in the axial direction (flow direction), for each reception line (there are 16 reception lines, i.e. *j* varies between 1 and 16). Thus,

$$r_{o_j}(x) = a_1^* x^4 + a_2^* x^3 + a_3^* x^2 + a_4^* x + a_5^* \quad (6.22)$$

The volume is calculated as

$$Vol_{o_j} = \int_0^L \pi r_{o_j}^2(x)dx \quad (6.23)$$

and finally, the oil holdup calculation is as

$$h_{o_j} = \frac{Vol_{o_j}}{Vol_T} \qquad (6.24)$$

where $Vol_T = \pi r^2 L$ is the pipe volume, L is a defined pipe length and r is the pipe radius.

The average holdup is obtained by

$$\bar{h}_o = \frac{1}{16}\sum_{j=1}^{16} h_{o_j} \qquad (6.25)$$

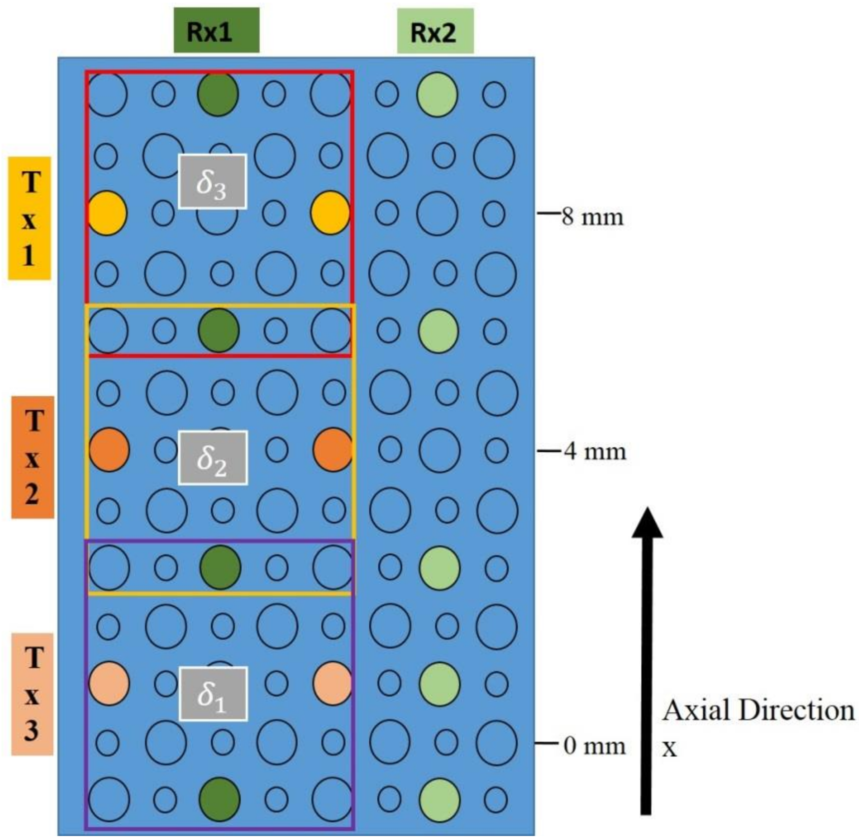

Figure 6.25 – Example of data interpolated to obtain the oil radius.

Comparisons between the oil holdup calculated using the capacitance system data and the oil holdup measure by the quick-closing-valve method are presented in Figure 6.26 and Figure 6.27 for unstable annular flow and oil-in-water dispersed flow, respectively. For unstable-annular flow, the oil holdup calculated from the capacitance system data has a relatively low error (ARE is 15.2%), but the trend indicates a high qualitative error (Figure 6.26). It systematically overestimates the oil holdup measured by the quick-closing-valves method, which is probably because the capacitive system could not detect water volumes trapped in between drops at the pipe core. On the other hand, the error is much higher for dispersed flow (ARE is 61.3%). This result was expected since there is a water-oil mixture in the center of the pipe and not only oil (Figure 6.27). In conclusion, this technique could be a possibility for a stable core-annular flow; perhaps if there is insignificant dispersion of oil droplets. However, the technique is definitely not recommended for the typical dispersed oil-in-water flow studied in this work.

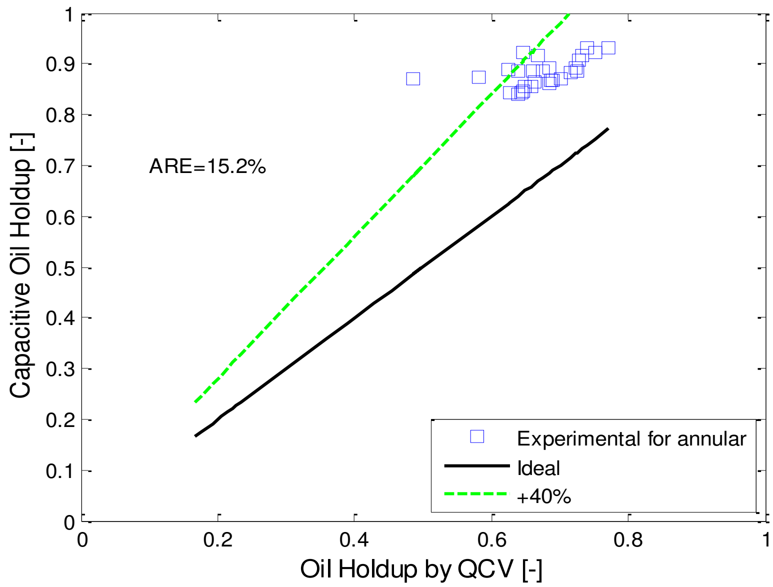

Figure 6.26 – Oil holdup using the capacitance system data against the oil holdup obtained from QCV for unstable annular flow experiments.

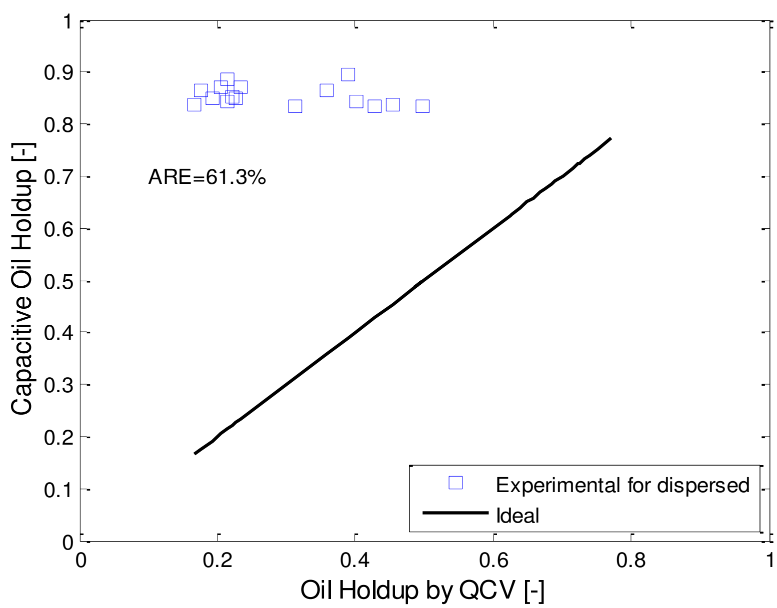

Figure 6.27 – Oil holdup using the capacitance system data against the oil holdup obtained from QCV for dispersed flow experiments.

6.3 Water-Film Topology

The characterization of the water-film topology is presented in this section. A narrow strips near the pipe wall clearly dominated by water were observed in this work and its characteristic average thickness, δ, has been measured. However, the observed water-film region is not a region completely free from oil drops. An oil drop may have been seen near the pipe wall eventually, but it was always repelled towards the dispersed core. It is adopted the pragmatic assumption that there is a water film, with a characteristic space and time-averaged thickness. The characterization includes collecting geometrical and kinematic parameters of an interfacial structure, which separates the wall region, dominated by water, from the core region, dominated by mixture of oil in water.

6.3.1 Preliminary Definitions

Some definitions for waves are used for the interfacial structure description. One can see in Figure 6.28 an artistic illustration of a typical image obtained from the high-speed camera in upward-vertical flow.

- Film thickness (δ) is the distance between the pipe wall and the oil-water interface in a determined point.
- Crest is the highest point of the film thickness.
- Trough is the lowest point of the film thickness.
- Wavelength (λ) is the distance between successive crests or troughs and it is related to the axial size and distance of the oil drops. The average wavelength can be obtained as:

  $$\bar{\lambda}_m = \frac{1}{n_w - 1}\sum_{j=1}^{n_w-1}\lambda_j, \qquad (6.26)$$

  where n_w is the number of crests identified in time and λ_j is the j-th wavelength in the frame (CASTRO et al., 2012).
- Amplitude (A) is the difference between the crest and its neighboring trough and it is related to perimetral size of the oil drops near to the pipe wall. The average amplitude can be calculated from the amplitude relative to the previous through A_{1b} and relative to the posterior through A_{1l} :

$$A_{m11} = \frac{A_{1b} + A_{1l}}{2} \qquad (6.27)$$

- Velocity is the ratio between the distance traveled by a crest between two known points and the correspondent elapsed time (BANNWART, 1998).

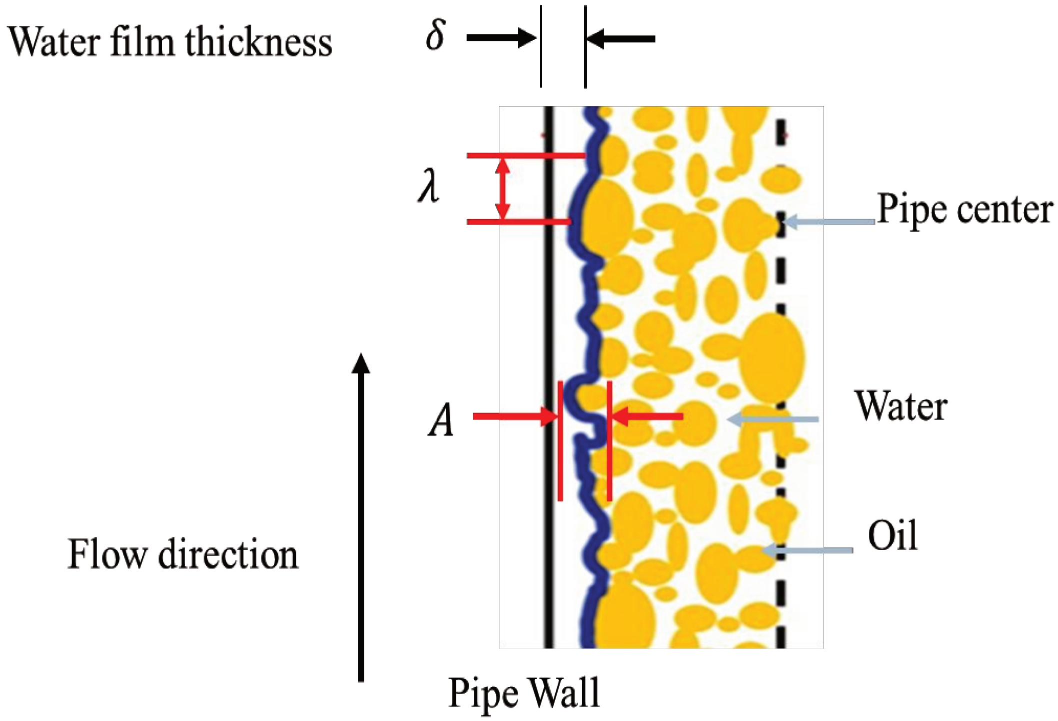

Figure 6.28 – Longitudinal section through of an interfacial structure in upward-vertical flow.

In Figure 6.30 and Figure 6.31, film thickness results of four experiments are presented; capacitive-system data for unstable-annular flow at the left-hand side and for dispersed flow at the right-hand side. Distributions of the water-film thickness are shown. In Figure 6.30a and Figure 6.31a, areas with large changes in film thickness are observed for unstable annular flow, whereas a more uniform water-film-thickness distribution is seen for dispersed flow (Figure 6.30d and Figure 6.31d). Zero-micrometer film thickness is represented by white color and intense blue refers to 2200 µm. It was possible to recognize similar behaviors in experiments with the same flow pattern. Unstable-annular flow can be described by big fluctuations in both the flow direction (axial) and perimeter direction, big interfacial structures and distributions (all the measurement points) with non-uniform regions. On the other hand, oil-in-water dispersed flow less fluctuations are spotted in both the flow direction and perimeter direction, smaller interfacial structures and more uniform water-film-thickness distributions.

The axial water-film thickness distribution over a line of Tx for a constant Rx in a given instant of time (refer also to Figure 6.29, green line) is showed in Figure 6.30b (unstable-annular flow) and e (dispersed flow) and Figure 6.31b (unstable-annular flow) and e (dispersed flow). Higher and more intense fluctuations are observed in the case of unstable-annular flow (Figure 6.30b and Figure 6.31b) than in dispersed flow (Figure 6.30e and Figure 6.31e).

The perimetral water-film distribution over a perimeter Rx for a constant Tx in a given instant of time (refer also to Figure 6.29, red line) is showed in in Figure 6.30c (unstable-annular flow) and f (dispersed flow) and Figure 6.31c (unstable-annular flow) and f (dispersed flow). The film thickness has strong oscillations in unstable-annular flow (Figure 6.30c and Figure 6.31c), slightly stronger than those seen in the axial distribution. The signals are much softer in dispersed flow, and almost no difference can be inferred when comparing the data in the axial or perimetral directions (Figure 6.30f and Figure 6.31f).

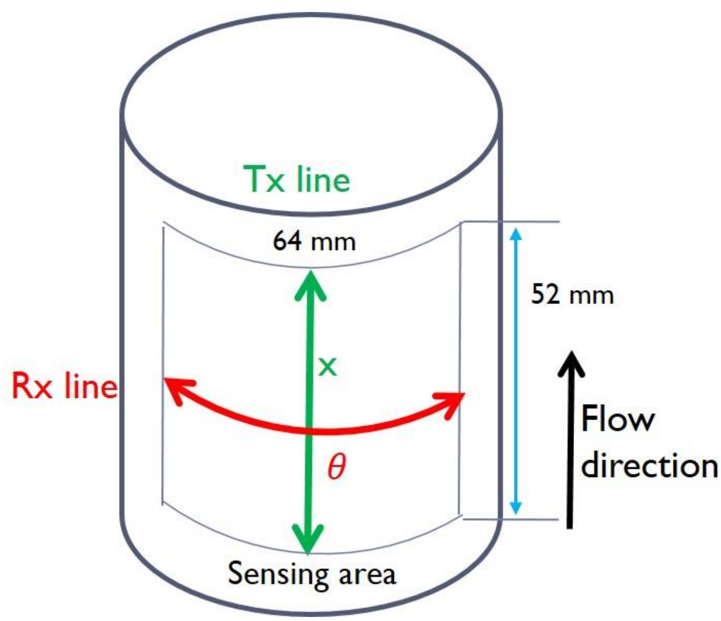

Figure 6.29 – Film thickness for all the Tx and one Rx in green (along the pipe) and film thickness for all the Rx and one Tx in red (pipe perimeter).

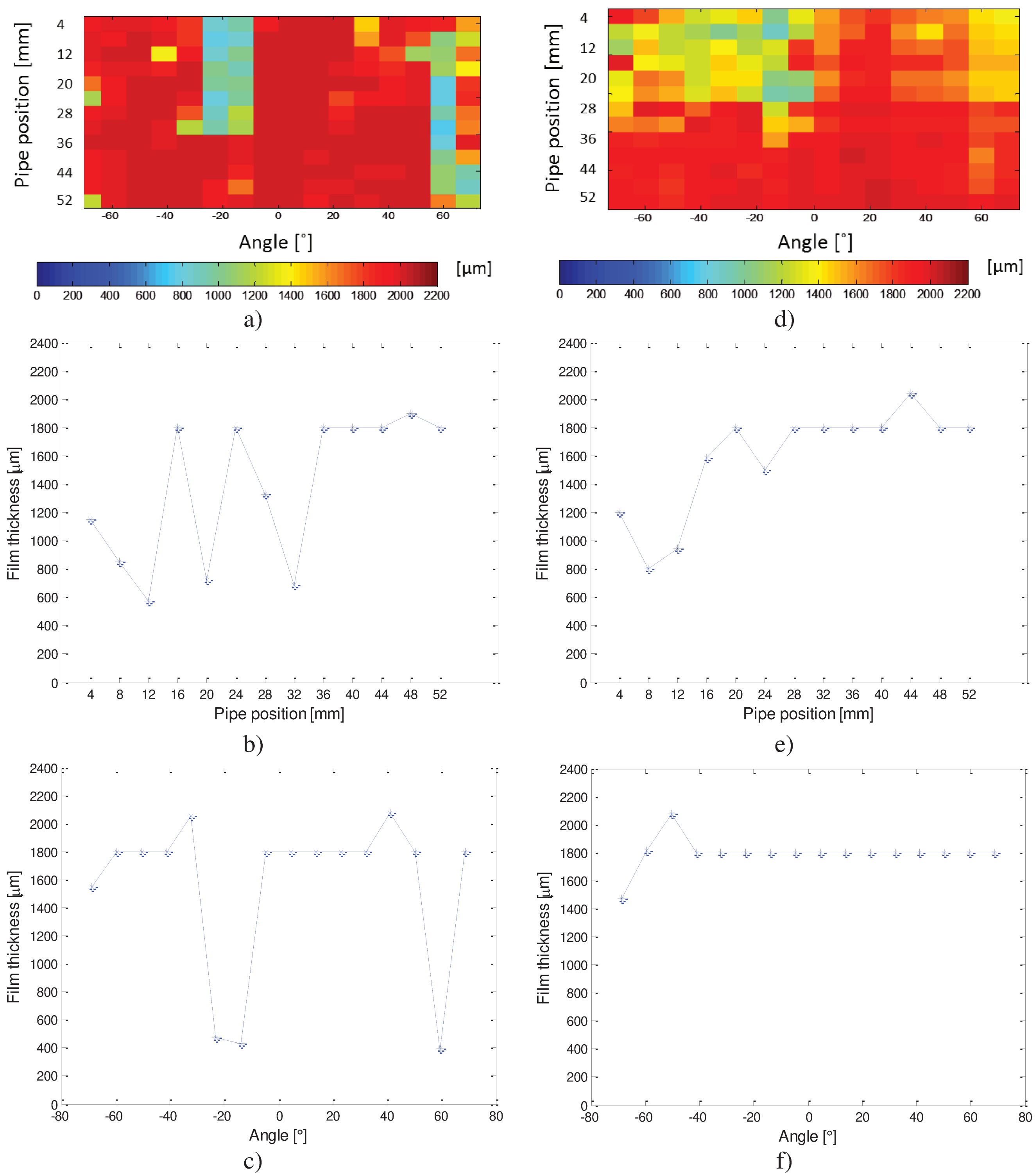

Figure 6.30 – Measurements obtained with the capacitive system for unstable annular flow (left images) at V_{sw} =0.1 m/s and V_{so} =0.3 m/s and dispersed flow (right images) at V_{sw} =1.5 m/s and V_{so} =0.8 m/s. a) and d) Snapshot image; b) and e) film thickness for all the Tx and one Rx (along the pipe); c) and f) film thickness for all the Rx and one Tx (pipe perimeter).

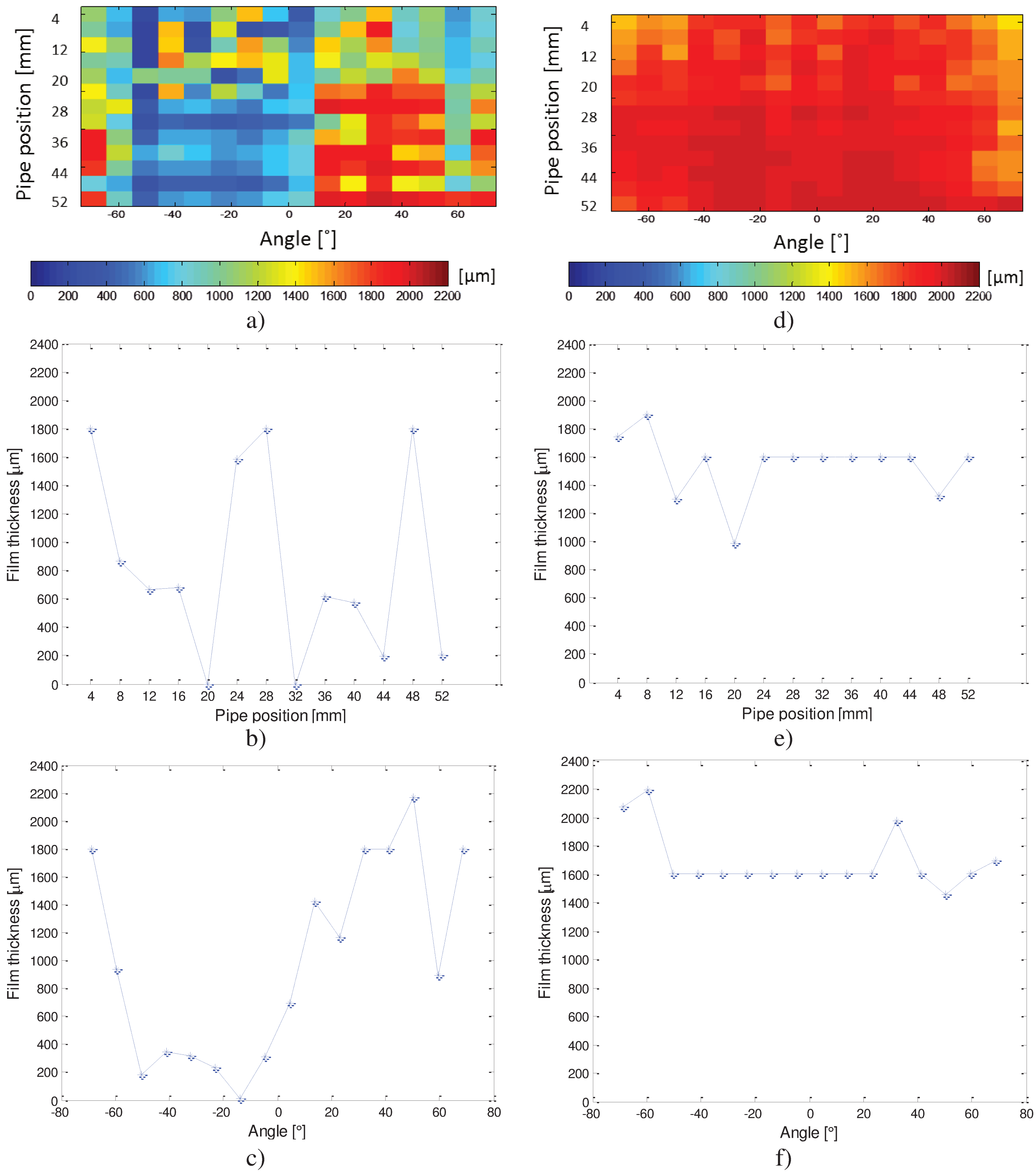

Figure 6.31 – Measurements obtained with the capacitive system for unstable annular flow (left images) at V_{sw} =0.15 m/s and V_{so} =0.4 m/s and dispersed flow (right images) at V_{sw} =1.7 m/s and V_{so} =0.6 m/s. a) and d) Snapshot image; b) and e) film thickness for all the Tx and one Rx (along the pipe); c) and f) film thickness for all the Rx and one Tx (pipe perimeter).

Snapshots taken with the high-speed camera synchronized with data from the capacitive-measurement system are presented in Figure 6.32 and Figure 6.33. In this figure, a film thickness with zero value means oil touching the tube wall. Figure 6.32 and Figure 6.33a correspond to unstable annular flow at two different flow rates and Figure 6.33b and c to dispersed flow. An advantage of the capacitive system is that it delivers 3-D representation of the water-film topology, instead of simple 2-D projections.

There are intense fluctuations in unstable-annular flow along the flow direction (axial) as well as on the perimeter direction (Figure 6.32). Nevertheless, the fluctuations along the flow direction are less intense than over the perimeter direction. An explanation is the shape of the oil drops. They are not spherical, but rather oval and oriented in the flow direction, as mentioned in section 6.2.3.2. The dynamics of the water flow (preponderant shear stress in the flow direction) and interaction between droplets (viscous wake) are responsible for stretching the oil drops in the flow direction. The bigger the drops, the stronger the drop-stretching phenomenon, as interfacial-tension forces, which act to keep the drops spherical, become less important.

The fluctuations in dispersed flow are less intense and similar in both directions (Figure 6.32). The observed uniformity in the water-film-thickness fluctuations can be explained by the existence of more spherical droplets; the smaller the drops, the stronger the interfacial-tension forces that try to keep them spherical. Therefore, a similar distribution of fluctuations is expected, regardless the direction, axial or perimetral.

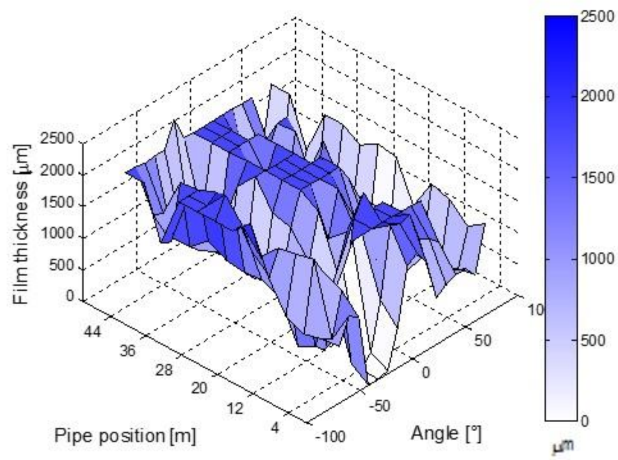

Figure 6.32 - Comparision of high-speed camera images with measured film thickness in 3D for unstable annular flow with V_{sw} =0.1 m/s and V_{so} =0.35 m/s.

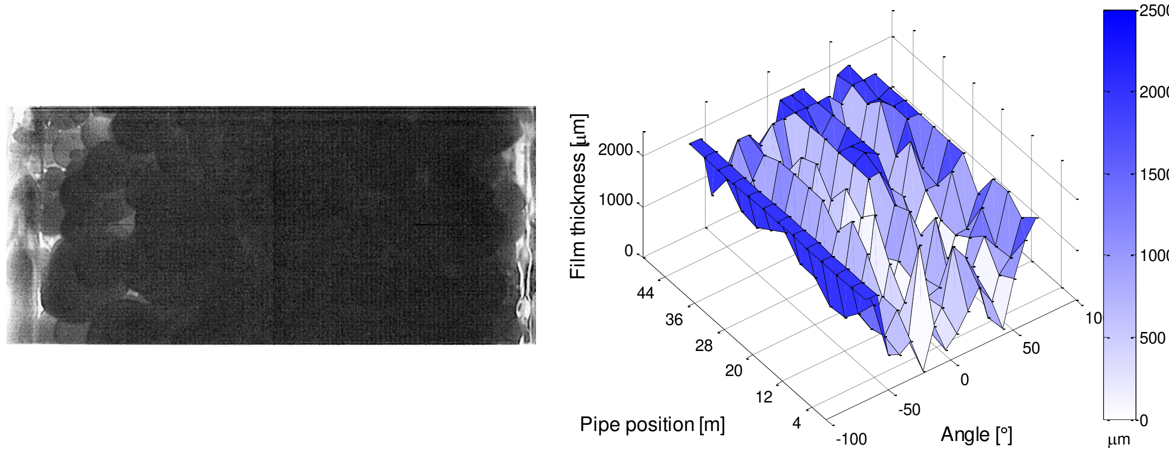

a)

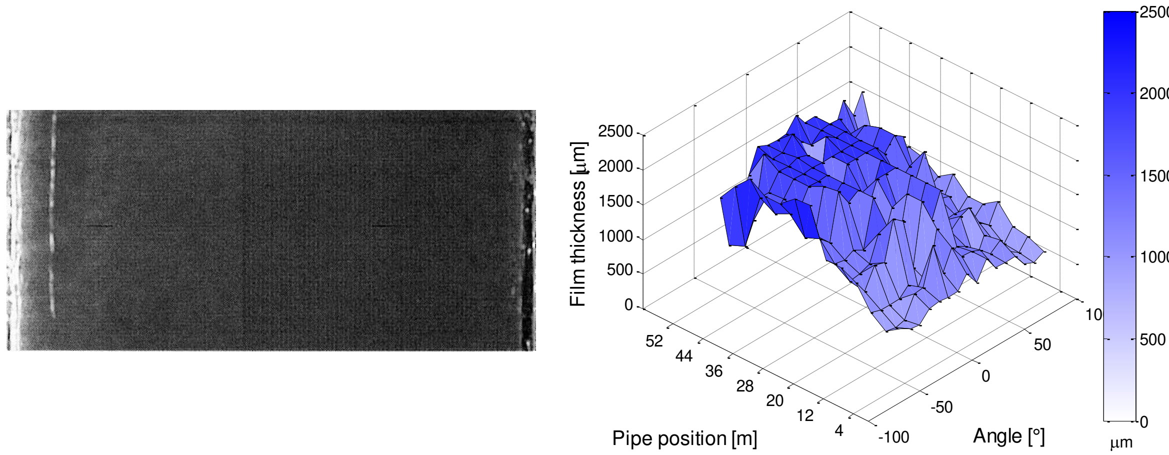

b)

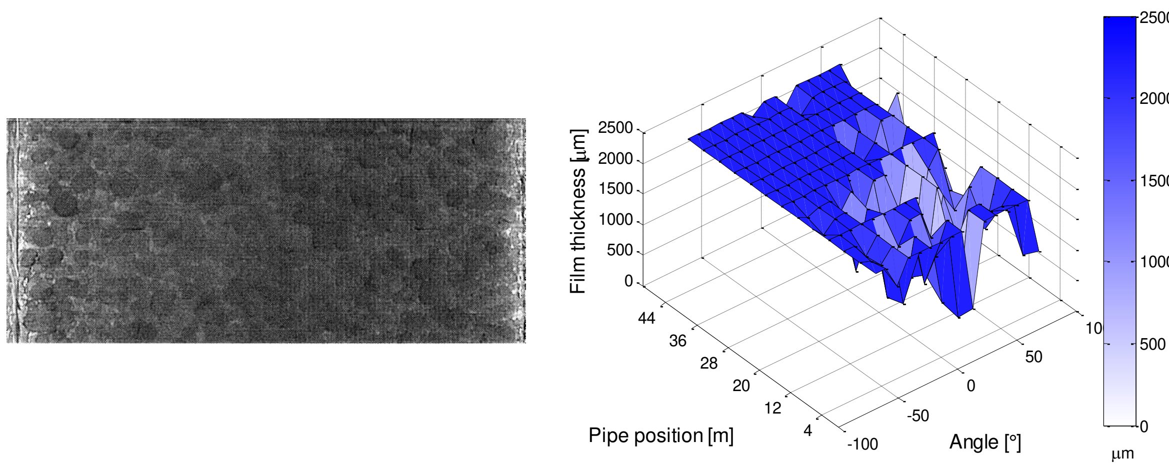

c)

Figure 6.33- Comparision of high-speed camera images with measured film thickness in 3D. a) Unstable annular flow with V_{sw} =0.2 m/s and V_{so} =0.75 m/s; b) dispersed flow with V_{sw} =1.2 m/s and V_{so} =0.8 m/s and c) dispersed flow with V_{sw} =1.3 m/s and V_{so} =0.5 m/s.

6.3.2 Data Treatment

6.3.2.1 Capacitance Measurement System

In this work, each measuring point of the capacitive sensor was studied separately. The amplitudes and velocities were measured in the time domain. The interfacial frequency was determined in the frequency domain. Finally, wavelength was calculated using the velocities and frequencies.

One can see in Figure 6.34 the time signal of a given measuring point during 0.02 (100 samples) for two experiments in unstable-annular flow (left side) and two experiments in dispersed flow (right side). The signals in unstable-annular flow have larger amplitudes (up to 1600 µm), while the dispersed one have smaller amplitudes (400 µm), refer to Table A.2.

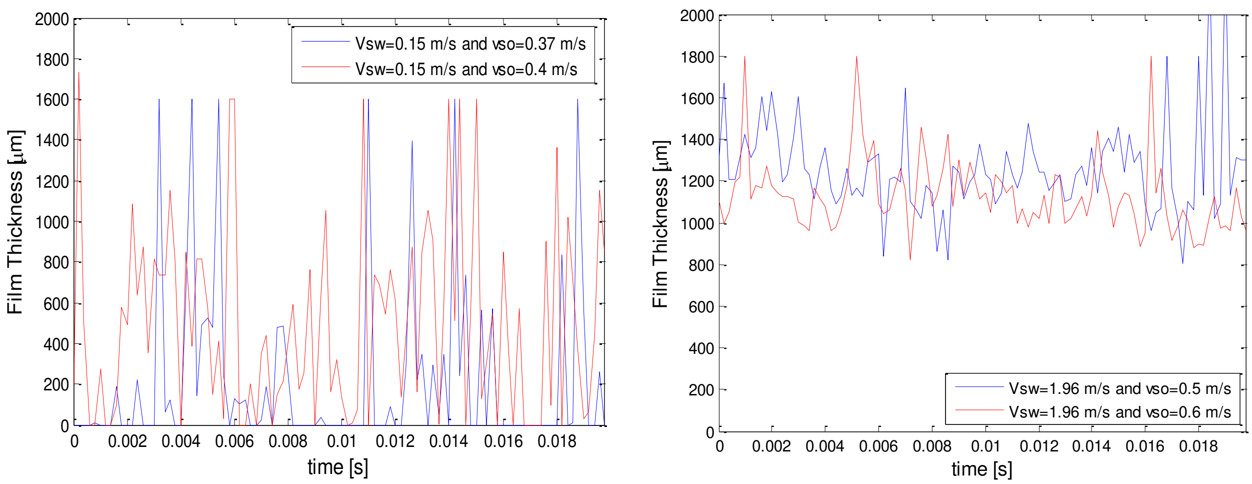

a) b)

Figure 6.34 – Measurments at a given measurig point as a function of time for four expriments. a) Unstable annular flow, in blue V_{sw} =0.15 m/s and V_{so} =0.37 m/s, in red V_{sw} =0.15 m/s and V_{so} =0.4 m/s. b) Dispersed fow, in blue V_{sw} =1.96 m/s and V_{so} =0.5 m/s, in red V_{sw} =1.96 m/s and V_{so} =0.6 m/s.

The velocity was calculated using the technique of cross-correlation. Notice that the velocity data may be, in fact, correlated to the average velocity of the interfacial structures that flow near the pipe wall, which are drops in unstable-annular flow or droplets in dispersed flow.

The cross correlation technique is a popular method to measure velocity in several fields, including in multiphase flows. Usually, two separated sensors are used and they measure an electrical property of the flow, such as its resistance or capacitance (LUCAS & JIN, 2001a;

2001b; TAN & DONG, 2010; ZANGL et al., 2009). Considering two pairs of identical sensors separated by a known distance along a pipe axis, as a disturbance passes through the sensor there is a change in its output signal. The disturbance is carried with the flow from the first sensor to the second one, causing a similar but not identical change in the output signal. The time delay between these changes in the output signal is equal to the time taken by the particle to travel the distance between the sensors. This is inversely proportional to the mean flow velocity.

The cross-correlation is defined as

$$RR_{xy}(\mathrm{d}_e, \tau) = \lim_{T\to\infty} \frac{1}{T} \int_0^T x(\mathrm{t}-\tau) y(\mathrm{t})\, \mathrm{dt}, \qquad (6.28)$$

where $x(t)$ and $y(t)$ are the two sensor signals, and $x(t-\tau)$ is the delayed version of signal $x(t)$. T is the averaging time/sampling period over which the signal is correlated. The delay is calculated as the lag for which the correlation function RR_{xy} is maximized. To calculate the time for the structure to pass between the two sensors, the lag is multiplied by the sampling rate. Thus, velocity of the interfacial structure is

$$V_{i\ \mathrm{Sensor}} = \frac{\text{Electrodes distance}}{\text{Delay}} = \frac{d_e}{\tau} = \frac{4\times10^{-3}}{Lag\,/\,\mathrm{f}_s}, \qquad (6.29)$$

with f_s=5000 frames per second.

Figure 6.35 shows signals obtained at two consecutive measuring points. The green signal is shifted by a time τ=3.4 ms. The velocity is 1.17 m/s.

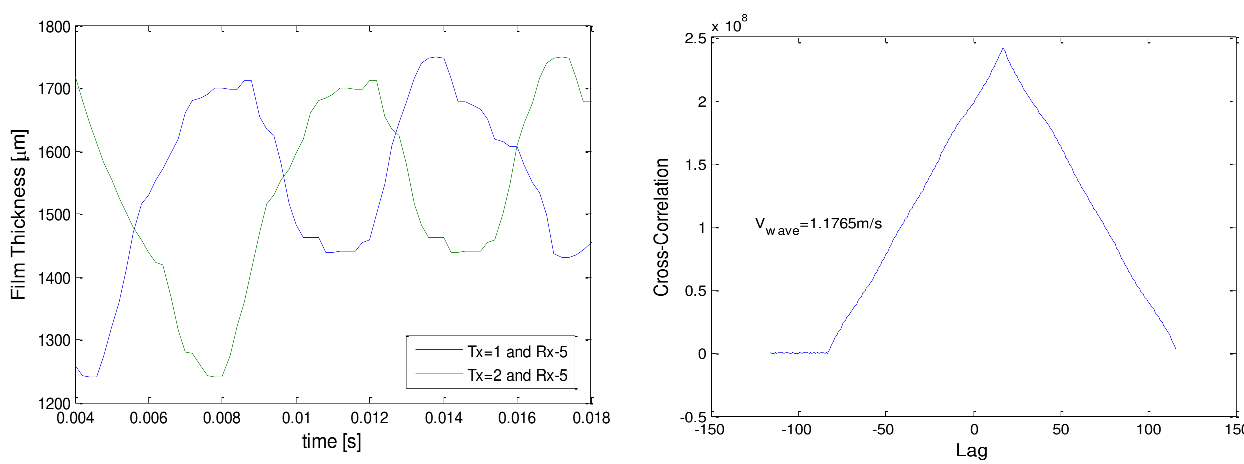

a) b)

Figure 6.35 – Example of time delay and cross-correlation between two consecutive measuring points with separation of 4 mm. a) Signals of pair Tx=1 and Rx=6 and pair Tx=2 and Rx=6; b) Cross-correlation result.

The interfacial structure frequency was obtained using spectral analysis on the time signals. The analysis was made dividing the signals in five parts of 1000 samples (0.2 s) and calculating the Fast Fourier Transform (FFT) to every fragment. The FFT provides a spectrum with a range between 0 Hz to half the sampling rate. The frequency resolution is the sampling frequency divided by the number of points. Our sampling frequency is 5 kHz and according to the Nyquist criteria, the largest frequency contained in the signal must be less than 2.5 kHz to avoid aliasing. The frequency resolution is 5 Hz. Signals were studied using dominant frequency analysis. The dominant frequency is the frequency of the component with highest amplitude. The resulting amplitude spectrum for unstable annular flow and dispersed flow experiments are presented in Figure 6.36; the dominant frequencies are 24 Hz and 160 Hz, respectively. It was expected that the dominant frequency would be higher for dispersed flow. The interfacial structures near the pipe wall are smaller (droplets) and the mixture velocity is significantly higher in dispersed flow.

The dominant frequency and velocity can be used to obtain the average wavelength. One should expect that the wavelength (λ_{Sensor}) is proportional to the droplet size. However, this information is restricted to the region near the pipe wall. Therefore, a method based on this technique to obtain average droplet size would be more suitable for fully dispersed flow, where a uniform distribution of droplets over the cross-sectional area is usually observed. The average wavelength of the signals can be obtained by $\lambda_{\text{Sensor}} = V_{i\,\text{Sensor}}/f_D$, where $V_{i\,\text{Sensor}}$ is the velocity and f_D is the dominant frequency.

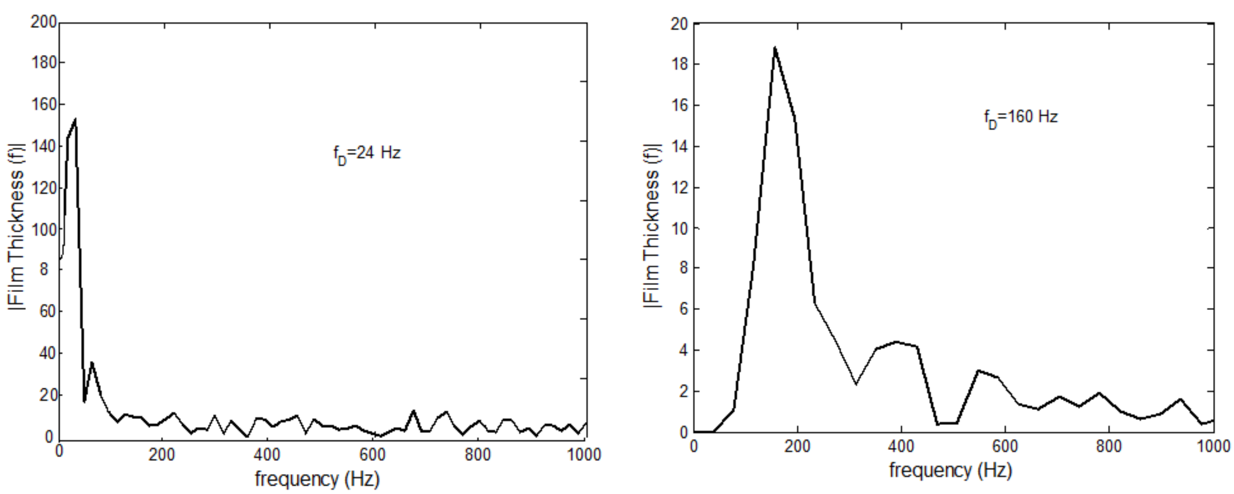

Figure 6.36 – Amplitude spectrum for two experiments. a) Unstable annular flow, V_{sw} =0.1 m/s and V_{so} =0.35 m/s and b) dispersed flow, V_{sw} =1.2 m/s and V_{so} =0.8 m/s.

6.3.2.2 High Speed Camera Images

The oil drops velocity and the distance between them (called wavelength in the section 6.3.2.1) near to the pipe wall were measured manually from four high speed camera images for each experiment. The velocity ($V_{i\text{Images}}$) was calculated by following oil drops in consecutive frames, the distance traveled by each drop of oil was calculated using the corresponding pixel scale factor, section 5.2.3, thus

$$V_{i\text{Images}} = \frac{\text{Traveled distance by a oil drop [m]}}{200\ \mu\text{s}}. \qquad (6.30)$$

The distance between two oil drops (λ_{Images}), Figure 6.28, was calculated in the same frame by counting the number of pixels among the highest point of two consecutive drops and multiplying it by the corresponding pixel scale factor.

6.4 Water-Film Topology Results

A comparison of the velocity measured by the sensor with the in-situ oil and water velocities as a function of the mixture velocity is shown in Figure 6.37 and Figure 6.38. If the interfacial structure was a kinematic wave, the velocity should have been in between the in-situ velocities of oil and water (WALLIS, 1969). However, the velocity values were always below those of oil and water.

The reader can see that there is a good agreement between the in-situ water velocity and the measured interfacial structure velocity below V_m = 0.8 m/s (Figure 6.37). For velocities higher than 0.8 m/s, it is possible to see that there is a significant disagreement (Figure 6.37 and Figure 6.38). Instead of a wave that would move in the flow direction, the sensor is actually measuring the velocity of the drops that may develop quite complex trajectories towards and away from the pipe wall, deform and rotate. In addition, the flow behavior near of the pipe wall is not equal to that at the core. For example, in unstable-annular flow the oil drops coalesce creating a continuous structure in the core of the pipe, while near to the pipe wall there are dispersed drops.

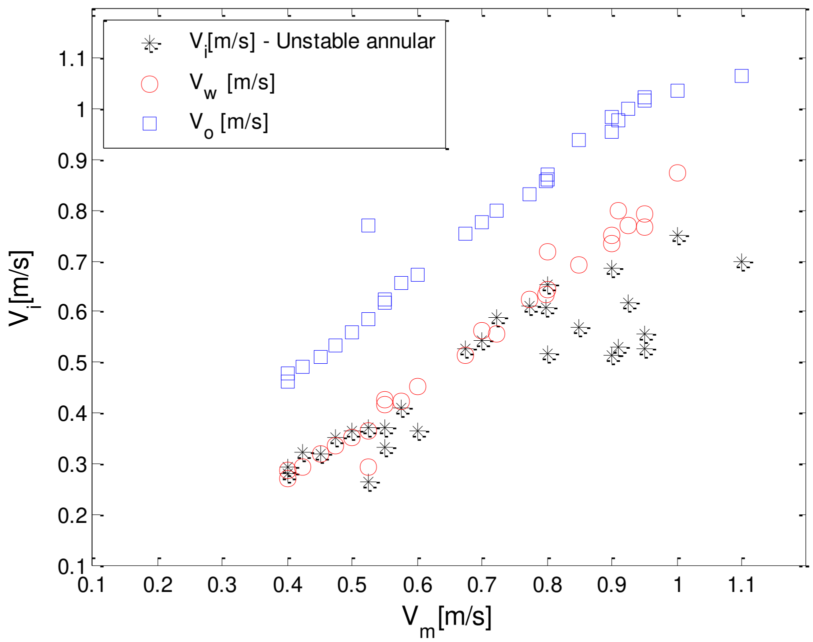

Figure 6.37 – Measured velocity compared with in-situ water and oil velocities and mixture velocity for unstable annular flow.

The interfacial velocity is clearly lower than those of water and oil in dispersed flow (Figure 6.38). As far as the classic parabolic velocity profile is concerned, the local water velocity near the pipe wall is expected to be lower than the average velocity. Therefore, the droplet velocity near the wall should present a velocity significantly lower than the average water velocity (V_w), which is confirmed by the experiments (Figure 6.38).

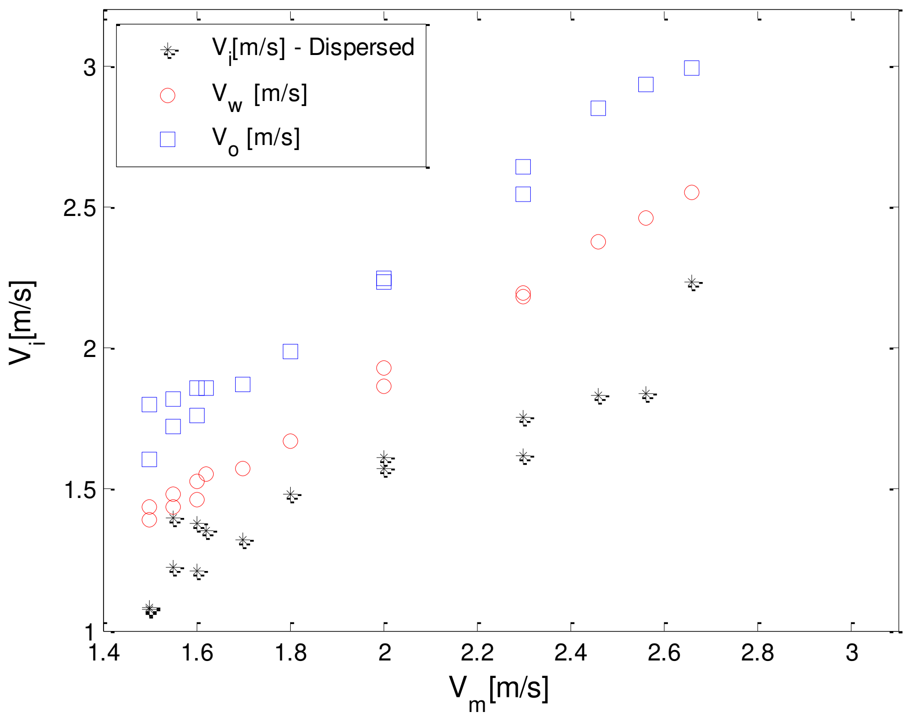

Figure 6.38 – Measured velocity compared with in-situ water and oil velocities and mixture velocity for dispersed flow.

The velocity was also compared with the velocity obtained by the images, Figure 6.39 and Figure 6.40. For unstable annular flow, the agreement between the data is regular, with an ARE=31.4%. It is possible to see a big dispersion, Figure 6.39. For dispersed flow (Figure 6.40), the ARE is 33.2%. The velocity obtained by the measurement system, for mixture velocities lower than 2 m/s, has a good agreement. For higher values, the dispersion is higher but the trend is the same.

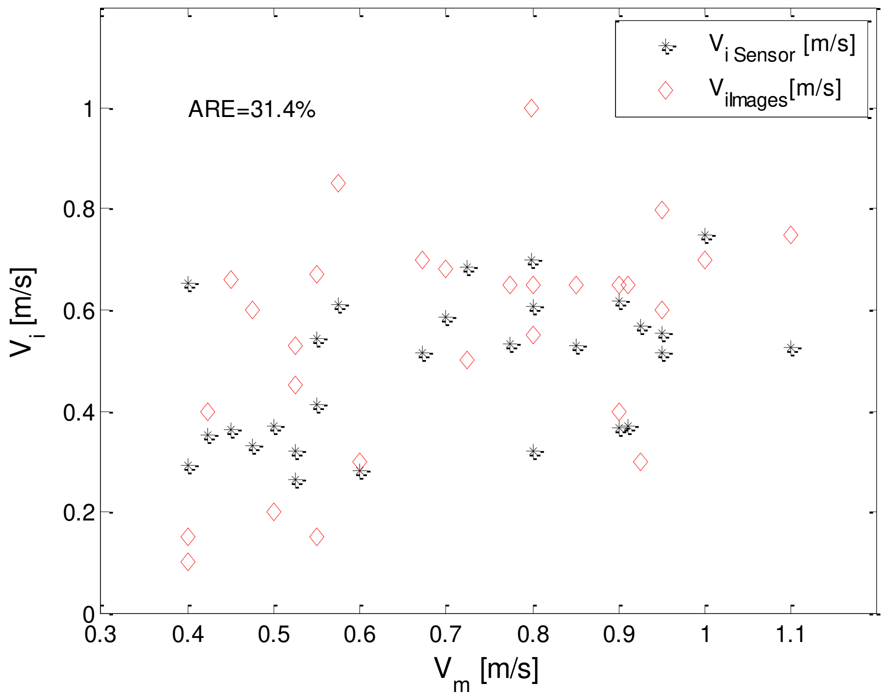

Figure 6.39 – Estimated velocity by system measurements and by images against mixture velocity for unstable annular flow.

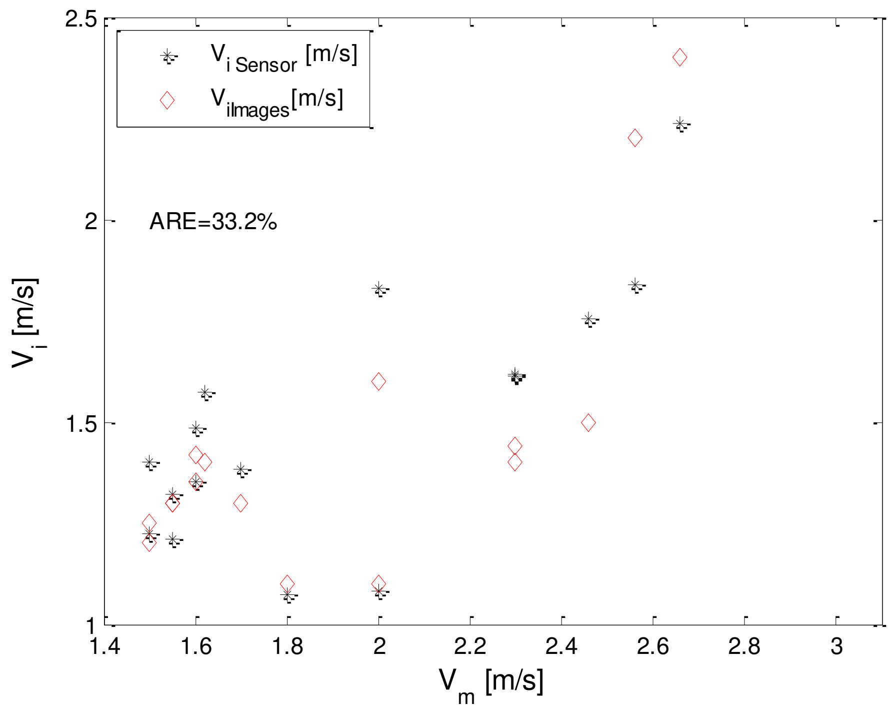

Figure 6.40 – Estimated velocity by system measurements and by images against mixture velocity for dispersed flow.

Another comparison is between the wavelengths measured with the sensor and those extracted from the recorded images for unstable annular flow, Figure 6.41. The error was ARE = 36.6%. The wavelength is between 4 mm and 13mm, according to the image data, and between 4 mm and 16mm, according to the capacitance system. This is in qualitative accordance with the relatively big drops observed in unstable-annular flow.

For the dispersed flows, Figure 6.42, the agreement is better, the error is ARE = 18.3%. Thus, the capacitance system technique was able to predict the wavelength. The measured wavelength is between 1 mm and 5 mm. As discussed before, the wavelength data may be related to the size of the oil droplets, as it represents the average distance between droplets. Rodriguez (2014) determined theoretically the average diameter of droplets for similar experimental conditions. The results of Rodriguez (2014) show a good correspondence with the present wavelength data (Figure 6.42). For instance, the diameter decreases with increasing the mixture velocity and the diameters are between 1.6 mm and 3.3 mm for V_m = 2.5 m/s and V_m =1.3 m/s, respectively.

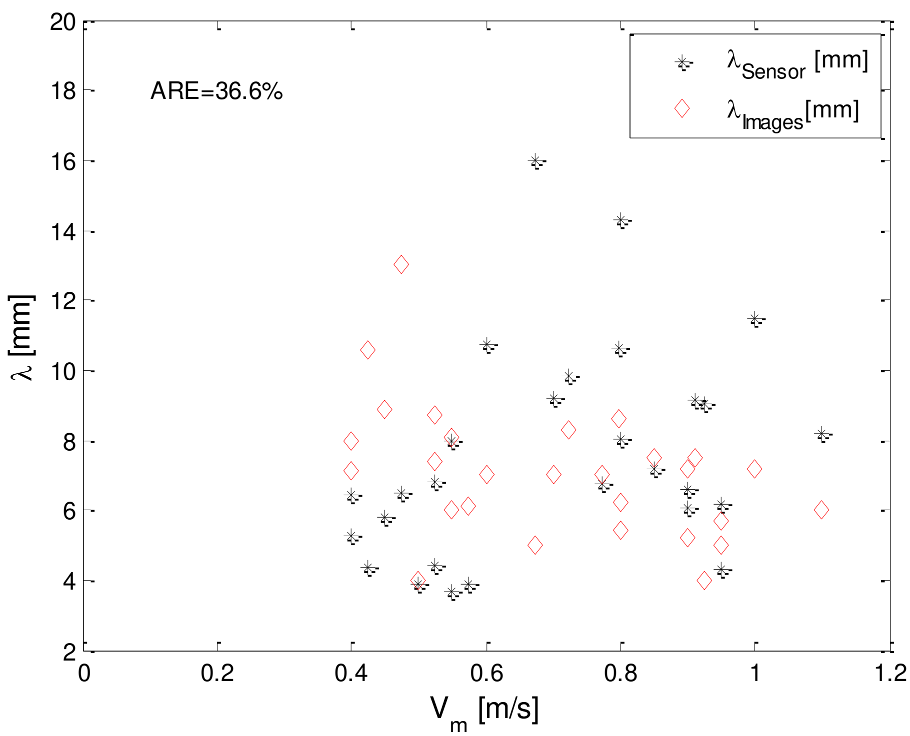

Figure 6.41 – Estimated wavelength by system measurements and by images against mixture velocity for unstable annular flow.

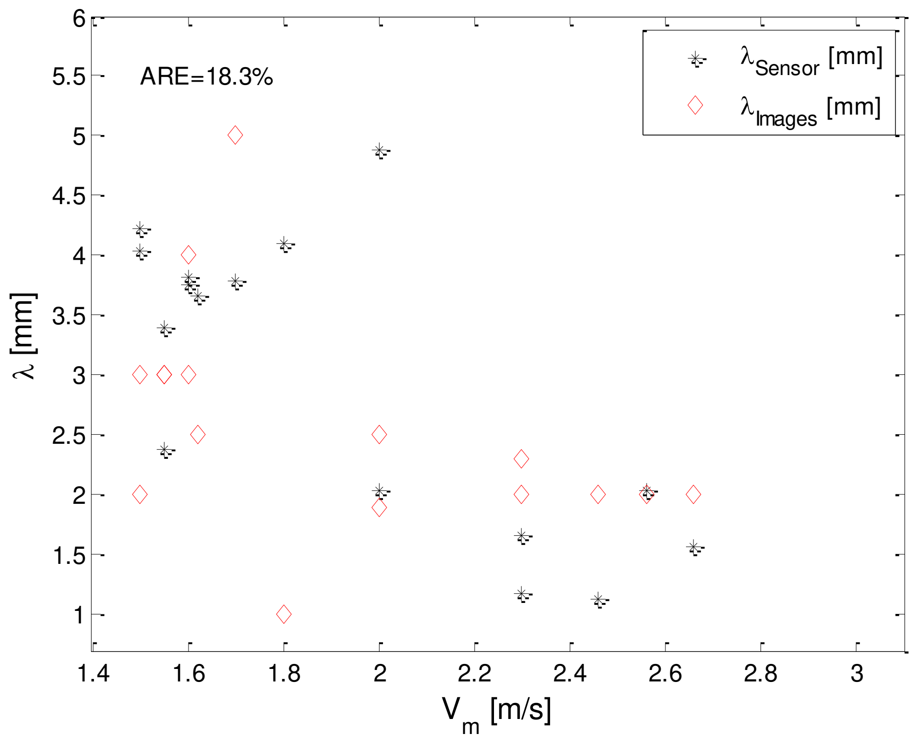

Figure 6.42 – Estimated wavelength by system measurements and by images against mixture velocity for dispersed flow.

The velocity was also compared with some experimental correlations developed for core-annular flow found in the literature, Table 6.3. These correlations were based on measurements made by high-speed camera images with the constraint of having only information about the focused plane or planes (2-D information only).The comparison is shown in Figure 6.43for unstable-annular flow. It is possible to observe that the velocities obtained from the sensor are closer to the model proposed by Rodriguez & Bannwart (2006). The correlation of Bannwart (1998) overestimates the experimental data.

Table 6.3 – Empirical correlations for oil-water interfacial wave velocity in core-annular flow.

Correlation	Flow pattern and Orientation	Reference
$V_{wave} = \dfrac{V_{so} + s_o V_{sw} + kV_{ref} h_o (1-h_o)^{n-1}[2(1-\mathrm{h}_o) - n\,\mathrm{h}_o]}{1+(s_o - 1)\,\mathrm{h}_o}$ where k = 0.0223, n=2, s_o=2 and $V_{ref} = \dfrac{(\rho_o - \rho_w)\,gD^2}{16\mu_w}$	Core-annular flow Horizontal and vertical	Bannwart (1998)
$V_{wave} = \dfrac{V_{so} + s_o V_{sw} + kV_{ref} h_o^{q-1} (1-h_o)^{m-1}[q - (\mathrm{m}+q)\,\mathrm{h}_o]}{1+(s_o - 1)\,\mathrm{h}_o}$ where k = 0.0122 , s_o=1,17 and $V_{ref} = 0.079_i^{\frac{1}{-1.75}} \sqrt{gD} \left(\dfrac{\Delta\rho}{\rho_w}\right)^{\frac{1}{1.75_i}} \left(\dfrac{\rho_w \sqrt{gD} D}{\mu_w}\right)^{\frac{0.25}{1.75}}$	Core-annular flow Vertical pipe	Rodriguez & Bannwart (2006)

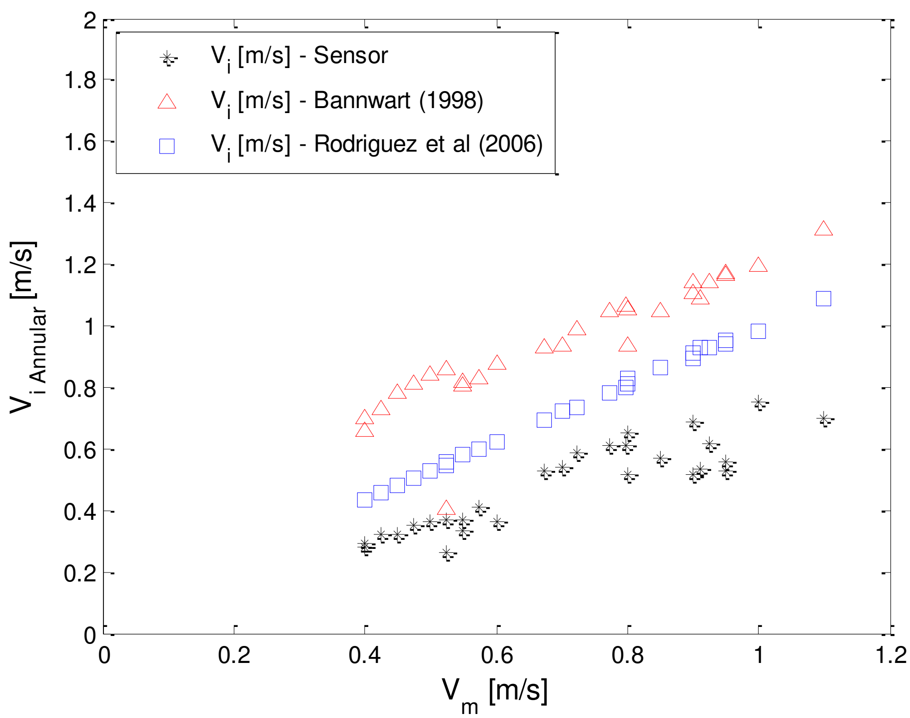

Figure 6.43 – Comparison between measured velocity by measuring system and literature correlations for unstable annular flow.

The average relative errors (ARE) for all different comparisons shown above (Figure 6.18, Figure 6.19 and Figure 6.43) are shown in Table 6.4. The interfacial structure velocity obtained in this study has a relatively good agreement with the predictions of the correlation of Rodriguez &

Bannwart (2006) for interfacial wave in unstable-annular flow. That correlation was obtained for a core-annular flow with interfacial waves, dispersed drops and a turbulent water flow. The collected velocity actually describes the average velocity of drops flowing near the pipe wall. A possible explanation for the agreement is that the unstable-annular flow observed in this work possesses some dynamic similitude with the core-annular flow studied by Rodriguez & Bannwart (2006). Finally, the wavelength obtained by the sensor has a relatively good agreement with that obtained via image analysis, especially for dispersed flow, but the latter systematically overestimates the former.

Table 6.4 – Average relative error for wavelength, wavelength/amplitude and velocity

Flow Pattern	ARE Wavelength Sensor-Images (%)	ARE Velocity Sensor-Images (%)	ARE Velocity Sensor-Bannwart (1998) Correlation (%)	ARE Velocity Sensor- Rodriguez & Bannwart (2009) Correlation (%)
Unstable Annular	36.3	31.4	48	33
Dispersed	18.3	33.2	-	-

Empirical correlations between the velocity obtained by the capacitance-measurement system and Froude number ($Fr = Vm/\sqrt{gD}$) are shown in Figure 6.44 and Figure 6.45. Table 6.5 presents the average relative errors and coefficient of determination (R^2) of the correlations of Figure 6.44 and Figure 6.45 for unstable-annular flow and dispersed flow, respectively. The correlations are useful for predicting the velocity of drops or droplets near the pipe wall. In fully dispersed flow (Figure 6.45), the correlation could be extrapolated to estimate the average velocity of droplets, since a nearly uniform cross-sectional droplet distribution is expected in this type of two-phase flow.

Table 6.5 – Correlations for interfacial-structure velocity in unstable annular and dispersed flow

Flow Pattern	Correlation	R^2	ARE (%)
Unstable Annular	$V_i = -0.23Fr^2 + 0.91Fr - 0.17$	0.81	19.8
Dispersed	$V_i = 0.032Fr^2 + 0.3Fr + 0.39$	0.88	16.7

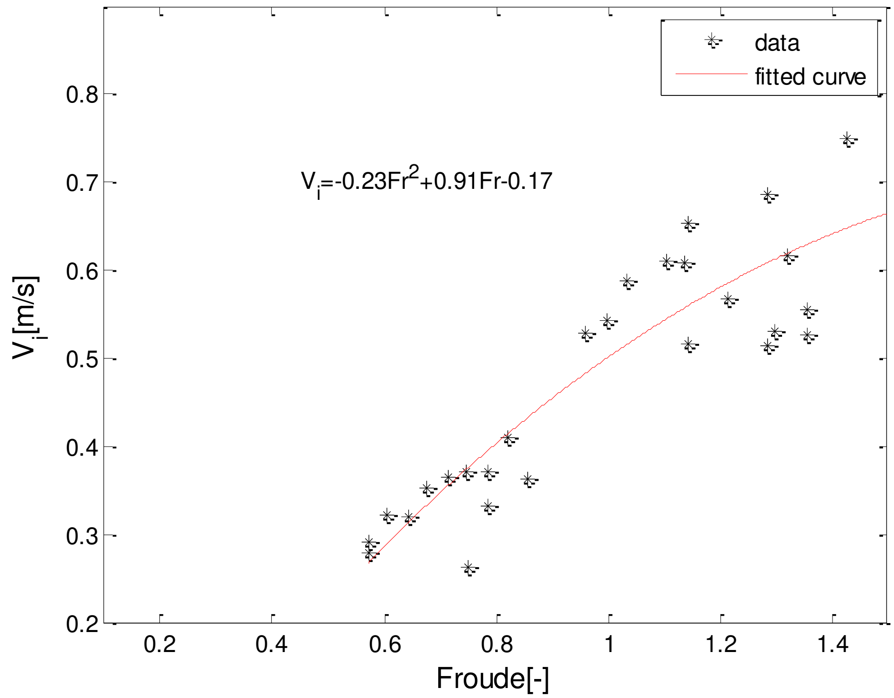

Figure 6.44 – Correlation between measured velocity by the capacitance measurement system and the Froude number for unstable annular flow.

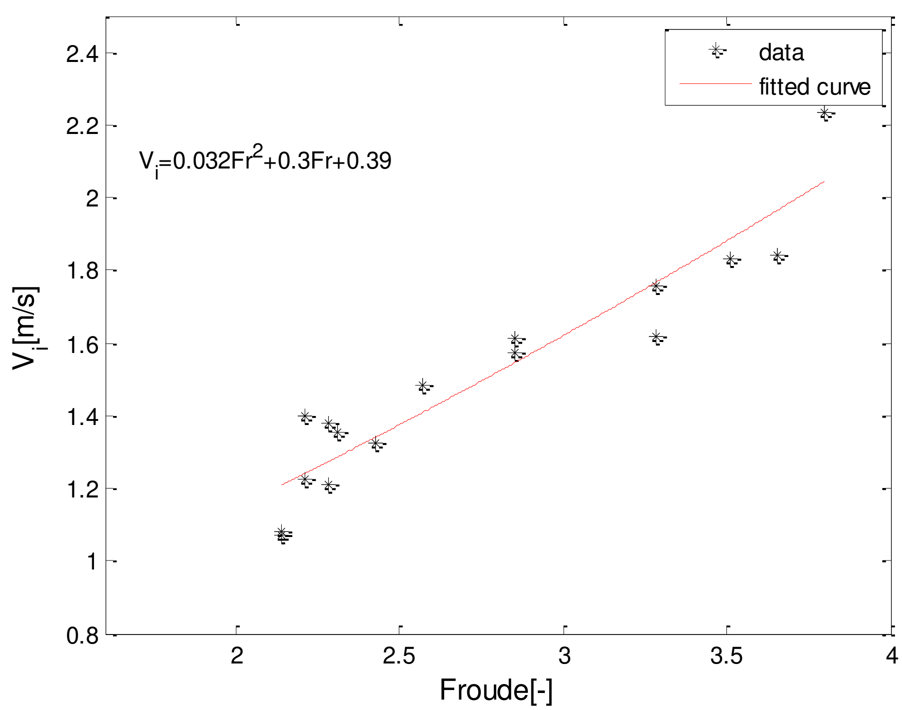

Figure 6.45 – Correlation between measured velocity by the capacitance measurement system and the Froude number for dispersed flow

7 FINAL REMARKS

The conclusions and the recommendations for future works are presented.

7.1 Conclusions

According to the literature review, it is necessary to obtain more experimental data and understanding to explain some phenomena and characteristics of unstable-annular and dispersed oil-water flows. There is only few water-film thickness measurement methods specifically developed for oil-water flow; it is shown that there is still need for further developments in this field.

The methods based on conductive or capacitive measurements and planar sensor are promising solutions to measure water film thickness in oil-water flows. They are more appropriate for oil-water flows because this system is able to measure the water film thickness in spite of oil sticking to the sensor surface.

Image-analysis technique

An image-based methodology has been developed and applied for studying the near-wall flow in order to detect the presence and measure the thickness of a water film in oil-water flow in pipes.

A combined method is proposed for image processing of the typical two-phase flow under study in this work, which is based on the systematic combination of different methods for pre-processing and segmentation of the images. The pre-processing comprises wavelet denoising, Unsharp filtering and contrast enhancement. The proposed methodology for segmentation is a combination of the following methods: wavelet decomposition, fuzzy partition and Tsallis entropy based thresholding, with three thresholds conversion to binary using the histogram, and morphological opening. The combined method performed significantly better when compared to the results obtained with traditional techniques applied individually.

Planar capacitive measurement system

A non-invasive and non-intrusive water film thickness measurement system based on capacitance measurements for high-viscosity-oil-in-water flow was presented. The system was used to study thin water films in unstable-annular flow and oil-in-water dispersed flow in a 12 m long vertical glass pipe, with 50.8 mm of inner diameter. The experiments were carried out at different water and oil superficial velocities (0.1 to 2.0 m/s and 0.3 to 0.8 m/s, respectively). These experimental points were chosen such that the water film thickness could be measured with the capacitive system.

It was verified that the expected water film thickness would be between 400 micrometers and 2000 micrometers, after preliminary experiments using high-speed camera. A planar sensor with spatial resolution of 4 x 4 mm2 was chosen for the measurement after the analysis of the numerical simulations. The effective measuring area for the sensor with 4 x 4 mm^2 spatial resolution is of 64 mm by 52 mm. The temporal resolution in all the experiments was 5000 frames per second.

Water-film thickness

The water film thickness ranged from 900 µm to 2100 µm for the unstable-annular flow pattern and from 1300 µm to 2200 µm for dispersed flow, respectively. The average film thickness obtained by the capacitance system was compared with the one obtained by the image-based technique. It was found a relatively good agreement between the two techniques, the average relative error for unstable-annular flow was 21.8% and 3.6% for dispersed flow. The value estimated by the images was always higher than the one measured with the capacitance system. The explanations are: (1) the capacitive measurement system is able to record tridimensional fluctuations, but the image-based technique only record 2-D information, (2) distortions related to problems about keeping the focus of the camera on the diametrical-vertical plane and 3) image segmentation errors.

Holdup

The measured water holdup using QCV was compared with predictions of the homogeneous model and a correlation for core-annular flow. It was found that the homogenous model should be used for predicting the water holdup in dispersed oil-in-water flow and the correlation of Rodriguez et al. (2009) should be used for predicting the water holdup in unstable-annular flow.

The measured oil holdup using QCV was also compared with the results of a proposed methodology using the capacitance system data. The approximation considers that the oil is flowing in the center of the pipe surrounded by a water film. This technique could be a possibility for a stable core-annular flow; perhaps if there is insignificant dispersion of oil droplets. However, the technique is definitely not recommended for the typical dispersed oil-in-water flow studied in this work.

Water-film topology

The mean film thickness for all the measurement points, the instantaneous film thickness in an axial line and the instantaneous film thickness a perimetral line were studied. Unstable-annular flow can be described by big fluctuations in both the flow direction (axial) and perimeter direction, big interfacial structures and non-uniform distributions (all the measurement points). On the other hand, in oil-in-water dispersed flow fewer fluctuations were spotted in both the flow direction and perimeter direction, smaller interfacial structures and more uniform water-film-thickness distributions.

There are intense fluctuations in unstable-annular flow along the flow direction (axial) as well as on the perimeter direction. Nevertheless, the fluctuations along the flow direction are less intense than over the perimeter direction. An explanation is the shape of the oil drops. They are not spherical, but rather oval and oriented in the flow direction. The dynamics of the water flow and interaction between droplets are responsible for stretching the oil drops in the flow direction.

The fluctuations in dispersed flow are less intense and similar in both directions. The observed uniformity in the water-film-thickness fluctuations can be explained by the existence of more spherical droplets. Therefore, a similar distribution of fluctuations is expected, regardless the direction, axial or perimetral.

The film-thickness time-trace data recorded by the each pair Transmitter-Receiver in the planar sensor were used to examine average characteristics of the film. The interfacial structure kinematic and geometrical characteristics measured with the capacitance system were compared with those estimated using the high-speed camera images.

Interfacial Structure Velocity

The velocity was compared with the in-situ oil and water velocities to establish if the interfacial structure was a kinematic wave. The velocity was lower than both, hence it was concluded the interfacial structure was not a kinematic wave.

The velocity was compared with the velocity obtained by the images. In both flow patterns studied, the agreement between the data was relatively good.

Wavelenght

Wavelength can be related to the droplet size and the distance between drops. However, this information is restricted to the region near the pipe wall. Therefore, a method based on this technique to obtain average droplet size would be more suitable for fully dispersed flow, where a uniform distribution of droplets over the cross-sectional area is usually observed.

The capacitance system technique was applied to measure the wavelength and compared with the results of the image-based technique with an average relative error of 36.6% for unstable-annular flow. For the dispersed flows, the wavelength is related to the distance between bubbles and the average relative error was 18.3%. There is an intrinsic error in the 2-D images-based technique due to the big number of oil drops at the interface, i.e., there were too many oil drops overlapping on another.

The wavelength results were compared with theoretical droplet-diameter data from the literature, showing a good agreement with the estimated wavelength.

Empirical Correlations

The interfacial structure characteristics measured with the capacitance system were compared with correlations found in the literature. Velocity was compared with two correlations based on core-annular flow data. For unstable-annular flow, the best agreement was observed with the Rodriguez & Bannwart (2006) correlations. That correlation was obtained for a core-annular flow with interfacial waves, dispersed drops and a turbulent water flow. The collected velocity actually describes the average velocity of drops flowing near the pipe wall. A possible explanation for the agreement is that the unstable-annular flow observed in this work possesses some dynamic similitude with the core-annular flow studied by Rodriguez & Bannwart (2006).

Empirical correlations between velocity and Froude number have been developed based on the capacitance-system data for the typical oil-water flow studied in this work. For dispersed flow, the correlation had a good agreement with the data. The average relative error was of 16.7%. For unstable-annular flow, the error was 19.8%.

7.2 Recommendations

Based on the present research, the following recommendations are proposed:

1. Investigating the influence of the oil viscosity on the water-film thickness and the frictional pressure drop.
2. Studying the effect of other flow parameters, including pipe material, diameter and roughness in the water-film thickness.
3. Testing other wave-analysis methods to improve the frequency estimation, as wavelet decomposition or Gabor decomposition.
4. Comparing the results with other measurement techniques to get more information about the studied characteristics and to explain better the difference between results provided by the image-analysis technique and the capacitance-measurement system. For instance, estimating wavelength using Wire-Mesh sensing and wave velocity using Particle Image Velocimetry (PIV).
5. Simulating the annular and dispersed oil-water flows using a finite elements software to predict the interfacial wave and compare with the experimental data.
6. Applying the obtained experimental data to improve empirical or theoretical models for holdup and pressure drop prediction.

REFERENCES

ADDLESEE, A. J.; CORNWELL, K. Liquid film thickness above a bubble rising under an inclined plate. Trans IChemE, v. 75, n. October, p. 663–667, 1997.

AGILENT. Agilent Technologies Impedance Measurement Handbook December 2003.

ALEKSEENKO, S. et al. Two-wave structure of liquid film and wave interrelation in annular gas-liquid flow with and without entrainment. Physics of Fluids, v. 21, n. 6, p. 061701, 2009a.

ALEKSEENKO, S. V. et al. Primary instabilities of liquid film flow sheared by turbulent gas stream. International Journal of Multiphase Flow, v. 35, n. 7, p. 617–627, jul. 2009b.

ALEKSEENKO, S. V et al. Secondary instability of waves in annular two-phase flow with and without entrainment. Journal of Physics: Conference Series, v. 216, p. 012006, mar. 2010.

ALEKSEENKO, S. V. et al. Experimental Study of the Linear Stability of a Falling Liquid Film in the Presence of a Turbulent Gas Stream. Fluid Dynamics, v. 39, n. 4, p. 612–620, jul. 2004.

ALEKSEENKO, S. V. et al. Investigation of Waves Interaction in Annular Gas–Liquid Flow Using High-Speed Fluorescent Visualization Technique. Microgravity Science and Technology, v. 20, n. 3-4, p. 271–275, jun. 2008.

ALEKSEENKO, S. V. et al. Analysis of spatial and temporal evolution of disturbance waves and ripples in annular gas–liquid flow. International Journal of Multiphase Flow, v. 67, p. 122–134, dez. 2014.

AL-WAHAIBI, T.; ANGELI, P. Transition between stratified and non-stratified horizontal oil–water flows. Part I: Stability analysis. Chemical Engineering Science, v. 62, n. 11, p. 2915–2928, jun. 2007.

AL-WAHAIBI, T.; ANGELI, P. Experimental study on interfacial waves in stratified horizontal oil–water flow. International Journal of Multiphase Flow, v. 37, n. 8, p. 930–940, out. 2011.

ANGELI, P.; HEWITT, G. F. Pressure gradient in horizontal liquid-liquid flows. International Journal of Multiphase Flow, v. 24, n. 7, p. 1183–1203, 1998.

ANGELI, P.; HEWITT, G. F. Drop size distributions in horizontal oil-water dispersed flows. Chemical Engineering Science, v. 55, p. 3133–3143, 2000.

ARAI, T. et al. Concurrent upward liquid slug dynamics on both surfaces of annular channel acquired with liquid film sensor. Experimental Thermal and Fluid Science, v. 60, p. 337–345, jan. 2015.

ARNEY, M. S. et al. Friction factor and holdup studies for lubricated pipelining--i. International Journal Multiphase Flow, v. 19, n. 6, p. 1061–1076, 1993.

ASALI, J.; HANRATTY, T. Ripples generated on a liquid film at high gas velocities. International Journal of Multiphase Flow, v. 19, n. 2, p. 229–243, abr. 1993.

AZZOPARDI, B. Drops in annular two-phase flow. International Journal of Multiphase Flow, v. 23, p. 1–53, dez. 1997.

BAGADE, S. S.; SHANDILYA, V. Use of Histogram Equalization in Image Processing for Image Enhancement. International Journal of Software Engineering Research & Practices, v. 1, n. 2, p. 6–10, 2011.

BAI, R.; CHEN, K.; JOSEPH, D. D. Lubricated Pipelining : Stability of Core-Annular Flow V : Experiments and comparison with theory. Journal fluid mech, p. 97–132, 1992.

BAI, R.; JOSEPH, D. D. Steady flow and interfacial shapes of a highly viscous dispersed phase. International Journal Multiphase Flow, v. 26, p. 1469–1491, 2000.

BALAKHRISNA, T. et al. Oil–water flows through sudden contraction and expansion in a horizontal pipe – Phase distribution and pressure drop. International Journal of Multiphase Flow, v. 36, n. 1, p. 13–24, jan. 2010.

BANNWART, A. C. Wavespeed and volumetric fraction in core annular flow. International Journal Multiphase Flow, v. 24, p. 961–974, 1998.

BANNWART, A. C. A simple model for pressure gradient in horizontal core-annular flow. Journal of the Brazilian Society of Mechanical Sciences, v. 21, p. 233–244, 1999.

BANNWART, A. C. Modeling aspects of oil – water core – annular flows. Journal of Petroleum Science and Engineering, v. 32, p. 127–143, 2001.

BANNWART, A. C. et al. Flow Patterns in Heavy Crude Oil-Water Flow. Journal of Energy Resources Technology, v. 126, n. 3, p. 184, 2004.

BANNWART, A. C. et al. Water-assisted flow of heavy oil in a vertical pipe: Pilot-scale experiments. International Journal of Chemical Reactor Engineering, v. 10, p. A32, 2011.

BARRAL, A. H.; EBENEZER, A.; ANGELI, P. Investigations of interfacial waves at the inlet section in stratified oil–water flows. Experimental Thermal and Fluid Science, v. 60, p. 115–122, jan. 2015.

BELT, R. J. et al. Time and spatially resolved measurements of interfacial waves in vertical annular flow. International Journal of Multiphase Flow, v. 36, n. 7, p. 570–587, jul. 2010.

BELT, R. J.; VAN'T WESTENDE, J. M. C.; PORTELA, L. M. Prediction of the interfacial shear-stress in vertical annular flow. International Journal of Multiphase Flow, v. 35, n. 7, p. 689–697, jul. 2009.

BINDU, C. H. An improved medical image segmentation algorithm using otsu method. International Journal of recent Trends in Engineering, v. 2, n. 3, p. 88–90, 2009.

BONILLA RIAÑO, A. et al. A High Spatial and Temporal Resolution Film Thickness Sensor in Oil - Water Flows. Instrumentation and Measurement Technology Conference (I2MTC) Proceedings, 2014 IEEE International. Proceedings...2014

BONILLA RIAÑO, A.; BANNWART, A. C.; RODRIGUEZ, O. M. H. Holdup Estimation in Core Flow Using Image Processing. Instrumentation and Measurement Technology Conference (I2MTC), 2013 IEEE International. Proceedings...2013

BRAUNER, N. Two-phase liquid-liquid annular flow. International Journal Multiphase Flow, v. 17, n. 1, p. 59–76, 1991.

BRUNO, K.; MCCREADY, M. J. Origin of Roll Waves in Horizontal Gas-Liquid Flows. AIChE Journal, v. 34, n. 9, 1988.

BUDWIG, R. Refractive index matching methods for liquid flow investigations. Experiments in Fluids, v. 17, n. 5, p. 350–355, set. 1994.

BURNS, J. Measurement of liquid film thickness and the determination of spin-up radius on a rotating disc using an electrical resistance technique. Chemical Engineering Science, v. 58, n. 11, p. 2245–2253, jun. 2003.

CASTRO, M. S. DE; RODRIGUEZ, O. M. H. Interfacial waves in stratified viscous oil–water flow. Experimental Thermal and Fluid Science, v. 62, p. 85–98, abr. 2015.

CASTRO, M. S. et al. Geometrical and kinematic properties of interfacial waves in stratified oil-water flow in inclined pipe. Experimental Thermal and Fluid Science, v. 37, p. 171–178, fev. 2012.

CENGEL, J. A. et al. Laminar and turbulent flow of unstable liquid-liquid emulsions. AIChE Journal, v. 8, n. 3, 1962.

CHEN, T. Capacitive sensors for measuring complex permittivity of planar and cylindrical structures. Doctoral thesis. Iowa State University, 2012.

CHEN, Z.; LUO, R. C. Design and implementation of capacitive proximity sensor using microelectromechanical systems technology. IEEE Transactions on Industrial Electronics, v. 45, n. 6, p. 886 – 894, 1998.

CHERDANTSEV, A. V.; HANN, D. B.; AZZOPARDI, B. J. Study of gas-sheared liquid film in horizontal rectangular duct using high-speed LIF technique: Three-dimensional wavy structure and its relation to liquid entrainment. International Journal of Multiphase Flow, v. 67, p. 52–64, dez. 2014.

CLARK, W. W. Liquid Film Thickness Measurement. Multiphase Science and Technology, v. 14, n. 1, p. 1–74, 2002.

DAMSOHN, M. Liquid films and droplet deposition in a BWR fuel element. Doctoral thesis. ETH Zurich, 2011.

DAMSOHN, M.; PRASSER, H. High-speed liquid film sensor for two-phase flows with high spatial resolution based on electrical conductance. Flow Measurement and Instrumentation, v. 20, n. 1, p. 1–14, mar. 2009a.

DAMSOHN, M.; PRASSER, H. M. High-speed liquid film sensor with high spatial resolution. Measurement Science and Technology, v. 20, n. 11, p. 114001, nov. 2009b.

DEMORI, M. et al. A capacitive sensor system for the analysis of two-phase flows of oil and conductive water. Sensors and Actuators A: Physical, v. 163, n. 1, p. 172–179, ago. 2010.

DIAS, F. Thresholding using the ISODATA Clustering Algorithm. IEEE Transactions on Systems, Man, and Cybernetics, v. SMC-10, n. 11, p. 771–774, 1980.

DONG, F. et al. Identification of two-phase flow regimes in horizontal, inclined and vertical pipes. Measurement Science and Technology, v. 12, n. 8, p. 1069–1075, 1 ago. 2001.

DONOHO, D. L.; JOHNSTONE, I. M. Ideal Spatial Adaptation via Wavelet Shrinkage. Biometrika, v. 81, p. 425–455, 1994.

DU, M. et al. Flow pattern and water holdup measurements of vertical upward oil–water two-phase flow in small diameter pipes. International Journal of Multiphase Flow, v. 41, p. 91–105, maio 2012.

DUCKLER, A. E.; WICKS, M. I.; CLEVELAND, R. G. Frictional pressure drop in two-phase flow: B. An approach through similarity analysis. AIChE Journal, v. 10, n. 1, p. 44–51, 1964.

EINSTEIN, A. Eine neue Bestimmung der Molekldimensionen. Ann. Phys., v. 19, p. 289–306, 1906.

EL-ZAART, A. Images thresholding using ISODATA technique with gamma distribution. Pattern Recognition and Image Analysis, v. 20, n. 1, p. 29–41, abr. 2010.

ERGEN, B. Signal and Image Denoising Using Wavelet Transform. [s.l.] InTech, 2012.

FARIAS, P. S. C. et al. Liquid film characterization of horizontal , annular , two-phase , gas-liquid flow using time-resolved LASER-induced fluorescence15th International Symposium on Applications of Laser Techniques to Fluid Mechanics. Proceedings...2010

FLORES, J. G.; SARICA, C.; BRILL, J. P. Characterization of Oil-Water Flow Patterns in Vertical and Deviated WellsSPE Annual Technical Conference and Exhibition. Proceedings...1997

FRANCO, A. An apparatus for the routine measurement of thermal conductivity of materials for building application based on a transient hot-wire method. Applied Thermal Engineering, v. 27, n. 14-15, p. 2495–2504, out. 2007.

GAWAS, K. et al. Wave characteristics in gas–oil two phase flow and large pipe diameter. International Journal of Multiphase Flow, v. 63, p. 93–104, jul. 2014.

GERACI, G.; AZZOPARDI, B.; VANMAANEN, H. Effect of inclination on circumferential film thickness variation in annular gas/liquid flow. Chemical Engineering Science, v. 62, n. 11, p. 3032–3042, jun. 2007.

GHOSH, S. et al. Review of oil water core annular flow. Renewable and Sustainable Energy Reviews, v. 13, n. 8, p. 1957–1965, out. 2009.

GONZALEZ, R. C.; WOODS, R. E. Digital Image Processing. Second ed.[s.l.] Prentice Hall, 2002.

GONZALEZ, R. C.; PEREZ, A. An Iterative Thresholding Algorithm for Image Segmentation. IEEE Transactions on Pattern Analysis and Machine Intelligence, v. PAMI-9, n. 6, p. 742–751, 1987.

GOVIER, G. W.; SULLIVAN, G. A.; WOOD, R. K. The upward vertical flow of oil–water mixture. The Canadian Journal of Chemical Engineering, v. 39, n. 2, 1961.

GRASSI, B.; STRAZZA, D.; POESIO, P. Experimental validation of theoretical models in two-phase high-viscosity ratio liquid – liquid flows in horizontal and slightly inclined pipes. International Journal of Multiphase Flow, v. 34, p. 950–965, 2008.

GUET, S. et al. An inverse dispersed multiphase flow model for liquid production rate determination. International Journal of Multiphase Flow, v. 32, n. 5, p. 553–567, 2006.

GUTIERREZ, K.; COATES, K. PCB Design Guidelines for 0 . 5mm Package-on-Package Applications Processor , Part I. n. June, p. 1–32, 2010.

HAN, H.; GABRIEL, K. A Numerical Study of Entrainment Mechanism in Axisymmetric Annular Gas-Liquid Flow. Journal of Fluids Engineering, v. 129, n. 3, p. 293, 2007.

HAN, H.; ZHU, Z.; GABRIEL, K. A study on the effect of gas flow rate on the wave characteristics in two-phase gas-liquid annular flow. Nu, p. 2580–2588, 2006.

HARALICK, R. M.; STERNBERG, S. R.; ZHUANG, X. Image Analysis using Mathematical Morphology. IEEE Transactions On Pattern Analysis And Machine Intelligence, v. PAMI-9, n. 4, p. 532–550, 1987.

HASAN, N. M.; AZZOPARDI, B. J. Imaging stratifying liquid–liquid flow by capacitance tomography. Flow Measurement and Instrumentation, v. 18, n. 5-6, p. 241–246, out. 2007.

HAZUKU, T.; TAKAMASA, T.; MATSUMOTO, Y. Experimental study on axial development of liquid film in vertical upward annular two-phase flow. International Journal of Multiphase Flow, v. 34, n. 2, p. 111–127, fev. 2008.

HU, X.; YANG, W. Planar capacitive sensors – designs and applications. Sensor Review, v. 30, n. 1, p. 24–39, 2010.

HUSSAIN, S. A.; XU, X. Y.; HEWITT, G. F. Water Local Volume Fraction on Oil in Water Dispersion. Journal of Applied Fluid Mechanics, v. 1, n. 2, p. 57–63, 2008.

IOANNOU, K.; NYDAL, O. J.; ANGELI, P. Phase inversion in dispersed liquid–liquid flows. Experimental Thermal and Fluid Science, v. 29, n. 3, p. 331–339, mar. 2005.

ITO, D. et al. Dynamic film thickness between bubbles and wall in a narrow channel. Experiments in Fluids, v. 51, n. 3, p. 821–833, 3 maio 2011.

IZWAN ISMAIL, A. S. et al. Experimental investigation of oil-water two-phase flow in Horizontal Pipes: Pressure losses, liquid holdup and flow patterns. Journal of Petroleum Science and Engineering, fev. 2015.

JACOB, N. E.; WYAWAHARE, M. V. Tibia Bone Segmentation in X-ray Images - A Comparative Analysis. International Journal of Computer Applications, v. 76, n. 9, p. 34–41, 2013.

JACOWITZ, L. A.; BRODKEY, R. S. An analysis of geometry and pressure drop for the horizontal, annular, two-phase flow of water and air in the entrance region of a pipe. Chemical Engineering Science, v. 19, n. 4, p. 261–274, abr. 1964.

JIN, F. et al. Adaptive Wiener Filtering of Noisy Images and Image SequencesImage Processing, 2003. ICIP 2003. Proceedings. 2003 International Conference on. Proceedings...2003

JIN, N.; WANG, J.; XU, L.-J. Multi-electrode array for the measurement of oil-water two-phase flow. Proceedings of the second international conference on machine learning and cybernetics. Proceedings...2003

JOHNSON, G. W.; BERTELSEN, A. F.; NOSSEN, J. A Mechanistic Model for Roll Waves for Two-Phase Pipe Flow. AIChE Journal, v. 55, n. 3908, 2009.

JULIASTUTI, E.; EPSILAWATI, L. Image contrast enhancement for film-based dental panoramic radiography. 2012 International Conference on System Engineering and Technology (ICSET). Proceedings...IEEE, set. 2012

KAMEI, T.; SERIZAWA, A. Measurement of 2-dimensional local instantaneous liquid film thickness around simulated nuclear fuel rod by ultrasonic transmission technique. Nuclear Engineering and Design, v. 184, p. 349 – 362, 1998.

KANG, H. C.; KIM, M. M. Measurement of three-dimensional wave form and interfacial area in an air - water stratified flow. Nuclear Engineering and Design, v. 136, p. 347–360, 1992a.

KANG, H.; KIM, M. The development of a flush-wire probe and calibration method for measuring liquid film thickness. International Journal Multiphase Flow, v. 18, n. 3, p. 423–437, 1992b.

KANUNGO, T. et al. An efficient k-means clustering algorithm: analysis and implementation. IEEE Transactions on Pattern Analysis and Machine Intelligence, v. 24, n. 7, p. 881–892, jul. 2002.

KAUR, M.; KAUR, J.; KAUR, J. Survey of Contrast Enhancement Techniques based on Histogram Equalization. International Journal of Advanced Computer Science and Applications, v. 2, n. 7, p. 137–141, 2011.

KEE, K. E. et al. Flow Patterns and Water Wetting in Oil-Water Two Phase Flow – A Flow Loop StudyCorrosion. Proceedings...2014

KUMARA, W. A. S.; HALVORSEN, B. M.; MELAAEN, M. C. Single-beam gamma densitometry measurements of oil–water flow in horizontal and slightly inclined pipes. International Journal of Multiphase Flow, v. 36, n. 6, p. 467–480, jun. 2010.

KURNAZ, M. N.; DOKUR, Z.; OLMEZ, T. Segmentation of ultrasound images by using wavelet transform. Proceedings of the 25th Annual International Conference of the IEEE Engineering in Medicine and Biology Society (IEEE Cat. No.03CH37439), n. i, p. 657–659, 2003.

LEVY, S. Two-Phase Flow in Complex Systems. New York: Jhon Wiley & sons, 1999.

LI, H. et al. Volume Flow Rate Measurement in Vertical Oil - in - Water Pipe Flow using Electrical Impedance Tomography and a Local Probe11th International Conference on Multiphase Flow in Industrial Plants. Proceedings...2008

LI, N.; HE, C. F. Capacitive Sensor Design for an Automatic Car-Wiper System. Advanced Materials Research, v. 211-212, p. 798–802, fev. 2011.

LOPEZ, J. M. et al. Experimental Investigation of Falling Liquid Film in Vertical Downward Two-Phase Pipe FlowASME 2012 Fluids Engineering Division Summer Meeting Volume 2: Fora. Proceedings...Rio Grande, Puerto rico: ASME, 8 jul. 2012.

LOVICK, J.; ANGELI, P. Experimental studies on the dual continuous flow pattern in oil–water flows. International Journal of Multiphase Flow, v. 30, n. 2, p. 139–157, fev. 2004a.

LOVICK, J.; ANGELI, P. Droplet size and velocity profiles in liquid–liquid horizontal flows. Chemical Engineering Science, v. 59, n. 15, p. 3105–3115, ago. 2004b.

LOWE, M. L.; KUTT, P. H. Refraction through cylindrical tubes. Experiments in Fluids, v. 320, n. 13, p. 315–320, 1992.

LUCAS, G. P.; JIN, N. D. A new kinematic wave model for interpreting cross correlation velocity measurements in vertically upward , bubbly oil-in-water flows. Measurement Science and Technology, v. 1538, 2001a.

LUCAS, G. P.; JIN, N. D. Measurement of the homogeneous velocity of inclined oil-in-water flows using a resistance cross correlation flow meter. Measurement Science and Technology, v. 12, n. 12, p. 1529–1537, 2001b.

LUISIER, F.; BLU, T.; UNSER, M. A new SURE approach to image denoising: interscale orthonormal wavelet thresholding. IEEE transactions on image processing : a publication of the IEEE Signal Processing Society, v. 16, n. 3, p. 593–606, mar. 2007.

MAMISHEV, A. V.; SUNDARA-RAJAN, K.; ZAHN, M. Interdigital sensors and transducers. Proceedings of the IEEE, v. 92, n. 5, p. 808–845, maio 2004.

MARTÍNEZ-PALOU, R.; MOSQUEIRA, M. D. L.; ZAPATA-RENDÓN, B.; et al. Transportation of heavy and extra-heavy crude oil by pipeline: A review. Journal of Petroleum Science and Engineering, v. 75, n. 3-4, p. 274–282, 2011.

MIYA, M.; WOODMANSEE, D. E.; TY, T. J. H. A model for roll waves in gas-liquid flow. Chemical Engineering Science, v. 26, n. 11, p. 1915–1931, 1970.

MOUZA, A. A. et al. Measurement of liquid film thickness using a laser light absorption method. Experiments in Fluids, v. 28, n. May 1999, 2000.

MUKHOPADHYAY, S. C.; NORTH, P.; ZEALAND, N. Novel Planar Electromagnetic Sensors: Modeling and Performance Evaluation. p. 546–579, 2005.

MYDLARZ-GABRYK, K.; PIETRZAK, M.; TRONIEWSKI, L. Study on oil–water two-phase upflow in vertical pipes. Journal of Petroleum Science and Engineering, v. 117, p. 28–36, maio 2014.

NADLER, M.; MEWES, D. Flow induced emulsification in the flow of two immiscible liquids in horizontal pipes. International Journal Multiphase FlowJ. multiphase Flow, v. 23, n. 1, p. 55–68, 1997.

NARROW, T. L.; YODA, M.; ABDEL-KHALIK, S. I. A simple model for the refractive index of sodium iodide aqueous solutions. Experiments in Fluids, v. 28, n. 3, p. 282–283, 6 mar. 2000.

NASSR, A. A; AHMED, W. H.; EL-DAKHAKHNI, W. W. Coplanar capacitance sensors for detecting water intrusion in composite structures. Measurement Science and Technology, v. 19, n. 7, p. 075702, 1 jul. 2008.

NASSR, A.; W.; EL-DAKHAKHNI. Improved interdigital sensors for structural health monitoring of composite retrofit systems. Journal of Reinforced Plastics and Composites, v. 30, n. 7, p. 621–629, 2011.

NEDDERMAN, R. M.; SHEARER, C. J. The motion and frequency of large disturbance waves in annular two-phase flow of air-water mixtures. Chemical Engineering Science, v. 18, n. 10, p. 661–670, out. 1963.

OLIEMANS, R. V. A. et al. Core-Annular Oil/Water flow: Turbulent -Lubricanting-Film Model and Measurement in a 5cm Pipe Loop. International Journal of Multiphase Flow, v. 13, n. 1, p. 23–31, 1987.

OLIVEIRA, F. S. DE; YANAGIHARA, J. I.; PACÍFICO, A. L. Film thickness and wave velocity measurement using reflected laser intensity. Journal of the Brazilian Society of Mechanical Sciences and Engineering, v. 28, n. 1, p. 30–36, mar. 2006.

OMER, A.; PAL, R. Pipeline Flow Behavior of Water-in-Oil Emulsions with and without a Polymeric Additive in the Aqueous Phase. Chemical Engineering & Technology, v. 33, n. 6, p. 983–992, jun. 2010.

ORFANIDIS, S. J. Introduction to Signal Processing. v. 20

OTSU, N. A Threshold Selection Method from Gray-Level Histograms. IEEE Transactions on Systems, Man, and Cybernetics, v. SMC-9, n. 1, p. 62–66, 1979.

PAL, R. Single-Parameter and Two-Parameter Rheological Equations of State for Nondilute Emulsions. Industrial & Engineering Chemistry Research, v. 40, n. 23, p. 5666–5674, nov. 2001.

PAL, R. Mechanism of Turbulent Drag Reduction in Emulsions and Bubbly Suspensions. Industrial & Engineering Chemistry Research, v. 46, n. 3, p. 618–622, 2007.

PAVITHRA, P.; RAMYASHREE, N.; SHRUTHI, T. V. Image Enhancement by Histogram Specification Using Multiple Target Images. Image (Rochester, N.Y.), v. 1, n. 2, p. 3–5, 2010.

PICCHI, D. et al. An experimental investigation and two-fluid model validation for dilute viscous oil in water dispersed pipe flow. Experimental Thermal and Fluid Science, v. 60, p. 28–34, jan. 2015.

PRASSER, H. et al. A new electrode-mesh tomograph for gas–liquid flows. Flow Measurement and Instrumentation, v. 9, n. 2, p. 111–119, jun. 1998.

RODRIGUEZ, I. H. et al. Slip ratio in dispersed viscous oil–water pipe flow. Experimental Thermal and Fluid Science, v. 35, n. 1, p. 11–19, jan. 2011.

RODRIGUEZ, I. H. et al. Drag Reduction Phenomenon in Viscous Oil-Water Dispersed Pipe Flow : Experimental Investigation and Phenomenological Modeling. AIChE Journal, v. 58, n. 9, p. 2900–2910, 2012.

RODRIGUEZ, I. H. et al. Experimental study on heavy oil-water dispersed flow8th International Conference on Multiphase Flow ICMF 2013. Proceedings...Jeju, Korea.: 2013

RODRIGUEZ, I. H. Experimental study and modeling of flow of inverse emulsion in pipes. Doctoral thesis. University of Sao Paulo, 2014.

RODRIGUEZ, O. M. H. Escoamento Multifásico. Rio de Janeiro: ABCM, 2011.

RODRIGUEZ, O. M. H.; BANNWART, A. C.; DE CARVALHO, C. H. M. Pressure loss in core-annular flow: Modeling, experimental investigation and full-scale experiments. Journal of Petroleum Science and Engineering, v. 65, n. 1-2, p. 67–75, mar. 2009.

RODRIGUEZ, O. M. H.; BANNWART, A. C. Experimental study on interfacial waves in vertical core flow. Journal of Petroleum Science and Engineering, v. 54, p. 140–148, 2006.

RODRIGUEZ, O. M. H.; OLIEMANS, R. V. A. Experimental study on oil – water flow in horizontal and slightly inclined pipes. International Journal Multiphase Flow, v. 32, p. 323–343, 2006.

SANTOS, R. G., et al. An overview of heavy oil properties and its recovery and transportation methods. Brazilian Journal of Chemical Engineering, 31(3), 571–590. jul. 2014.

SARKAR, S.; DAS, S. Multilevel Image Thresholding Based on 2D Histogram and Maximum Tsallis Entropy— A Differential Evolution Approach. IEEE Transactions on Image Processing, v. 22, n. 12, p. 4788–4797, dez. 2013.

SAWANT, P. et al. Properties of disturbance waves in vertical annular two-phase flow. Nuclear Engineering and Design, v. 238, n. 12, p. 3528–3541, dez. 2008.

SCHAGEN, A. et al. Simultaneous measurement of local film thickness and temperature distribution in wavy liquid films using a luminescence technique. International Journal of Heat and Mass Transfer, v. 49, n. 25-26, p. 5049–5061, dez. 2006.

SCHUBRING, D. et al. Planar laser-induced fluorescence (PLIF) measurements of liquid film thickness in annular flow. Part I: Methods and data. International Journal of Multiphase Flow, v. 36, n. 10, p. 815–824, out. 2010.

SCHUBRING, D.; SHEDD, T. Wave behavior in horizontal annular air–water flow. International Journal of Multiphase Flow, v. 34, n. 7, p. 636–646, jul. 2008.

SCHUBRING, D.; SHEDD, T. A.; HURLBURT, E. T. Planar laser-induced fluorescence (PLIF) measurements of liquid film thickness in annular flow. Part II: Analysis and comparison to models. International Journal of Multiphase Flow, v. 36, n. 10, p. 825–835, out. 2010.

SCHUBRING, D.; SHEDD, T.; HUR. Studying disturbance waves in vertical annular flow with high-speed video. International Journal of Multiphase Flow, v. 36, p. 385–396, 2010.

SEKOGUCHI, K.; TAKEISHI, M. Interfacial Structures in Upward Huge Wave Flow and Annular Flow Regimes. October, v. 15, n. 3, p. 295–305, 1989.

SEKOGUICHI, K. et al. On Ripple of Annular Two-Phase Flow. Bulletin oh the The Japan Society of Mechanical Engineers, v. 21, n. 152, 1978.

SERWAY, R. A.; JOHN W. JEWTT, J. Physics for scientists and engineers with modern physics. Ninth Edit ed.[s.l.] Brooks/Cole Cengage Learning, 2014.

SHARMA, D. Non-destructive Testing of Materials using Capacitive Sensing Technique. MIT International Journal of Electronics and Communication Engineering, v. 1, n. 2, p. 73–77, 2011.

SHOHAM, O. Mechanistic modeling of gas-liquid two-phase flow in pipes. Richardson: Society of Petroleum Engineers, 2006.

SIHVOLA, A. Electromagnetic Mixing Formulas and Applications. Institution of Engineering and Technology, 1999.

SILVA, M. J. et al. Planar Array Sensor for High-speed Component Distribution Imaging in Fluid Flow Applications. Sensors, v. 7, n. 10, p. 2430–2445, out. 2007.

SILVA, M. J. Impedance Sensors for Fast Multiphase Flow Measurement and Imaging. Doctoral thesis. TUDpress, 2008.

SILVA, M. J.; SCHLEICHER, E.; HAMPEL, U. Capacitance wire-mesh sensor for fast measurement of phase fraction distributions. Measurement Science and Technology, v. 18, n. 7, p. 2245–2251, jul. 2007.

SINGH, B.; MISHRA, R. S.; GOUR, P. Analysis of Contrast Enhancement Techniques For Underwater Image. International Journal of Computer Technology and Electronics Engineering, v. 1, n. 2, 2011.

SOTGIA, G.; TARTARINI, P.; STALIO, E. Experimental analysis of flow regimes and pressure drop reduction in oil – water mixtures. International Journal of Multiphase Flow, v. 34, n. 12, p. 1161–1174, 2008.

STEELE, J. J.; TASCHUK, M. T.; BRETT, M. J. Nanostructured Metal Oxide Thin Films for Humidity Sensors. IEEE Sensors Journal, v. 8, n. 8, p. 1422 – 1429, 2008.

STRAZZA, D. et al. Core-annular flow in horizontal and slightly inclined pipes: Existence, pressure drops, and hold-up. Chemical Engineering Science, v. 66, n. 12, p. 2853–2863, jun. 2011a.

STRAZZA, D. et al. Capacitance sensor for hold-up measurement in high-viscous-oil/conductive-water core-annular flows. Flow Measurement and Instrumentation, v. 22, n. 5, p. 360–369, out. 2011b.

STRAZZA, D.; POESIO, P. Chemical Engineering Research and Design Experimental study on the restart of core-annular flow. Chemical Engineering Research and Design, v. 90, n. 11, p. 1711–1718, 2012.

TAKESHIMA, K. et al. The flow characteristics of an upward gas-liquid two-phase flow in a vertical tube with a wire coil: Part 2. Effect on void fraction and liquid film thickness. Heat Transfer—Asian ResearchAsian Research, v. 31, n. 8, p. 652–664, dez. 2002.

TAN, C.; DONG, F. Cross Correlation Velocity of Oil-water Two-Phase Flow by a Dual-Plane Electrical Resistance Tomography SystemInstrumentation and Measurement Technology Conference. Proceedings...2010

TAYLOR, N. H.; HEWITT, G. F.; LACEY, P. M. C. The motion and frequency of large disturbance waves in ammlar two-phase flow of air-water mixtures. Chemical Engineering Science, v. 18, p. 537–552, 1963.

THIELE, S.; DA SILVA, M. J.; HAMPEL, U. Capacitance Planar Array Sensor for Fast Multiphase Flow Imaging. IEEE Sensors Journal, v. 9, n. 5, p. 533–540, maio 2009.

TIWARI, R. et al. Multi-range sensors for the measurement of liquid film thickness distributions based on electrical conductance. Flow Measurement and Instrumentation, v. 40, p. 124–132, 2014.

TODA, K.; FURUSE, H. Extension of Einstein's viscosity equation to that for concentrated dispersions of solutes and particles. Journal of bioscience and bioengineering, v. 102, n. 6, p. 524–8, dez. 2006.

U.S. ENERGY INFORMATION ADMINISTRATION. EIA - International Energy Outlook 2013. Disponível em: <http://www.eia.doe.gov/oiaf/ieo/highlights.html>. Acesso em: 17 maio. 2014.

VERMA, R.; ALI, J. A Comparative Study of Various Types of Image Noise and Efficient Noise Removal Techniques. International Journal of Advance Research in Computer Science and Software Engineering, v. 3, n. 10, p. 617–622, 2013.

WADA, S.; KIKURA, H.; ARITOMI, M. Pattern recognition and signal processing of ultrasonic echo signal on two-phase flow. Flow Measurement and Instrumentation, v. 17, n. 4, p. 207–224, ago. 2006.

WALLIS, G.B. One dimensional two-phase flow. MacGraw-Hill, 1969.

WANG, W.; GONG, J.; ANGELI, P. Investigation on heavy crude-water two phase flow and related flow characteristics. International Journal of Multiphase Flow, v. 37, n. 9, p. 1156–1164, nov. 2011.

WANG, Z.; GABRIEL, K. S.; ZHU, Z. A model of interfacial waves in annular two-phase flow at different gravity levels. Microgravity - Science and Technology, v. 16, n. 1-4, p. 259–263, mar. 2005.

WITT, B. J.; CORONADO-DIAZ, H.; HUGO, R. J. Optical contouring of an acrylic surface for non-intrusive diagnostics in pipe-flow investigations. Experiments in Fluids, v. 45, n. 1, p. 95–109, 9 fev. 2008.

WOLF, A.; JAYANTI, S.; HEWITT, G. F. On The Nature of Epehmeral Waves In Vertical Annular Flow. International Journal of Multiphase Flow, v. 22, n. 2, p. 325–333, 1996.

XU, J. et al. Investigations of phase inversion and frictional pressure gradients in upward and downward oil–water flow in vertical pipes. International Journal of Multiphase Flow, v. 36, n. 11-12, p. 930–939, nov. 2010.

YU, Y.; ACTON, S. T. Speckle Reducing Anisotropic Diffusion. IEEE Transactions on Image Processing, v. 11, n. 11, p. 1260–1270, 2002.

ZANGL, H.; FUCHS, A.; BRETTERKLIEBER, T. Non-invasive measurements of fluids by means of capacitive sensors. Elektrotechnik und Informationstechnik, v. 126, n. 1-2, p. 8–12, fev. 2009.

ZHAO, D. et al. Experimental study on local characteristics of oil–water dispersed flow in a vertical pipe. International Journal of Multiphase Flow, v. 32, n. 10-11, p. 1254–1268, out. 2006.

ZHAO, X.; LUCAS, G. P. Use of a novel dual-sensor probe array and electrical resistance tomography for characterization of the mean and time-dependent properties of inclined, bubbly oil-in-water pipe flows. Measurement Science and Technology, v. 22, n. 10, p. 104012, 1 out. 2011.

ZHAO, Y. et al. Disturbance wave development in two-phase gas–liquid upwards vertical annular flow. International Journal of Multiphase Flow, v. 55, p. 111–129, out. 2013.

APPENDIX A

Table A.1 – Experimental data: superficial velocities, mixture velocities, water holdups, average film thicknesses by the capacitance system and the high speed camera images, and observed flow patterns.

Run	V_{sw} [m/s]	V_{so} [m/s]	V_m [m/s]	h_w [-]	$\bar{\delta}_{Sensor}$ [µm]	$u_{\bar{\delta}_{Sensor}}$ [µm]	$\bar{\delta}_{camera}$ [µm]	$u_{\bar{\delta}_{camera}}$ [µm]	Flow pattern
1	0.1	0.3	0.4	0.35	1932	106	2210	100	UA
2	0.1	0.3	0.4	0.37	2063	103	2245	100	UA
3	0.1	0.32	0.42	0.34	1907	105	2230	100	UA
4	0.1	0.35	0.45	0.31	1821	100	1569	100	UA
5	0.1	0.37	0.47	0.29	1697	102	2438	100	UA
6	0.1	0.4	0.5	0.28	1534	107	1544	100	UA
7	0.15	0.37	0.52	0.51	1712	103	1590	100	UA
8	0.1	0.42	0.52	0.27	1514	106	1729	100	UA
9	0.15	0.4	0.55	0.36	1503	105	2334	100	UA
10	0.15	0.4	0.55	0.35	2019	101	2130	100	UA
11	0.15	0.42	0.57	0.35	1109	111	1788	100	UA
12	0.15	0.45	0.6	0.33	1070	107	1987	100	UA
13	0.17	0.5	0.67	0.33	1797	108	1708	100	UA
14	0.2	0.5	0.7	0.35	2077	104	2152	100	UA
15	0.17	0.55	0.72	0.31	1753	105	1695	100	UA
16	0.17	0.6	0.77	0.27	1416	113	1708	100	UA
17	0.17	0.62	0.79	0.27	1228	111	2071	100	UA
18	0.2	0.6	0.8	0.31	1742	105	1533	100	UA
19	0.3	0.5	0.8	0.42	1653	99	2122	100	UA
20	0.25	0.6	0.85	0.36	2142	105	1998	100	UA
21	0.2	0.7	0.9	0.26	1094	109	1823	100	BD
22	0.25	0.65	0.9	0.34	1497	120	1815	100	BD
23	0.3	0.61	0.91	0.37	1474	118	1458	100	UA
24	0.25	0.67	0.92	0.32	1486	119	1432	100	BD
25	0.2	0.75	0.95	0.26	905	91	2281	100	BD
26	0.25	0.7	0.95	0.31	1400	112	2325	100	BD
27	0.2	0.8	1	0.22	903	90	2360	100	BD
28	0.3	0.8	1.1	0.24	1004	100	2168	100	BD
29	0.7	0.8	1.5	0.50	2196	103	1755	100	BD
30	1.2	0.3	1.5	0.83	2168	106	2310	100	D O/W

UA: Unstable Annular flow, BD: Big Drops flow, D O/W: Dispersed Oil-in-Water flow

Table A.1 – (Continuation) Experimental data: superficial velocities, mixture velocities, water holdups, average film thicknesses by the capacitance system and the high speed camera images, and observed flow patterns.

Run	V_{sw} [m/s]	V_{so} [m/s]	V_m [m/s]	h_w [-]	$\bar{\delta}_{Sensor}$ [μm]	$u_{\bar{\delta}_{Sensor}}$ [μm]	$\bar{\delta}_{camera}$ [μm]	$u_{\bar{\delta}_{camera}}$ [μm]	Flow pattern
31	1.2	0.35	1.55	0.80	1976	109	1505	100	D O/W
32	0.88	0.67	1.55	0.61	1384	125	1692	100	BD
33	0.8	0.8	1.6	0.54	2183	107	2014	100	BD
34	1.2	0.4	1.6	0.78	2087	104	1868	100	D O/W
35	1.22	0.4	1.62	0.78	1508	106	1807	100	D O/W
36	0.9	0.8	1.7	0.57	2185	107	1898	100	BD
37	1	0.8	1.8	0.60	2059	103	1520	100	BD
38	1.2	0.8	2	0.64	1798	108	1426	100	D O/W
39	1.5	0.5	2	0.78	1937	107	2050	100	D O/W
40	1.5	0.8	2.3	0.68	2192	103	1787	100	D O/W
41	1.7	0.6	2.3	0.77	1985	109	2250	100	D O/W
42	1.96	0.5	2.46	0.82	1790	107	1442	100	D O/W
43	1.96	0.6	2.56	0.79	1717	103	1713	100	D O/W
44	1.96	0.7	2.66	0.76	1684	101	1966	100	D O/W

UA: Unstable Annular flow, BD: Big Drops flow, D O/W: Dispersed oil-in-water flow

Table A.2 – Experimental data: superficial velocities, mixture velocities, interfacial estructure velocities, interfacial estructure frequencies, interfacial estructure amplitudes and interfacial estructure wavelength.

Run	V_{sw} [m/s]	V_{so} [m/s]	V_m [m/s]	V_{wave} [m/s]	f_{wave} [Hz]	A_{wave} [µm]	λ_{wave} [µm]
1	0.1	0.3	0.4	0.28	43.57	1000	6419
2	0.1	0.3	0.4	0.29	55.21	988	5279
3	0.1	0.32	0.42	0.32	73.05	980	4407
4	0.1	0.35	0.45	0.32	73.60	965	4352
5	0.1	0.37	0.47	0.35	60.52	967	5816
6	0.1	0.4	0.5	0.36	56.30	955	6482
7	0.15	0.37	0.52	0.37	66.04	878	3864
8	0.1	0.42	0.52	0.26	38.67	855	6791
9	0.15	0.4	0.55	0.33	61.02	985	3647
10	0.15	0.4	0.55	0.37	65.08	869	3905
11	0.15	0.42	0.57	0.41	51.51	855	7974
12	0.15	0.45	0.6	0.36	33.81	845	10753
13	0.17	0.5	0.67	0.53	32.97	1005	16017
14	0.2	0.5	0.7	0.54	55.13	1068	9835
15	0.17	0.55	0.72	0.59	63.80	945	9208
16	0.17	0.6	0.77	0.61	70.37	755	6758
17	0.17	0.62	0.79	0.61	57.25	910	10618
18	0.2	0.6	0.8	0.52	36.06	958	14312
19	0.3	0.5	0.8	0.65	71.02	953	7183
20	0.25	0.6	0.85	0.57	71.00	1158	8003
21	0.2	0.7	0.9	0.51	75.00	945	6048
22	0.25	0.65	0.9	0.69	73.82	935	6615
23	0.3	0.61	0.91	0.53	76.40	856	6150
24	0.25	0.67	0.92	0.62	68.37	955	9026
25	0.25	0.7	0.95	0.53	72.07	789	4313
26	0.2	0.75	0.95	0.56	60.67	695	9160
27	0.2	0.8	1	0.75	65.43	750	11463
28	0.3	0.8	1.1	0.70	105.47	670	8190
29	1.2	0.3	1.5	1.08	157.63	375	2386
30	0.7	0.8	1.5	1.07	97.89	251	4222
31	1.2	0.35	1.55	1.40	116.22	207	4039
32	0.88	0.67	1.55	1.22	185.15	407	3826
33	1.2	0.4	1.6	1.38	99.82	267	3403

Table A.2 – (Continuation) Experimental data: superficial velocities, mixture velocities, interfacial estructure velocities, interfacial estructure frequencies, interfacial estructure amplitudes and interfacial estructure wavelength.

Run	V_{sw} [m/s]	V_{so} [m/s]	V_m [m/s]	V_{wave} [m/s]	f_{wave} [Hz]	A_{wave} [μm]	λ_{wave} [μm]
34	0.8	0.8	1.6	1.21	96.25	268	3759
35	1.22	0.4	1.62	1.35	147.48	356	3668
36	0.9	0.8	1.7	1.32	132.91	213	3785
37	1	0.8	1.8	1.49	193.15	37	4107
38	1.2	0.8	2	1.61	99.18	267	2035
39	1.5	0.5	2	1.58	169.99	335	4880
40	1.5	0.8	2.3	1.76	159.73	350	1180
41	1.7	0.6	2.3	1.62	107.42	380	1660
42	1.96	0.5	2.46	1.83	162.48	320	1127
43	1.96	0.6	2.56	1.84	153.69	325	2033
44	1.96	0.7	2.66	2.24	141.92	336	1575

APPENDIX B

Depth resolution calculation

Having that the ADC resolution of 14 bits for the range ±1 V and the average maximum and the minimum voltages were $U_{x_{2200\mu m}}$=0.51 V and $U_{x_{0\mu m}}$=0.4666 V. The ADC voltage resolution is ADC_{res}=2V/16384 levels= 122 μV/level. Thus, for the measurement range

$$\frac{U_{x_{2200\mu m}} - U_{x_{0\mu m}}}{ADC_{res}} = \frac{0.0434 \text{ V}}{122 \text{ μV/level}} = 355 \text{ levels,}$$

and the depth resolution can be estimated as

$$\frac{2200 \text{ μm-0 μm}}{355 \text{ levels}} = 6.2 \text{ μm / level}$$

Temporal resolution calculation

The measured transient time for each transmitter was 5.2 μs (Figure B.1). To have a safety margin was set a time of 6 μs.

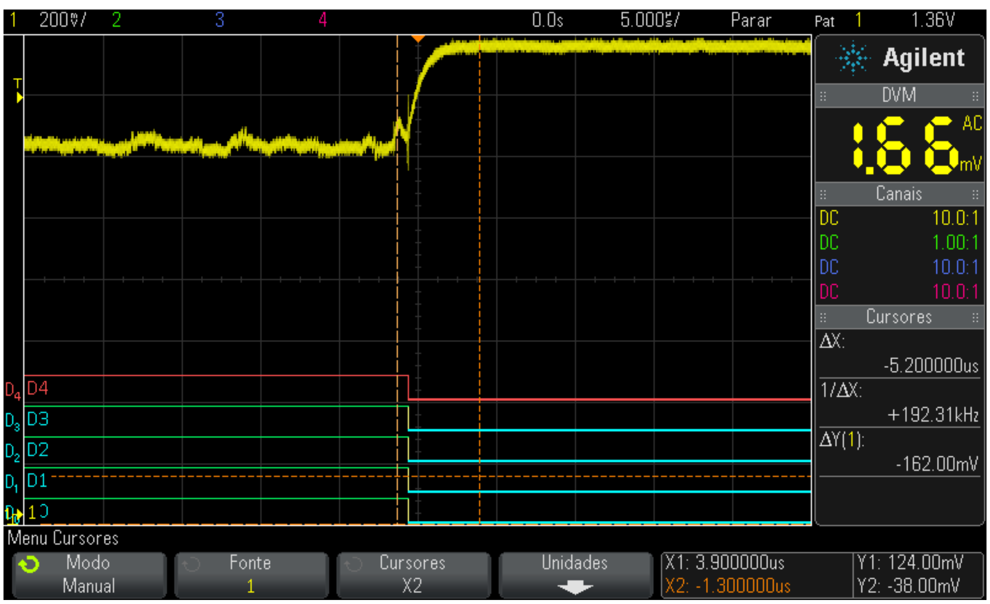

Figure B.1 – Transient time for a signal in the measurement system.

The transmission circuit has 32 transmission lines then the time to get a frame is

$$T_{32Tx} = 6 \text{ μs} \times 32 = 196 \text{ μs / frame}$$

which gives a maximum rate of frames of 5208 frames/second. In this work, it was used a frame rate of 5000 frames/second to ensure that the system was working in steady state.

APPENDIX C

List of publications

This thesis has been in part based on the following papers:

BONILLA RIAÑO, A., RODRIGUEZ, I.H., BANNWART, A. and RODRIGUEZ, O. M. H. (2015). Film Thickness Measurement in Oil-Water Pipe Flow using Image Processing Technique. In Experimental Thermal and Fluid Science, Vol.68, November 2015. (pp. 330-338). DOI: 10.1016/j.expthermflusci.2015.05.004

BONILLA RIAÑO, A., BANNWART, A. AND RODRIGUEZ, O. M. H. (2015). Film thickness planar sensor in oil-water flow: prospective study. In sensor Review Journal , Vol. 35 Iss: 2, pp.200 - 209. DOI: 10.1108/SR-09-2014-702

BONILLA RIAÑO, A. and RODRIGUEZ, O. M. H. (2015). Improvement of Dispersed Oil-Water Pipe Flow Images. Presented in IV Journeys in Multiphase Flows (JEM 2015).

BONILLA RIAÑO, A., BANNWART, A., PRASSER, H.-M., DUPONT, J., and RODRIGUEZ, O. M. H. (2014). A High Spatial and Temporal Resolution Film Thickness Sensor in Oil - Water Flows. In Instrumentation and Measurement Technology Conference (I2MTC) Proceedings, 2014 IEEE International (pp. 57–61). DOI:10.1109/I2MTC.2014.6860522

BONILLA RIAÑO, A., BANNWART, A., and RODRIGUEZ, O. M. H. (2013). Holdup Estimation in Core Flow Using g Image Processing. In Instrumentation and Measurement Technology Conference (I2MTC), 2013 IEEE International, pp. 1–5. DOI:10.1109/I2MTC.2013.6555435

Publications not included in this thesis:

RODRIGUEZ, I.H., VELASCO, H., BONILLA RIAÑO, A., HENKES, R.A.W.M. and RODRIGUEZ, O.M.H (2015). Experiments with a Wire-Mesh Sensor for Stratified and Dispersed Oil-Brine Pipe Flow. In International Journal of Multiphase Flow, Vol. 70, April 2015, pp. 113-125. DOI: 10.1016/j.ijmultiphaseflow.2014.11.011

RODRIGUEZ, I.H., VELASCO, H., BONILLA RIAÑO, A., and RODRIGUEZ, O.M.H (2014). Capacitive Wire-Mesh Sensor Measurements in Oil-Water Flow. 10TH International Conference on Heat Transfer, Fluid Dynamics and Thermodynamics (HEFAT 2014), 2014.

VELASCO, H., BONILLA RIAÑO, A., RODRIGUEZ, I.H. and RODRIGUEZ, O.M.H (2013). Evaluation of Permitivity models for holdup measurements of viscous oil in water dispersed flow. Presented in 4th International Conference on Multiphase Flow, 2013.

RODRIGUEZ, I.H., VELASCO, H., BONILLA RIAÑO, A., and RODRIGUEZ, O.M.H (2013). Experimental study on heavy oil-water dispersed flow. Presented in 4th International Conference on Multiphase Flow, 2013.

BONILLA RIAÑO, A.,VEGA, R., LENZI, K.G. and MELONI, L.G.P (2012). Design and Implementation of Fast Fourier Transform Algorithm in FPGA. In XXX Simpósio Brasileiro de Telecomunicações, 2012.